# Synchrotron Radiation Studies of Spintronic Hybrid Systems

Wenqing Liu

Doctor of Philosophy

University of York

Electronics

September 2014

# Abstract

Spintronics is an emergent interdisciplinary topic for the studies of spin-based, other than or in addition to charge-only-based physical phenomena, which promises not only new capabilities of electronic devices, but also abundant science. For applied materials, the spin ordering has long been investigated within the context of conventional ferromagnetic materials (FMs), while the study of spin generation, relaxation, and spin-orbit coupling (SOC) in semiconductors (SCs) took off only recently with the advent of spintronics and it is here that many novel materials and FM/SC hybrid structures can find their greatest potential in both science and technology. In the pursuit for such goals, the intrinsic material properties are important indicators and the artificially synthetized hybrid systems (layered FM/SC structures and FM-doped SCs) are valuable models for studying spin-dependent phenomena and could potentially be used as actual components for an eventual spintronic device. These results are expected to contribute to some of the most fundamental questions of the contemporary spintronic materials research, such as the FM/SC interfacial hybridization and magnetism, the spin and orbital ordering of ferrites, and the fundamental magnetism of doped TIs, and the proximity effects in FM/DMS and FM/doped TI heterostructures.

# List of Contents

# List of Tables

# List of Figures

# Acknowledgements

The author would like to acknowledge and thank the Ph. D supervisors, Prof. Yongbing Xu (York) and Prof. Rong Zhang (Nanjing), for their guidance. Without their full support, it is impossible to finish this rather challenging project.

The author would like to acknowledge and thank the collaborators who have provided the samples and the supporting characterizations, even though some of their results are not shown in this thesis. Dr. Fengqiu Wang (who is now a Prof. of Nanjing University, Nanjing, China) of the Cambridge Graphene Centre has provided the graphene substrate. Prof. Qingming Zhang and his team (Feng Jin and An-min Zhang) of the Physics Department, Renmin University, China has performed the Raman scattering measurement of the Fe/graphene sample. Prof. Jianghua Zhao and her team (Shuaihua Nie) of the Superlattices and Microstructures Laboratory, Chinese Academy of Science (CAS), China has provided the $Co_2FeAl/Ga_{1-x}Mn_xAs$ sample. Dr. Ping K. J. Wong has provided the $Fe_3O_4$/MgO/GaAs sample and locally performed the RHEED based on the Spintronics and Nanodevice Laboratory of the University of York. Dr. Volado Lazarov and his team (James Sizeland) of the York Physics Department has provided the $Fe_3O_4$/YZO and performed TEM measurements. Prof. Stuart S. P. Parkin of Almaden Research Center, US and Dr. Grace J. Lin of the Center for Condensed Matter Sciences, National Taiwan University, Taiwan and their teams (Ming. Y. Song) have grown the $Fe_3O_4$/MgO in the IBM research Centre and locally examined the sample quality by RHEED and electrical-transport measurements. Prof. Caroline. A. Ross and her team (Dr. Mehmet C. Onbasli) of the Department of Materials Science and Engineering, Massachusetts Institute of Technology, US have grown the YIG/GGG. Prof. Kang L. Wang and his team (Liang He, Koichi Murata, Xuefeng Kou, and Murong Lang) of the Device Research Laboratory of the University of California (UCLA), US have grown the $Bi_{2-x}Cr_xSe_3$ and locally performed RHEED and magneto-transport measurements. Prof. Yong Wang and his team (Ying Jiang) of the Electron Microscope Centre of Zhejiang University, China, performed the STEM measurement of the $Bi_{2-x}Cr_xSe_3$/YIG.

The author would also like to acknowledge and thank the colleagues who helped with theoretical caculations. Prof. Qunxiang Li and his team (Weiyi Wang and Jiajun Wang) of the National Laboratory for Physical Sciences at the Microscale, University of

Science and Technology, China performed the calculations of Fe/graphene system. Prof. Shengbai Zhang and his team (Dr. Damien West) of Rensselaer Polytechnic Institute, US performed the calculations of $Bi_{2-x}Cr_xSe_3$.

For the results solely contributed by the author, the author would like to credit the beamline scientists Dr. Paul Steadman, Dr. Peter Benock, Dr. Alexey Dobrynin, and Dr. Ray Fan of Diamond Light Source, Dr. Gunnar Öhrwall of Max-Lab, Dr. Matthew Marcus and Dr. Anthony Young of Advance Light Source (ALS) for their support with the XMCD and SQUID-VSM measurement. Dr. Jill Weaver has offered the macro of the sum rules used in this study and Dr. Gerrit van der Laan has helped checked through the XMCD results and has given valuable suggestions, especially towards the publications. The York colleagues Nick. J. Maltby and Dr. Shunpu Li have participated in most of the author's beamtime in UK and Dr. Iain Will has offered useful lab training.

This project has been made possible by funding from the Science and Technology Facilities Council (STFC) and the Natural Science Foundation of China (NSFC). The author has been funded by the University of York, Nanjing University, and the Institute of Electrical and Electronics Engineers (IEEE).

# Declaration of Authorship

The work presented in this thesis, titled "Synchrony Radiation Studies of Spintronic Hybrid Systems", represents the contribution of the author, Wenqing Liu, to the research described. It has been submitted for consideration of the research degree at the University of York and has not been submitted previously for any other qualification at this or any other institute of learning.

In all cases XMCD analysis is the sole work of the author, as has been the XMCD measurements and SQUID-VSM measurements performed in the Diamond Light Source and Max-lab. In the instances where samples have been supplied through collaborative research this is clearly noted in the text, as well as in the appendix, along with the methodologies of their growth and origins. All the sources of help, including supporting sample characterizations, theoretical simulations, and useful discussions, are acknowledged. Some of the studies included in this thesis have led to book chapters, conference presentations, and peer-reviewed publications with the author either as primary author or contributing to larger projects.

**List of Publications**

- S. H. Nie, Y. Y. Chin, W. Q. Liu, J. C. Tung, J. Lu, H. J. Lin, G. Y. Guo, K. K. Meng, L. Chen, L. J. Zhu, D. Pan, C. T. Chen, Y. B. Xu, W. S. Yan, and J. H. Zhao, "Ferromagnetic Interfacial Interaction and the Proximity Effect in a $Co_2FeAl$/(Ga,Mn)As Bilayer", *Phys. Rev. Lett.* **111**, 027203 (2013);

- W. Q. Liu, Y. B. Xu, P. K. J. Wong, N. J. Maltby, S. P. Li, X. F. Wang, J. Du, B. You, J. Wu, P. Bencok, R. Zhang, "Spin and orbital moments of nanoscale $Fe_3O_4$ epitaxial thin film on MgO/GaAs(100)", *Appl. Phys. Lett.* **104**, 142407 (2014).

- W. Q. Liu, L. He, Y. B. Xu, K. Murata, M. Lang, M. Onbasli, N. J. Maltby, S. P. Li, X.F.Wang, K. L. Wang, C. A. Ross, P. Bencok, G. van der Laan, R. Zhang,

"Enhancing Magnetic Ordering in Cr-doped $Bi_2Se_3$ using High-$T_c$ Ferromagnetic Insulator", *Nanolett*. DOI: 10.1021/nl504480g (2014).

- W. Q. Liu, M. Y. Song, N. J. Maltby, S. P. Li, J. G. Lin, M. G. Samant, S. S. P. Parkin, P. Bencok, P. Steadman, A. Dobrynin, Y. B. Xu, R. Zhang, "XMCD Study of Epitaxial Magnetite Ultrathin Film on MgO(100)", Arxiv: 1501.01803 (2015).

- J. Ge, T. S. Chen, M. Gao, X. F. Wang, X. C. Pan, M. Tang, B. Zhao, W. Q. Liu, J. Du, F. Q. Song, Y.B. Xu, R. Zhang "Evidence of layered transport of bulk carriers in Fe-doped $Bi_2Se_3$ topological insulators", *APEX*, AP141079 (2015).

- J. R. Zhang, Z. Y. Wu, Y. J. Liu, Z. P. Lv, W. Niu, X. F. Wang, J. Du, W. Q. Liu, R. Zhang, Y. B. Xu, "Fabrication and characterization of Fe-doped $In_2O_3$ nanowires", *Chin. Phys. Lett.* **32**, 037501 (2015)

- Q. Y. Xu, Y. Sheng, M. Khalid, Y. Q. Cao, Y. T. Wang, X. B. Qiu, W. Zhang, M. C. He, S. Q. Zhou, Q. Li, D. Wu, Y. Zhai, W. Q. Liu, Y. B. Xu, and J. Du, "Magnetic interactions in $BiFe_{0.5}Mn_{0.5}O_3$ films and $BiFeO_3$/$BiMnO_3$ superlattices", *Sci. Rept.*, SREP-14-06656 (accepted);

- W. Q. Liu, W. Y. Wang, J. J. Wang, F. Q. Wang, C. Lu, F. Jin, A. Zhang, Y. B. Xu, Q. X. Li, Q. M. Zhang, P. Bencok, G. van der Laan, R. Zhang, "Interface Magnetism of Graphene and Ferromagnetic Transition Metals", *Phys. Rev. Lett.* LY14446 (under review).

- W. Q. Liu, L. He, Y. B. Xu, K. Murata, K. L. Wang, P. Bencok, R. Zhang, "Direct Observation of a Robust Surface Magnetization in Topological Insulator" (to be submitted).

- W. Q. Liu, L. He, Y. B. Xu, K. Murata, K. L. Wang, P. Bencok, R. Zhang, "Spin and Orbital Ordering of Magnetically Doped Topological Insulators" (to be submitted).

- W. Q. Liu, Y. B. Xu, N. J. Maltby, S. P. Li, V. Lazarov, P. Bencok, R. Zhang, "Site-Specific Study of Verwey Transition" (to be submitted).

- W. Q. Liu and Y. B. Xu, "High Efficient Spintronic Materials", *Prog. Mater. Sci.*, (invited and to be published in 2015).

- W. Q. Liu and Y. B. Xu, "The XMCD Studies of Magnetite", *SPIN*, (invited and to be published in 2015).

- W. Q. Liu, Y. B. Xu, S. Morton, J. Weaver and G. van der Laan, "XMCD Studies of Spintronic Materials", chapter for "Handbook of Spintronics", Springer, (invited and to be published in 2015).

- Y. B. Xu, P. K. J. Wong, W. Q. Liu, Y. X. Lu, S. Hassan, D. X. Niu, I. Will, E. Ahmad, "Hybrid Magnetic-Semiconductor Spintronic materials", chapter for "Handbook of Spintronics", *Springer*, (to be published in 2015).

**List of Presentations**

- W. Q. Liu, L. He, Y. B. Xu, K. Murata, M. Lang, M. Onbasli, N. J. Maltby, S. P. Li, X. F. Wang, K. L. Wang, C. A. Ross, P. Bencok, G. van der Laan, R. Zhang, "Evidence for ferromagnetic coupling at the TI/FMI interface", **talk**, CE-10, *IEEE Intermag,* Beijing (2015).

- W. Q. Liu, D. West, L. He, S. B. Zhang, Y. B. Xu, R. Zhang, K. L. Wang, "The magnetic moment of Cr-doped $Bi_2Se_3$ thin film topological insulator", **talk**, CC-08, *IEEE Intermag,* Beijing (2015).

- W. Q. Liu, Y. B. Xu, "Atomic-scale interfacial magnetization of FM/SC heterostructure", **talk**, AC-08, *IEEE Intermag,* Beijing (2015).

- W. Q. Liu, P. K. J. Wong, N. J. Maltby, S. P. Li, Y. B. Xu, R. Zhang, "The Spin and Orbital Ordering of Magnetite Thin Film across Verwey Transition", **talk**, GB-04, *IEEE Intermag,* Beijing (2015).

- W. Q. Liu, Y. B. Xu, "Probing the Fundamental Magnetism with Advanced

Spectroscopy Techniques", **invited talk**, 5th *Annual World Congress of Nanoscience & Technology*, Xi'an, (2015).

- W. Q. Liu, L. He, Y. B. Xu, K. Murata, M. Lang, M. Onbasli, N. J. Maltby, S. P. Li, X. F. Wang, K. L. Wang, C. A. Ross, P. Bencok, G. van der Laan, R. Zhang, "Proximity Effect in Cr-doped $Bi_2Se_3$/YIG Bilayer Structure", **talk,** AF-11, *59th MMM,* Honolulu (2014).

- W. Q. Liu, W. Y. Wang, J. J. Wang, F. Jin, A. Zhang, F. Wang, C. Lu, N. J. Maltby, S. P. Li, Q. Li, Q. Zhang, P. Bencok, Y. B. Xu, R. Zhang, "The Magnetic and Electronic Structure of Fe/Graphene Interface", **talk** DF-14, *59th MMM,* Honolulu (2014).

- W. Q. Liu, M. Song, N. J. Maltby, S. P. Li, J. Lin, S. S. Parkin, P. Bencok, Y. B.Xu, R. Zhang, "XMCD Study of Epitaxial Magnetite Thin Films", **poster,** CQ-14, *59th MMM,* Honolulu (2014).

- J. Sizeland, X. Lu, D. Gilks, V. Lazarov, J. Wu, Y. B. Xu, W. Q. Liu, "Ultrafast Magnetization Dynamics Investigation of Verwey Transition in $Fe_3O_4$ thin films", **poster**, GP-05, *59th MMM,* Honolulu (2014).

- W. Q. Liu, L. He, D. West, K. Murata, K. L. Wang, S. B. Zhang, Y. B. Xu, R. Zhang, "Spin and Orbital Ordering of Magnetically Doped Topological Insulators", **poster,** A1-P17, 3rd international conference of AUMS, Haikou (2014).

- W. Q. Liu, L. He, K. Murata, N. J. Maltby, S. P. Li, J. Wu, P. Bencok, K. L. Wang, Y. B. Xu, "XMCD study of the ferromagnetism in Cr-doped $Bi_2Se_3$" **talk**, DG-08, *IEEE Intermag*, Dresden (2014).

- W. Q. Liu, N. J. Maltby, S. P. Li, C. Lu, F. Q. Wang, J. Wu, P. Bencok, G. van der Laan, Y. B. Xu, "XMCD study of the interface magnetism between graphene and ferromagnetic transition metals", **talk,** DG-04, *IEEE Intermag,* Dresden (2014).

- W. Q. Liu, P. K. J. Wong, N. J. Maltby, S. P. Li, J. Wu, P. Bencok, Y. B. Xu, "Spin and orbital moments of nanoscale $Fe_3O_4$ epitaxial thin film on MgO/GaAs(100)",

**poster**, FS-10, *IEEE Intermag*, Dresden (2014).

- P. K. J. Wong, W. Q. Liu, J. Sizeland, W. Zhang, J. Wu, I. G. Will, Y. B. Xu, R. Zhang, I. Farrer, and D. A. Ritchie, "Spin transport in Fe/GaAs Vertical Spin-Valves", **poster,** AX-03*, 58th MMM* (2013).

- Y. B. Xu, Y. X. Lu, P. K. J. Wong, Z. C. Huang, Y. Zhai, W. Q. Liu, "$Fe_3O_4$ Epitaxial Films on GaAs(100), MgO/GaAs(100), and GaN(0001)", **Poster,** *IOP Current Research in Magnetism,* Durham (2011).

# 1 Chapter I Introduction

## 1.1 Introduction

Spintronics, also known as spin electronics, is an exciting new topic of physics and electronics. It studies spin-based, other than or in addition to charge-only-based physical phenomena, which promises not only new capabilities of electronic devices, but also interesting science.[1]

From an industry point of view, spintronics is expected to offer solutions to the so-called "IT crisis". Since the mid 20th century, the semiconductor (SC) based electronics industry has followed the famous Moore's law that the number of transistors per square inch increases exponentially, i.e., doubles every eighteen months.[2] However, this trend will eventually hit a limit where the computing units enter the regime of nanometer scale and the quantum mechanisms starts to dominate. One of the key problems that restrict further device minimization is the electron tunneling effect. When the length of the gate is scaled down to 2 – 5 nm (which can be predicated within the next ten years if the Moore's law applies), considerable leakage current from the source to drain can occur. Another issue is the growing power density in circuits, leading to the ever-increasing operating temperature. This heating effect has serious consequences for the reliability and controllability of the shrinking transistors. To engineer new transistors and electronic circuits that can break through the physical limitations has been the major challenge of the contemporary IT industry. Spintronics is involved in this subject by offering novel material/structure candidates to which the quantum computation is applicable, or in other words, where the spin of electrons can be utilized as an extra degree of freedom for data processing to create spintronics devices. Such devices are expected to present abundant desirable properties including high processing speed, low power consumption and non-volatile memory storage capabilities etc..

Meanwhile, the spin-based or related phenomena themselves are valuable subjects for fundamental physics. Spin has long been a mysterious quantity in the history of physics. It is a solely quantum phenomenon and has no counterpart in classical mechanics, which makes it an ideal platform to examine the many concepts

and hypotheses in quantum mechanism and condensed matter physics theories. Nowadays, spin has been generally accepted as an intrinsic form of angular momentum carried by elementary particles, composite particles, and atomic nuclei. However, a comprehensive description of spin, spintronics and their related phenomena (such as spin scattering, spin transfer, spin wave, spin-orbital interactions etc.) is still physically and mathematically subtle.

The rest of the chapter presents an overall introduction to the subject, of this thesis (i.e. spintronics hybrid systems) by reviewing a few historical moments of the discovery of spin, followed by highlighting some landmarks of the recent twenty years development of spintronics. Following that, an overview of this thesis will be given at the end of the chapter.

## 1.2 Spin

As a purely quantum-mechanical entity, the concept of spin was first proposed by Wolfgang Pauli in 1924. Here the author highlights three experimental observations of spin in history.

**Sodium spectrum fine structures**. The earliest experiment revealing a hint of "spin" might be the observation of discrete lines in the emission spectra of atomic gases. As early as 1880s, Albert A. Michelson found that some atomic spectrum lines actually consist of two or more closely spaced lines, called the fine structure. For example, the sodium spectrum is dominated by the brightest line known as the sodium D-lines ($\lambda_D$ = 589.3 nm), arising from the transition from the 3*p* to the 3*s* levels. When taking a close look, one could see that $\lambda_D$ splits in two lines, namely $\lambda_{D1}$ = 589.6 nm and $\lambda_{D2}$ = 589.0 nm (see Figure 1-1 for the interpretation). Before that, the energy levels of Hydrogen and Hydrogen-like atoms, such as Lithium and Sodium, had been well explained by the Bohr model. Yet such fine structure seems to imply an unknown angular momentum beyond Bohr's picture.

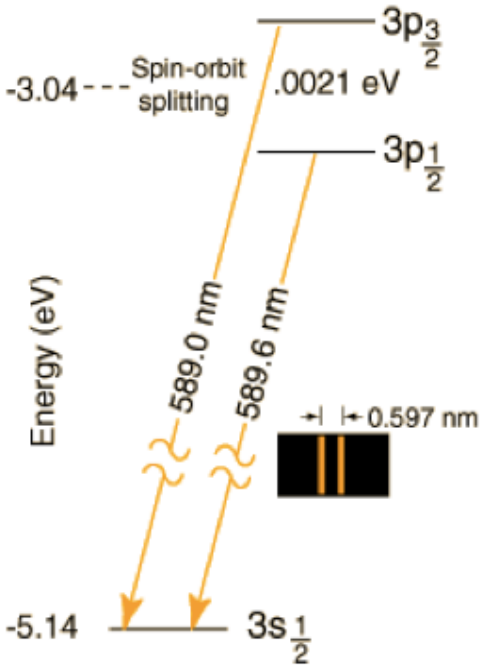


Figure 1-1 | Conceptual illustration of the spin-induced spectral splitting, or the fine structure of sodium D-lines, in which the 3*p* level degenerates into $3p_{3/2}$ and $3p_{1/2}$, resulting in two closely spaced lines of the spectrum. Image adapted from the Internet (http://hyperphysics.phy-astr.gsu.edu/hbase/quantum/sodzee.html).

**Anomalous Zeeman Effect.** Another degeneration phenomenon with significance is the spectral line splitting of atoms in the presence of static magnetic field. In 1912, Friedrich Paschen and Ernst E. A. Back found that the sodium D1 splits into 4 lines and D2 splits into 6 lines in a magnetic field below 50 kOe, which was referred as Paschen-Back effect or anomalous Zeeman effect. Considering the orbital-field interaction, the spectrum is only expected to split into $2l+1$ lines (always an odd number), in which $l$ is the electron orbital quantum number (will be introduced in the next chapter). Such splitting of even numbers can be a sign of extra momentum in addition to the orbital momentum (see Figure 1-2).

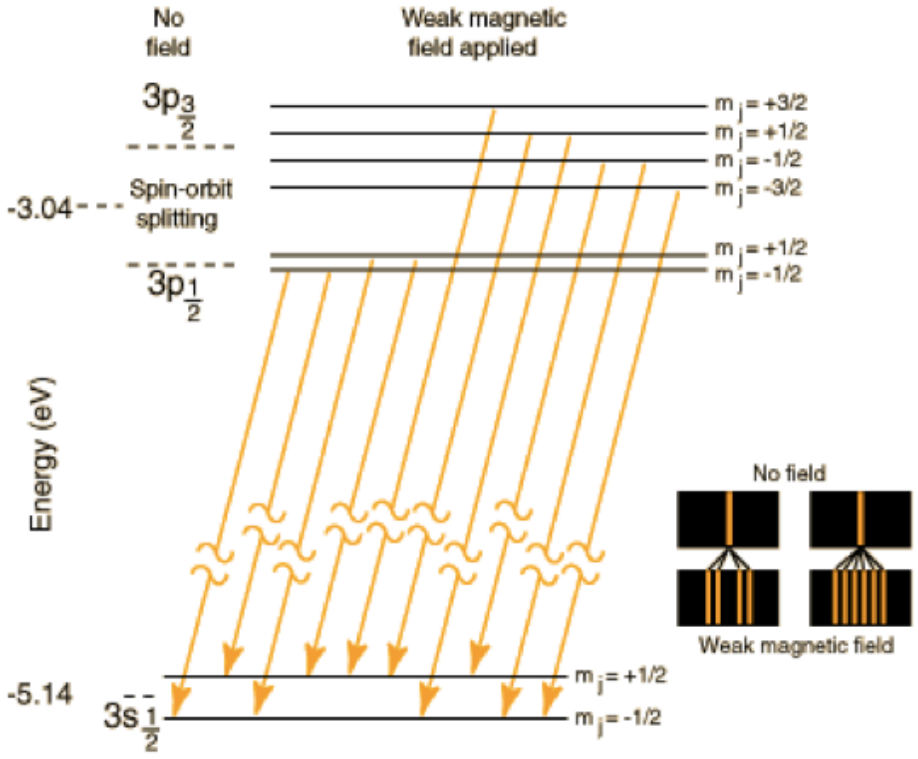


Figure 1-2 | Conceptual illustration of Anomalous Zeeman effect, or Paschen-Back effect, in which sodium D1 and D2 furthermore split into 4 and 6 lines in the presence of static magnetic field. Image adapted from the Internet (http://hyperphysics.phy-astr.gsu.edu/hbase/quantum/sodzee.html).

**Stern–Gerlach Experiment**. A furthermore clear illustration of electron spin is the Stern-Gerlach experiment in 1922, named after German physicists Otto Stern and Walther Gerlach. The experiment is essentially set up with a furnace with silver, a collimating slit, an inhomogeneous magnetic field and a photographic plate (see Figure 1-3). Electrically neutral atoms are heated, passing through the special shaped magnet and eventually captured by the fluorescent screen, where the distribution of these atoms is a function of the force they have sensed in the non-uniform magnetic field. In classic electromagnetism, the force applied on each electron is

$$\vec{F} = -\nabla V = \nabla(\vec{M} \bullet \vec{B})$$

Equation 1-1

in which V, $\boldsymbol{M}$, and $\boldsymbol{B}$, respectively, represent the potential energy, the magnetic moment of silver atoms and the flux density of the magnetic field. Considering the orbital magnetic moment only, one could expect the distribution to be continuous and uniformly filled on the screen, however, in reality the beam turns out to be fragmented into two equal components.

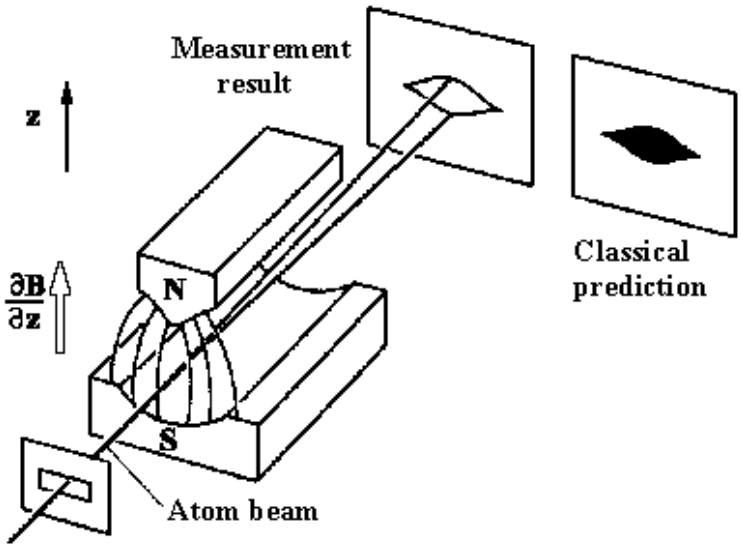


Figure 1-3 | Schematic diagram of Stern-Gerlach experiment, in which the neutral silver atomic beam go through an inhomogeneous magnetic field. One can observe fragmentation of the incident beam into two symmetrical bright lines in z direction. Image adapted from Wikipedia (http://en.wikipedia.org/wiki/Stern–Gerlach_ experiment).

All the above experiments are of historical significance, as they give not only the insight into the quantum nature of atoms, but also the necessity to introduce electron spin. Spectral fine structure and Paschen-Back effect are rather combined effects from spin-orbital interaction, because $l \neq 0$ for the sodium $p$ electrons. Even though they are important discoveries that people cannot explain if merely considering the electron orbital momentum. Stern-Gerlach experiment takes advantage of the $s$ electrons of silver, in which the spin-dependent effect dominates. It has avoided the effect of electron orbital momentum and unambiguously exhibited the two-value degree of freedom of spin momentum.

## 1.3 Spintronics

### 1.3.1 GMR and the first generation spintronics - metallic multilayers

#### *1.3.1.1 GMR*

The rise of spintronics can be marked by the discovery of the Giant Magneto-Resistive (GMR) effect in 1988 by A. Fert[3] and P. Grünberg[4] (who shared the 2007 Nobel Prize of physics). In their experiment, the magnetoresistance (MR) effect as high as 50% at low temperature of Fe/Cr multilayers was observed (see Figure 1-4) and that the ferromagnetic Fe layers are antiferromagnetically coupled through the non-magnetic Cr interlayers. Later Parkin *et al*.[5] found that the interlayer coupling between the magnetic layers can oscillate between ferromagnetic and antiferromagnetic exchange depending on the thickness of the non-magnetic layers (see Figure 1-5). Although the earliest GMR effect had been demonstrated in the current in plane (CIP) geometry, it was later suggested by T. Valet and A. Fert[6] that longer spin diffusion length and an even higher effect could be realized in current perpendicular to plane (CPP) geometry.

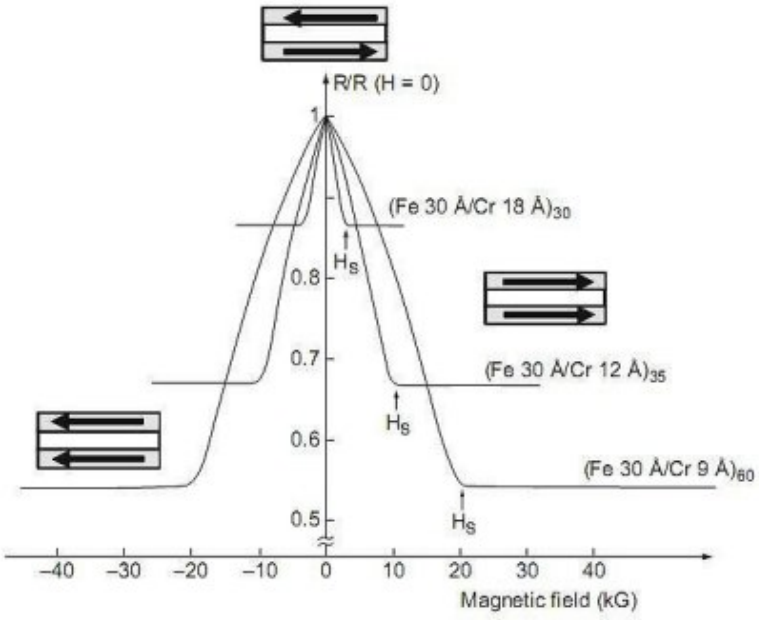


Figure 1-4 | The experimental diagram of the GMR effect of three Fe/Cr superlattices at 4.2 K in CIP geometry. Data are normalized for all the samples. Image adapted from the literature.[3]

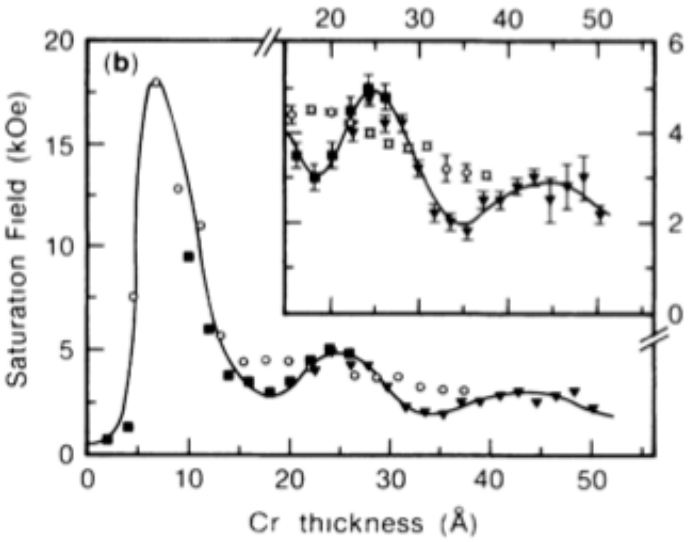


Figure 1-5 | The experimental diagram of the exchange coupling oscillations and magnetoresistance in Co/Cr superlattice structures, i.e., the saturation field vs. Cr thickness. Image adapted from the literature.[5]

#### *1.3.1.2 Spin valve*

The GMR effect has been demonstrated based on a successive FM/NM/FM trilayer structure, known as a spin-valve, in which the two FM layers have distinctly different magnetic coercive fields ($H_c$). Due to the shape anisotropy, the magnetization lies in the plane of the FM layer which gives rise to two possible magnetic configurations of the spin valve. One of the FM layer is magnetically hard, such that relatively large magnetic fields are required to switch its magnetization, whilst the other layer is magnetically soft, requiring much smaller magnetic fields to change its magnetization direction.[7] Considering an increasing magnetic field applied to the spin valve, initially the field is only large enough to saturate the soft layer and thus at this moment the two FM layers have antiparallel magnetization. And when the field is sufficient to re-orientate both the soft and the hard layers, the two are aligned in parallel. This alignment of the magnetization of the two FM layers relative to each other changes the electrical resistance of spin valve between two values, also known as spin scattering.

#### *1.3.1.3 Two-current model*

The principals underlying spin valve can be qualitatively interpreted by the Mott's two current model, which was proposed as early as 1936 to explain the sudden increase in resistivity of ferromagnetic metals as they are heated above the $T_c$. Mott's mode assumes that the electrical conductivity in metals can be described in terms of two independent conducting channels, corresponding to the up-spin and spin-down electrons respectively. It also assumes that the two spin channels do not mix over long distances and thus the electrical conduction of them occurs simultaneously. In spin valve, for the parallel-aligned FM layers, the spin-up electrons pass through the structure almost without scattering while the spin-down electrons are scattered strongly within both FM layers. On the contrary, both the up-spin and spin-down electrons are scattered strongly within one of the ferromagnetic layers for the antiparallel-aligned trilayer.

By the two current model, the total resistance of parallel $R_{\uparrow\uparrow}$ and anti-parallel $R_{\uparrow\downarrow}$ configuration can be written as

$$R_{\uparrow\uparrow} \propto \frac{2\rho_{\uparrow}\rho_{\downarrow}}{\rho_{\uparrow}+\rho_{\downarrow}}, \quad R_{\uparrow\downarrow} \propto \frac{\rho_{\uparrow}+\rho_{\downarrow}}{2}$$

Equation 1-2

where $\rho_{\uparrow}$ and $\rho_{\downarrow}$ represent the resistivity of the spin-up and spin-down channels, referring to the electron spin parallel and antiparallel with the magnetization direction of the magnetic layer, respectively. According to Mott's s-d scattering theory, $\rho_{\uparrow} << \rho_{\downarrow}$. From Equation 1-2, one can immediately have $R_{\uparrow\uparrow} < R_{\uparrow\downarrow}$ Figure 1-6 presents a schematic illustration of two current model, in which the spin transport in parallel aligned trilayer (left) are less scattered than that in anti-parallel aligned trilayer (right). If one defines GMR as

$$GMR \propto \frac{R_{\uparrow\downarrow} - R_{\uparrow\uparrow}}{R_{\uparrow\uparrow}}$$

Equation 1-3

its amplitude will then be determined by the ratio of $\rho_{\uparrow}$ and $\rho_{\downarrow}$.

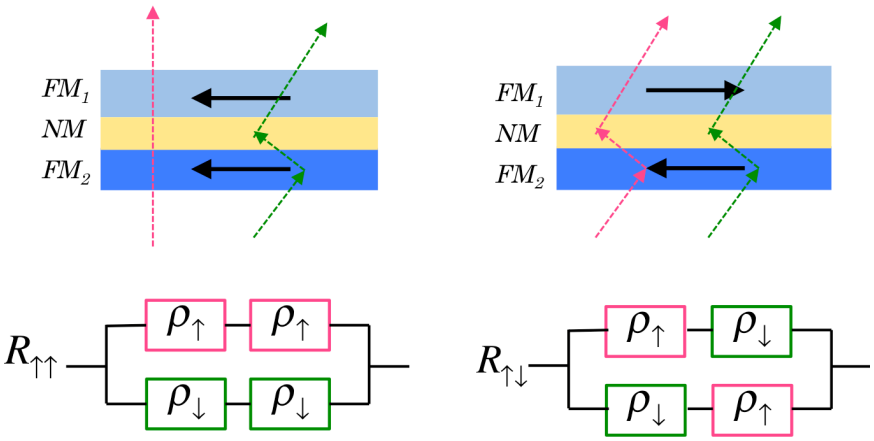


Figure 1-6 | Schematic illustration of two current model, in which the spin transport in parallel aligned trilayer (left) are less scattered than that in anti-parallel aligned trilayer (right) Bottom panels show the corresponding resistor network.

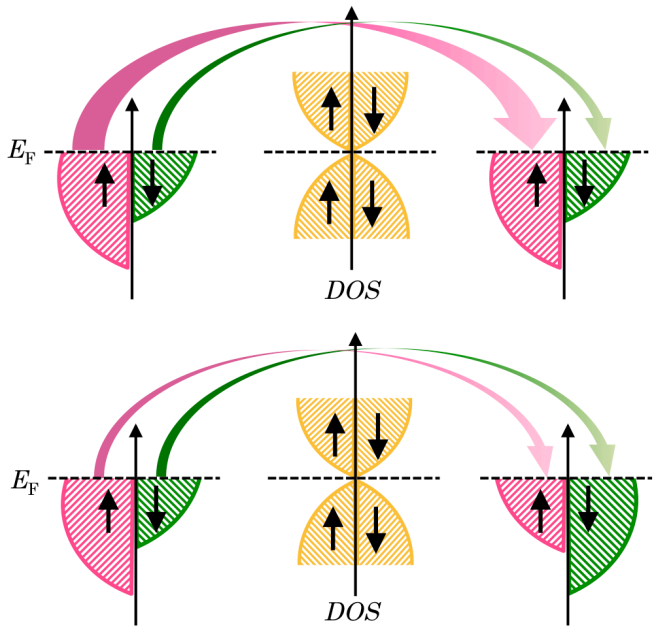


Figure 1-7 | Conceptual illustration of the origin of different spin scattering rate in a spin valve trilateral structure, associated with the relative asymmetry of the DOSs near the $E_F$ of the two FM layers

The different spin scattering rate between the up- and down- spin channels is proportional to the asymmetry of the density of states (DOSs) near the $E_F$. Figure 1-7 presents a conceptual illustration of spin scattering. In the magnetized FM layers, the DOSs differ between the spin-up and down spins and hence have more states available to one spin orientation than another. When a bias voltage is placed across FM/NM/FM trilayer, electrons will pass through this structure depending on the availability of free states for its spin direction. If two magnetic layers are parallel (Figure 1-7 upper row), a majority of electrons in one will find many states of similar orientation in the other, causing a large current to tunnel through and a lowering of overall resistance. On the other hand, if they are antiparallel (Figure 1-7 lower row), both spin directions will encounter a bottleneck in either of the two plates, resulting in a higher total resistance.

#### *1.3.1.4 The significance of GMR*

Shortly after the successful demonstration of GMR, a device based on this effect was quickly implemented by IBM in the form of a GMR read head for hard disk divers (HDD) in 1991, which had increased the HDD areal recording density by three orders of magnitude within ten years. Furthermore in 1995, by replacing the NM spacer layer of the spin valve by a thin non-magnetic insulator, magnetic tunnel junctions (MTJ) emerged[8] and was then applied to Magnetic Random Access Memory (MRAM).

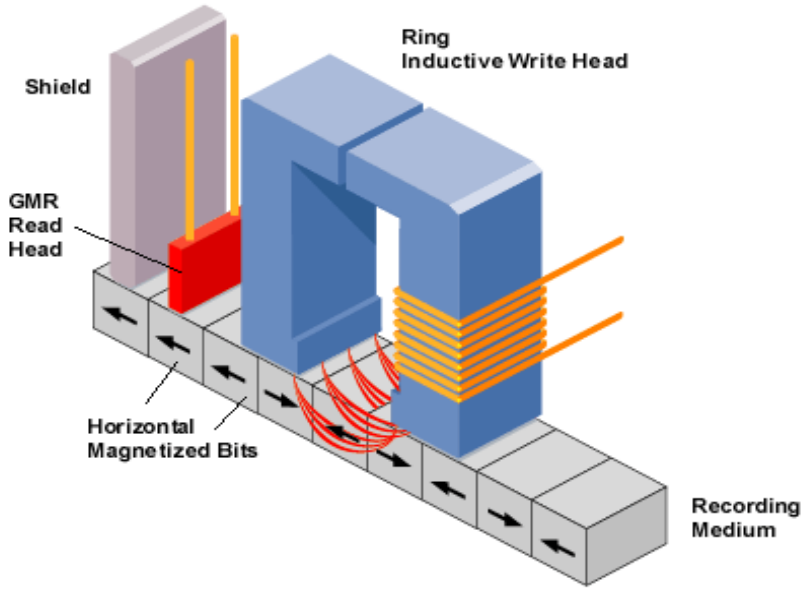


Figure 1-8 | The schematic structure of the modern HDD recording introduced by IBM in 1991, using inductive coils for writing and GMR heads for reading. Image adapted from the internet (http://www.pcmag.com/encyclopedia/term/50247/read-write-head).

### 1.3.2 Spin-FET and the second generation spintronics – FM/SC hybrid systems

#### *1.3.2.1 FM/SC hybrid spintronics*

The great success of GMR and its derivatives (usually classified as the first generation spintronics) have boosted the research and technology of spin-based phenomena and has encouraged people to move forward an even more fascinating step, which is to induce spin polarization into non-magnetic or paramagnetic semiconductors (SC), referred as spin injection. FM/SC hybrid spintronic systems combine the desirable properties of both SC and FM, and could provide new types of control of conduction in electronic devices. Using SCs for spintronic applications bears several distinguished advantages over the aforementioned metal-based GMR devices. Unlimited to the context of spintronics, SCs have the ability to amplify signal and serve as a multi-functional device.[9] Easy integration of novel spin-based architectures with the concrete

SC technology creates a strong bond between these self-contained bodies.

The transport and the manipulation of carrier spins represent two key elements of SC spintronics. The electron spin relaxation time in SCs is found to be several orders of magnitude longer than the electron momentum and energy relaxation times.[10] Further experimental signatures indicate that electrons in GaAs can be dragged over a distance of 100 $\mu$m without losing their spin coherence using an electric field.[11] These observations suggest that spin information could be transported efficiently in a given channel length. Another benefit exists in the flexibility of varying carrier doping profiles in the SCs, which not only allows the tailoring of specific purposes in the spintronic devices design, but also opens up opportunities for realizing novel physical phenomena. One particular example has been the spin Hall effect (SHE), by which a dissipationless spin current could exist in the absence of a net charge current in suitable SCs.[12, 13, 14]

#### *1.3.2.2 Spin injection*

Pioneering work on the creation of nonequilibrium spin by means of transport, optical or resonance methods pave the way of spin injection. The earliest experimental signature of diffusive spin transport in SC can be tracked back to 1973 by Clark and Feher,[15] while there was little convincing experimental evidence supporting that electrical spin injection from FMs into SCs was possible. Optical pumping is another widely used technique for generating highly polarized carriers in SCs by irradiation with circularly polarized light, decided by a competition between the creation of nonequilibrium spin and factors such as carrier recombination and spin relaxation in the system.[16] The third method to introduce magnetism into SCs is by direct magnetic doping and the magnetically doped SCs, known as DMSs, which can globally form the long-order magnetic phase under an optimized synthesis condition. Figure 1-9 presents a conceptual illustration of spin-based electronic devices. Two representative products bred by the incorporation of magnetism, photonics and SC technologies are the spin field effect transistors (FETs) and the spin light-emitting diodes (LEDs), which, respectively, will be introduced in the following two sub-sections.

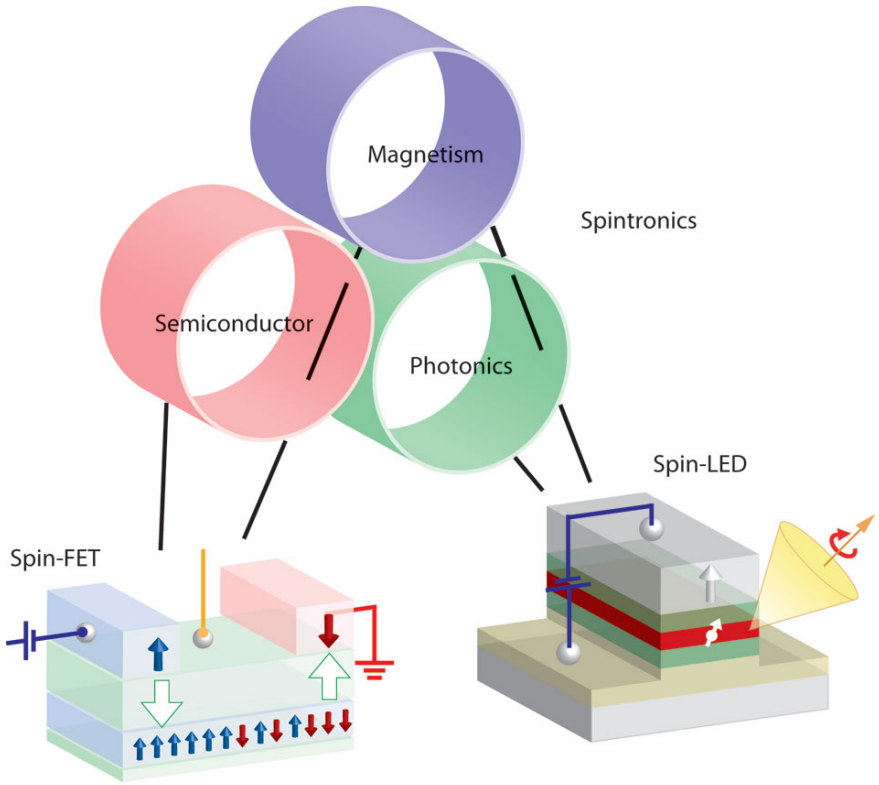


Figure 1-9 | Conceptual illustration of spin-based electronic devices. In a spin-FET, spin-polarized electrons are injected from a source ferromagnet into a semiconductor and detected using a ferromagnetic drain electrode. In a spin-LED, circularly polarized light emission also occurs under spin injection. Image adapted from the literature.[17]

#### *1.3.2.3 Spin FET*

A large portion of the research work reported to date in the hybrid spintronics community was very much stimulated by the novel idea of Datta and Das[18] whom proposed the spin FET – an analogy of the conventional FETs, as illustrated in Figure 1-9 (left). In such devices, spin-polarized electrons are generated from the first FM source, injected into the SC channel and detected by the second FM electrode. During this process, transport of the electron spins is confined in a high mobility two-dimensional electron gas (2DEG) channel and can be manipulated by the application of a gate voltage.[19] Without bias from the gate, the relative magnetization directions in the source and drain dominate the conductivity in the device, while applying a gate voltage

across the channel, the spin polarized electrons experience an effective magnetic field due to the Rashba spin-orbit interaction leading to precession of spin of the electrons and consequently a change in polarization of the injected current. The spin FET combines the functionality of passive thin film devices and active SCs structures, which is a fundamental goal for which many researchers are pursuing today. The spin FET is structurally similar to the conventional FETs, e.g. the metal-oxide field effect transistor (MOSFET) but functions by a remarkably different mechanism. Since only a small energy and a short period of time are needed to change the spins precession compared to that required in a MOSFET where the channel needs to be under inversion, spin FETs are expected to present high computing speed with low power consumption.[18, 20, 21, 22]

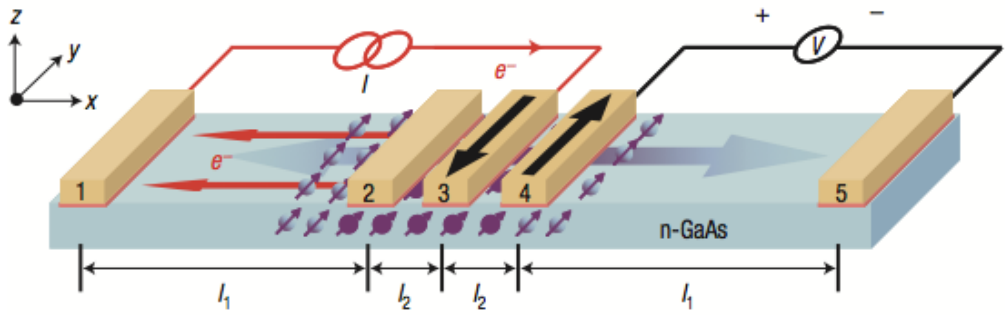


Figure 1-10 | Schematic diagram of the nonlocal experiment. Electron spins are injected into the GaAs with a Fe/AlGaAs Schottky tunnel barrier (contact 3). Due to diffusion, some injected spins will diffuse in the opposite direction from the charge current. The voltage measured at the second Fe contact (contact 4) is dependent on the relative magnetization orientation of the two Fe contacts (contact 3 and 4), leading to the electrical spin detection. Image adapted from the literature.[24]

The idea of spin FET also stands for an all-electrical device design (compared with the optical pumping and detecting of spin in spin LED, which will be introduced in the following sub-section). A notable advancement has been the detection of spin dependent effects in the nonlocal device geometries performed by Lou *et al.*,[23, 24] as presented in Figure 1-10 | Schematic diagram of the nonlocal experiment. Electron spins are injected into the GaAs with a Fe/AlGaAs Schottky tunnel barrier (contact 3). Due to diffusion, some injected spins will diffuse in the opposite direction from the charge

current. The voltage measured at the second Fe contact (contact 4) is dependent on the relative magnetization orientation of the two Fe contacts (contact 3 and 4), leading to the electrical spin detection. The FM/SC interfacial mixture, magnetic dead layer, and conductivity mismatch (will be introduced in Chapter II) are the major obstacles for the electrical spin injection, which limit the efficiency generally below ~10% at RT (ambiguity may exist here due to the different definitions). This situation was later improved by inserting spin dependent tunneling barriers (which also led to the successful spin injection in spin LEDs with the tunneling barriers, see the following sub-section). It worth mention that although earlier investigations of spin injection and accumulation have been mainly focused on the classical SCs such as GaAs,[25, 26] InAs,[27, 28] and GaN[29, 30] etc., a new trend of the very recent few years rises, directed toward 2D materials such as graphene and TIs, (will be introduced in Chapter II). Figure 1-11 presents a schematic diagram of a spin FET in which the channel is a TI nanoribbon, in which the electrons with opposite spins move in opposite directions as the red arrows indicate.[33] This spin polarization could prove more effective than the regular Rashba-coupled 2DEG counterpart.[31, 32]

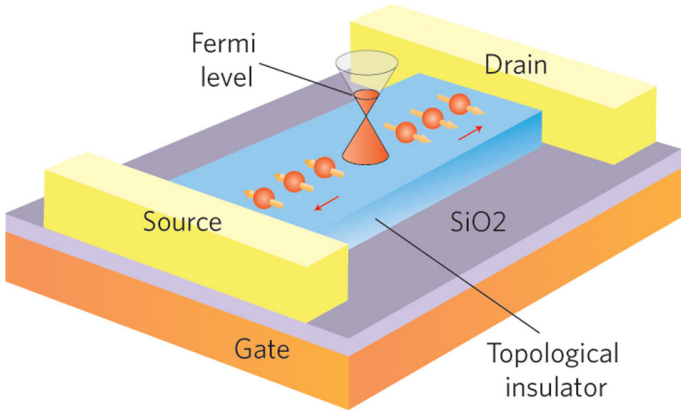


Figure 1-11 | Schematic diagram of a spin FET in which the channel is a TI nanoribbon, in which the electrons with opposite spins move in opposite directions as the red arrows indicate The spins of the surface electrons (orange arrows) are also polarized, and electrons with opposite spins move in opposite directions (red arrows). Image adapted from the literature.[33]

#### 1.3.2.4 Spin LED

Optical pumping is another widely used technique for generating highly polarized carriers in SCs by illumination with circularly polarized light.[16] In this process, the spin polarization is determined by a competition between the creation of non-equilibrium spin and factors such as carrier recombination and spin relaxation in the system. The recombination in this case occurs between the photo-excited spin polarized electrons and the unpolarized holes and is accompanied by a partially polarized luminescence.[34] Because the inter-band transition probabilities for the polarized electrons follows the optical selection rule, quantities such as spin relaxation time, recombination time and spin orientation can be obtained by analyzing such electroluminescence. Zhu *et al.*[25] demonstrated in 2001, for the first time, with the use of a ferromagnetic Schottky tunnel junction to inject spin polarized electrons from Fe into a GaAs/(In,Ga)As quantum well structure. Over the years, this scheme has been routinely used as a detection methodology for measuring spin injection efficiency, as it is less ambiguous than those based on resistance measurements and allows angle resolved studies.[35, 36, 37] One of the most striking results was reported by Jonker *et al.*,[38] who demonstrated a spin injection efficiency of 30%, corresponding to an injected spin polarization from the Fe electrode of approximately 13%, using a reverse-biased Fe/AlGaAs Schottky diode (see Figure 1-12).

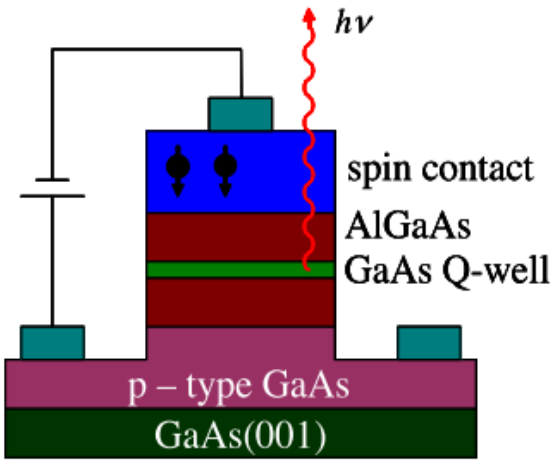


Figure 1-12 | Schematics diagram of a reverse-biased spin LED using ZnMnSe as the injector and AlGaAs GaAs as the quantum well. Image adapted from the literature.[38]

#### *1.3.2.5 DMSs*

One of the most useful aspects of SCs resides in the ability to dope them with impurities to change their electrical properties. This approach can be followed to introduce magnetic ions into non-magnetic SCs to make them magnetic.[39] The concept behind it is that to transfer spin between similar materials would be a simpler task than over a metal-SC interface due to the retained control over band-gap engineering. The long established presence of spin filtering effects in these SCs[40] and more recently observed propensity for spontaneous[41, 42] or field controlled[43, 44] magnetic ordering add to their viability in this field. The early experimental efforts on the demonstration of DMSs started from II-VI (such as CdTe and ZnSe) in which the transition metal ions (such as Mn) are easy to be doped to high concentrations.[45] The fabrication of III–V DMSs, on the other hand, was limited mostly to (In,Mn)As,[41] (Ga,Mn)Sb,[46] and (Ga,As)Mn,[42, 47, 48] in which demonstrably carrier-mediated ferromagnetism already persists.

While DMSs may offer opportunities of easy integration with conventional SC devices, it is however a great challenge to improve the quality of DMS and in particular to increase their $T_c$.[49] For example, (Ga,As)Mn is a technological important material due to its potential use in short-range optical communications, however, whose highest $T_c$ up to now is around 200 K[48, 47, 50] after combining ways of heavy Mn doping, nano-patterning, optimizing the growth conditions, and post-growth annealing (see Figure 1-13). RT ferromagnetism has been predicted and demonstrated in magnetic oxide SCs such as Co- and Mn-doped ZnO, though debates exist on whether the ferromagnetism obtained in diluted SC oxides is intrinsic or not.[51]

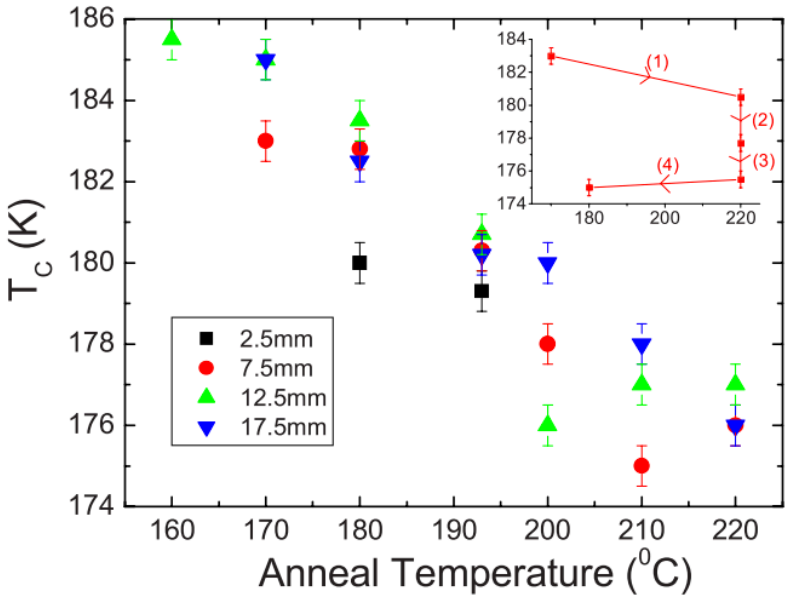


Figure 1-13 | $T_c$ of (Ga,Mn)As after annealing for 2.6 h (220 °C), 5.2 h (210 °C),13 h (200 °C),18 h (193 °C), 48 h (180 °C), 116 h (170 °C), and 280 h (160 °C). Inset: $T_c$ for a sample at 170 °C for 116 h then at 220 °C for (1 ) 1 h (2) 2 h, and (3) 2 h intervals, then at 180 °C for 48 h (4). Image adapted form the literature.[47]

## 1.4 Overview of this thesis

This thesis presents the study of a selection of spintronics hybrid systems, particularly by means of the synchrony radiation technique, i.e. XMCD, in combination with a series of in-house electronic, magnetic and crystallinity characterization techniques, such as the superconducting quantum interference device – vibrating sample magnetometer (SQUID-VSM), magneto-transport, and transmission electron microscope (TEM) measurements and theoretical tools like first-principals simulations.

The following chapter follows the historical path in introducing some most relevant concepts of magnetism, followed by a review of the recent advances in hybrid material synthesis and spin device architectures that are found promising towards future applications. Material systems of relevance are introduced, including the FM/SC heterostructures, the magnetically coupled graphene, the half metallic materials (i.e. magnetite and Heusler alloy), and the magnetically doped topological insulators (TIs), aiming to provide some useful background knowledge on the understanding of the experimental works and the motivations presented in this thesis.

Chapter III presents the working principals and set up details of the experimental tools, which have facilitated the studies of this project. These techniques are classified into two main categories: the sample fabrication techniques and characterization techniques and later furthermore breaks down into in-house characterization techniques and synchrotron-based characterization techniques.

Chapter IV demonstrates the interfacial magnetic and electric nature of FM/SC systems including Co/GaAs, Ni/GaAs, Fe/GaAs, Fe/Graphene and $Co_2FeAl$/(Ga,Mn)As. Suppressed magnetizations of the epitaxial ML Co and Ni on GaAs(100) have been observed, which can be attributed to a combined effect of the island growth geometry at low coverage, the tendency to follow the bcc stacking of the GaAs substrate, and the detrimental interdiffusion. A specially designed $FM_1/FM_2/SC$ structure is introduced, which enables unambiguous demonstration of the interfacial magnetic phenomena. Further applying this method to an emerging field of graphene spintronics, a reduced but still sizable magnetic moment of the ML Fe on graphene is presented and interpreted with DFT calculations, which attributes it to the strong hybridization of C $2p_z$ and Fe $3d_{z2}$ orbitals and the delocalization of the Fe $3d$ electrons. Due to the interfacial exchange coupling, a significantly enhanced $T_c$ is demonstrated in

the $Co_2FeAl$/(Ga,Mn)As bilayer. Parallel alignments of the Fe, Co and Mn magnetization have been demonstrated, which agree well with the DFT calculations.

Chapter V presents a detailed XMCD study of three distinct magnetite thin film samples, namely, a $Fe_3O_4$/MgO/GaAs(100) prepared by post-growth annealing method, $Fe_3O_4$/MgO(100) prepared by plasma-assisted simultaneous oxidation and a $Fe_3O_4$/YZO(111) prepared by PLD. Significant unquenched orbital moments ($m_{orb}$) have been observed from all the three systems, which may partially originate from the broken symmetry of the thin film and partially due to an intrinsic property of the magnetite. By comparing the relative contributions of the Fe cations before and after Verwey transition, the super-exchange (SE) mechanism is demonstrated to be preliminarily responsible for the magnetization Verwey transition of magnetite. Furthermore, the observation supports the recognition that Verwey transition is a sensitive probe to the stoichiometry and homogeneity of magnetite.

Chapter VI presented the magnetism of a model magnetically doped TI, i.e. $Bi_{2-x}Cr_xSe_3$. Strong dichroic XAS spectra with the feature of predominated $Cr^{3+}$ was observed in a 10 nm globally doped $Bi_2Se_3$ epitaxial thin film. A reduced but sizable spin moment ($m_{spin}$) and a vanishing and opposite $m_{orb}$ were obtained and are well reproduced by the first-principals simulations, which suggest the observed magnetic moment of Cr is due to a mixture of $Cr_I^{3+}$, $Cr_{Bi}^{0}$, and $(Cr_{Bi} - Cr_I)^{3+}$ complex defects. The magnetic proximity effect of the $Bi_{2-x}Cr_xSe_3$ with a high-$T_C$ ferromagnetic insulator (FMI) is studied for the first time and an enhanced $T_C$ is demonstrated. In the pursuit of distinguishing the roles of the surface and the bulk magnetization in a 3D TI, the XMCD of a pair of Δ-doped $Bi_{2-x}Cr_xSe_3$ is presented, from which significantly enhanced surface magnetic ordering has been observed.

Chapter VI gives a brief summary of this work and concludes this thesis.

# 2 Chapter II Background

## 2.1 Introduction

In applied materials, the spin ordering has long been investigated within the context of conventional magnetic materials, such as iron, cobalt, and permalloy. The study of spin generation, relaxation, and spin - orbit coupling (SOC), in contrast, took off only recently with the advent of spintronics and it is here many novel materials and hybrid structures could find their greatest potential in both science and technology. For carrying out quantum-bit operations as required for quantum computing, to generate and to tune spin-polarized current are prerequisites. An ideal spin-injected SC would demonstrate high spin polarization, operate at RT and be both robust and easily fabricated for potential high throughput needs. In the pursuit of such goals, the intrinsic material properties are useful indicators of suitable potential materials. Meanwhile, artificially synthetized hybrid systems (layered FM/SC structures and FM-doped SCs) are valuable models for studying spin-dependent phenomena and could potentially be used as actual components for an eventual spintronic device.

This chapter follows the historical path in introducing some of the most relevant concepts of magnetism, followed by a review of the recent advances in hybrid material synthesis and spin device architectures that are found promising towards future applications. A selection of material systems of close relevance will be introduced, including the FM/SC and FM/DMS heterostructures, the magnetically coupled graphene, the half metallic materials (i.e. magnetite and Heusler alloy), and the magnetically doped TIs, aiming to provide some useful background knowledge for understanding the experimental works of Chapter IV - VI. This chapter does in no way try to give a complete overview of these materials, neither is it intended to give deep theoretical descriptions of why the many fascinating phenomena occur in them (such as the uniaxial anisotropy, the interface hybridization, the half metallicity, and the edge states to name a few). The purpose of this chapter is, instead, to present some of the most important properties of these material systems and to highlight a few hotly debated topics of the contemporary spintronics research.

## 2.2 Magnetism

### 2.2.1 Atom magnetism

The model of atoms serves as a conceptual starting point of people's understanding of the smallest building blocks of matters and the basis of the electronic and structural properties of materials. The modern atomic model as it is known today was founded about 100 years ago, during which some giant steps are taken including the discovery of the electron by J. J. Thompson in 1892 and the nucleus by E. Rutherford in 1910.[52] Later Bohr established the relationship between wavelengths measured in spectra and energy levels in the atom, and also proposed a mechanical model of the hydrogen atom. This model suggests that in isolated atoms or ions, the electrons are moving around the nucleus in a potential due to the nucleus and the other electrons and the eigenstates of electrons are characterized by three quantum numbers, namely

- *the principal quantum number* ($n$ = 1, 2, 3…) that determines the spatial variation of the wave function of each electronic shell;
- *the orbital quantum number* ($l$ = 0, 2…$n$-1) that determines the value of kinetic orbital momentum; and
- *the magnetic quantum number,* or the projection of kinetic orbital momentum on axis z ($m = -l, -l+1 \ldots l-1, l$).

The fourth quantum number – the spin quantum number ($m_s$) was defined later in the history to describe the spin of the electron within that orbital and to give the projection of the spin angular momentum on axis z. Two electrons are forbidden to carry identical sets of quantum numbers, known as the Pauli exclusion principal. Pauli principal suggests that the relative direction of two interacting spins cannot be changed without changing the spatial distribution of charge and this fact has significant impact on the Coulomb electrostatic energy of the whole system, which will be discussed later.

Although the nucleus also has a magnetic moment, its value is usually $10^{-3}$-$10^{-4}$ of that of electrons and therefore have been neglected in this study. The atoms with an intrinsic magnetic moment are found among the atoms that have unpaired electrons, or in other words, where the Pauli principal can be fulfilled without a complete pairing of the electrons. For a many-electron system, i.e. an atom or an ion, the net magnetic moment is determined by the vector sum of the spin and orbital angular momentum of

its electrons. (For filled shells both sums vanish so that only partially unfilled shells contribute to the magnetic moment.) It is worthy to note apart from the contribution of spin and orbital momentum, respectively, an third item, known as spin-orbit coupling (SOC, whose origin is relativistic) must be taken into account. It is especially important for heavy atoms as the coupling increases strongly with the atomic number Z (see its significant role in TIs in later sections). In presence of this coupling, ***L*** (total orbital momentum) and ***S*** (total spin momentum) are no longer good quantum numbers and the new good one ***J*** ( total angular momentum) was created as written in:

$$\vec{J} = \vec{L} + \vec{S}$$

Equation 2-1

The way the individual electrons order within a ground state atom is set by the empirical Hund rules, which apply to ***J***, ***L***, and ***S*** such that:

(i) The maximum total atomic spin quantum number $S = \sum m_s$ is obtained without violating the Pauli exclusion principal;

(ii) The maximum value of total atomic orbital quantum number $L = \sum m_l$ is obtained, while remaining consistent with the given value of S;

(iii) The total atomic angular momentum number J is equal to |L–S| when the shell is less than half-filled, and is equal to |L+S| when the shell is more than half-filled. When the shell is exactly half-filled L = 0 so that J = S.

Hund's rules suggest that the electrons, as far as possible, will occupy states with all spins parallel within a shell and will also start by occupying the state with the largest orbital angular momentum followed by the state with the next largest orbital angular momentum, and so on.

### 2.2.2 Solid magnetism

Although an individual atom carries a magnetic moment, the solid that is formed does not necessarily show a net magnetization. That's because in solids, electrons can be no

longer treated in a spherical potential, instead, due to neighboring ions, they sense a crystal potential, which carries the symmetry information of the environment. The effect of such crystal potential varies for the 3*d* transition metals and the 4*f* rare earth elements because (i) SOC is much larger in 4*f* than in 3*d*, and (ii) 4*f* wave functions are more localized than the 3*d* ones and thus are less sensitive to the crystal potential. In 3*d* ions, the crystal field is much larger than SOC. Thus Hund's rules still determine the ground state values of $\boldsymbol{L}$ and $\boldsymbol{S}$ and the largest perturbation is the crystal field. By contrast, in 4*f* ions, the SOC is much larger than the crystal field. So $\boldsymbol{J}$ is determined by the sign of the SOC, and crystal potential becomes a smaller perturbation. The different roles of the crystal potential, or crystal field in 3*d* and 4*f* electrons have significant consequences in the magnetism models of the two types, namely the itinerant magnetism model that applies to transition metals, and the localized magnetism model that applies to the rare earth elements. The localized model for magnetism can often be applied for atoms (or ions) with an part-filled electron shell localized on the atomic core, and the interaction between these atoms (or ions) is addressed to the molecular field. While in itinerant model, electrons are treated collectively as waves traveling through the whole crystalline solid and magnetism is considered as collective phenomena. To confine the discussions within the context of this project, thereafter the introduction will be limited to 3*d* transition metals only, whose spontaneous magnetizations can be predominately described by the exchange interaction between localized spins and will be described in further details later in this section.

### 2.2.3 Quenching of $m_{orb}$ in 3*d* ions

One of the most significant effects of the crystal field on 3*d* ions is the quenching of orbital moment. A cubic crystal field can remove the degeneracy of the five *d* orbitals, resulting in the splitting in $e_g$ and $t_{2g}$ states. In these new states, the orbital moment vanishes to first order and thus the main contribution to the magnetic moment comes from the spins. Another consequence of the large crystal field is the possibility of violating the Hund's rules: if the crystal field is large, the electrons can fill the low energy crystal field states, without taking into account Hund's rules. In particular, the first rule may be violated, leading to a "low spin" state, which eventually can be non-magnetic. Thus in 3*d* ions, crystal field effect can be the most important factor in modifying both orbital and spin magnetic moments. Compared with the crystal field, in

3*d* ions SOC is a perturbation which leads to anisotropy energies which are usually small (see the later sections).

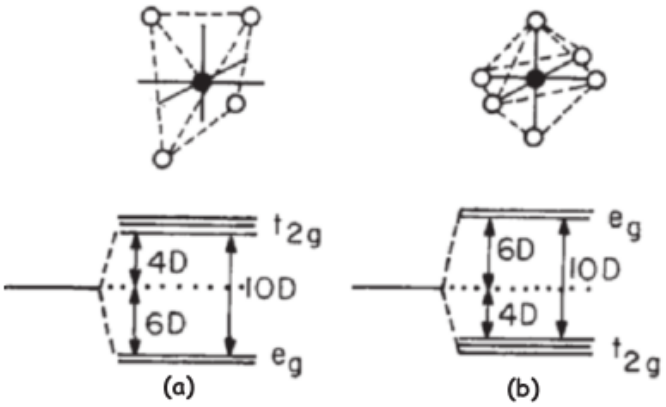


Figure 2-1 | Crystal field splitting of 3d orbitals for (a) tetrahedral and (b) octahedral environment. Image adopted from the literature.[53]

### 2.2.4 Magnetism at Finite Temperature

The magnetic behavior of materials is usually predicted by mean field approximation, which qualitatively explains the reduction of $T_c$ often observed in thin films. At low temperature, in this approximation the magnetization decreases exponentially, while near $T_c$, it varies as (in the following the susceptibility $\chi$(T) will be used, which is a measure on how a material responds to an applied magnetic field)

$$\chi(T) \propto \sqrt{T_c - T}$$

Equation 2-2

And above $T_c$, $\chi$(T) is found to follow the Curie-Weiss law:

$$\chi(T) \propto \frac{1}{T - T_c}$$

Equation 2-3

Here, the individual atomic magnetic moments interact strongly with each other through an exchange field, and spontaneously align. Below $T_c$ the thermal energy is insufficient to cause random paramagnetic alignment because of the dominating exchange field.

### 2.2.5 The magnetic domain

Magnets always show a magnetic response in the presence of an applied magnetic field and such process can be interpreted based on the magnetic domain. The domain hypothesis was firstly introduced by Weiss in 1906, and not until 1949 was there any direct experimental evidence for, and clear understanding of, the domain structure of a real material; in that year H. J. Williams, R. M. Bozorth, and W. Shockley published their work, performed at the Bell Telephone Laboratories, on domains in silicon-iron single crystals.[54] Since that time, domain theory has become central to any discussion of magnetization processes.

A *magnetic domain* is a region within a magnetic material that has uniform magnetization. Each domain is spontaneously magnetized to the saturation value $M_s$ due to the strong exchange interaction, but the directions of magnetization of the various domains are such that the material as a whole has no net magnetization. The interfaces between regions are called *domain walls*, in which the spontaneous magnetization has different directions. At or within the wall the magnetization must change direction from one easy crystallographic direction to another. The process of magnetization is then one of converting the material from a multi-domain state into one in which it is a single domain magnetized in the same direction as the applied magnetic field, as illustrated in Figure 2-2.

From the energetic point of view, the formation of multi-domains rather than a single domain in materials quite often can minimize the total energy of the system. For a region of ferromagnetic material with a constant magnetization throughout, a magnetic field extending into the space outside itself will be created. This leads to a large magnetostatic energy stored in the field. To reduce this energy, the sample can split into two or more domains, with the magnetization in opposite directions in each domain. The magnetic field lines pass in loops in opposite directions through each domain, reducing the field outside the material. To reduce the field energy further, each of these domains can split also, resulting in smaller parallel domains with magnetization

in alternating directions, with smaller amounts of field outside the material. Practically, however, the domain structure of actual magnetic materials does not usually form by the process of large domains splitting into smaller ones as described above. When a sample is cooled below the $T_c$, for example, the equilibrium domain configuration simply appears. But the description of domains splitting is often used to reveal the energy tradeoffs in domain formation.

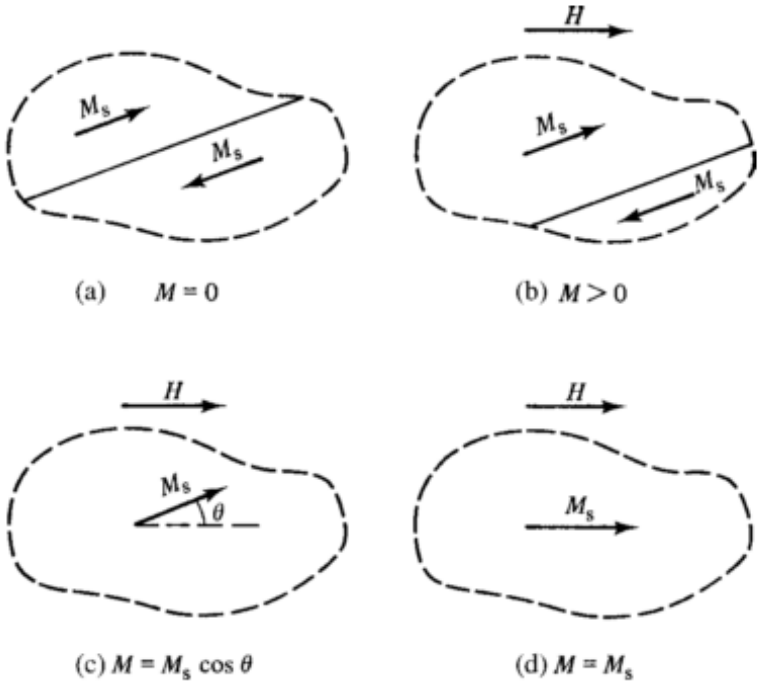


Figure 2-2 | The magnetization process in a ferromagnet. The dashed line encloses a portion of a crystal in which there are parts of two domains; the boundary separating them is called a domain wall. The two domains are spontaneously magnetized in opposite directions, so that the net magnetization of this part of the crystal is zero. In (a)-(b) field H has been applied, causing the upper domain to grow at the expense of the lower one by downward motion of the domain wall, until in (c) the wall has moved right out of the region considered. Finally, at still higher applied fields, the magnetization rotates into parallelism with the applied field and the material is saturated, as in (d). Image taken from the literature.[52]

### 2.2.6 The magnetic anisotropy

Spontaneous magnetization is the appearance of an ordered spin state at zero applied magnetic field in a ferro- or ferri- magnetic material below the $T_c$. Such spontaneous magnetization prefers certain directions, which can be described by magnetic anisotropy, i.e. how the total energy of the system depends on the direction of the spontaneous magnetization. This total energy is the sum of several factors including (i) the exchange energy ($E_{ex}$), (ii) the magneto-crystalline anisotropy energy ($E_k$), (iii) the demagnetization energy ($E_M$), and (iv) the Zeeman energy ($E_H$), and can be written as

$$E_{total} = E_{ex} + E_k + E_M + E_H$$

Equation 2-4

In the remainder of this section, each of these items will be introduced conceptually.

**The Exchange Energy.** Magnetic long-range order occurs because the local magnetic moments interact with each other. There are several mechanisms which are responsible for this interaction and the simplest one is the Heisenberg exchange interaction between localized spins, which can be written as

$$E_{ex} \propto -\sum_{ij} J_{ex} \vec{S}_i \bullet \vec{S}_j$$

Equation 2-5

where $J_{ex}$ represents the exchange constant. The Heisenberg model of ferromagnetism is an approximate representation of the quantum mechanical exchange interactions and its origin is the Pauli expulsion and electrostatic interactions. Based on Equation 2-5, the minimization of $E_{ex}$ leads to two cases – for $J_{ex} > 0$ that $\boldsymbol{S}_i$ and $\boldsymbol{S}_j$ favours a parallel alignment or ferromagnetic coupling and for $J_{ex} < 0$ that $\boldsymbol{S}_i$ and $\boldsymbol{S}_j$ favors a antiparallel alignment or antiferromagnetic coupling. The sign of $J_{ex}$ of 3d transition metals is given by the Bethe-Slater curve (see Figure 2-3), which can be found in many textbooks. Positive $J_{ex}$ is only found in Fe, Co, and Ni among all the transition metals, which explains their unique ferromagnetic behavior. In other words, the exchange interaction leads to the splitting of electronic band into spin-up and spin-down sub-bands in a ferromagnetic metal. There are also other important types of the exchange interaction such as the super-exchange (arises frequently in transition metal oxides where the 3d

magnetic ions are separated by non-magnetic oxygen ions), double exchange (where the 3d ions are in a mixed valence state), and Ruderman-Kittel-Kasuya-Yosida (RKKY) interaction (as in rare earth metals or intermetallics), which are all indirect interactions and will not be discussed in further detail here.

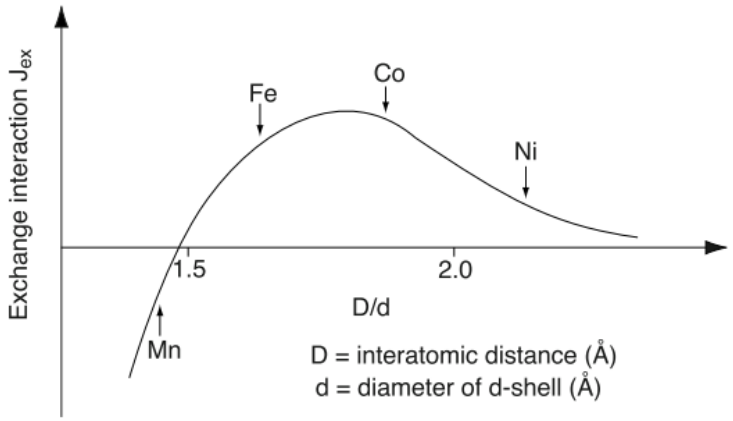


Figure 2-3 | The Bethe-Slater curve describing the value of the exchange constant $J_{ex}$ dependent on the ratio D/d, where D and d denotes the inter-atomic distance and the diameter of the d-shell, respectively. Image adapted from the literature.[51]

**The magneto-crystalline anisotropy energy**. Magneto-crystalline anisotropy energy reflects the fact that the moments prefer to stay along some particular directions in the crystal: this is due to the non-spherical charge distribution in the presence of a crystal field; the spin is coupled to the orbital moment through SOC, and it is sensitive to the charge distribution. In cubic crystals for example this energy is written as of

$$E_k \propto K_0 + K_1(\alpha_1^2\alpha_2^2 + \alpha_2^2\alpha_3^2 + \alpha_3^2\alpha_1^2) + K_2\alpha_1^2\alpha_2^2\alpha_3^2 + \cdots$$

Equation 2-6

where $K_0$, $K_1$, $K_2$ ... are empirical constants which vary with temperature and material and $\alpha_1$, $\alpha_2$, and $\alpha_3$ are the cosines of the angle between the magnetization vector and the x, y, z axis. Calculations of $E_k$ suggest that for bcc Fe, the easy axis in a six-folded symmetry along its principal axis, e.g. [100]. Co has a hcp structure with a twofold easy axis symmetry along the c-axis. Ni has a fcc structure with an eightfold easy axis symmetry diagonal through the cube, e.g. along the [111] direction (see Figure 2-4).

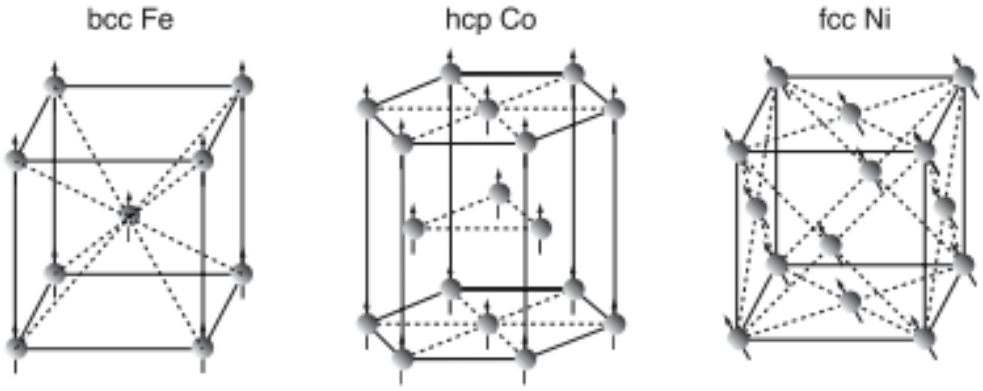


Figure 2-4 | The easy direction by minimization of $E_k$ for the three ferromagnetic elements in the 3d transition metal series, namely, bcc Fe, hcp Co and fcc Ni.

**The Demagnetization Energy.** The demagnetization term is associated with the interaction between $\boldsymbol{M}$ and $\boldsymbol{H_M}$ produced by $\boldsymbol{M}$ itself and can be written as

$$E_M \propto \sum_{i,k} N_{ik} M_i M_k$$

Equation 2-7

Where factor $N_{ik}$ represents the demagnetizing factor. Because $N$ strongly depends on the shape of the solid and the coordinate, $E_M$ is also known as shape anisotropic energy. Imagine a sample with spherical shape, N is isotropic in all directions. However, for a thin disc, $N$ has much larger elements in the direction perpendicular to the plane of the disc compared to in the plane of the disc. In this case the spontaneous magnetization would favor an in-plane direction over an out-of-plane direction because of this demagnetization. This is the origin of the in-plane easy axis of magnetic thin and ultrathin films.

**The Zeeman energy.** Zeeman energy is proportional to the negative of the cosine of the angle between the field and magnetization vectors as can be written as:

$$E_H \propto -\sum \vec{\mu} \cdot \vec{H}_e = -\vec{M} \cdot \vec{H}_e$$

Equation 2-8

and is associated with interaction between the magnetic material and an externally

applied magnetic field. Domains with their magnetic field oriented parallel to the applied field reduce this energy, while domains with their magnetic field oriented opposite to the applied field increase this energy. Therefore applying a magnetic field to a ferromagnetic material causes its domain walls to move so as to increase the size of domains lying parallel to the field and this is what happens when ferromagnetic materials are magnetized.

## 2.3 The FM/SC interface

### 2.3.1 The FM/SC interfacial magnetism

FM metals and alloys have been most thoroughly exploited in the history, as they are relatively easy to grow epitaxially on SCs including GaAs, InAs and InGaAs etc.. In the artificially engineered FM/SC layered structures, substantial spin accumulation and diffusion can occur at the FM/SC interface, which is a decisive process in spin injection. For the proposed spin FET, spin LED and their derivatives (as introduced in Chapter I), the best opportunity for spin transport could only be achieved when no magnetic dead layer exists at the FM/SC interface.

Many researchers have reported on high quality epitaxial growth of Fe on GaAs, among which there exist the long lasting debate over the presence of magnetic dead layer at the Fe/GaAs interface.[55, 173, 174] This detrimental effect used to be attributed to the formation of antiferromagnetic $Fe_2As$[56] and half-magnetized $Fe_3Ga_{2x}As_x$[55] in the vicinity of the interface, until Xu *et al*.[57] obtained a bulk-like magnetic moment of Fe on GaAs(100) - 4 × 6 at RT and demonstrated the evolution of the magnetic phase of Fe/GaAs corresponding to the growth morphology (see Figure 2-5). This result was further confirmed with unambiguous XMCD observation of the Fe/GaAs(100) down to monolayer (ML) scale.[58] By careful analyses of the RHEED patterns, Monchesky *et al*.[59] demonstrated a ferromagnetically dead layer in Co/GaAs system associated with the formation of interfacial $Co_2GaAs$ for Co thickness less than 3.4 ML. In the study of the evolution of interface properties of the electrodeposited Ni film on GaAs upon annealing, significant increase of As out-diffusion has been observed for annealing temperatures up to 623 K accompanying a rise in Schottky barrier height which has been attributed to the Ni-Ga-As compound formation.[60] In the recent attempts to incorporate magnetic perturbation into TIs, a ~1.2 nm magnetic dead layer of Co was observed on $Bi_2Se_3$.[61]

All these studies revealed the possibilities that the magnetic ordering near a region of the surface or interface of FM/SC may be modified due to interdiffusion, termination and hybridization; and controversial reports make this issue rather complex. Whether a deposited FM on SC is magnetically ordered at the FM/graphene interface is a must-addressed issue before any functional spintronic devices can be practically developed.

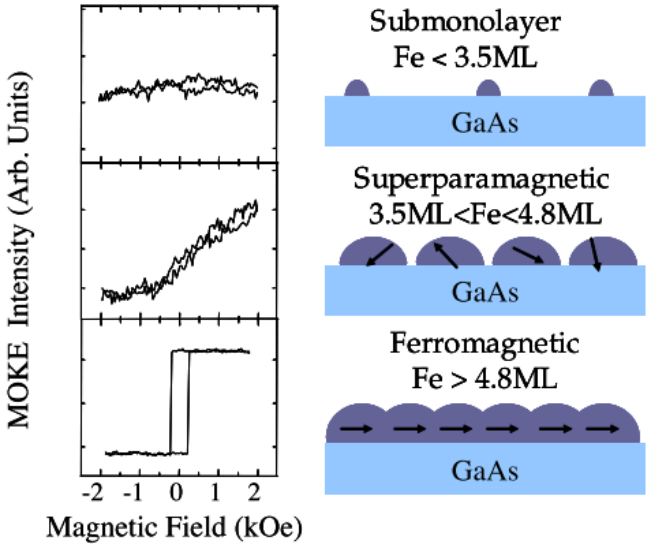


Figure 2-5 | Evolution of the magnetic phase of Fe/GaAs corresponding to the growth morphology. Image adapted from the literature.[57]

### 2.3.2 The FM/SC conductivity mismatch

Another important issue of the FM/SC interface is known as conductivity mismatch, based on the fact that a FM metal has a conductivity typically several orders of magnitude larger than that of a SC, which has also limited the efficiency of spin injection. Low resistance contacts or Ohmic contacts are desired, however, they only form when the SCs are highly doped, typically beyond $10^{-19}/cm^3$, for a direct FM/SC contact.[62] Unfortunately, high doping level leads to unfavorable strong spin scattering or spin depolarization in the SCs. Fe/InAs system is one of the very rare FM/SC heterostructures where ohmic contact (see Figure 2-6) can form naturally due to the band gap of InAs being as small as 0.36 eV at room temperature and therefore became a focus of the heterostructure researches in the early stage.[63] By contrast, the spin injection efficiencies reported for other FM/SC heterojunctions like Fe/GaAs,[64] are quite low, typically only a few percent, across Schottky contact.

Recent studies reveal the possibility that inserting an oxide tunneling barrier like MgO,[65, 66] may modify the barrier height of the FM/SC interface (and eliminates the interface diffusion as an extra bonus) and consequently improves the spin injection

efficiency. The barrier profile required not only has to be narrow but also the barrier transport needs to satisfy the Rowell criteria for single-step tunneling.[65] Prior to the spin injection studies, the proposal of FM/insulator/SC (FM/I/SC) has been realized using scanning tunnelling microscope (STM) with a ferromagnetic tip and proven to be effective by Alvarado and Renaud.[67] Rashba[68] pointed out that if the impedance of the barrier at the interface is sufficiently high, the transport through the interface would be spin dependent. This idea has been implemented later on using two approaches. The first approach is tunnelling through the native Schottky barrier, which could be achieved by inserting a heavily doped thin SC layer at the vicinity of the interface.[69, 38, 23, 24] Using this approach, Hanbicki *et al*. have reported 30 % electrical spin injection efficiency at up to 200 K using Schottky barrier.[69] The second approach is the use of discrete insulator, such as $Al_2O_3$ and MgO, between the metal and semiconductors.[70, 71] Using MgO tunneling barrier, Jiang *et al*.[71] demonstrated up to 30% spin injection efficiency at 290 K.

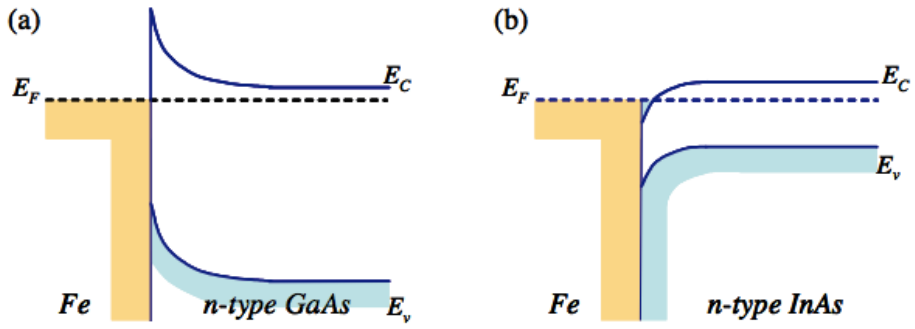


Figure 2-6 | Schematic illustration of the two types of FM/SC direct connection: (a) Schottky barrier (high) forms at Fe/GaAs and most of the other FM/SC junctions while (b) Ohmic barrier (low) forms at Fe/InAs junction. Image adapted from the literature.[72]

### 2.3.3 The FM/graphene heterojunction

Since its successful synthesis by mechanical exfoliation from graphite in 2004, graphene has attracted enormous attention. As a prototypical two-dimensional quantum system, graphene displays a combination of exceptional properties including large

charge carrier mobility, high thermal conductivity, strong mechanical strength, excellent optical characteristics, as well as the recently discovered long spin coherence length.[73, 74, 75] Perfect spin filtering for interfaces of graphite and Ni or Co has been predicted, which is insensitive to interface roughness due to the intrinsically ordered nature of graphite.[76] Electronic transport in single or a few layers of graphene is the subject of intense interest at present. Figure 2-7 presents an example of the experimental demonstration of the electrical spin transport in the nonlocal geometry, reported by Tombros *et al.*,[77] who use graphene channel and Co electrodes (analogy to the experimental configuration presented by *Lou et al.*,[23, 24] see Chapter I).

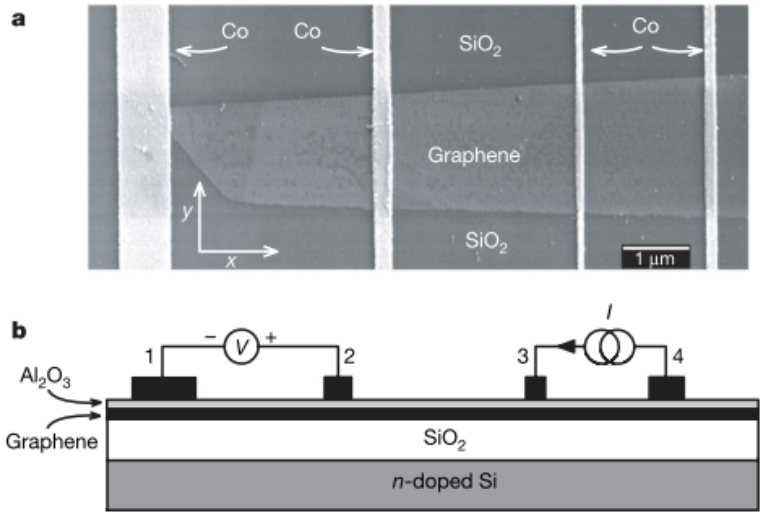


Figure 2-7 | The demonstration of the electrical spin transport experiment in nonlocal geometry. Upper row: typical micrograph of a four-terminal single-layer graphene spin valve using Co electrodes and lower row: the schematic diagram of this nonlocal geometry. Image adapted from the literature.[77]

Fascinating properties of spin transport phenomena have been presented in the Co/graphene system,[78, 79] though theoretical calculations show that the atomic magnetic moment of Co can be reduced by more than 50% when absorbed on graphene surface.[80] The graphene-based FET has been demonstrated in back gated devices on highly doped Si,[81] and the conductance of the top surface of such structure can be modulated via gas exposure and top-back dual gates.[77] The spin valve effect was also successfully demonstrated in NiFe/graphene/NiFe vertical structures and the signal is enhanced when the number of graphene layers is doubled.[82] An inserted graphene sheet can

drastically improve the spin-injection efficiency from a ferromagnet into silicon.[83] All these demonstrations indicate that the interaction of graphene with FM surface plays a fundamental role in the related technological process, which has renewed the interest of FM/SC heterojunctions, although the binding mechanism of the FM/graphene interface is still far from a complete understanding.

### 2.3.4 The FM/DMS bilayer

In a magnetic bilayer system, the exchange coupling from a FM layer can induce a spin moment in the NM layer or enhance the $T_C$ in the other magnetic layer with low ordering temperatures through the proximity effect. This approach has recently been explored and utilized in enhancing the ferromagnetic ordering in DMSs and magnetically doped TIs (will be introduced at the end of this chapter).

A substantial increase of $T_C$ from 40 to 70 K due to the presence of a few monolayers of Fe atop (Ga,Mn)As was also reported by Song *et al*. in a lateral spin injection device.[84] The magnetic proximity effect persists to room temperature at Fe/(Ga,Mn)As interfaces was reported by Maccherozzi *et al*.,[85, 86] who observed a significant induced magnetic order in the (Ga,Mn)As layer that extends over more than 2 nm, even at RT. As shown in figure 2-8, an antiparallel magnetic coupling between Fe and Mn, with FM order in the (Ga,Mn)As layer was observed and high exchange bias up to 240 Oe was revealed in this system by Olejnik *et al*..[87]

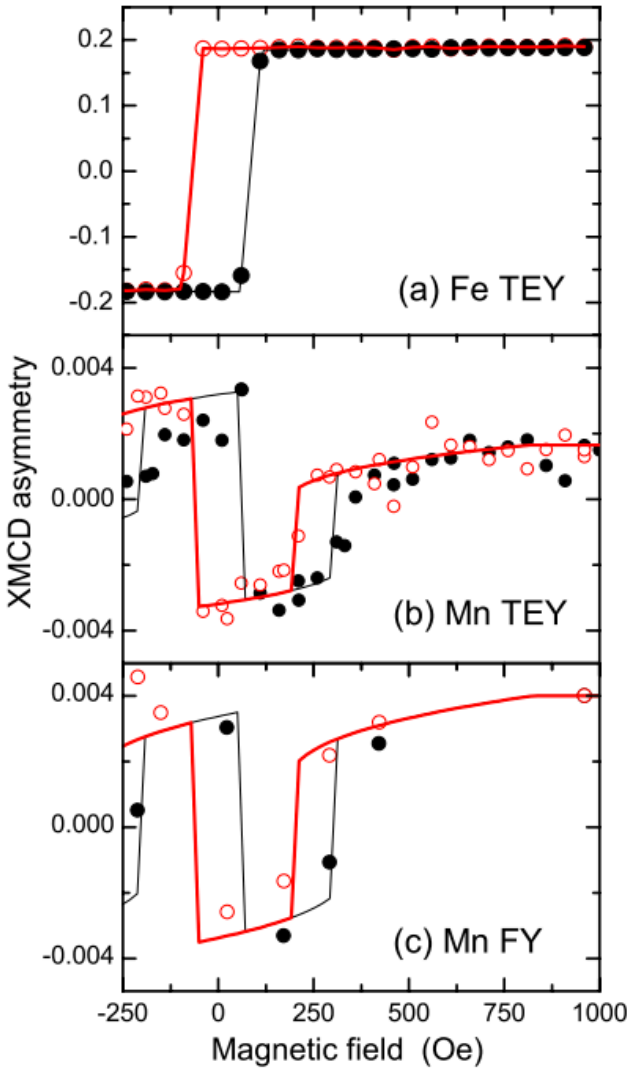


Figure 2-8 | XMCD asymmetry versus applied field at 2 K for Fe (2nm)/(Ga,Mn)As (10 nm) film, (a) - (c)Fe by TEY detection, Mn by TEY detection and Mn by FY detection, respectively. Image adapted from the literature.[87]

A special type of DMSs, the very newly emerged magnetically doped TIs also suffer the low $T_C$ towards the RT applications. The interface magnetism of (anti-) FM/TI heterostructures, such as Fe/$Bi_2Se_3$,[88,89,90] Co/$Bi_2Se_3$,[91,61] and Cr/$Bi_2Se_3$[92] has also been investigated. Remarkably, Vobornik *et al.*[298] demonstrated that long-range ferromagnetism at ambient temperature can be induced in $Bi_{2-x}Mn_xTe_3$ by a deposited a Fe overlayer. Again Fe and Mn was found antiferromagnetically coupled up to RT in this system (see Figure 2-9).

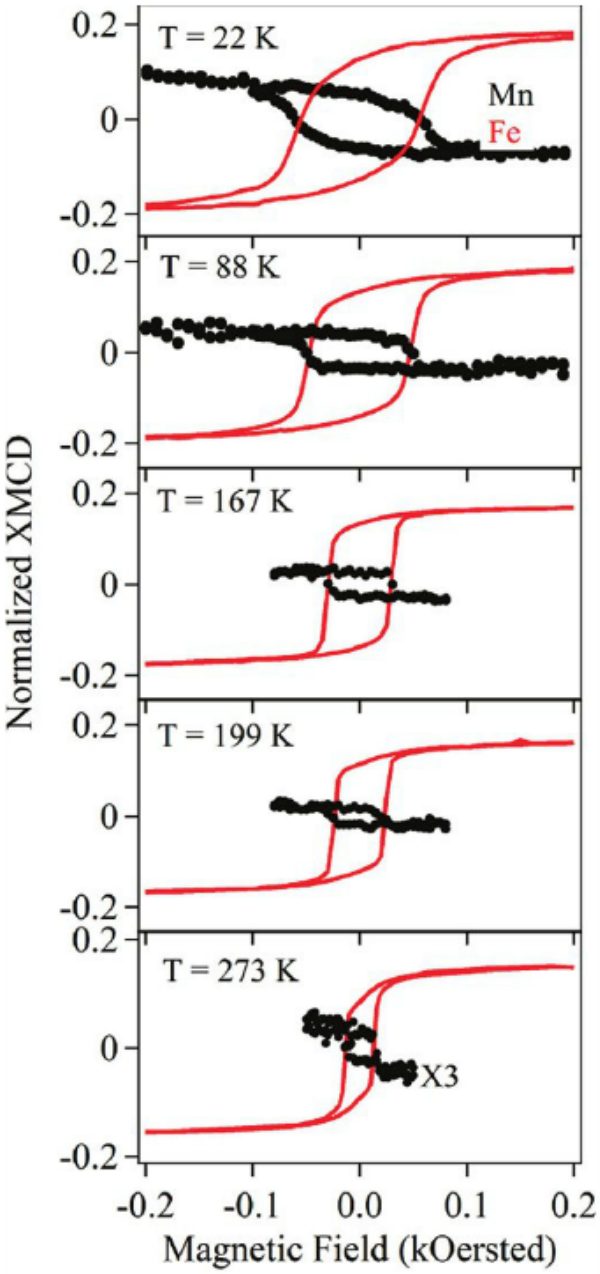


Figure 2-9 | Mn and Fe XMCD hysteresis loops versus temperature in Fe/BiMnTe bilayer. Image adapted from the literature.[298]

## 2.4 The historical perspective of half metallic materials

### 2.4.1 Half metallicity

Half metals are ferro- or ferri-magnetic materials that act as conductors to electrons of one spin orientation, but as insulators or semiconductors to those of the opposite orientation. Figure 2-10 presents a schematic diagram of the partial DOS near $E_F$ of paramagnetic, ferromagnetic and half metal materials respectively. The DOS of up-spin and down-spin electrons are identical in numbers in paramagnetic materials leading to P = 0, while these spin sub bands show imbalance in ferromagnetic materials resulting in 0 < P < 1. Half metals represent an extreme case where either the up-spin or the down-spin states are empty at the $E_F$, giving P = 1. The discovery of half metallicity originates from the early studies of Heusler alloys, some of which yielding the properties of metals as well as insulators at the same time in the same material, depending on the spin direction. By performing electronic structure calculations in the Heusler alloy NiMnSb, such property was identified as half-metallic magnetism by de Groot *et al*.[93] in 1983 and since then the exploration of half metals has received a strong boost.

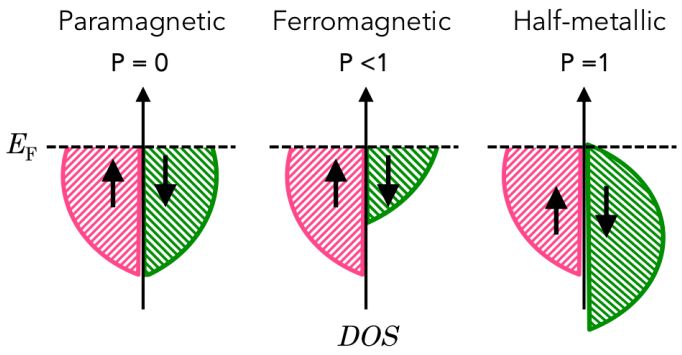


Figure 2-10 | A schematic diagram of the partial DOS near $E_F$ of paramagnetic, ferromagnetic and half metal materials. DOS of up-spin and down-spin electrons are identical in numbers in paramagnetic materials leading to P = 0, while these spin sub bands show imbalance in ferromagnetic materials resulting in 0 < P < 1. Half metals represent an extreme case where either the up-spin or the down-spin states are empty at the $E_F$, giving P = 1.

Half-metallic magnetism as a phenomenon has been generally accepted today, though whose mechanism of becoming existent is still not exactly clear. The most direct

measurement is spin-resolved positron annihilation spectroscopy (SP-PAS) - an expensive technique used in the study of polarized band structures of bulk ferromagnets.[94] Due to the experimental complications, the number of well-established half metals remains a puzzle and electronic structure calculations continue playing a leading role in the search for new half metals. Formally the expected 100% spin polarization of charge carriers in a half- metallic ferromagnet is a hypothetical situation that can be approached only in the limit of vanishing temperature and by neglecting spin-orbital interactions. However, at low temperatures (as compared with the high $T_c$, which exceeds 1000 K for typical half metals and minor spin-orbit interactions, a half metal deviates so markedly from a normal material that the treatment as a special category of materials is justified. Nowadays, a diverse collection of materials including Heusler alloys, zinc-blende structure compounds, chromium dioxides, and magnetite have been found to carry half-metallicity.

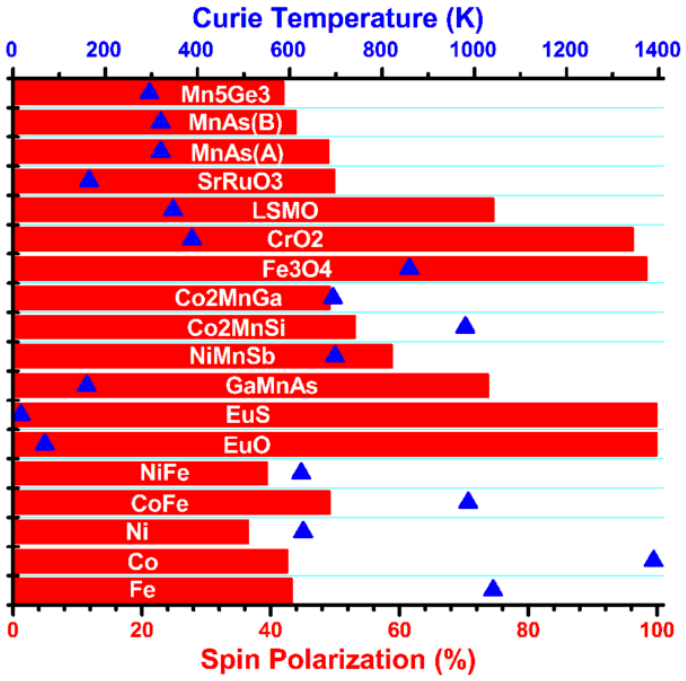


Figure 2-11 | Spin polarization and $T_c$ of a list of selected magnetic materials found in the literature. The triangles refer to the $T_c$ of the materials and the bars indicate the spin polarization.[95]

Half metals offer a mixture of the desired properties for spintronics applications. The overwhelming high spin polarization makes half metals ideal spin sources in the proposed hybrid spintronic devices. In general, half metals have high $T_c$ that are well in excess of RT,[96] promising their application at finite temperature, since many of the depolarization mechanisms scale with the reduced temperature $T/T_c$. Figure 2-11 presents a survey of the P and $T_c$ of some of the aforementioned materials which might be of potential use in spintronics applications, from which the clear advantages of half metals can be seen. The following sections will briefly review the research development of two types of primary half metals spintronic materials of interest, i.e. Heusler alloys and magnetite.

### 2.4.2 Heusler alloys

Heusler alloys are intermetallic compounds with particular composition and crystal structure, which can be categorized into two distinct classes: the half Heuslers with the form XYZ (referred as $C1_b$ structure) and full Heuslers with the form $X_2YZ$ (referred as $L2_1$ structure) where X and Y atoms are transition metals while the Z atom is either a semiconductor or a non-magnetic metal (see Figure 2-12 for the major combinations of Heusler alloy formation). The unit cell of the $L2_1$ structure consists of four fcc sublattices, while that of the $C1_b$ structure is formed by removing one of the X sites, as schematically shown in Figure 2-13.

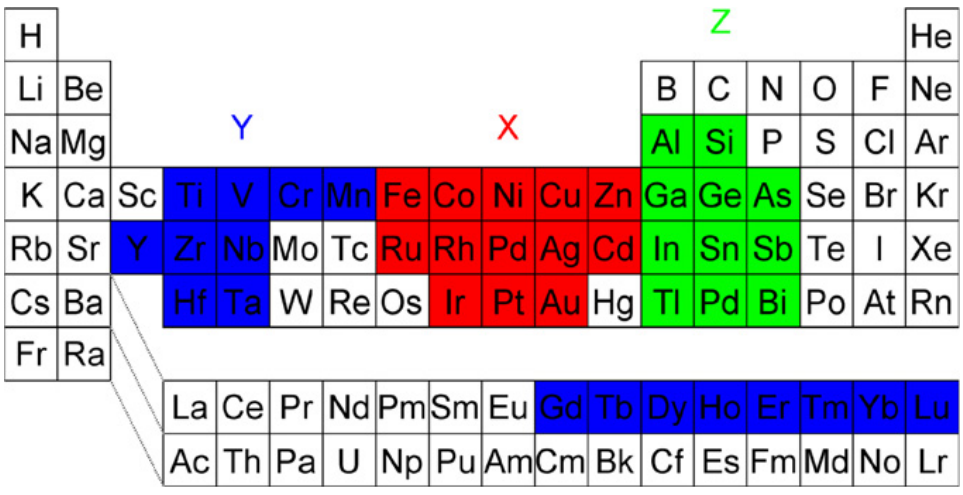


Figure 2-12 | Major combinations of Heusler alloy formation. Image adapted from the literature.[96]

The term 'Heusler phase' was named after Friedrich Heusler, who discovered a mysterious ferromagnetic behavior in a ternary alloy formed from non-ferromagnetic constituents as early as 1903.[93] The Heusler alloys have been the subjects of a large number of studies over more than a century and especially since 1983, when Heusler alloys were predicted to possess a half metallic character,[93] these materials have drawn an even more intensive attention with the particular interest in their half mentality. NiMnSb, as the first predicted half metallic Heusler alloy, was hotly investigated at the early stage. Although the bulk single crystals have shown ~ 100% spin polarization at the Fermi energy level by means of spin polarized positron annihilation,[97] the thin films NiMnSb has only shown 28% at 0.4 K by TMR[98] and ~ 58% with Andreev reflection.[99] Later on, the focus of the research on Heusler alloys shifted toward the Co-based Heusler alloys with the formula $Co_2YZ$, which were found to have half metallicity[100, 101] and high $T_c$ (for example in $Co_2FeSi$, $T_c$ =1120 K). Up to 317% TMR ratio has been obtained at 4 K from $Co_2Cr_{0.6}Fe_{0.4}Al$.[102] This achievement was followed by even larger TMR ratios from magnetic tunnelling junctions (MTJs) with different Co-based Heusler alloys electrodes such as $Co_2FeAl$,[103] $Co_2MnSi$,[104] $Co_2Cr_{1-x}Fe_xAl$,[105] and $Co_2FeSi$.[100] While $Co_2MnSi$ has shown a giant low temperature TMR ratio of about 570% which corresponds to 0.89 spin polarization, this value has tremendously reduced at room temperature to 90%.

Heusler alloys are ferromagnetic as a result of the double-exchange mechanism between neighboring magnetic ions. Both half and full Heusler alloys show the Slater-Pauling behaviour of the binary transition metal alloys, i.e. the total number of valence electrons per formula unit (f.u.) determines the total magnetic moment per f.u.. and this behavior enables people to tailor the magnetic properties of new compounds by substituting the Y atoms with the different transition metals. Heusler alloys also exhibit structural similarity to the zinc-blende structure adopted by binary semiconductors like GaAs, InAs and ZnS,[106,107] and large band gap at $E_F$ in general, which could facilitate their use in devices such as spin-FET and spin-LED.[18, 19, 25, 34]

Disadvantages exist in Heusler alloys because of their fragile half metallicity against atomic disorder. As schematically shown in Figure 2-13 (c)-(d), for the $L2_1$ structure, when X atoms remain ordered while full disorder occurs between Y and Z sites, the alloy transforms into the $B_2$ structure. And if disorder occurs between one X site and either Y or Z sites, the atomic arrangement may lead eventually to the $A_2$ structure. Such disorders result in suppression of the inversion centers that is present in

the ordered Heusler alloys, which have important consequences for the half-metallic band gaps. It was reported that more than 7% of atomic disorder is enough to vanish the energy gap for the minority spins at $E_F$. The earlier mentioned discrepancy of spin polarization in NiMnSb thin films, compared with that in bulk NiMnSb is a typical example.[108]

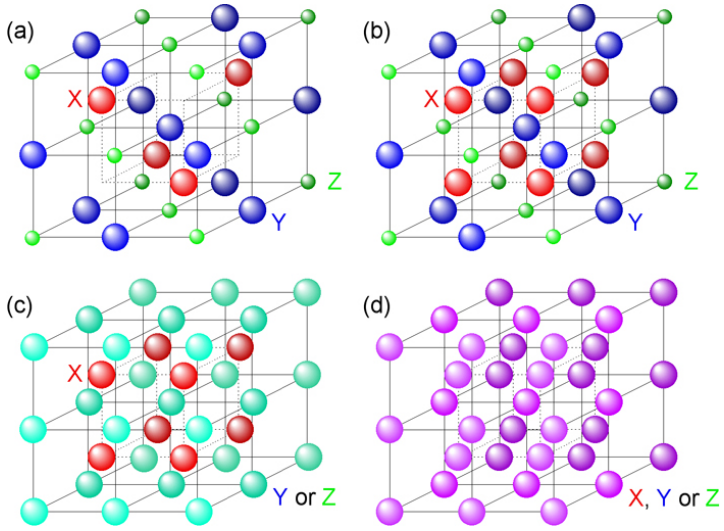


Figure 2-13 | Schematic diagram of the crystalline structures of both (a) half and (b) full Heusler alloys; $C1_b$ and $L2_1$ structures, respectively. Atomically disordered structures, (c) *B2* and (d) *A2*, obtained from P. J. Webster and K. R. A. Ziebeck, "Heusler Alloys," in *Landolt-B_rnstein New Series Group III, Vol. 19C*, H. R. J. Wijn (Ed.) (Springer, Berlin, 1988) p. 75. The unit cell of the $L2_1$ structure consists of four fcc sublattices, while that of the *C1b* structure is formed by removing one of the X sites.

### 2.4.3 Magnetite

Magnetite or $Fe_3O_4$ is one of the most widespread natural iron compounds and the most ancient magnetic material known (discovered more than 2,500 years ago). The experimentally true half-metallic state was reported by Dedkov *et al.*[109] by means of spin and angle-resolved photoemission spectroscopy, from which P = - (80 ± 5)% was obtained near $E_F$, consistent with the spin-split band energies from DFT calculations. Fascinating properties of spin transport have also been presented in $Fe_3O_4$, i.e. spin Seebeck effect,[110] spin filter effect,[111] gate voltage-induced phase

transition,[112] and spin valve effect of $Fe_3O_4/MgO/Fe_3O_4$ junctions.[113] Yet at the meantime, many fundamental properties of magnetite such as the half-metallicity, spin and orbital ordering, Verwey transition mechanism and the coupling mechanism between different sites have long been open issues.

The famous transition of magnetite was discovered by Verwey as early as 1939 that at $T_v \sim 120$ K magnetite undergoes a first-order metal–insulator phase transition, called Verwey transition.[114] When the temperature is lowered through $T_v$ the electrical resistivity increases by two orders of magnitude. Typically, such an abrupt change of crystallographic structure at $T_v$ is accompanied by further anomalies in a series of related parameters controlling the magnetic, thermodynamic, electric and mechanical interactions in the solid (see Figure 2-14 for some examples). Even today the origin of this abnormal transition and the low- temperature phase of magnetite are still the subject of numerous investigations and controversial reports, which question the fundamental theories.

The rather complicated magnetic structure of magnetite was partly proposed by Verwey and Haayman in 1941 and the total structure was proposed by N´eel in 1948, and then confirmed three years later by neutron scattering.[115] It has cubic inverse spinel structure with fcc unit cells where oxygen ions are placed regularly in cubic close packed positions along the [111] axis. Its unit cell is comprised of 56 atoms: 32 $O^{2-}$ anions, 16 $Fe^{3+}$ cations and 8 $Fe^{2+}$ cations. Three inequivalent sites for the cations exist and their arrangements are such that 8 $Fe^{3+}$ occupy the tetrahedral sites (A sites) and 8 $Fe^{3+}$ and another 8 $Fe^{2+}$ cations occupy the octahedral site (B sites), as schematically shown in Figure 2-15.

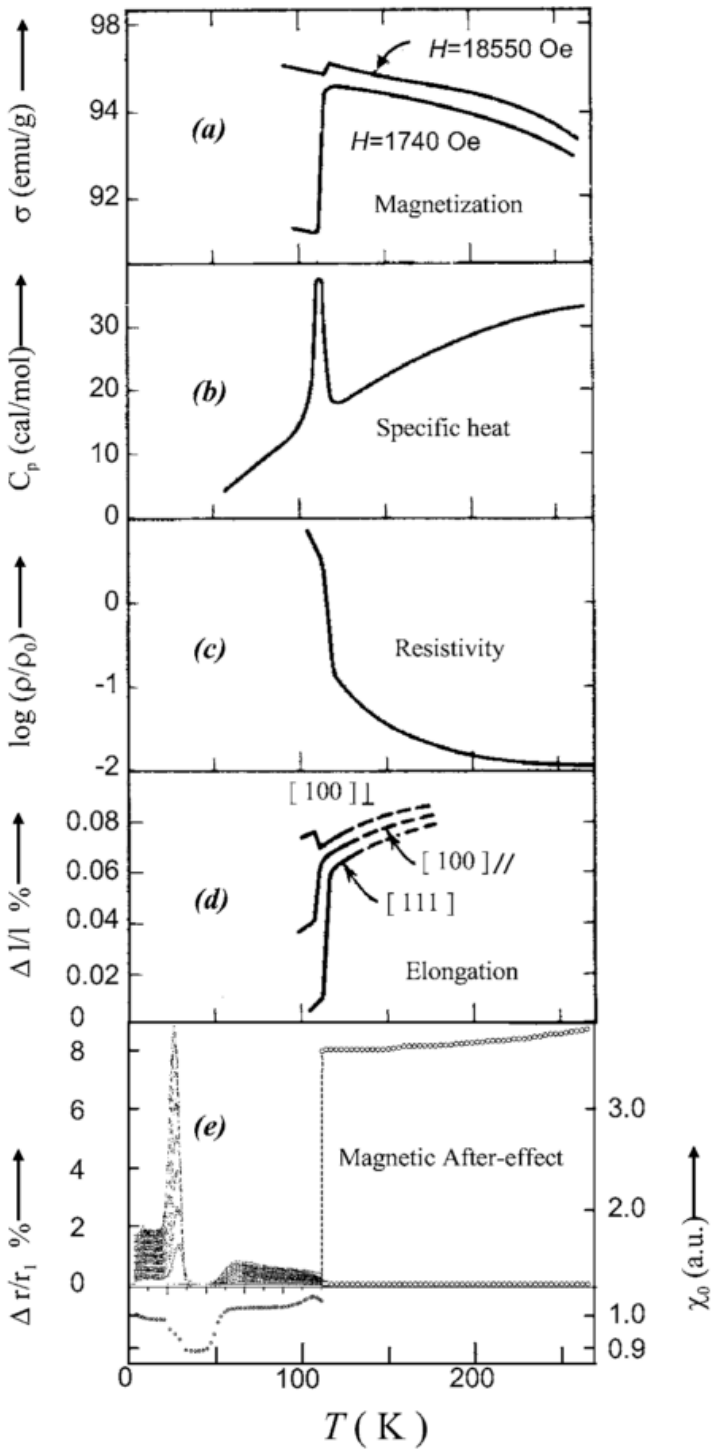


Figure 2-14| Basic manifestations of the Verwey transition in $Fe_3O_4$ near $T_V$ ~ 125 K, arranged in the historical order of their detection. (a) spontaneous jump of the magnetization, (b) specific heat anomaly, (c) spontaneous drop of specific resistivity, (d) thermal expansion along selected directions, (e) Magnetic After-effect spectrum, Image adapted from the literature.[116]

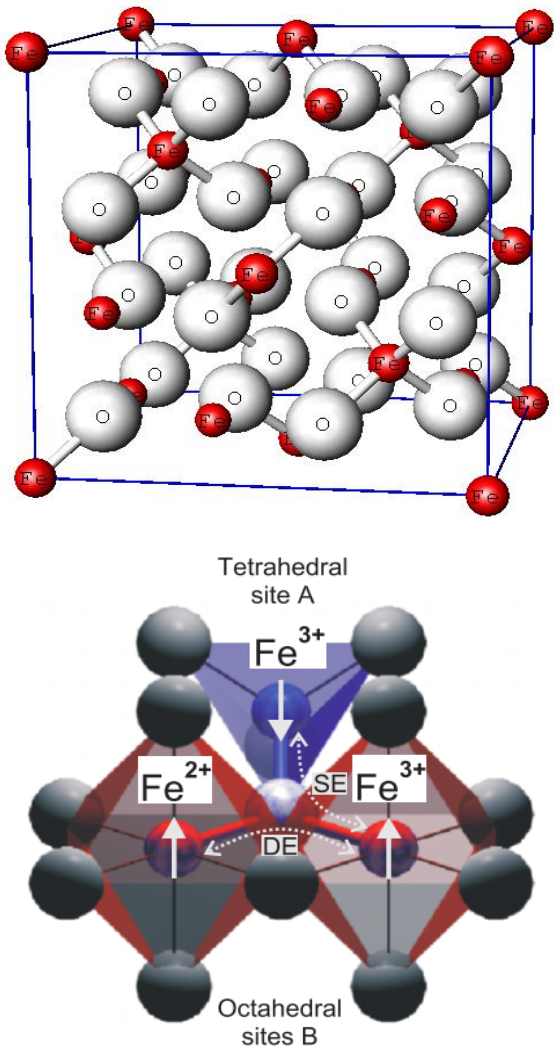


Figure 2-15 | Crystallographic and magnetic structure in magnetite, Fe3O4, near tetrahedrally (site A) and octahedrally (site B) coordinated Fe atoms. The cages around the 3 shown iron atoms are formed by O atoms. The moment on a given Fe atom is coupled antiferromagnetically via SE to another Fe atom of the same valency and ferromagnetically via DE to a Fe atom of different valency. Both exchange interactions go via the same O atom which because of the DE interaction carries a magnetic moment. Image adapted from the literature.[117]

Two important types of exchange interactions, namely super exchange (SE) and double exchange (DE), occur in magnetite, whose strength and sign depend on the angle between the ions and on the filling of the orbitals. The 90° indirect superexchange interactions of the Fe ions in A and B sites as mediated via the O anions lead to an antiparallel alignment of spins on the A and B sublattices. Such coupling is substantially

weaker than the 125° DE, in which electrons hop between ferromagnetically coupled 28 B site $Fe^{2+}$ and $Fe^{3+}$ ions, resulting in an average charge of $Fe^{2.5+}$. Because the spin of the extra electron of $Fe^{2+}$ is oppositely directed to the electrons of $Fe^{3+}$, electron transfer is only possible when both ions are aligned ferromagnetically. The DE then increases the bandwidth or delocalization of the extra electron, thereby decreasing its kinetic energy and favoring a ferromagnetic alignment. Taking into account all these exchange mechanisms, the net magnetic moments of 4 $\mu_B$/f.u of magnetite are imparted from the B site $Fe^{2+}$ ions.

Complexities also exist in the theoretical model of magnetite. Unlike the Heusler alloys, magnetite is a system with a narrow 3d band and therefore strong-correlation effects. To this day the debate continues whether magnetite can be described by band theory or whether the size of the correlation effects requires other methods, such as the LDA+U or even multiplet schemes. The LDA calculation by Zhang and Satpathy[118] and Antonov *et al.* [264] suggest high spin configuration, which yields an exchange splitting (~3.5eV) that is larger than the $e_g$ – $t_{2g}$ splitting (< 2 eV). Band theory finds that magnetite is metallic because the $E_F$ falls at the bottom of the minority spin band on the octahedral sites, which is of $t_{2g}$ character. However, at low temperature, below the $T_v$, magnetite is known to be an insulator, not the predicted metal. Another direct consequence of such transition is a modification of the electronic structure of $Fe_3O_4$. It is known that, at the Verwey transition, electron energy states are introduced into the spin-up gap, as well as a small spin-down gap opening up.

### 2.4.4 Magnetite thin films

When integrating with SCs, between $T_v \sim$ 120 K to 320 K, magnetite has the advantage in having less conductivity mismatch that exists in FM/SC heterostructures and hence can be used as efficient spin injectors in the diffusive transport regime.[119] Efforts have been made in preparing magnetite thin films by a variety of deposition techniques such as MBE, PLD, reactive magnetron sputtering on different substrates such as MgO, $MgAl_2O_4$, $\alpha$-$Al_2O_3$, $SrTiO_3$, Pt, Si, GaAs to name a few.[120, 121,122, 256] and with the thickness down to nanometer scale, those unanswered fundamental questions of magnetite become even more sophisticated. One of the most intriguing properties of magnetite is the half metallicity. However, just as Heusler alloys, the half metallic

magnetite also suffers from problems, such as the antiphase boundaries (APBs) structural defects,[272] deviation from the stoichiometry, and strain, that could quench the expected high spin polarization.

The Antiphase boundary (APB) defects have been observed in epitaxial thin films of magnetite regardless of the type of the substrates or the growth techniques.[272, 273, 274] In the thin film regime, APB can cause a significant changes in the film properties from that of the bulk single crystal of $Fe_3O_4$. For example, in contrast with the single crystal, the magnetization of the thin films cannot saturate at high fields, epitaxial ultrathin magnetite films less than 5nm thick show a superparamagnetic behavior,[273] the modified exchange interaction at the APB results in an exchange bias on the neighbouring ferromagnetic domains, and the magnetotransport measurements show a large linear magnetoresistance at high fields which is not seen in the bulk.[272, 274] Therefore, obtaining a magnetite thin film with properties approaching those of the bulk remains a significant challenge for the future spintronic applications of $Fe_3O_4$ thin films.

The stoichiometry of the thin $Fe_3O_4$ films is of paramount importance in controlling the electric and magnetic properties for iron oxide–based magneto-resistive devices, as the coexistence of small amounts of other phases of iron oxide, such as FeO and $Fe_2O_3$ could result on a quenching of the high spin polarization. Previous studies on bulk crystals have shown that small deviation from the ideal stoichiometry strongly influences the Verwey transition temperature.[123] The stoichiometry of magnetite has been efficiently obtained by various techniques, like conversion electron Mössbauer spectroscopy (CEMS) and XMCD. [124]

Furthermore, the physical properties of magnetite films would be significantly influenced by strain. A comparable study of the microstructure and magnetic properties of magnetite thin films deposited on (100) oriented MgO and $SrTiO_3$ (STO) substrates has recently revealed an obvious difference in magnetic properties of the two films.[125] Compared to $Fe_3O_4$/MgO, a larger domain structure and significant out-of-plane magnetization components were observed in $Fe_3O_4$/STO as a consequence of the in-plane compressive strain. It has also been shown that the change in the lattice mismatch from -0.3% for $Fe_3O_4$/MgO structure to 4% for the $Fe_3O_4/MgAl_2O_4$ structure has increased the fraction of the film that is relaxed to 40% and this consecutively broadened out the Verwey transition.[126]

## 2.5 The development of magnetically doped TIs

### 2.5.1 The edge state of TIs

As a newly discovered class of matter with eccentric electronic phase, the spin-orbit induced TIs have a very short history but great attractions to the community of condensed matter physicists. Since they were first theorized in 2005 and later experimentally produced in 2007, TIs, with their ability to insulate on the inside and conduct on the outside, have presented new possibilities for the future spintronics applications.

Topology is the branch of mathematics that deals with quantities that are invariant under continuous changes. Topological ideas were first applied to quantum condensed-matter physics in the 1980s to understand the integer quantum Hall effect. To view the non-trivial surface of TIs, it is essential to understand the insulating state of matter. Figure 2-16 schematically illustrate the character feature of 2D-3D TIs by analogy with quantum Hall (QH) effect. The insulating state occurs when an energy gap separates the occupied and empty electronic states – a behaviour that can ultimately be traced to the quantization of energy levels in an atom, as shown in Figure 2-16(a). The QH state, which is the simplest topologically ordered state, occurs when electrons are confined to a 2D interface between two semiconductors and experience a strong magnetic field (see Figure 2-16(b)). The field gives rise to Landau quantization, where the electron motion curves into a circle, rather like the circular motion of electrons bound to an atom. Just as in an atom, quantum mechanics replaces this circular motion by orbitals that have quantized energies, resulting in an energy gap separating the occupied and empty states. At the boundary of the system, however, the electrons undergo a different kind of motion, because the circular orbits can bounce off the edge, leading to “skip-ping orbits”, as shown in Figure 2-16(b) In quantum theory, these skipping orbits lead to electronic states that propagate along the edge in one direction only and do not have quantized energies. Given that there is no energy gap, these states can also conduct. Moreover, the one-way flow makes the electronic transport in the edge states perfect. Normally, electrons can scatter off impurities, but given that there are no backward-moving modes, the electrons have no choice but to propagate forwards. This leads to what is known as “dissipationless” transport by the edge states – no electrons scatter and so no energy is lost as heat – and is ultimately responsible for the precise quantized transport.

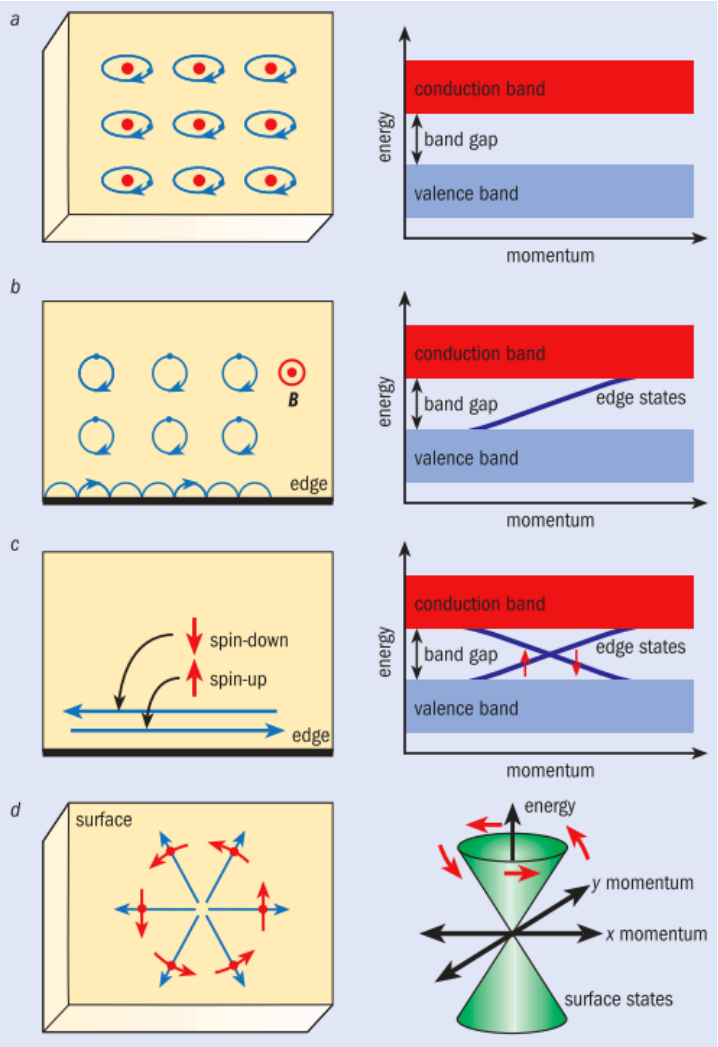


Figure 2-16 | Schematic diagram of the insulating state of matters. (a) The normal insulating state characterized by an energy gap separating the occupied and empty electronic states, (b) the QHE, whereby the circular motion of electrons in a magnetic field, B, is interrupted by the sample boundary. (c) The edge state of the QSHE or 2D TI, whereby spin-up and spin-down electrons propagating in both directions. (d) The surface of a 3D TI supports electronic motion in any direction along the surface, but the direction of the electron's motion uniquely determines its spin direction and vice versa.

2D TIs have many similarities with QH insulators, but occur in the absence of a magnetic field. In these materials the role of the magnetic field is played by spin–orbit coupling (SOC) based on the electrons' intrinsic angular momentum, or spin, with the orbital motion of the electrons through space. Some atoms with a high atomic number (e.g. Hg, Bi) naturally satisfy the criteria of intrinsic strong SOC. Electrons travelling

through materials composed of such atoms therefore feel a strong spin- and momentum-dependent force that resembles a magnetic field, which changes with the spin. Furthermore, in contrast to the QH insulator, a 2D TI has two sets of edge states that propagate in opposite directions, as shown in Figure 2-16(c). This was first predicted in 2005, and occurs when the spin-up and spin-down electrons, which feel equal and opposite spin–orbit "magnetic fields", are each in QH states. The Hall conductance of this state is zero because the spin-up and spin-down electrons cancel each other. They form a 1D conductor that is essentially half of an ordinary 1D conductor (a "quantum wire", which can have spin-up and spin- down electrons moving in either direction).

The next tier of completion in the family of TI is the 3D TI, whose surface states strongly resemble the edge states of 2D TI, though cannot be understood using the simple picture of a spin-dependent magnetic field. As presented in Figure 2-16(d), the direction of electron motion along the surface of a 3D TI is determined by the spin direction, which now varies continuously as a function of propagation direction. The result is an unusual "planar metal" where the spin direction is locked to the direction of propagation.

### 2.5.2 The experimental discovery of TIs

The past ten-years has been a rapid developing time for TIs, during which both 2D and 3D versions of these materials have been theoretically predicted[127] and subsequently produced in laboratories. The first experimental signature of TIs was the observation of the 2D quantum spin Hall effect sandwiched by layers of $Hg_xCd_{1-x}Te$, reported by König *et al*.[128] in 2007. They performed transport measurement of this trilayer device and observed the predicted $2e^2/h$ conductance, which is independent of the width of the sample as expected for a conductance resulting only from edge states (see Figure 2-17).

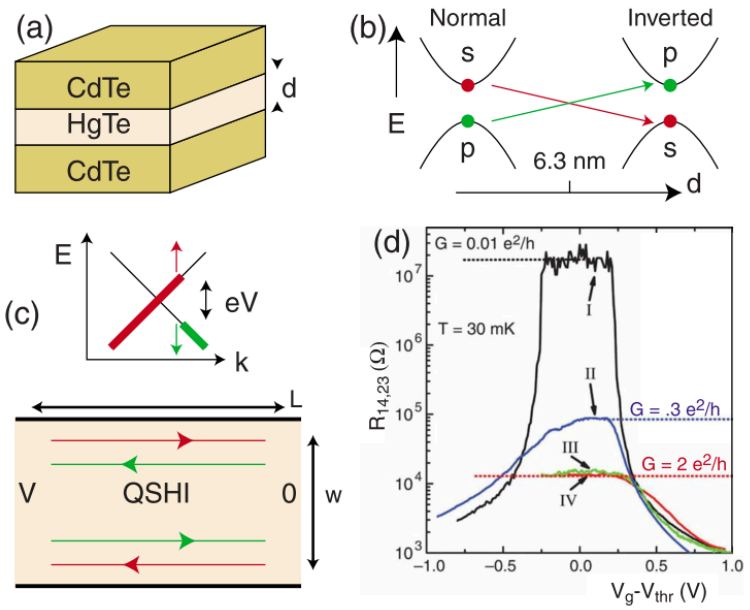


Figure 2-17 | Experiments on HgTe/CdTe quantum wells. (a) Quantum well structure. (b) As a function of layer thickness d the 2D quantum well states cross at a band inversion transition. (c) that have a nonequilibrium population deermined by the leads. (d) Experimental two terminal conductance as a function of a gate voltage that tunes $E_F$ through the bulk gap. Image adapted from the literature.[128]

The 3D TI was demonstrated in 2008, by Hsieh *et al.*,[129] who mapped out the surface states of bismuth antimonite ($Bi_xSb_{1-x}$). Unfortunately, however, the surface states were more complicated than they had to be (see Figure 2-18), prompting the community to search for other classes of materials that might have a simpler structure. This search led to the discovery that bismuth selenide ($Bi_2Se_3$) and bismuth telluride ($Bi_2Te_3$) can be TIs. These materials have a relatively large bulk energy gap and hence can work at RT. They also have the simplest possible surface-state structure (refer to Figure 2-19), which thereafter have unleashed a worldwide experimental effort to understand their electrical and magnetic properties.

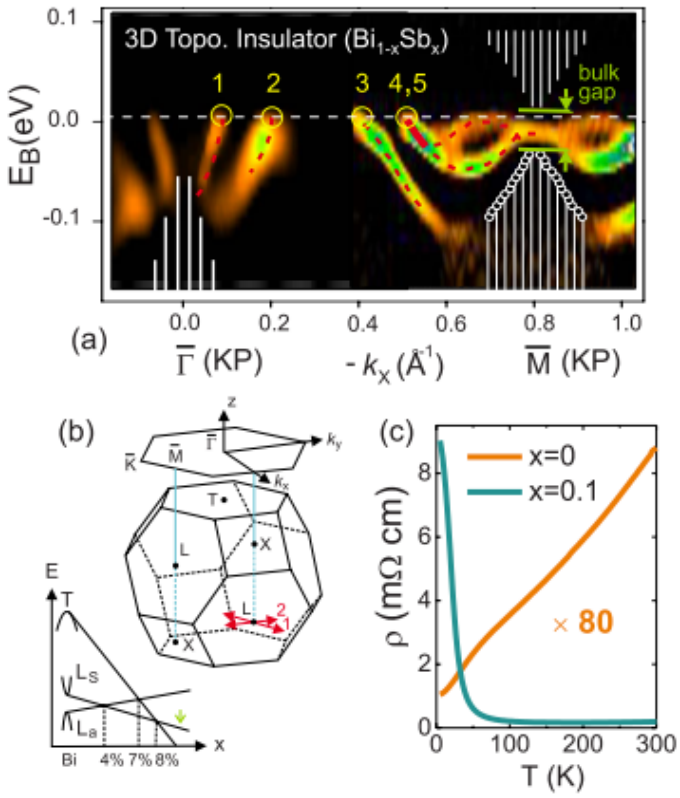


Figure 2-18 | Topological surface states in $Bi_{1-x}Sb_x$: (a) ARPES map of $Bi_{0.9}Sb_{0.1}$ which probes the occupied surface states as a function of momentum in the surface Brillouin zone. (b) Schematic of the 3D Brillouin zone and its (111) surface projection. (c) The resistivity of pure Bi contrasted with the alloy. Image adapted from the literature.[129]

### 2.5.3 The magnetically doped TIs

The effect of magnetic perturbation is an important aspect of the TI research with strong implication in not only the spintronics applications, but also the fundamental science. Efforts to dope the tetradymite family materials with magnetic impurities were made before the discovery of their topological characteristics. The discussions of such magnetic doped materials at that time had been limited to the scope of conventional DMSs, despite that the doping concentration did go far beyond the "dilute" regime. In magnetically doped TI systems, ferromagnetic moments can be developed through two

major mechanisms: the van Vleck mechanism from the large spin susceptibility of the valence electrons in TI materials,[130] and the RKKY interaction between neighboring magnetic ions,[284] which are mediated by either the bulk itinerant carriers or the TI surface Dirac- fermions. These two magnetic mechanisms have been independently observed in Mn-doped $Bi_2Te_2Se_1$ and Cr-doped $(BiSb)_2Te_3$ systems, respectively.[131, 132]

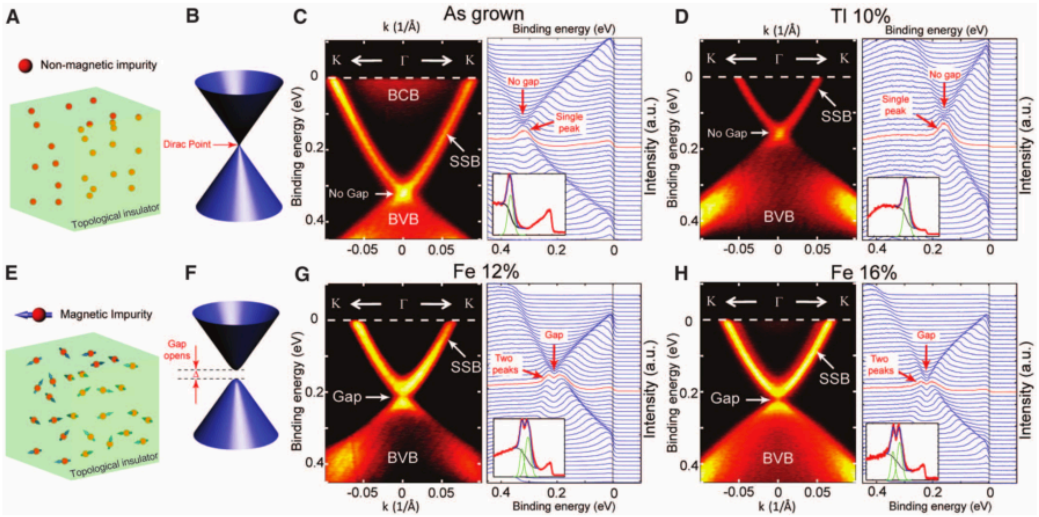


Figure 2-19 | The ARPES map of Fe-doped $Bi_2Se_3$ 3D TI with the concentration of (C) 0%, (D) 10%, (G) 12%, and (H) 16%. (A) and (B) nonmagnetically doped topological insulator with a Dirac point connecting the upper and lower Dirac cones as in the undoped case. Image adapted from the literature.

The interplay of magnetism and TI can be both mathematically and physically subtle. On one hand magnetic perturbation, i.e. doping or coating can open a gap of the surface band structure of a 3D TI (see Figure 2-19). On the other hand, Dirac gap can be observed in magnetically doped samples with or without bulk ferromagnetism. If $E_F$ can be tuned into this surface-state gap, an insulating massive Dirac fermion state is formed, which supports many striking topological phenomena, such as magnetic monopole induced by a point charge,[278, 280, 281, 282] the half QHE on the surface with a Hall conductance of $e^2/2h$, [283] and a topological contribution to the Faraday and Kerr effects.[286]

### 2.5.4 The spintronic applications of TIs

One of the most striking features of TIs comes from the TRS protected surfaces, in which the electronic momentum and spin are locked preventing backscattering of electrons from any impurity that does not interact with the spin. This can be akin to the edge states of the QHE in conventional 2DEG systems, but superior in the ability of functioning without the presence of magnetic field. Such unique features make TIs beneficial for the many emerging spintronic applications with low dissipation but high performance. The linear E–k dispersion relation gives rise to the massless Dirac fermion, and thus enables coherent transport with an ultra-high mobility on the topologically robust surface state. The spin-momentum-lock mechanism promises potential applications using an effective spin-polarized current, which can be generated by simply applying a lateral electric-field across a TI film. Since the ratio of the current-induced spin density to the total electron density is equal to that of the transport drift velocity to the surface Fermi velocity ($V_d/V_F$), this TI- based spin generator is expected to be much more effective than the regular Rashba-coupled 2DEG counterpart. Another interesting spin-related property of TIs is the exotic surface-mediated RKKY interactions.[32] Because of the linear energy spectrum of surface Dirac fermions, the RKKY coupling does not have conventional FM/AFM oscillations when the $E_F$ is tuned close to the Dirac point.[133, 134] This effect smooths out the coupling coefficient compared with conventional DMSs and will thus minimize local magnetic moment disorders and can produce much more robust ferromagnetism.

# 3 Chapter III Method

## 3.1 Introduction

The rise of spintronics has been strongly linked with the development of instrumentation in nanofabrication and characterization in the past thirty years. The experimental side of spintronics research today has marched to a historical point where the paramount urgency is to use materials of the highest perfection and homogeneity and detection tools with atomic sensitivity. Such criteria require usually expensive techniques, dedicated equipment and extreme physical conditions, e.g. ultra high vacuum, low temperature, and high field etc.

This chapter presents some of the key experimental tools, which have facilitated the studies of this project. These techniques are classified into two main categories: the sample fabrication techniques and characterization techniques and later furthermore breaks down into in-house characterization techniques and synchrotron-based characterization techniques. The Molecular beam epitaxy (MBE) growth, which is a favoured deposition method to fabricate artificially layered crystals with a high degree of control and reproducibility, has been the main sample preparation technique utilized in project (will be introduced in Section 3.2). The SQUID-VSM and the magneto-transport measurement system are two representative methods of in-house magnetic measurements and have been utilized for revealing the presence of weak magnetic phases and giving information of the global magnetic properties of the samples (will be introduced in Section 3.3). The TEM, where accessible during the study, has been employed to have an insight into the internal structure of a sample and the interface geometry of a heterostructure down to the atomic level (and will be introduced in Section 3.4). And XMCD, a synchrotron-based photoemission technique, has enabled direct determination of the magnetic and electronic ground states of all the samples presented in this thesis, owing to its unique elemental specificity, site selectivity, and surface sensitivity (will be introduced in Section 3.5).

The author would like to note that some of these instruments could be found readily in York, while others were either supported by external facilities (see the list of beamtime) or provided by worldwide collaborators (see the author acknowledgement).

## 3.2 MBE

### 3.2.1 The MBE technology

Molecular beam epitaxy (MBE) is an epitaxial process by which growth of materials takes place under ultra-high vacuum (UHV) conditions on a crystalline substrate by the interaction of adsorbed species supplied by atomic or molecular beams. MBE technique has contributed to a lot of experimental research of spintronics materials and devices. It is a favoured chemical deposition method to fabricate artificially layered crystals of various complexities with high degree of control and reproducibility. Compared with other growth techniques, the most advanced characteristic of MBE is its slow deposition rate, typically ～1 ML/sec, which allows the film to grow epitaxially. Many classes of materials have been prepared by MBE such as semiconductors, oxides, magnetic materials and metals in the last four decades, whereas this section reviews only a few key aspects that are most closely related to the scope of this thesis, i.e. the application of MBE in fabricating spintronics hybrid systems.

MBE machines can have different layouts, depending on (i) whether they are used for research or production, (ii) the materials to be grown and (iii) the specific variant of MBE technology that is actually implemented. Modern machines generally have a modular design, where each module is optimised for a definite process. The York MBE system used in this study was assembled by Dr. Iain Will and the layout is presented in Figure 3-1 and Figure 3-2. The system essentially consists of a growth chamber, a load-lock chamber, and a sample transfer arm. The wafers are introduced in and extracted from the system through individually pumped load-lock chamber, so that the growth and the sample transfer modules, are always under UHV. It is worthy to note that the MBE system presented here is a rather simplified one while commercial machines can integrate multiple chambers for the interest of preparing heterostructures consisting of layers with significantly different compositions, which can be grown in different chambers to avoid any cross-contamination.

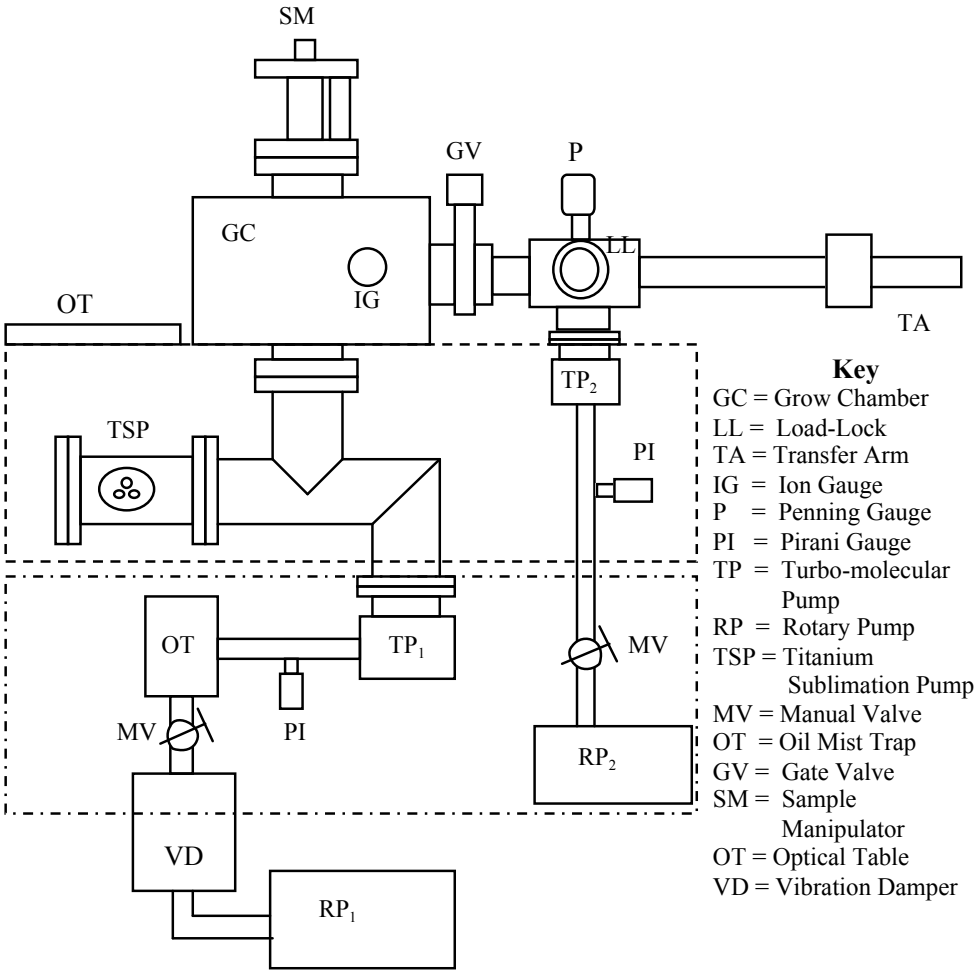


Figure 3-1 | A schematic of the MBE system, showing the pumping system, main growth chamber and load-lock chamber. There is an upper frame which rigidly links the growth chamber with the optical table. The MOKE apparatus is located on the latter. There is also a vibration damping block of cast concrete (VD) to isolate the rotary pump ($RP_1$) from the rest of the vacuum system; this is used to reduce forced vibrations in the MOKE system. $RP_2$ and $TP_2$ are switched off during MOKE and RHEED measurements. The two dashed boxes represent the upper and lower supporting frames. Image adapted from the literature.[135]

In the last four decades, it has been largely proved that epitaxial technologies for material growth have unique advantages over simpler counterparts, despite their higher technological costs. Some of the key aspects are listed as below,

- To grow materials with reduced concentrations of thermodynamical defects, due to the relatively low growth temperatures;

- To grow structures where composition or doping profiles in the growth direction can be modulated in abrupt or continuous ways (see chapter VI for its application in this project);
- To grow quantum structures, where engineered composition and doping profiles confine carriers in two- or three- dimensional regions with sizes smaller or comparable to the de Broglie wavelength of carriers, by which effects of quantum confinement may show up.

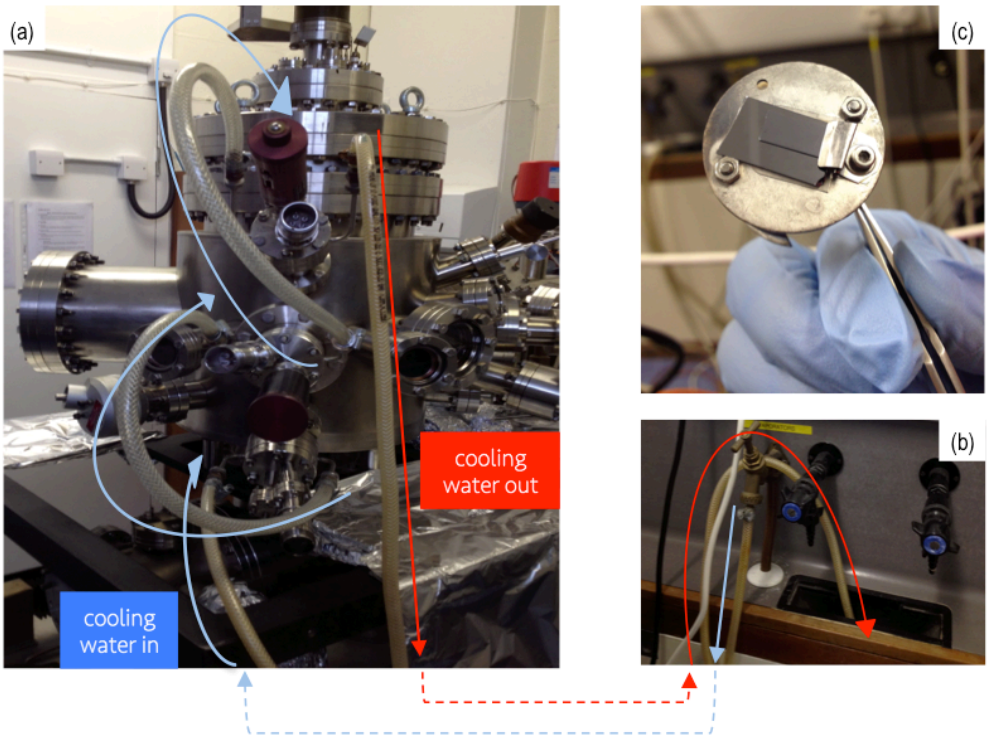


Figure 3-2 | (a)-(b) Photographs of the York MBE and the water cooling system utilized in this study. (c) sample holder with two substrates simutanouesly clamped on the stage.

### 3.2.2 The vacuum

MBE growth takes place in a molecular regime, which is characterized by mean free paths between collisions of atoms and molecules in the beams larger or comparable to critical lengths of the growth system, such as distances between cells and substrates

(<0.2 m). According to the kinetic theory of gases the mean free path between collisions of atoms or molecules at a pressure p is given by

$$\lambda = \frac{k_B T}{2^{1/2} \pi p D^2}$$

Equation 3-1

where D is the diameter of atoms or molecules in the beam. Therefore, for typical MBE operating pressures of $10^{-6}$-$10^{-4}$ mbar, it follows that λ= 5-0.05 m, respectively. Under this regime, atoms and molecules basically do not interact during their paths and, then, mechanical beam shutters can be used to switch on and off the beams directed towards the substrate; in such a way, the composition of the nourishing phase can be abruptly changed in times given by the actuation times of shutters, that is, in the order of 0.1 s. Since the MBE growth rate generally is in the ML/s range, the thickness of interfaces between layers with different composition or doping can be in the order of or smaller than tenths of a ML. It is noteworthy such features of MBEs allow the use of mechanical shutters and has strong implication in achieving interfaces abrupt on the atomic scale, when no hindrance is set by kinetic growth mechanisms (refer to Chapter IV-VI for its utilizations).

The slow deposition rate of MBE in turn requires UHV condition. A MBE chamber is usually evacuated to base pressures of $\sim 10^{-10}$ mbar using a combination of rotary, ion, and titanium pumps. The initial work reducing the chamber pressure from atmospheric to around $10^{-3}$ mbar is done by a rotary vane pump that sweeps large quantities of air rapidly. The remaining two pumps rely on the rotary pumps at all times. The first of these is the turbo-molecular pump, which is essentially a gas turbine and operates at high angular velocities (typically 20,000 - 50,000 rpm) to pump light and fast partial pressures of hydrogen gas. The turbo-molecular pump has a range from $1x10^{-1}$ to $1 \times 10^{-10}$ mbar. The next pump type is the titanium sublimation pump (TSP), which is able to reduce the pressure up to $10^{-12}$ mbar. It functions by heating up a Titanium filament to the point of sublimation and when the sublimation occurs, Titanium coats all the neighboring surfaces forming a reactive layer which traps active elements such as O, N and H.

Three types of pressure gauges are used to monitor the quality of the vacuum, whose working range are restrictively observed. The first is the pirani gauge, which has

a pressure range from atmospheric pressure to $1 \times 10^{-3}$mbar. This gauge was used to monitor the vacuum produced by the rotary pump. The second type is the penning gauge with a pressure range of $1 \times 10^{-3}$ to $1 \times 10^{-8}$ mbar. This was used in the load-lock chamber, described later. The third type of gauge was called an ion gauge. This was used in the main vacuum chamber and had a pressure range of $1 \times 10^{-5}$ to $1 \times 10^{-11}$ mbar. By combining the use of these three gauges, it was possible to monitor the quality of the vacuum from atmospheric pressure to $1 \times 10^{-10}$ mbar.

### 3.2.3 The evaporators

A variety of sources can be used for flux generation in MBE, and their design depends on the nature of the source materials. The effusion cells (also known as K-cells or Knudsen cells) comprises a crucible where highly purified elements are radiatively heated using resistive heater filaments. The maximum temperature of an effusion cell is limited by thermal stability of constructional materials (usually pyrolytic boron nitride (PBN)), and because of that, it is usually used for relatively low partial pressure elementary sources (e.g. Si and III-V including Ga, Al, In, Sb, As etc.). Cracker cells were developed in response to the perceived advantages of using dimer group V molecules ($As_2$ and $P_2$), rather than the more conventional tetrameric species ($As_4$, and $P_4$) by involving an additional cracking zone to decompose tetramers into dimers. E-beam evaporators are the workhorse of metal MBE systems, especially for materials with have high evaporation temperatures. It provides the energy required for evaporation by bombardment of the source material directly with a high-energy e-beam (typically a few keV). The stability of atomic fluxes generated from effusion cells only depends on the temperature fluctuation in the cell (typically < 1 °C) and the slope of the vapor pressure curve. E-beam evaporators are more prone to flux instabilities and closed-loop setups, where the flux is monitored and used as a feedback signal to adjust the evaporation parameters, are employed to minimize the fluctuations The rate of evaporation can be precisely controlled by varying the applied current through Tantalum filament and be monitored by means of a calibrated emission current, defined as the current between the evaporant and earth. A schematic diagram of the e-beam evaporator used in York MBE system is presented in Figure 3-3.

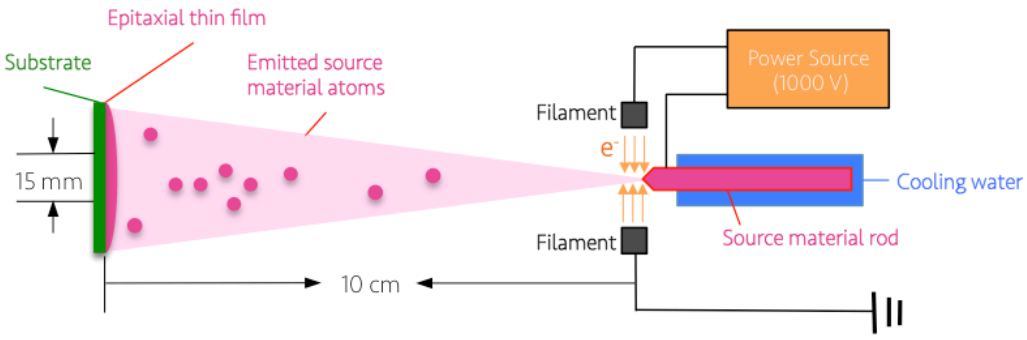


Figure 3-3 | Schematic diagram of the flux generation using electron beam evaporator (side view). Electrons emit from the filament and heat on the top of the rod. Atoms emitted from the source material slowly land on the substrate on the opposite and epitaxial grow with respect to the substrate orientation. Note that the probability density of the atoms landing position follows Gaussian distribution. Therefore only a narrow area of the thin film is considered to be uniform, e.g. the central 15 mm × 15 mm in the York MBE system.

Regardless of the variety of MBE sources, there are some general rules for the use of evaporators:

- The flux should be free of contaminants generated by the constructional materials.
- The source should operate at a temperature which is as low as possible, commensurate with obtaining the desired flux, to minimize contamination of the flux by outgassing.
- The source should permit good and reproducible control of the flux.
- The source should be capable of providing a wide dynamic range of flux (e.g., over five orders of magnitude for dopants).
- Response times to programmed changes in source conditions (e.g., temperatures, gas flow) should be rapid.
- The flux distribution emanating from the source should be commensurate with the MBE system geometry to obtain optimized deposit uniformity;
- The source design should be rugged and reliable. Prior to any growth, it is essential that the sources be degassed thoroughly to minimize the impurities released into the vacuum during evaporation.

The hardware components needed for an oxide MBE system are similar to the

general setup of a conventional MBE system. There are various ways to supply oxidizing agents to the substrate. The most straightforward approach is to use molecular oxygen by injecting the gas directly into the chamber. Molecular oxygen is not very reactive and is therefore only suitable for the growth of compounds that easily oxidize or if lower oxidation states of the constituent cations are desired. More reactive species, such as ozone or atomic oxygen, are commonly applied if higher oxidation activity is needed during growth. In addition, $NO_2$ has also been used as an efficient oxidizer to effectively reduce the gas load into the system. Using a highly reactive oxidizer a sufficiently large mean free path can be guaranteed to avoid gas phase reactions, while at the same time sufficient oxygen is supplied to the substrate to ensure oxygen stoichiometry of the growing film. The complete oxidation of the growing film can be a major challenge in oxide MBE. Complex oxides with low oxygen affinity are prone to reduction in vacuum. The oxidizing agent not only has to oxidize the metal atoms supplied from the evaporator that arrive at the film surface but also has to compensate for the loss of oxygen that occurs because the sample is kept at elevated temperatures in vacuum.

### 3.2.4 The flux monitoring

The thickness of the thin film growth of MBE can be monitored and recorded by a quartz microbalance, provided that the flux profile of the evaporator in use is stable or repeatable every time. The tooling factors of the quartz microbalance are usually defined by measuring the step between a thin film and a shuttered as-grown area by means of ex-situ AFM or cross-sectional TEM (see Figure 3-2 (c)). Another widely used technique is the commercially available flux monitor that attacheds to the source gun. Such technology detects the charge carried by the outgoing metal particles. Through a circle in the flux, a certain part of the flux is blocked and a small current is generated and through a feedback circuit, this flux is automatically stabilized by controlling the voltages or currents applied.

### 3.2.5 The substrate

The selection and etching of substrates play crucial roles in MBE process. To realize the

epitaxial growth, the deposits and the substrate must have (i) the same crystalline structure or a structure with a similar symmetry, and (ii) a small lattice constant mismatch, i.e. typically no more than 3%. The lattice mismatch constant $\varepsilon_0$ is defined as the ratio $(a_e-a_s)/a_s$, where $a_e$ and $a_s$ are, respectively, the in-plane lattice parameters of the free-standing epilayer and the substrate. For the regime where $\varepsilon_0 < 3\%$, it has been proved that under optimum MBE growth conditions and their free energies the epitaxial growth takes place according to the 2D layer-by-layer mechanism. However, in many cases, the initial stage follows the island growth (see Chapter II, Figure 2-5). The crystalline structure and the lattice constant of the materials involved in the study of the present project are summarized in Table 3-1.

| **materials** | **structure** | **$a_0$ (Å)** |
|---|---|---|
| Fe | bcc | 2.866 |
| Co | hcp | 2.507 |
| Ni | fcc | 3.524 |
| $Fe_3O_4$ | spinel | 8.396 |
| GaAs | zinc blende | 5.653 |
| Si | fcc | 5.431 |
| MgO | halite | 4.212 |
| $Co_2FeAl$ | $L2_1$ | 5.720 |

Table 3-1 | The crystal structure and lattice constant of the materials utilized in this thesis.

The major semiconductors utilized have been the III-V compounds epi-ready GaAs(100) wafers. These substrates were purchased from Wafer Technology Ltd, who supplies the materials as single side polished, 2" wafers in a specific shape format which denotes the orientation of the crystal axes, known in this case as the EJ option and US option, respectively (see Figure 3-4). Commercial GaAs(100) wafers are prepared using vertical gradient freeze (VGF) method, in which the single crystal structure is induced to grow from a polycrystalline basis in a low pressure environment. In some occasions, MBE can also be used to add fine quality epilayers to the VGF prepared wafers in addition (see Chapter IV, the sample growth section 4.4 for an example).

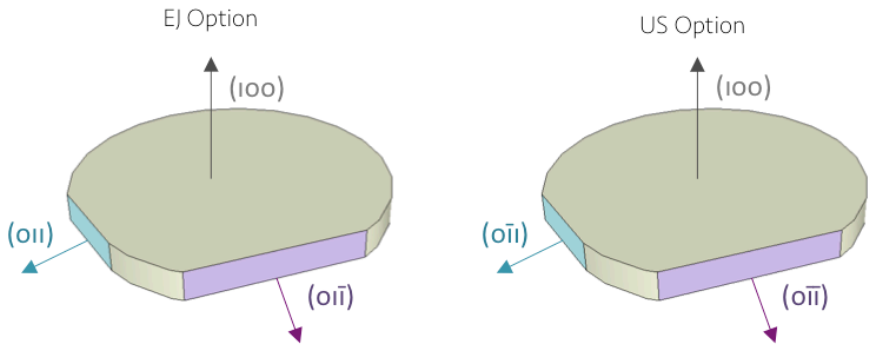


Figure 3-4 | Two common wafer configuration options, European (EJ) and American (US).

A wide variety of etching solution can be found in the literature for etching GaAs. In this project, a mixture of solution comprised of $H_2SO_4$ : $H_2O_2$ : $H_2O$ in a ratio of 4:1:1 by volume was used. The solution was always freshly prepared with the recipes as presented in Figure 3-5 in details. This solution is rather gentle for polishing and etching away a very thin layer of GaAs on its surface when used at RT, while at the same time maintaining a relatively flat surface on top of which magnetic thin films can be deposited epitaxially. Prior to the etching, the GaAs substrates were ultrasonically cleaned with detergent (RBS), acetone, iso-propanol (IPA), with deionized (DI) water rinsing between each step. An etching time of 50 s with the $H_2SO_4$ + $H_2O_2$ + $H_2O$ solution was found to be adequate to avoid structural effects of anisotropic etching of the substrates. Furthermore, the surface roughness of the etched GaAs substrates can be improved by in-situ annealing at around 550 ◦C for 50 min in the MBE growth chamber.

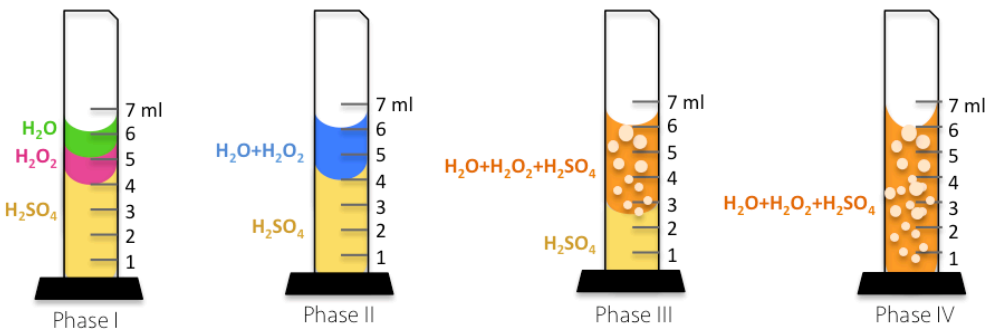


Figure 3-5 | The recipes of the $H_2SO_4$ + $H_2O_2$ + $H_2O$ solution preparation process utilized in this study.

### 3.2.6 RHEED

The relatively low chemical aggressiveness of MBE growth environment makes it possible to install in the growth or in interconnected chambers a number of diagnostic techniques, not generally available to other epitaxial technologies. Reflection high energy electron diffraction (RHEED) is the most commonly used diagnostic instruments allowing the exploitation of controlled MBE growth. The technique facilities the study of in-situ and in real time crystallinity and morphology of epitaxial deposits and allowed an instantaneous feedback of the influence of growth conditions on properties of growing layers. RHEED operates by detecting the reflected electrons with high kinetic energy (typically in the 10 – 50 keV regime) and low incident angle (typically 0.5 – 2.0°) from the surface of a solid. As illustrated in Figure 3-5, the diffraction pattern received on the screen describes the **k**-space Ewald sphere of the sample crystalline, in accordance with Bragg's Law. Assuming elastic scattering occurs, one could calculate the lattice spacing of the sample if the distance from the sample to the recording screen and the energy of the electron source are known, e.g. for a simple cubic structure

$$a_0 = \frac{\lambda L \sqrt{h^2 + k^2}}{t}$$

Equation 3-2

in which $a_0$ is the lattice constant, $h$ and $k$ are Miller indices, $\lambda$ is the wavelength of the incident electrons, L the distance between sample and screen and t the distance between the streaks on the screen.

The condition for constructive interference of elastically diffracted electrons is given by the Laue law, which states that the wavevectors of incident and diffracted beams must differ by a reciprocal lattice vector. Under grazing incidence (typically 1 degree) and with atomically smooth surfaces, electrons may emerge from the crystal only when the diffracting planes are at depths of few MLs; in this case, the electron beam is diffracted by a two-dimensional lattice, whose reciprocal lattice consists of parallel lines. On the other hand, in case of atomically rough surfaces, electrons emerge even if they were diffracted by deeper planes; under these conditions, electrons sense a three-dimensional lattice, the reciprocal lattice of which is represented by points. For any incident wavevector, the Laue condition implies that the wavevectors of diffracted

beams are determined by the intersection of reciprocal lattice lines or points with the Ewald sphere, that has a radius equal to the electron momentum. Two important features of electron (as opposed to X-ray) diffraction from real crystals are (i) the radius of the Ewald sphere is much longer than the distance between reciprocal lattice points or lines and (ii) the surface of the Ewald sphere has a finite thickness, due to the energy spread (and, hence, the momentum spread) of electrons; moreover, lattice defects and vibrations broaden the reciprocal lattice points and lines that, therefore, can be represented by spots and rods, respectively. As a consequence, depending on whether the surface is atomically rough or smooth, the diffraction pattern consists of spots or streaks, respectively; therefore, the occurrence of streaks, instead of spots, is the clear proof that diffraction takes place from few shallow lattice planes and, then, that the diffracting surface is atomically smooth.

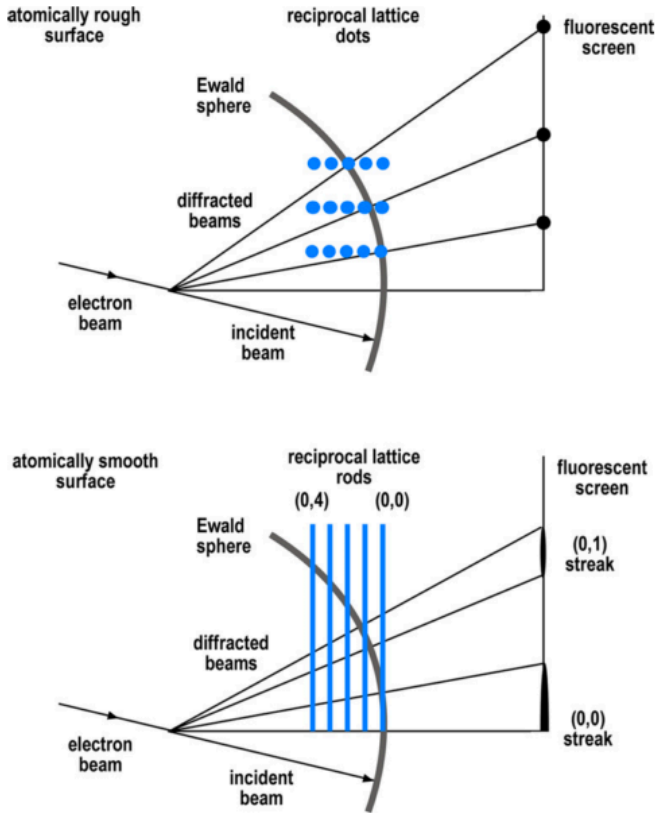


Figure 3-6 | Schematic representation of the origin of RHEED diffraction patterns from atomically rough (upper panel) and smooth (lower panel) surfaces characterized by reciprocal lattices given by spots and rods, respectively, a few of which are sketched in the figure; the intersections of the Ewald sphere with the features of the reciprocal lattice define diffracted spots and streaks visualized on a fluorescent screen. Image adapted from the literature.[136]

The streaky diffraction pattern of RHEED depends on not only the azimuth of the impinging electron beam with respect to the crystallographic directions of diffracting layer but also the surface reconstructions which, in turn, depend on growth conditions. Figure 1.9 shows typical examples of diffraction patterns from a clean GaAs (100) surface grown under As-rich conditions (see below), observed under [011] and [0-11] azimuths; the patterns are characterized by one and three "fractional order" streaks in between the "integer order" ones, respectively; these features show that (i) the surface smooths out during the early stages of growth and, (ii) along the two perpendicular directions, the GaAs (100) surface unit cell shows a twofold (2 x) and a fourfold (4 x) periodicity, respectively, as compared to that of the unreconstructed unit cell.

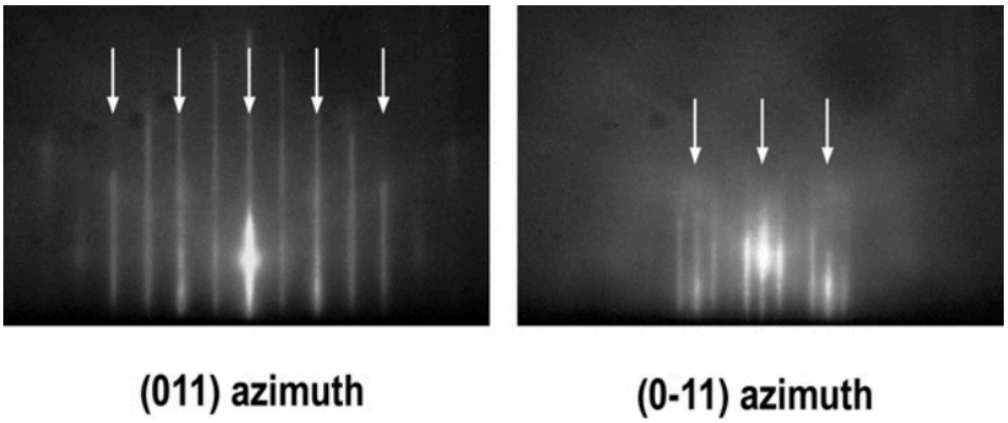


Figure 3-7 | Typical RHEED patterns observed along the (011) (left panel) and (0-11) (right panel) azimuths during the MBE growth of epitaxial GaAs on a (100) GaAs substrate; the surface reconstruction is the As-stabilized (2x4) one. The arrows mark the position of diffraction features from bulk layers ("integer order" streaks). Image adapted from the literature.[137]

Arthur[138] first proposed that surface reconstructions could be related to surface stoichiometry and, in particular, to As gain or loss. Then, other researchers[139, 140] studied by auger electron spectroscopy (AES) the variations of surface stoichiometry associated with GaAs (100) reconstructions and confirmed the As- or Ga- rich nature of surfaces with different reconstructions; photoemission spectroscopy provided rather precise values of As coverage for many GaAs (001) surface reconstructions.[141, 142, 143] These results allow the identification of different regimes of surface stoichiometry by simply

analyzing RHEED diffraction patterns during growth. The observation that different surface reconstructions are associated with different surface stoichiometries is consistent also with the previous observation that amphoteric dopants such as Ge are incorporated in GaAs as donors or acceptors depending on whether the growth is carried out on (2 x 4) or (4 x 2) reconstructed surfaces, respectively. Most of the GaAs (100) surface reconstructions, ranging from As rich to Ga rich, were thoroughly studied by Deparis and Massies[144] by relating RHEED observations to the accurate control Ga and As fluxes supplied to surfaces.

## 3.3 Global magnetism measurement

### 3.3.1 SQUID-VSM magnetometry

This section introduces two distinct types of techniques for making magnetic measurements of nanostructure samples: SQUID magnetometry and magnetoresistance (MR) measurement system, both of which are representative methods of in-house measurements and particularly useful for revealing the presence of weak magnetic phases and giving information of the global magnetic properties of samples.

As a representative induction-based magnetism measurement system, SQUID-VSM is one of the most widely used instruments for bulk magnetic characterization of materials by sensing the flux change in a coil when a magnetized sample is vibrated near it. In a typical SQUID-VSM, the sample under (typically a few millimeters in size) is usually mounted on a nonmagnetic rod, attaching to a mechanical vibrator (typically the frequency < 40 Hz and the vibration amplitude ～a few millimeters) or a loud speaker (typically the frequency < 100 Hz and the vibration amplitude ～0.1 millimeters). When the sample is scanned through the center of a first- or second-order superconducting gradiometer, a closed flux transformer will form, comprising of a pick-up loop and an input coil tightly coupled to SQUID. Owing to flux quantization in superconducting rings, any change in magnetic flux through the pick-up loop due to the signal of interest results in a flow of screening current in the flux transformer coupling magnetic flux through the SQUID loop and the SQUID responds by generating a proportional output voltage. This voltage can be recorded as a function of sample position in the form of a flux profile, and the magnetization of the sample is inferred by fitting the shape and magnitude of the measured flux profile to that expected for a point dipole. In a modern SQUID-VSM, the sample can also be fixed at a point where the slope of the flux profile is maximum and is vibrated about this mean position at a low frequency. Since the full flux profile does not have to be recorded, measurements over an extended range of T and H can be completed in a relatively short period of time by doing so. To apply a magnetic field to the sample, the detection coils are located in the bore of a superconducting magnet. Temperature control is made possible by placing the sample and sample rod in a sealed variable temperature insert, which is thermally isolated from the 4.2-K gradiometer and magnet by an annular vacuum space.

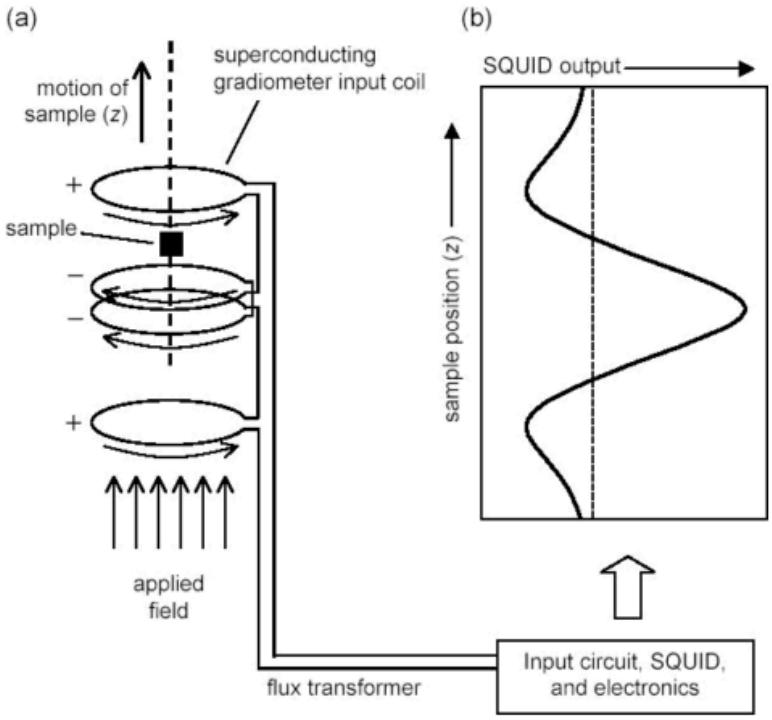


Figure 3-8 | (a) Schematic of SQUID magnetometer–susceptometer. (b) Calibrated output from SQUID electronics, recorded as a function of position. Image adapted from the literature.[145]

SQUID-VSM has ~100 times sensitivity advantage over a conventional VSM ($10^{-9}$ $Am^2$ for a 1 second average) due to the application of the SQUID unit, which works based on Josephson effect. Such effect occurs when an electric current (Cooper pairs) flows between two superconductors separated by a thin non-superconducting layer through quantum tunneling. Figure 3-9 presents a schematic diagram of a usual form SQUID unit consisting of a loop of superconductor (typically ~ 100 $\mu$m) with two Josephson junctions. A superconducting measuring current flows through the ring, dividing so that equal currents pass through each of two Josephson junctions. A changing magnetic flux through the ring generates a voltage and a current in the ring, according to Faraday's Law. This induced current adds to the measuring current in one junction, and subtracts in the other. Because of the wave nature of the superconducting current, the result is a periodic appearance of resistance in the superconducting circuit, and the appearance of a voltage between points A and B. Such type is so called DC-SQUID. SQUID also has RF versions, in which the interactions between the superconducting ring and an external resonant LC circuit is measured alternatively. RF-

SQUID is cheaper and easier to manufacture in smaller quantities, since only one Josephson junction is used in it, but with a sacrifice of sensitivity. It should be noted that although instrumentation and calibration techniques determine the accuracy of a SQUID magnetometer (in principal < $10^{-8}$ emu), the sensitivity limit for a given measurement is likely to be dominated by the environment.

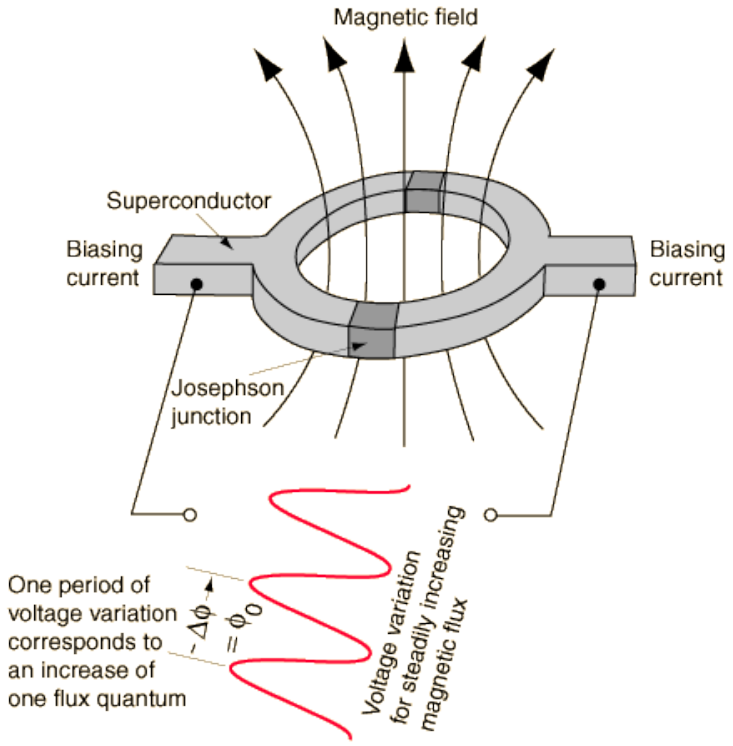


Figure 3-9 | A schematic diagram of a usual form SQUID unit consisting of a loop of superconductor with two Josephson junctions. Image adapted from the literature.[145]

### 3.3.2 Magneto-transport measurement system

The electro- and magneto- transport measurements are important routines to observed materials' overall electric and magnetic properties. The commercial electro- and magneto- transport measurement systems can have various layouts depending on the techniques incorporated, such as the cryogen and magnetic field, and are usually integrated with instruments like Physical Property Measurement System (PPMS®).

Figure 3-10 present a schematic diagram of the custom-built setup of York's electro- and magneto- transport measurement system, which can be a prototype of apparatus of such kind. The sample with bonding pads is placed on chip carriers and bonded to the pins of the chip. The chip carrier contains 20 pins; each of them can be accessed electrically from the selection box. The rotating sample holder where the chip carrier is accommodated has been utilized, allowing for angular dependent electrical transport and magnetotranpsort measurement up to 360◦ of a given sample respect to the applied magnetic field. A Keithley 2300 source meter is used to send out a Labview programme defined voltage or current signal and to measure a current or voltage value. By programming the system, either a MR measurement may be taken by cycling the magnetic field and measuring the resistance of the samples at each field or an I-V measurement may be taken by changing the current value and measuring the resulting voltage or vice-versa.

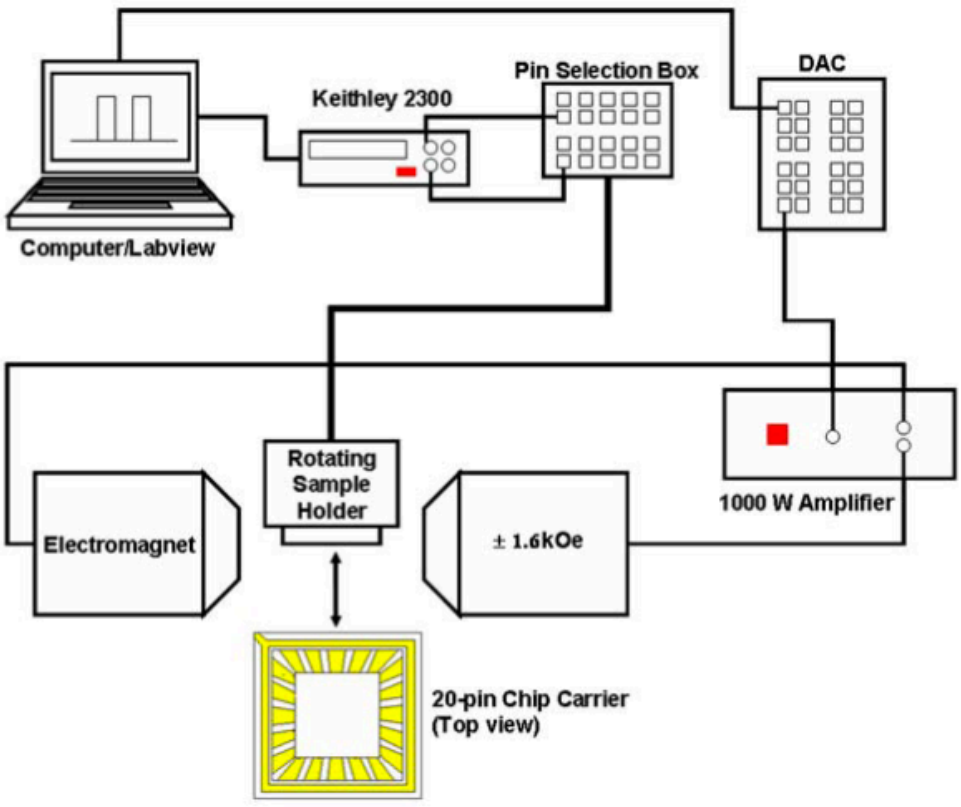


Figure 3-10 | A schematic diagram of the electrical and magnetotransport measurement setup. The source signal is sent to a sample from a source meter and simultaneously the output signal is picked up by the same meter which is connected to a computer with a Labview control programme for data acquisition. Image adapted from the literarure.[95]

## 3.4 Electron Microscopy Techniques

### 3.4.1 The EM technique

Electron Microscopes (EMs) are used where it is desired to study the internal structure of samples down to the atomic level. In the research of spintronics materials, they have long played key roles in driving people's scientific understanding of extended defects and their control of the properties of materials. EMs were developed for the purpose of observing fine structure of matters beyond the diffraction limitation of optical microscopes. Analogous to optical microscopes, EMs use highly energetic electrons to probe a sample and to produce a magnified image of the sample morphology and surface topography. Yet because of the wavelength of electrons (e.g., $\lambda = 0.005$ nm at an accelerating voltage of 50 keV) are much shorter than that of photons, electron microscopes are able to give spatial resolution down to atomic scale. With the current generation of aberration corrected and monochromated EMs, one can now obtain images with a spatial resolution approaching 0.05 nm in both the plane-wave, phase-contrast TEM and the focused probe, Z-contrast scanning-TEM (STEM) modes of operation. In addition to the increase in the spatial resolution, aberration correctors also provide an increase in the beam current and subsequently the signal-to-noise levels (contrast) in the acquired images. This means that small differences in structure and composition can be more readily observed. And contrary to what might be expected, most samples are not adversely affected by the electron bombardment as long as beam conditions are controlled judiciously.

### 3.4.2 The electron diffraction

There are mainly two types of electron sources used in EMs, categorized by the distinct mechanisms in producing electrons, namely, thermal emission and field emission. The electron gun materials can be tungsten filaments or a lanthanum hexaboride crystal ($LaB_6$), and each of them represents a different combination of costs and benefits. At temperatures in excess of around 2700 K, a tungsten wire emits an abundance of both photons and electrons; in an electron gun the electrons are accelerated across a potential difference of tens of hundreds of kV to generate a beam of electrons of controlled energy between 2 - 40 keV. The electron gun filament of $LaB_6$ field-emission type uses

strong electric field to extract the electrons of the filament to tunnel out of the filament surface. High beam currents can be achieved in a small beam diameter by field emission and usually this type of electron guns gives better resolution for the EMs. The electron probe is produced by two or three stage demagnification of the smallest cross-section of the electron beam after acceleration. The electron probe, 2 - 10 nm in diameter, is scanned in a raster over a region of the specimen by the scan coils.

Electron diffraction is a phenomenon that has been intensively exploited because it can assess the nature of crystalline habits present in nanostructures. When an electron beam interacts with the atoms of a sample, individual incident electrons undergo two types of scattering - elastic and inelastic. In the former, only the trajectory changes and the kinetic energy and velocity remain constant while in the case of inelastic scattering, electrons collide with and displace electrons from their orbits (shells) around nuclei of atoms. This interaction places the atom in an excited (unstable) state. Most of the signals in SEMs come from inelastic scattering process while in TEMs, elastic scattering is the predominated process.

In the electron-matter interactions, the electron penetration depth can be calculated from Kanaya-Okayama Formula, which considers the combined effect of elastic and inelastic scattering process

$$R_{k0} = \frac{0.0276 A E_0^{1.67}}{Z^{0.89} \rho}$$

Equation 3-3

in which $R_{ko}$ (in $\mu m$), A (in g/mol), $E_0$ (in keV), Z, and ρ (in g/cm$^3$), respectively, represents the dimension of interaction volume, the atomic number weight, the beam energy, the atomic number, and the density. A generalized illustration of interaction volumes for various electron-matter interactions is presented in Figure 3-11.

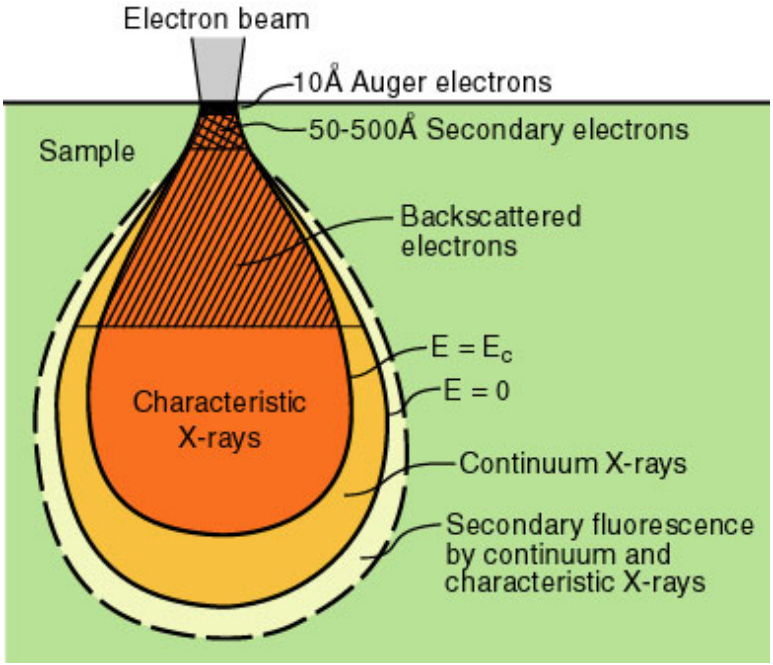


Figure 3-11 | A generalized illustration of interaction volumes for various electron-matter interactions. Auger electrons emerge from a very thin region of the sample surface (maximum depth about 50 Å) while secondary electrons interact deeper inside (50-500 Å). Image adapted from the Internet. (http://www.physics.ucf.edu/~lc/5937_ lecture_8.pdf)

### 3.4.3 SEM

The 3D image contrast of SEM image is produced by edge effect that more electrons shall emit out of the sample at edges leading to increased brightness, as schematically illustrated in Figure 3-12. SEM detects signals resulting from interactions of the electron beam with atoms at or near the surface of the sample including secondary electrons (SEs) with most probable exit energies of 2-5 eV and the backscattered electrons (BSEs) with energies that range from the energy of the primary electrons. Analytical information can be obtained from the X-ray spectrum and Auger electrons and the signals are detected by various kinds of detectors in corresponding.

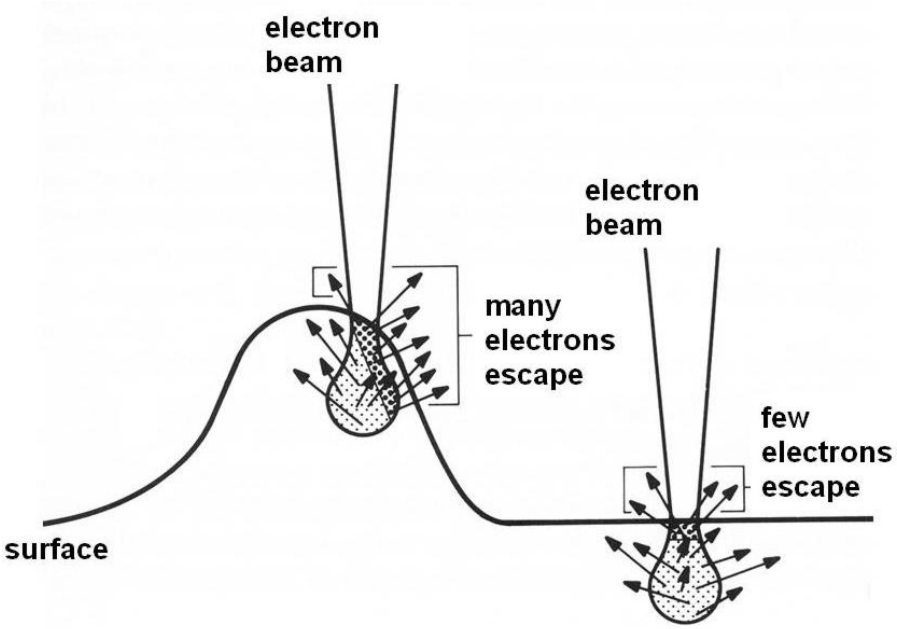


Figure 3-12 | A schematic illustration of edge effect. More secondary electron shall leave the sample at edges, where results in increased brightness while for the flat areas, less secondary electrons escape. Image adapted from the Internet.(http://www.microscopy.ethz.ch/se.htm)

The most important signals in SEM come from SEs, which are generated as ionization products. When an incident electron excites an electron in the sample and loses most of its energy in the process. The excited electron moves towards the surface of the sample undergoing elastic and inelastic collisions until it reaches the surface, where it can escape if it still has sufficient energy. Production of secondary electrons is very topography related. Due to their low energy (5 eV) only secondaries that are very near the surface (<10 nm) can exit the sample and be examined. Any changes in topography in the sample that are larger than this sampling depth will change the yield of secondaries due to collection efficiencies. Collection of these electrons is aided by using a "collector" in conjunction with the secondary electron detector.

### 3.4.4 TEM

The image generation principal behind TEMs is analogous to that of a slide projector. In a slide projector light from a light source is made into a parallel beam by the condenser

lens; this passes through the slide (object) and is then focused as an enlarged image onto the screen by the objective lens. In the electron microscope, the light source is replaced by an electron source, the glass lenses are replaced by magnetic lenses, and the projection screen is replaced by a fluorescent screen, which emits light when struck by electrons, or, more frequently in modern instruments, an electronic imaging device such as a CCD (charge-coupled device) camera. On the way from the source to the viewing device, the electron beam passes through a series of apertures with different diameters. The whole trajectory from source to screen is under vacuum and the specimen (object) has to be very thin to allow the electrons to travel through it. Alternatively, if one wants to look at the surface of the sample, rather than a projection through it, a SEM (as previously discussed) is employed.

TEM exploits three different interactions of electron beam-specimen; unscattered electrons (transmitted beam), elastically scattered electrons (diffracted beam) and inelastically scattered electrons. Samples being measurement by TEM must be stable and small enough (typically no larger than a few mms) to permit its introduction into the evacuated microscope column and thin enough (typically no more than 500 nms) to permit the transmission of electrons. When incident electrons are transmitted through the thin sample without any interaction occurring inside the specimen, then the beam of these electrons is called transmitted. The transmission of unscattered electrons is inversely proportional to the specimen thickness. Areas of the sample that are thicker will have fewer transmitted unscattered electrons and so will appear darker, conversely the thinner areas will have more transmitted and thus will appear lighter. Another part of the incident electrons, are scattered (deflected from their original path) by atoms in the specimen in an elastic fashion (no loss of energy). These scattered electrons are then transmitted through the remaining portions of the sample. All electrons follow Bragg's Law and thus are scattered according to

$$n \bullet \lambda = 2d \sin(\theta)$$

Equation 3-4

in which $\lambda$, $\theta$, d, respectively represent the wavelength of the electron X-rays, the angle between the incident X-rays. and the surface of the crystal, and the spacing between layers of atoms. All incidents that are scattered by the same $n \cdot \lambda = 2 \cdot d \cdot \sin(\theta)$ atomic spacing will be scattered by the same angle. These scattered electrons can be

collected using magnetic lenses to form a pattern of spots; each spot corresponding to a specific atomic spacing (a plane). This pattern can then yield information about the orientation, atomic arrangements and phases present in the area being examined.

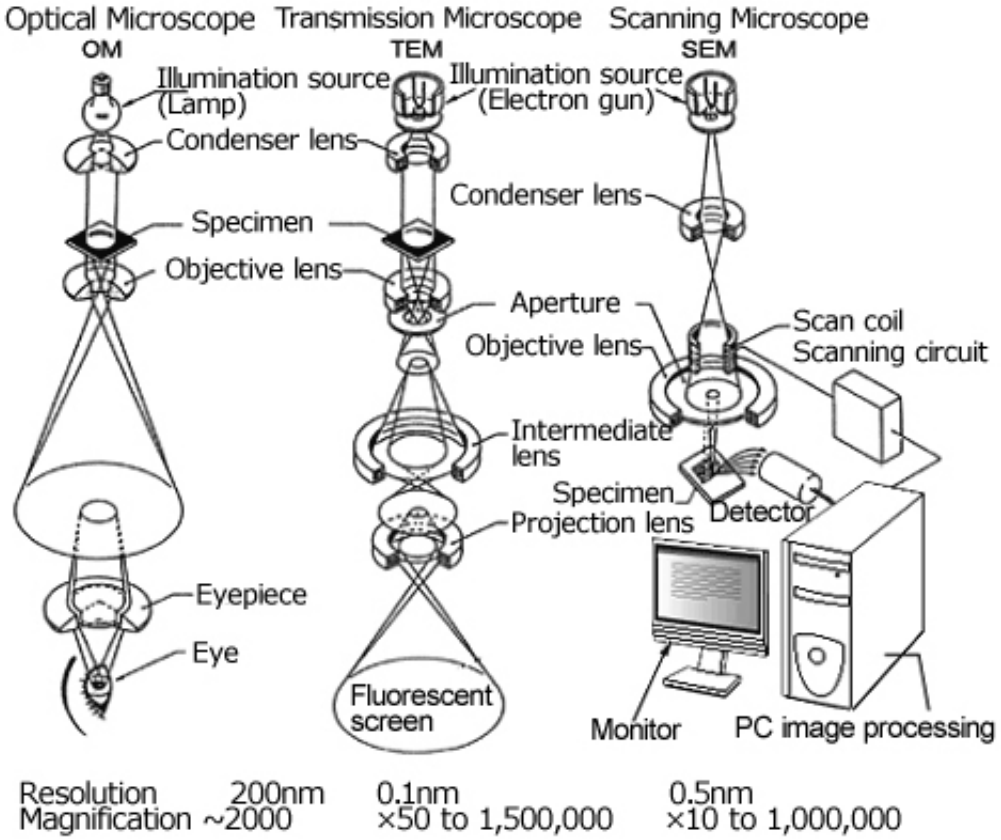


Figure 3-13 | Schematic layout of an optical microscope, a TEM, and a SEM. Image adapted from JOEL website.(http://www.jeol.com)

### 3.4.5 STEM

STEM is an associated technique of TEM, in which the focused beam (probe) of electrons is scanned across the surface of the sample and a 2-D image is created by displaying the output from one of these detectors as a function of the beam position. The STEM operated in a very similar way to a SEM, but, as with the TEM, backscattered electrons and X-rays are also produced giving additional imaging modes. One of the most common ways of carrying out STEM has been to add transmission

detectors to an SEM or to add scanning coils to a TEM. However, these modified versions are always limited either by the low accelerating voltage of the original SEM, or the minimum probe diameter and the small the microanalysis resolution of the original TEM.

Modern STEMs combines the advantages of both SEMs and TEMs. Transmitted electrons collected on axis in the STEM give the bright field or phase signal. These electrons have either not been scattered at all or have been inelastically scattered through angles of milliradians or less and exhibit largely crystallographic information. A unique imaging mode of STEM is called high-angle annular dark field (HAADF) detection, in which the scattering that is collected is proportional to the Rutherford scattering cross-section that has a second power $Z^2$ dependence on the atomic number Z of the scattering center—giving rise to the name Z-contrast imaging. From the earliest images of individual heavy atoms on a light support, the technique evolved to be able to image crystals with atomic spatial resolution. An additional bonus offered by the STEM is the ability to collect SEs and backscattered images in the same way as a standard SEM, making it possible to correlate surface information with bulk information of the sample. Furthermore, the use of optional live diffraction units bring even more versatility to the STEM by allowing diffraction images and Z contrast images to be obtained simultaneously.

### 3.4.6 Aberration correction

The recent development of aberration correction techniques has enabled major advances in both TEM and STEM capability. Without correction, TEM resolution is limited primarily by spherical aberration, which causes information from a point in the object to be spread over an area in the image. This results not only in a general blurring of the image, but also in a phenomenon called delocalization, in which periodic structures appear to extend beyond their actual physical boundaries. In an optical microscope, spherical aberration can be minimized by combining lens elements that have opposing spherical aberrations. Unfortunately, such approach is not directly applicable for EMs, since the round magnetic lenses they use exhibit only positive spherical aberration. Also the ability to correct spherical aberration leaves the reduction or correction of the effects of chromatic aberration as the next major challenge in improving TEM performance.

As with other high-resolution methods, defocus can be used to balance out the effects of aberrations up to some optimum value, usually called the Scherzer defocus, with a resolution given by

$$d = 0.43(C_s\lambda^3)^{1/4}$$

Equation 3-5

As can be seen from this equation, there are two principal factors that control resolution—the wavelength of the electrons (determined by the acceleration voltage of themicroscope) and the spherical aberration coefficient $C_s$ of the lens (typically in uncorrected state-of-the-art 200 keV TEM/STEM, $C_s$ ~ 0.5 mm, giving an optimum probe size of 0.12 nm). Figure 3-14 presents a schematic illustration of the effect $C_s$ correction, which makes a larger area of the lens is free from spherical aberration.[146] Today significant progresses have been made by engineering extremely stable high voltage and lens current power supplies, by using specially optimized field emission electron sources, and by directing the beam through a monochromator, which passes only a very narrow band of energies. Spherical aberration has essentially been removed as the limitation in the probe size and as was with the Scherzer defocus, the aberration corrector can now be adjusted to compensate for those higher order aberrations by tuning $C_s$ itself to an optimal value.[147]

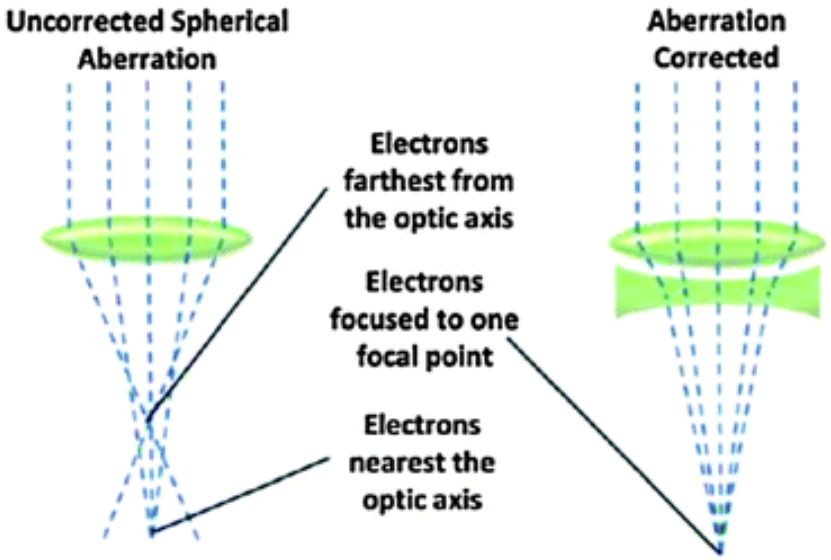


Figure 3-14 | Conceptual illustration of the spherical aberration for an uncorrected lens and aberration correction using a compensating lens system (depicted as a concave lens). Image adapted from the literature.[148]

## 3.5 XMCD

### 3.5.1 The XMCD technique

XMCD technique uses soft X-ray to probe the core level electrons of atoms, directly addressable to the electronic and magnetic ground states of the materials under interrogation. It offers unique elemental selectivity and allows one to identify the origin of magnetic signal in a given material ranging from simple elemental films to complex alloys and compounds. XMCD is furthermore a surface sensitive technique. Generally the photoelectrons created deeper in the sample lose too much energy to overcome the work function of the sample and cannot be detected. The sampling depth *L* of XAS experiments is typically a few nms, but can vary depending on the incident X-ray intensity and the type and the form of the samples it probes.

| Edge | | 3d TM | 4d TM | 5d TM |
|---|---|---|---|---|
| K | 1s → p | 5 - 11 keV | 17 - 27 keV | 65 - 81 keV |
| $L_{2,3}$ | 2p → d | 450 - 950 eV | 2 - 4 keV | 9 - 14 keV |
| $M_{2,3}$ | 1s → p | 30 - 125 eV | 150 - 650 eV | 1.7 - 3 keV |
| $N_{2,3}$ | 4p → d | | | 380 - 610 eV |

Table 3-2 | X-ray absorption edges for magnetic 3d, 4d, and 5d TMs and their photon energy region. Data adapted from the X-ray data booklet.[149]

One of the most powerful aspects of X-ray is the high photon energy (PE), making it possible to excite the core level electrons of the material under interrogation (see Table 3-2 for the X-ray absorption edges for magnetic 3d, 4d, and 5d TMs and their photon energy region). The core-level state is an ideal probe to study the local electronic configuration of the valence states. Compared to the magneto-optical effects in the visible, X-ray transitions are more straightforward to calculate due to the well-defined core state. By using laser sources, electronic and magnetic information probed is confined substantially within the valence band of solids by the conventional in-house photoemission techniques, owing to the excited optical transitions of samples by low energy photons of only a few eV. Although efforts have been made in the very recent few years in developing the in-house X-ray ultraviolet (XUV) generation, the photon

energy (PE) it achieves is still far beyond that needed to excite the core level electrons of magnetic elements, e.g. *3d* transitions metals and the rare earth. That is why synchrony radiation (will be introduced latter) has been employed in this study.

### 3.5.2 The synchrotron radiation

The high intensity, highly tunable polarized X-rays used in XMCD is one of byproducts of the synchrotron radiation, produced when electrons in asynchronous orbit are accelerated to very nearly the speed of light. As most of the XAS and XMCD data presented in this thesis have been obtained mainly from Diamond light Source, UK (see appendix for a list of the beam time that the author has participated), in the remainder of this section, the station and end station conditions of it will be introduced as an example. The worldwide synchrotron radiation sources have experienced continual development and improvement in the past few decades. Among them, Diamond light Source is relative modern one and can be representative of the latest synchrotron radiation techniques.

The synchrotron generation starts by passing electrons from their source into initially a linear accelerator (known as Linac) where they achieve energies of 100 MeV at which point they are injected into the booster synchrotron where their energies increase to around 3 GeV with the aid of RF cavities to provide energy and bending magnets to direct the beam. The electrons then transfer to the main synchrotron storage ring, which has a diameter of ~30 m. In this ring electrons complete the circuit in approximately two millionths per second and the orbit of the electrons is maintained by bending magnets that apply a magnetic field to the electron beam. The speed of these high energetic electrons is now so close to that of light that further acceleration provokes the emittance of radiation.

A mulitipole wiggler is a device that sits in the stream of the electron beam, an array of magnets are positioned above and below, altering the beam course. The "wiggling" of the electron beam by the wiggler results in a cone of X-rays being emitted in the forward direction.[150, 151] Polarized X-rays are produced using an asymmetric multipole wiggler. In a conventional wiggler, the right-handed and left-circularly polarized light cancel, resulting in no net circular polarization. An asymmetric wiggler no longer has a symmetric magnetic field profile in the longitudinal direction, rather, it

has a large positive field over a short distance followed by a smaller negative field over a longer distance designed as to have a net zero integrated field per period. In this case the circular polarization contributions of the two poles are not equal and so although there still exists a cancellation, there is a resultant net circular polarization off-axis. In the beamline I10 of Diamond Light Source, circularly polarized X-rays with ~100% degree of polarization[152] is created by using two APPLE II undulators and therefore the derived magnetic moments, as presented in this thesis, need no corrections due to the complete polarization.

Figure 3-15 presents a schematic diagram of the synchrony radiation station layout, consisting of (1) the injection system, (2) the booster synchrotron, (3) the storage ring, (4) the beamlines, (5) the front end where light is extracted from the storage ring, (6) the optics hutch where certain wavelengths of light are selected and focused, (7) the experimental hutch housing the experimental equipment, (8) the control cabin where the scientific team monitors and controls every aspect of the experiment and takes data, and (9) the radiofrequency (RF) cavity.

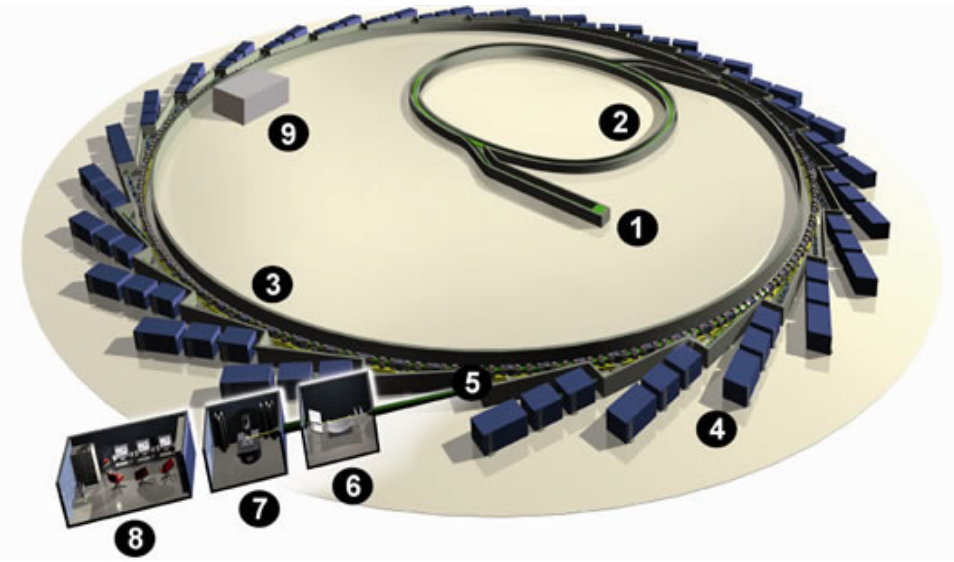


Figure 3-15 | A schematic diagram of the synchrony radiation station layout. The numbered parts are (1) the injection system, (2) the booster synchrotron, (3) the storage ring, (4) the beamlines, (5) the front end where light is extracted from the storage ring, (6) the optics hutch where certain wavelengths of light are selected and focused, (7) the experimental hutch housing the experimental equipment, (8) the control cabin where the scientific team monitors and controls every aspect of the experiment and takes data, and (9) the radiofrequency (RF) cavity. Image adapted from Diamond Light Source.(www.diamond.ac.uk)

### 3.5.3 Interactions of polarized photons with matters

In the last section, the electron-electron collision, or the electron scatterings have been discussed for the mechanism underlying EMs. Although photons can also be treated as 'particles' to certain extent, the interaction of them with electrons can be distinctly different from that between electrons themselves. Because photons are electrically neutral, they do not steadily lose energy via coulombic interactions with atomic electrons, as do charged particles. Interactions of photons with matters come along with energy lose (in the form of photoemission) and momentum transfer. Three types of physical process can occur when materials are traversed by a beam of photons, namely, photoelectric effect, Compton effect, and electron-positron pair production. Each of them dominates at a specific PE range and within the scope of this thesis (soft X-rays, PE < 1000 eV), photoelectric effect is the dominant process.

### 3.5.4 XMCD mechanism

#### *3.5.4.1* XAS

A X-ray absorption experiment is usually regarded as a two-step process.[153] In the first step, the core electrons of atoms are excited by the incident X-ray and the PE exceeds the binding energy of these electrons. After absorbing the incident photons, the core level electrons are promoted to a higher energy level in the form of photoelectron. This is accompanied by a sharp absorption of the photon at a certain PE, creating an absorption edge in the X-ray absorption spectrum (XAS). Several processes can come about by such photon absorption. Fluorescence occurs when the holes left behind by the excited core electrons are filled by electrons from a higher level. This process is in turn accompanied by the release of X-rays (usually known as characteristic X-rays) of the characteristic energy of the transition. Another process is the generation of Auger electrons, which happens when the fluorescent photon subsequently produced is reabsorbed by a third electron, which is then promoted to a higher energy state. It is noteworthy that during the latter process, secondary electrons (see the previous section) can also be created via inelastically scattering by the generated Auger electrons. Because the electric transmissions happening in the X-rays absorption process always

undergo a pattern that is characteristic to a specific element, such technique is able to give elemental resolved information of the electric and magnetic information of the material. For 3*d* transition metals which this thesis scopes for, the XAS is usually taken at the *L* edge, corresponding to the excitation of 2*p* core electrons into the unoccupied 3*d* states. Such transition call for soft X-rays with a PE range between 500 to 1000 eV.

#### *3.5.4.2* XMCD

XMCD refers to the absorption difference of circularly polarized X-rays near the resonant absorption edges of magnetic elements. Take the 3*d* transition metal as an example, such dichroism can be seen as a result of the spin-dependent transmission of electrons from 2*p* to the 3*d* orbitals, whose band asymmetry is closely linked with the magnetism of the metal. Considering a circularly polarized photon is used to excite a photoelectron in an X-rays absorption experiment. The photon transfers its angular momentum to the photoelectron in this process, resulting in a change in the angular momentum of the electron (known as magnet-optical interaction). If the electron lies in a spin-orbit split band such as the $L_2$ and the $L_3$ edge of 3*d* transition metals, some of the momentum will be transferred to the spin of the electron via spin-orbit coupling. Left (right) circularly polarized photons excite more spin-up (spin-down) electrons from the $2p_{3/2}$ level. The opposite is the case for the $2p_{1/2}$ level. In another word, the photoelectrons with defined angular momentums are excited to an empty 3*d* valance band and the fulfilled band in turn, works as a detector of their momentums. By theory, this unbalanced transmission of excited electrons can be described by the optical selection rule

$$\triangle m = \pm 1$$

Equation 3-6

which determines that 2*p* electrons of one spin direction will preferentially be promoted to 3d level according to whether right or left circular polarization is used (see for a schematic illustration). Due to the selection rule, the electric-dipole transitions from the ground state can reach only a limited subset of final states. The XAS therefore provides the fingerprint of a specific ground state and results in a local probe with a high sensitivity to crystal field, spin–orbit interaction, site symmetry, and spin configuration of the valence states.

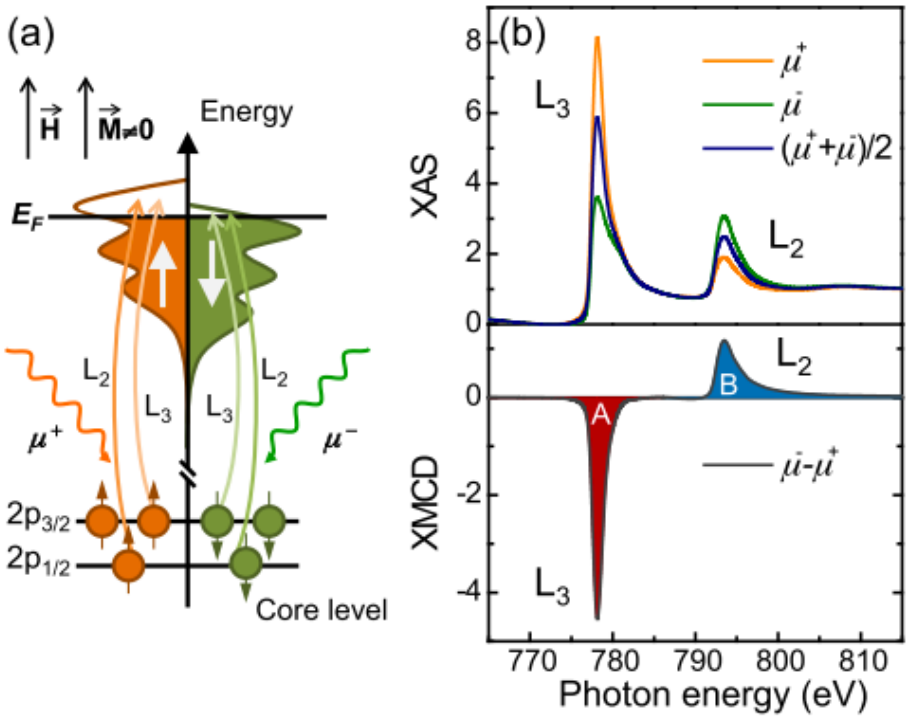


Figure 3-16 | Conceptual illustration of the two-steps process for a single-electron in the resonant excitation process for a magnetic material (left) and typical pair of dichroic XAS and XMCD spectra of Fe. Image was adopted from the literature.[154]

#### 3.5.4.3 TEY

As discussed above, strong secondary electron emission exists in the X-rays absorption process and that renders the total electron yield (TEY) as a preferred detection method. TEY is a commonly adopted detection mode for XMCD, which measures the number of photoelectrons created and escaping from the surface in the absorption process.[155] From a XAS, quantitative information of the DOSs of the valence band of the sample can be obtained via the application of a suitable solid state model which would usually be based around Fermi's golden rule

$$\mu(E) \propto \sum_{f}^{E_f > E_F} < f \mid \hat{\varepsilon} \cdot r \mid i >^2 \delta(E_f)$$

Equation 3-7

where the symbols $\hat{\varepsilon}\cdot r$ represents the coupling to the electronic field and $E_f$ represents the final state. Equation 3-7 presents an approximation of the transition probability of an electron from a deep core state (initial state) $|i>$ into an unoccupied state (final state) $<f|$. As illustrated in Figure 3-17, TEY sums over all energies of photoelectrons emitted, including those which have been directly emitted and those which have undergone many scattering events on their journey to the surface. In other words, it counts the total joint density of states of the initial core level with all final states simultaneously. Equation 3-8 presents a general expression of the drain current by TEY mode, in which $L$ is the electron escape depth and is approximately constant over the region of the spectrum.

$$I_{TEY}(\gamma) \propto \frac{\sigma(\gamma)L}{\sigma(\gamma)L + \cos(\theta)}$$

Equation 3-8

A distinct concept here is the X-rays absorption depth, $L'$, which can be much larger than $L$ due to the strong penetration ability of X-rays. When $L$ and $L'$ are comparable in length, the saturation effects curb the intensities of the largest absorption peaks compared to the rest of the spectrum. Here $\theta$ is the angle between the sample plane and the X-ray propagation direction. At grazing incidence angle the spectra are more prone to saturation. Conversely, the saturation is minimized at normal incidence and this configuration has been adopted thoroughly for the studies in this thesis. TEY detection shows a high surface sensitivity due to the short $L$ and that makes it rather sensitive to oxidation, which can be an issue for the observation of thin film samples. Such oxidation effects in the XAS usually show up as extra features (typically a few eV) above the main peak, which can affect the results of sum rule calculations (will be introduced later). Therefore, samples prone to oxidation necessitate a special treatment, such as *in situ* preparation (evaporation, cleaving, ion sputtering) or alternatively the sample should be capped with an inert material with appropriate thickness, such as Al, Au, and Cr etc.. The later treatment has been adopted for the studies of this thesis wherever applicable. Nevertheless, the positive side of the high surface sensitivity of TEY detection is its ability to measure very lower coverage of materials, e.g. sub-ML thin films and adatoms. The lowest limit so far is 0.005 ML coverage reported by Shelford *et al*..[156] The absorption process was historically carried out in transmission mode and was largely limited to the investigation of diffuse thin samples. Nowadays in

order to study the dense films in-situ with substrates, electrons are generally detected using the TEY method.

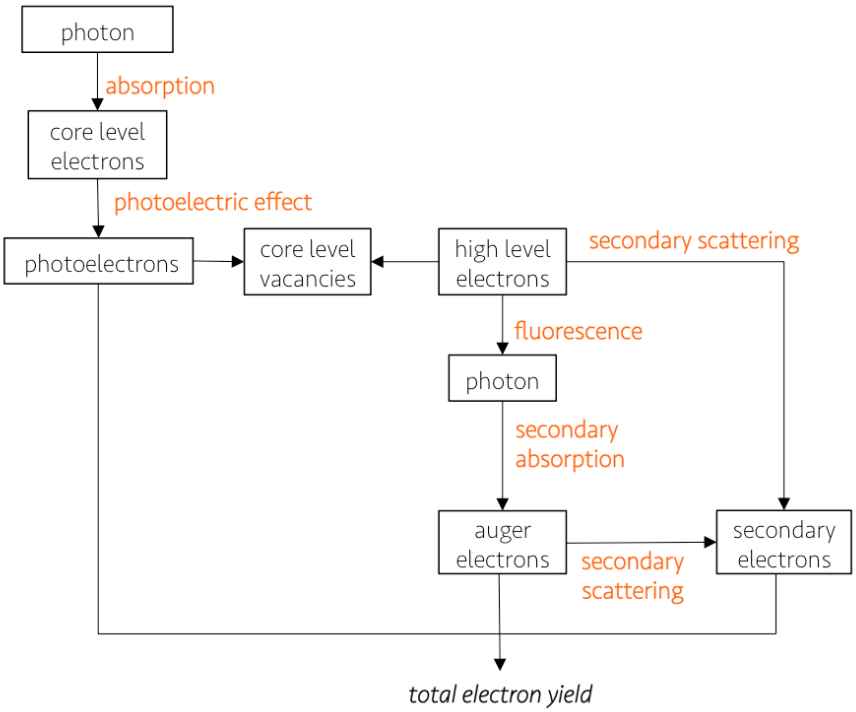


Figure 3-17 | The photoemission, florescence, auger process and other scattering process which may occur in atoms when aborting X-ray photons. XASs sum over all possible final states of the photoelectrons

#### *3.5.4.4 Site sensitivity*

Within the soft X-ray regime, the instrumental resolution is of similar width as the core hole life time broadening in the order of a few hundred meV, making it possible to resolve the detailed multiplet structure and charge-transfer satellites, or in other words, making XMCD possible to separate different sites of the magnetic ions. The most well-known example is the of complex cation occupancies is that in spinels, such as magnetite, where the different Fe sites are distinguished by their opposite magnetic alignments. The distribution of Fe cations within the magnetite structure can be determined by comparison of the XMCD to atomic multiplet calculations.[157] As can be seen from

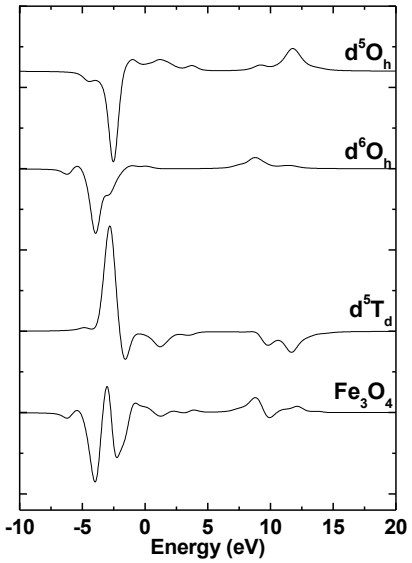


Figure 3-18 | The calculated Fe $d^5T_d$, $d^6O_h$, and $d^5O_h$ components of the XMCD spectrum and the resulting summed calculated spectrum of $Fe_3O_4$. Image adapted from the literature.[158]

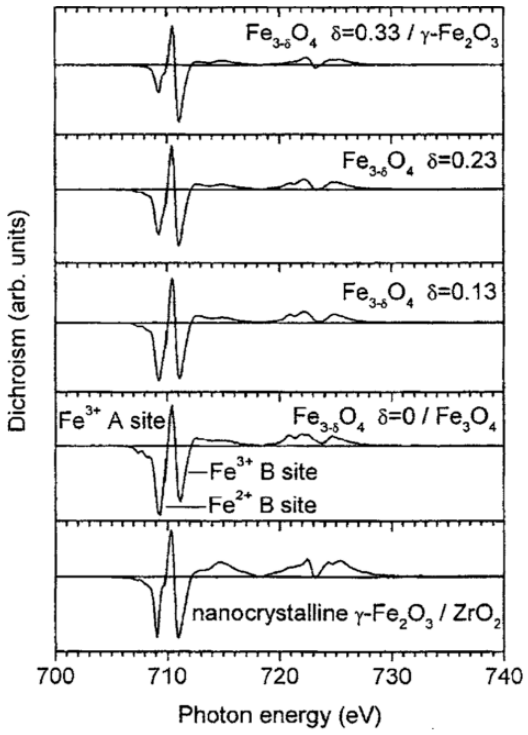


Figure 3-19 | Fe $L_{2,3}$ XMCD spectra of non-stoichiometric $Fe_{3-\delta}O_4$ thin films compared compared to γ -$Fe_2O_3$/$ZrO_2$.[159]

Figure 3-18 and Figure 3-19, each peak in the $L_3$ XMCD corresponds primarily to a different site in the $Fe_3O_4$, the first negative peak corresponds to $d^6O_h$ (i.e. B sites $Fe^{2+}$), the second positive peak to $d^5O_h$ (i.e. B sites $Fe^{3+}$), and the final negative peak to $d^5T_d$ (i.e. A sites $Fe^{3+}$). Furthermore the relative intensity of these contributions are quantities proportional to the number of different Fe cations and can be utilized to diagnose the sample stoichiometry (refer to Chapter IV for its utilization in our study of $Fe_3O_4$ thin films).

### 3.5.5 XMCD experimental set up

Figure 3-20 presents a schematic diagram of an experimental XMCD setup at a beamline, where circularly polarized X-rays are produced by an Apple-II type insertion device. To make an XMCD measurement, a magnetic field is applied to provoke disparity between the population of the spin-up and spin-down of the spin-orbit split band. In the systems wherever mentioned in this thesis, the magnetic field is directed along the direction of the X-ray beam. The chamber is fitted with one of two sample helium cryostats (inserts) and each cryostat can vary the sample temperature within a specific temperature range. This modern instrument provide ± 90° rotatable sample stage around the vertical axis, high magnetic field up to 14 T, and low temperature down to 2 K, optimized for XMCD studies of magnetic materials. Figure 3-21 displays a typical XMCD end station (adopted from the beamline I10, Diamond Light Source), which consists of a rotatable sample stage, a magnet, a cooling system, detectors (not shown) and other electrical units. Figure 3-22 presents a photograph of the sample stage used in the high magnet system of beamline I10, Diamond Light Source. Multiple samples can be loaded in to vacuum in one go and they are usually mounted in a regular array on the stage for easy optimization. Samples in the dense form (see 1, 2, and 3) can be mounted using silver paste and those in powder form can be pressed onto the conducting sticky paste (see 4).

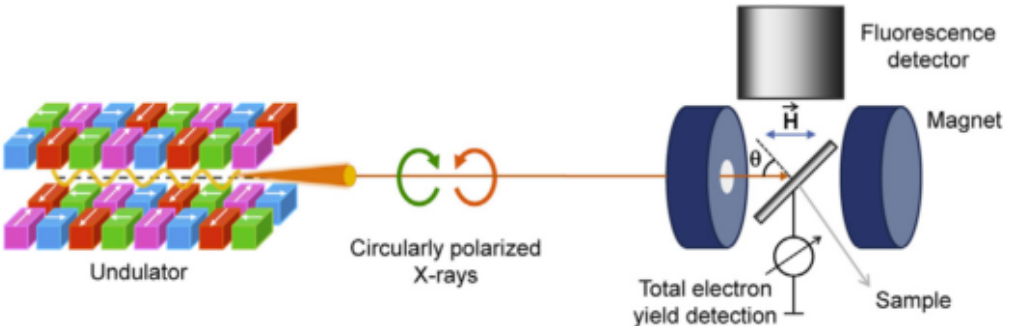


Figure 3-20 | Schematic diagram of an experimental XMCD setup at a beamline, where circularly polarized X-rays are produced by an Apple-II type insertion device. The beamline optics has been omitted in the diagram. The magnetic field is directed along the direction of the X-ray beam. Image adopted form the literature.[154]

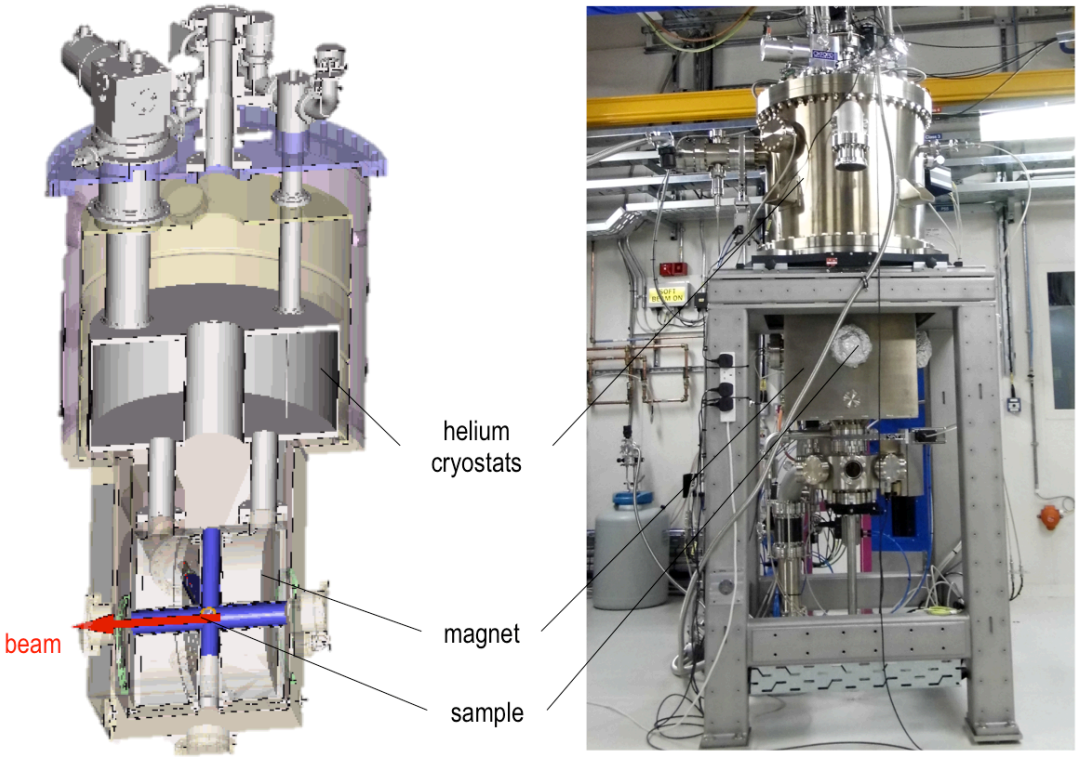


Figure 3-21 | The XMCD end station of beamline I10, Diamond Light Source, which consists of a ratable sample stage, a magnet, a cooling system, detectors (not shown) and other electrical units. The red arrow indicates the incident beam.

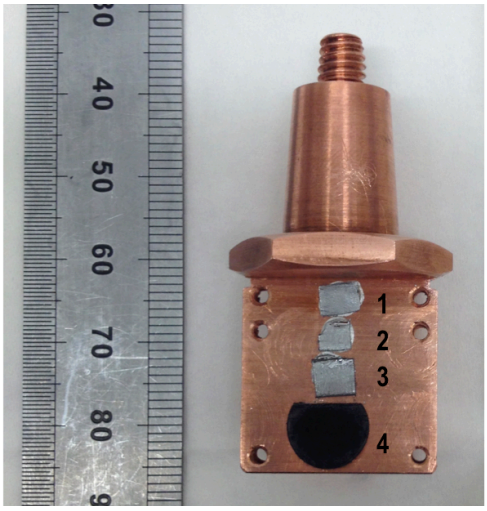


Figure 3-22 | A photograph of the sample stage used in the high magnet system of beamline I10, Diamond Light Source. Multiple samples can be loaded in to vacuum in one go and they are usually mounted in a regular array on the stage for easy optimization. For the case presented in this photograph, sample 1, 2, and 3 are dense films and are mounted by silver paste, while sample 4 is in powder form and is pressed onto the conducting sticky paste.

### 3.5.6 XMCD data analysis

Because the XAS obtained by means of the total electron yield (TEY) is proportional to the absorption cross section times the photon energy, these data can be used to work out the $m_l$ and $m_s$ of the element under interrogation based on sum rules. Equation 3-9 gives the general form of the spin and orbital sum rules,[160, 161] where $E$, $n_h$, $SC$, and $<T_z>$, respectively, represents the photon energy, the number of $d$ holes, the spin correction (SC) factor and the magnetic dipole term.

$$m_{orb} = -\frac{4}{3} n_h \frac{\int_{L_{2,3}} (\sigma^+ - \sigma^-)\, dE}{\int_{L_{2,3}} (\sigma^+ + \sigma^-)\, dE}$$

$$m_{spin} = -n_h \frac{6\int_{L_3} (\sigma^+ - \sigma^-)\, dE - 4\int_{L_{2,3}} (\sigma^+ - \sigma^-)\, dE}{\int_{L_{2,3}} (\sigma^+ + \sigma^-)\, dE} \times SC + <T_z>$$

Equation 3-9

Processing the spectra is made up of several distinct steps as discussed below, and each of them introduces different statistical and system errors to the results.

#### 3.5.6.1 Normalization

One of the drawbacks of using a TEY detection method is that a change in the applied magnetic field can affect the magnitude of the sample photocurrent due to the Lorenz force. Since it is impossible to gain full alignment of the spectra through the experimental hardware, the XAS spectra obtained in this study were all scaled and aligned with respect to one another at a given point preceding the primary peak, i.e. the $L_3$ edge for 3d transition metals. Without this intervention the dichroism will be slightly distorted and offset relative to zero.

#### 3.5.6.2 Background Removal

For the application of the sum rules, it is necessary to remove the contribution of photoelectron excitations into continuum states from the absorption cross section. This task is usually carried out by involving a step-like function to locate the threshold between the magnetic and non-magnetic parts. During development of this function, results were cross compared with earlier results calculated using more basic step functions, e.g. a square two-steps shape, and with standard spectra.[162] Generically, different step functions give deviations no more than 3%. The spectra processed in this study have all been fitted with the a sigmoidal function, as it is more able to cope with a slightly curved background and hence allows the use of more spectra than might ordinarily be possible based on the linear-shape step functions. Furthermore, sometimes another background need to subtracted by fitting a curve to the parts of the spectra unaffected by magnetism. This aids cross comparison of spectra and is advantageous to the integrals calculated subsequently.

#### 3.5.6.3 Integration

The integration range should principally be infinite. Practically, the integration range is set from just below the $L_3$ edge to 10 - 20 eV and above the $L_2$ edge where the integrals

approach their saturation values. Figure 3-23 presents a typical XAS and XMCD spectrum of Fe from this study, illustrating the practical application of the sum rules, based on which, $m_l$ and $m_s$ are determined by the integral of XMCD and XAS over $L_3$ and $L_2$ edges after removal of the non-magnetic background as discussed previously .

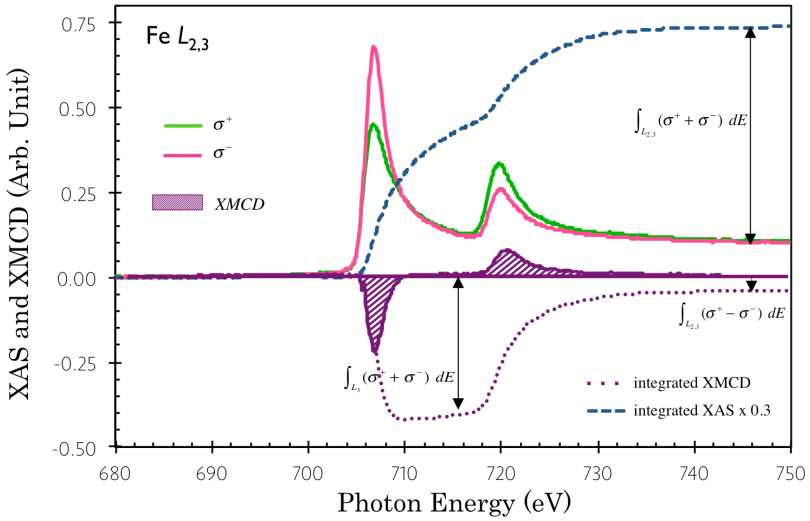


Figure 3-23 | A typical XAS and XMCD spectrum of Fe $L_{2,3}$ edge and their integration range for the sum rules application. Data are scaled for clearness.

#### 3.5.6.4 $n_h$ value

The hole number, $n_h$, refers to the empty states of the valance band and can be written defined as

$$n_h = \int_{E_F}^{\infty} \rho(E) dE$$

Equation 3-10

For an accurate assessment of the $n_h$, it is necessary to obtain an accurate measurement of the DOSs of the sample in question and such assessment can be subtle, since for the DOSs of certain elements in the form of ultrathin film and of impurities can differ from that of bulks. In the present project, $n_h$ were carefully quoted for the elements involved

and applied where appropriate, as summarized in Table 3-3. It is worthy to note that although the $n_h$ used in sum rules calculations may be inaccurate for certain material systems, utilizing the sum rules for them can yield more information than the rather muddled picture dictated by line shape alone.

| Material | $n_h$ | Ref. |
|---|---|---|
| Fe | 3.39 | 163 |
| Co | 2.49 | 164 |
| Ni | 1.59 | 165 |
| Cr | 7 | |
| $Fe_3O_4$ | 13.5 | 166, 167 |

Table 3-3 | A summary of the $n_h$ values used in this study and their references.

#### 3.5.6.5 SC factor

While a deconvolution of the $L_3$ and $L_2$ edges is not required for the orbital sum rule, they need to be separated for the spin sum rule. In case of the late *3d* transition metals the separation of $L_3$ and $L_2$ edges can be performed without difficulties because the spin-orbit splitting of the core states is large enough. However, the deconvolution becomes subsequently problematic going towards the early *3d* transition metals. In this study, The spectral overlap (also known as *j-j* mixing) was taken into account for Cr because of the relatively small spin-orbit coupling in the Cr 2*p* level. The value of SC, i.e. 2.0 ± 0.2 for Cr, was estimated by calculating the $L_{2,3}$ multiplet structures for a given ground state, applying the sum rule on the calculated XMCD spectrum, and comparing the result with the spin moment calculated directly for this ground state.[157]

#### 3.5.6.6 $\langle T_z \rangle$ term

The $\langle T_z \rangle$ term is a measure of the anisotropy of the spin density and it appears (even though the spin is isotropic) because the spin couples to the spatial space through the spin-orbit coupling. For the metallic systems, the influence of spin-orbit coupling on

$\langle T_z \rangle$ is very small due to the relatively weak spin-orbit coupling. $\langle T_z \rangle$ can be neglected for cubic symmetric systems and its contribution increases subsequently with lowering the symmetry or reducing the dimensionality of the material. In this study, the derived $m_s$ was not corrected for $\langle T_z \rangle$, however, its gives an error < 5%.

#### 3.5.6.7 Errors

The XMCD data analysis in this study was performed using the macros edited by J. S. Weaver, based on the method given by Chen *et al*.[168] and on a pre-existing program by C. M. Teodorescu and incorporated suggestions from T. K. Johal, Teodorescu's immediate successor at Daresbury. As discussed above, the derived the $m_s$ and $m_l$ strongly rely on the choice of the integration range and the simulation of the continuum and the non-magnetic background. To eliminate such statistical error, data of each complete measurement were performed for a minimum of 3 times to reduce the effect of any beam irregularities. The mean of the values calculated from these spectra can then be found and the standard deviation between values was quoted as the error. This error does not however take into account the margin of error within the sum rules themselves such as the limitations in possible allowed transitions covered by the theory, *j-j* mixing, and the assessment of $n_h$ etc.. The uncertainty of these features is generally expected to fall within a ~10% margin of error and since as of yet there is no mathematical way of accurately deriving the degree of error, it is thought safest to sum the standard deviation between spectra with the ~10% expected error.

Furthermore, it is worth noting that XMCD spectrum does not necessarily become zero above the $L_{2,3}$ edges, where its signal determined by spin-dependent scattering processes of the photo-electron, and could give large contribution to the $L_{2,3}$ XMCD signal of rare earth's elements.[169] However, for the transition metals the signal of such process is two orders of magnitude smaller than the XMCD response at the $L_{2,3}$ resonances and therefore can be neglected. Hence, after proper normalization, background removal and continuum simulation, the XASs can become independent of the experimental artifacts and are comparable on a per-atom basis. Generically, these assessments result in an overall ~10% error and that was how the error bars have been given in this thesis.

# 4 Chapter VI FM/SC Interface

## 4.1 Introduction

The atomic scale interfacial magnetization of FM/SC is closely linked with two general questions, namely (i) how magnetic ordering changes with the reduced dimensionality, (ii) how magnetic ordering changes while bonded to the substrate. By the band theory of solids, such effects can be seen as a symmetry broken at the boundary of a periodical structure.

The direct demonstration of the magnetic and electronic state of epitaxial FM/SC interface down to the ML scale remains a nontrivial task, even to this day, partially due to the inaccessibility of the buried layer between the topmost atoms and the substrate. With the exception of cross-sectional TEM, which provides structural information, researchers are still mostly in the dark about the electronic and magnetic properties of such interfaces. Therefore a large portion of studies over the last thirty years has focused instead on a special kind of interface - the surface, or the ultrathin FM films on SCs.

An unambiguous determination of the interface, which is already subtle in theories, can be more problematic in experiments. On the one hand, for samples comprising of several nms thick FM, it is always hard to separate the contributions of the interface and the bulk magnetization (though being a surface sensitive technique, the probing depth of XMCD can be up to several nanometers even in partial electron yield mode[170]). On the other hand, minute amount of FM (in the form of atoms and clusters) will be paramagnetic or ferromagnetic with extremely low $T_c$,[171, 172] and consequently no longer be representative of a realistic device. Moreover, while the FM atoms reduce to a minute amount, many conventional detection techniques become invalid, as conditions such the vacuum, sensitivity, cryogen etc. must be simultaneously satisfied at a high level.

To overcome these obstacles, in this chapter, we employed a specially designed $FM_1/FM_2/SC$ structure in combination with the powerful elemental selectivity of XMCD technique. Here, the ML $FM_2$ ($FM_2$ = Fe, Co, Ni) are epitaxially deposited on SC (SC = GaAs or graphene) and then capped off with a thick layer of $FM_1$ ($FM_2$ = Fe,

Co, Ni ≠ $FM_1$ in each sample), who serves as a stabilizing layer. Generically, the magnetic interaction can be described as the transfer of an effective magnetic field between the contacted magnetic materials and such effective field can be a regular magnetic field or a field produced by the quantum mechanical exchange interaction. In the $FM_1/FM_2$/SC structure, the thick $FM_1$ provides the ML $FM_2$ with a source of exchange interaction, simulating the interfacial behavior of a ferromagnetic $FM_2$ film or bulk on the SC. Combined with the elemental selectivity (or layer selectivity in this case) of XMCD, this method allows easy observation of the magnetization of $FM_2$ in atomic scale, which can be representative of the real interface of $FM_2$/SC. To start with, section 4.2 firstly demonstrates it in a prototypical FM/SC heterostructure, i.e. Ni/GaAs, as well as Co/GaAs for comparison purpose. Section 4.2 furthermore develops this method into an emerging topic by alternating the SC with graphene.

Using high-$T_c$ FM to induce or enhance the magnetic ordering of the adjacent paramagnetic materials or DMSs with low $T_c$ is a new topic in the research of FM/SC interface, which have enlightened the RT use of hybrid spintronics with the assistance of the magnetic proximity effect as a pathway.[243, 244, 84, 246, 247, 248] The utilization of the technique of XMCD to study the interfacial magnetism of such bilayer systems is therefore necessary again and will be presented in Section 4.3 in the $Co_2FeAl$/GaMn)As exchange coupled system as an example.

When it became possible to produce atomically clean crystalline surfaces of a metal and add atomically engineered additional layers of a different material, a very rich field of new magnetic phenomena can open up. For this reason, MBE growth has been employed as the major sample preparation method for the studies presented in this chapter. Moreover, wherever applicable, supporting characterization techniques (such as TEM and SQUID-VSM) and theoretical tools (like first-principals simulations) have been utilized to understand the XMCD observations.

## 4.2 Atomic scale magnetization of the FM/GaAs interface

### 4.2.1 Introduction

As a prototypical FM/SC heterostructure, Fe/GaAs has been most thoroughly studied due to two fundamental facts, namely, (i) the nearly perfect epitaxial growth of Fe on GaAs can be performed since the lattice constant of bcc Fe ($a_0$ = 2.866Å) is almost exactly half that of GaAs ($a_0$ = 5.654Å), i.e. the lattice mismatch as small as ~1.3%, and (ii) the high $T_c$ of Fe promises its availability for practical applications. Many researchers have reported on high quality epitaxial growth of Fe on GaAs, among which there exist the long lasting debate over the presence of magnetic dead layer at the Fe/GaAs interface.[173, 174, 57] This detrimental effect used to be attributed to the formation of antiferromagnetic $Fe_2As$[175] and half-magnetized $Fe_3Ga_{2x}As_x$[55] in the vicinity of the interface, until Xu *et al*.[57] obtained a bulk-like magnetic moment of Fe on GaAs(100) - 4 × 6 at RT in 1998. This result was further confirmed with unambiguous XMCD observation of the Fe/GaAs(100) down to ML scale.[176] Another negative opinion of Fe/GaAs towards spintronic application, i.e. the high conductivity mismatch between Fe and GaAs, was overcome with the assistant of an MgO tunneling barrier, as it was reported by X. Jiang *et al*.,[177] who demonstrated up to 32% spin injection at RT using electroluminescence detection in 2005. In the same year, electrical detection was reported by S. A. Crooker *et al*.,[178] who demonstrated Kerr imaging of the spin accumulation in the GaAs channel of a lateral spin-transport device using Fe contacts as the source and drain. By demonstrating spin-valve and Hanle effect, X. Lou *et al*.[179] reported epitaxial Fe Schottky-tunnel-barrier contacts on an n-doped GaAs channel via non-local geometry in 2007.

Co is another promising spin source with equally strong spin polarization near $E_F$ as that of Fe and even higher $T_c$ (1400°C, see Figure 3.1). Co/GaAs carries a mixture of fascinating characteristics including the structural transfer, the possibility of displaying perpendicular magnetic anisotropy, and the ability to form self-assembled patterns on GaAs substrates that may be magnetically harder and oxidize less readily than Fe. Though bulk-like Co has its stable and metastable phase as hcp and fcc, it can form into a bcc stacking by epitaxial growth on GaAs. The bcc Co/GaAs was firstly demonstrated by Prinz[180, 181, 182] in 1985 and since then many experiments on Co/GaAs were reported with inconsistency, making this issue rather complex. Difficulties exist in

unambiguously confirming the phase evolution of Co during the growth, due to the fact that the lattice constant of Co parameter is nearly half that of GaAs and experimental data from techniques such as RHEED may easily be interpreted incorrectly. Another interesting phenomenon of Co is the perpendicular magnetization. M. Hehn *et al.*[183] analyzed the domain structure of Co films over a large thickness range and found that as the thickness of the film is increased, the magnetization turns from fully in plane below 10 nm to fully out of plane at 50 nm. The result was in coherence with the prediction of C. Kittel[184] that for thin films with a strong perpendicular magnetocrystalline anisotropy $K$, their magnetization may switch again out of plane at certain thickness.

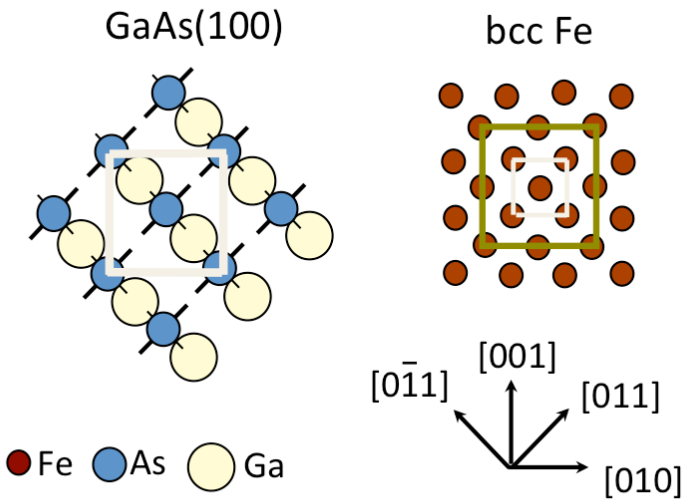


Figure 4-1 | Illustration of the epitaxial relation Fe on GaAs(100). The crystal symmetry and lattice constant of bcc Fe is almost half that of GaAs, suggesting that nearly perfect epitaxial growth of Fe on GaAs can be performed.

The tendency to form into bcc stacking, which doesn't exist in nature, has also been found in epitaxial Ni thin films on GaAs. This was firstly demonstrated by Tang *et al.*[185] as early as 1986 by growing Ni on GaAs(001) at RT and the presence of bcc phase was observed up to 2.5 nm. This study was late on reproduced by X. M. Jiang *et al.*,[186] who alternatively did the growth at 170 K and obtained a thicker bcc Ni, i.e. 3.5 nm. The bcc Ni/GaAs(100) as having a $T_c$ of 456 K and a magnetic moment of 0.52 $\mu_B$/atom, reveals a remarkably different electronic structure to that of fcc Ni and crucially a positive cubic anisotropy of $+4.0\times10^5$ ergs/cm$^3$, as opposed to $-5.7\times10^4$ ergs/cm$^3$ for the naturally occurring fcc Ni. All these intriguing phenomena of the FM/SC interfaces have strong consequences on their interfacial magnetism. In the remainder of this

section, the Co/GaAs(100) and Ni/GaAs(100) interfaces will be studied by XMCD in the specially designed $FM_1/FM_2/SC$ structure as introduced in the last section.

### 4.2.2 The sample preparation

The 10 ML Cr/7 ML Fe/1 ML Co/GaAs (100) and 10 ML Cr/7 ML Co/1 ML Ni/GaAs (100) samples used in this study were prepared using MBE in Thin Film Magnetism (TFM) group of the Cavendish Laboratory of Cambridge University. Prior to growth, the As-caped GaAs (100) substrate was annealed initially at 340 °C to desorb the As capping layer from the surface before further annealing at 550 °C for 1 hour to promote a clean and ordered Ga - rich (4 × 6) surface. Once the system had cooled to RT, the Fe was deposited onto the surface at a rate of approximately 1 ML per minute at a base pressure of $10^{-10}$ mbar. After the desired thicknesses were achieved, the samples were capped off with a different element for several MLs, i.e. 7 ML Co atop 1 ML Ni on GaAs for one sample and 7 ML Fe atop 1 ML Co on GaAs for the other. The two samples were all finally capped by 7 ML Cr to protect it from oxidation during transport to the synchrotron facility (refer to Figure 4-2 for the sample configuration).

### 4.2.3 The XMCD measurements

The XAS and XMCD at the Fe, Co, and Ni $L_{2,3}$ absorption edges were performed partially at the beamline I10 of Diamond Light Source and partially at the beamline 5U.1 of Daresbury Laboratory. Data obtained from the two stations were carefully compared and calibrated, so to make sure their comparability with respect to each other. XAS were perform in Faraday geometry, i.e. with the X-ray in normal incidence with respect to the sample plane and parallel to the applied magnetic field, as schematically shown in Figure 4-2. The XMCD was obtained by taking the difference of the XAS spectra, i.e. $\sigma^+ - \sigma^-$, by flipping the X-ray helicity at fixed magnetic field of 45 kOe, under which the sample is fully magnetized.

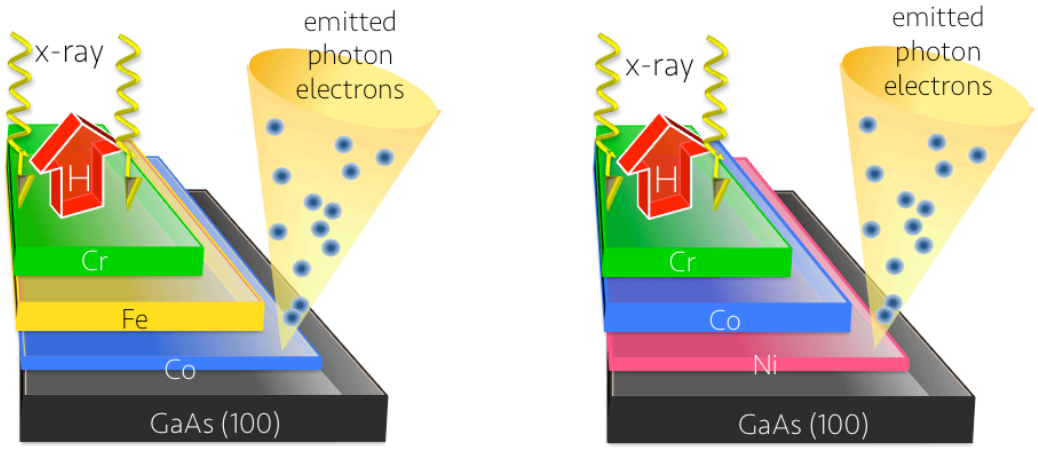


Figure 4-2 | Schematic diagrams of the experimental configuration of the XMCD measurement with both the incident X-rays and the magnetization directions perpendicular to the sample surface. The two samples consist of nominally 10 ML Cr/7 ML Fe/1 ML Co/GaAs (100) (left) and 10 ML Cr/7 ML Co/1 ML Ni/GaAs (100) (right), respectively.

Typical pairs of XAS and XMCD spectra of the two samples, normalized to the incident beam intensity, are presented in Figure 4-3 (Fe $L_{2,3}$ edge of the 7 ML Fe/1 ML Co/GaAs (100)), Figure 4-4 (Co $L_{2,3}$ edge of the 7 ML Fe/1 ML Co/GaAs (100)), Figure 4-5 (Co $L_{2,3}$ edge of the 7 ML Co/1 ML Ni/GaAs (100)), and Figure 4-6 (Ni $L_{2,3}$ edge of the7 ML Co/1 ML Ni/GaAs (100)), respectively. The XAS of Fe, Co, and Ni of the two samples show a white line at each spin-orbit split core level without prominent splitting for both left- and right-circularly polarized X-rays, suggesting that the sample has been well protected from oxidation. Strong dichroic XAS were obtained for the 1 ML Co at the Co/GaAs (100) interface, whilst the same coverage Ni at the Ni/GaAs (100) interface shows no appreciable XMCD within the experimental accuracy, or in other words, points to a magnetic dead layer. To confirm that, the elemental specific XMCD of the 1 ML Ni and the topmost 7 ML Co of the 7 ML Co/1 ML Ni/GaAs (100) epitaxial thin film were performed as a function of the magnetic field (perpendicular) with the temperature down to 5 K . The magnetization of the Co (left) and Ni (right), respectively, were estimated by the on-peak and off-peak ratio at the Co and Ni $L_3$ edge and depicted against the field as shown the Figure 4-7. In consistent with the last experiment, Ni shows no appreciable magnetic signatures while Co exhibit a clear ferromagnetic hysteresis loops along its hard axis, as expect.

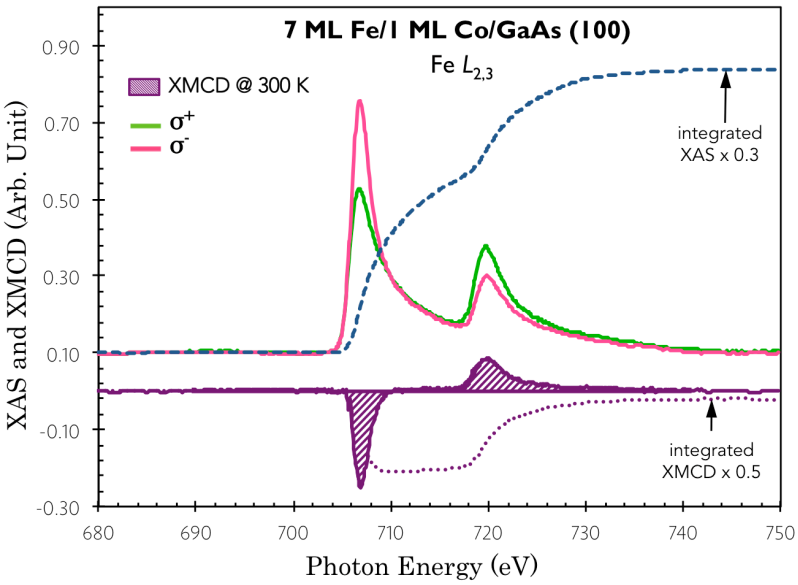


Figure 4-3 | Typical pair of XAS and XMCD spectra, normalized to the incident beam intensity, at the Fe $L_{2,3}$ edge of the 10 ML Cr/7 ML Fe/1 ML Co/GaAs (100), obtained at 300 K, normal incidence. The dashed lines indicate the integration of the spectra. Data are offset and scaled for clearness.

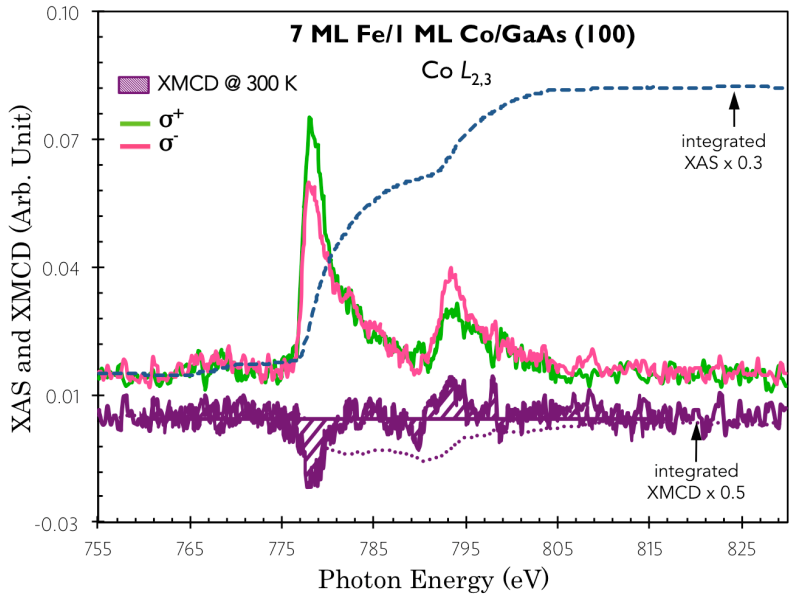


Figure 4-4 | Typical pair of XAS and XMCD spectra, normalized to the incident beam intensity, at the Co $L_{2,3}$ edge of the 10 ML Cr/7 ML Fe/1 ML Co/GaAs (100), obtained at 300 K, normal incidence. The dashed lines indicate the integration of the spectra. Data are offset and scaled for clearness.

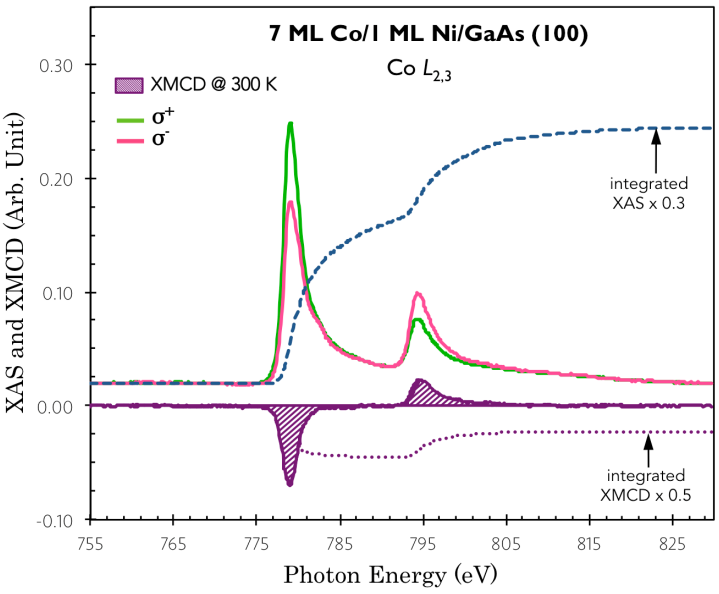


Figure 4-5 | Typical pair of XAS and XMCD spectra, normalized to the incident beam intensity, at the Co $L_{2,3}$ edge of the 10 ML Cr/7 ML Co/1 ML Ni/GaAs (100), obtained at 300 K, normal incidence. The dashed lines indicate the integration of the spectra. Data are offset and scaled for clearness.

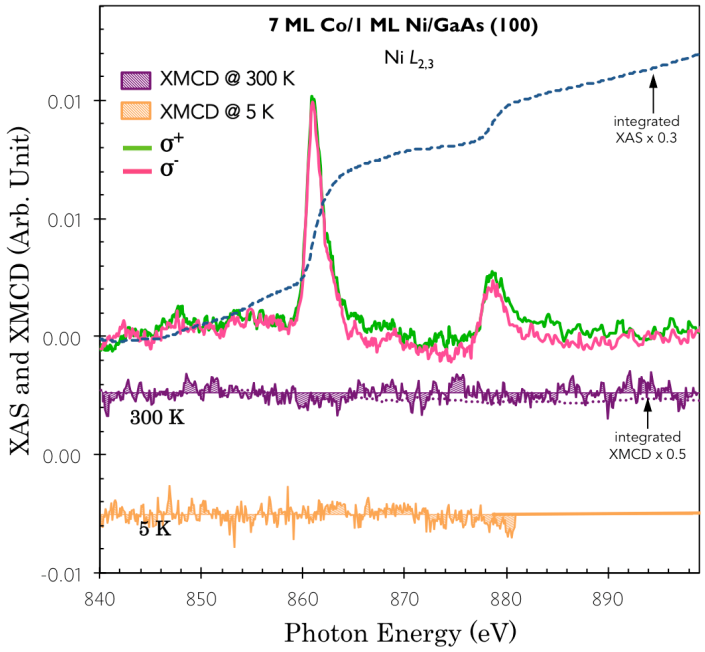


Figure 4-6 | Typical pair of XAS and XMCD spectra, normalized to the incident beam intensity, at the Ni $L_{2,3}$ edge of the 10 ML Cr/7 ML Fe/1 ML Co/GaAs (100), obtained at 300 K and 5 K, respectively, normal incidence. The dashed lines indicate the integration of the spectra. Data are offset and scaled for clearness.

The $m_{spin}$ and $m_{orb}$ of the 7 ML Fe/1 ML Co/GaAs (100) and 7 ML Co/1 ML Ni/GaAs (100) epitaxial thin films were calculated, respectively, by applying sum rules on the integrated XMCD and total XAS spectra of Fe, Co, and Ni $L_{2,3}$ utilizing the method described in chapter III. In order to rule out non-magnetic parts of the XAS spectra an arctangent based step function was used to fit the threshold. As can be seen from Figure 4-3 to Figure 4-6, the integration (dashed lines) of both XMCD and total XAS spectra becomes flat within the selected range, proving a proper background offset. The effective number of *3d*-band holes, $n_h$, was assumed as 3.39 for Fe, 2.49 for Co and 1.49 for Ni. The calculated $m_{spin}$ and $m_{orb}$ were finally corrected because of the partially polarized X-ray source utilized in Daresbury, i.e. 80%, but not for those obtained in Diamond Light Source, which uses two APPLE II undulators and generates the 100% polarization for the X-rays. The sum-rules derived $m_{orb}$, $m_{spin}$, $m_{total}$, and $m_{spin}/m_{orb}$ and the numeric results from the literatures are gathered in Table 4-1. The 1 ML Co at the Co/GaAs (100) interface shows sizable magnetization, i.e., $m_{orb}$ = (0.14±0.05) $\mu_B$/f.u. and $m_{spin}$ = (0.71±0.10) $\mu_B$/f.u. while in contrast, the 1 ML Ni at the Ni/GaAs (100) interface shows nearly vanished magnetic moments, i.e. $m_{orb}$ = (0.05±0.05) $\mu_B$/f.u. and $m_{spin}$ = (0.07±0.10) $\mu_B$/f.u., which are almost undistinguishable from the spectra.

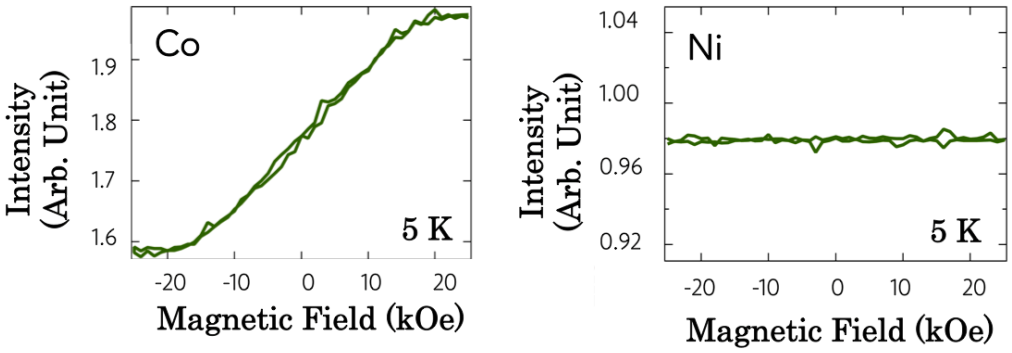


Figure 4-7 | The elemental specific XMCD hysteresis loops of the 1 ML Ni and the topmost 7 ML Co of the 7 ML Co/1 ML Ni/GaAs (100) epitaxial thin film.

| Fe | $m_{orb}$ ($\mu_B$/atom) | $m_{spin}$ ($\mu_B$/atom) | $m_{total}$ ($\mu_B$/atom) | $m_{orb}/m_{spin}$ | Ref. |
|---|---|---|---|---|---|
| 7 ML Fe/1 ML Co/GaAs(100) | 0.14±0.05 | 1.54±0.10 | 1.68±0.15 | 0.09±0.01 | ✣ |
| 8 nm Fe/parylene | 0.086 | 1.98 | 2.006 | 0.043 | 187 |
| 8 nm Fe/GaAs (100) | 0.26±0.03 | 2.03±0.14 | 2.29±0.17 | 0.13 | 188 |
| **Co** | $m_{orb}$ ($\mu_B$/atom) | $m_{spin}$ ($\mu_B$/atom) | $m_{total}$ ($\mu_B$/atom) | $m_{orb}/m_{spin}$ | Ref. |
| 7 ML Fe/1 ML Co/GaAs(100) | 0.21±0.05 | 0.71±0.10 | 0.93±0.15 | 0.30±0.03 | ✣ |
| 7 ML Co/1 ML Ni/GaAs(100) | 0.24±0.05 | 1.32±0.10 | 1.56±0.15 | 0.18±0.02 | † |
| 8 nm Co/parylene | 0.153 | 1.55 | 1.703 | 0.009 | 187 |
| **Ni** | $m_{orb}$ ($\mu_B$/atom) | $m_{spin}$ ($\mu_B$/atom) | $m_{total}$ ($\mu_B$/atom) | $m_{orb}/m_{spin}$ | Ref. |
| 7 ML Co/1 ML Ni/GaAs(100) | 0.05±0.05 | 0.07±0.10 | 0.12±0.15 | 0.80±0.10 | † |
| Ni single crystal | 0.06±0.03 | 0.54±0.05 | 0.60±0.08 | 0.45±0.01 | 189 |

Table 4-1 | List of the sum-rules derived $m_{orb}$, $m_{spin}$, $m_{total}$, and $m_{orb}/m_{spin}$ based on this study and those reported in the literatures. Note our definitions of the $m_{spin}$ differ by a factor of 2 and hence the number quoted here is twice that initially presented by Vogel et al..[189] The symbol ✣ and † here refer to our samples, i.e. 7 ML Fe/1 ML Co/GaAs (100) and 7 ML Co/1 ML Ni/GaAs (100), respectively.

### 4.2.4 Discussions

The powerful elemental selectivity (or layer selectivity in the case of the present study) has enabled unambiguous determination of the magnetic ground state of each layer of the specially designed $FM_1/FM_2/SC$ structure ($FM_1$ = Fe, Co, and $FM_2$ = Co, Ni ≠ $FM_1$). If one first turns the attention to the interfacial $FM_2$ elements in conjunction with the SC, significant contrast can be seen for the Co/GaAs (100) and Ni/GaAs (100) with the identical coverage. The sum-rules derived $m_{spin}$ of the 1 ML Co reduces by ~ 50% compared with that obtained by Chen *et al*.,[187] using *in situ* growth method of a ~ 5 ML Co on parylene (the thickness here is an estimation based on the original paper which acknowledges it as 50 – 70 Å).

#### 4.2.4.1 The suppressed magnetization of Co on GaAs(100)

Three factors may be predominately responsible for the suppressed $m_{spin}$ observed at the 1 ML Co/GaAs interface. One is the reduced thickness. It is well known that FM materials follow the so-called island growth geometry at low coverage. In other words, Co atoms at these thicknesses, typically less than a few MLs, may be too diffused for them to intensively interact with one another, even with the assistant of the topmost stabilizing layer. Another reason rises from the stacking of Co when epitaxially deposited on GaAs. It has been found that, in general, the bcc phase develops at the initial growth while hcp Co starts building up at higher coverage on GaAs, although debates last to today over the lattice structure and magnetic properties of Co thin films on GaAs. Mangan *et al*.[181] demonstrated the coexistence of bcc and hcp phases in Co on GaAs(001) with the help of TEM observations, in consistent with the observation by Gu *et al*.,[190] and Idzerda *et al*. confirmed the bcc structure of Co on GaAs(110) using EXAFS.[191] However, the theory suggests that the bcc Co is not a metastable phase but a forced structure originating from imperfections.[192] The third possibility is associated with the detrimental interdiffusion between the FM and the SC atoms. Theoretical calculations suggest a bulk bcc Co can carry a $m_{spin}$ as large as 1.7 $\mu_B$/atom,[193, 194] while experimental reports are always below this value. By careful analyses of the RHEED patterns, Monchesky *et al*.[195] demonstrated a ferromagnetically dead layer associated with the formation of interfacial $Co_2GaAs$ for Co thickness less than 3.4 ML and an abrupt in-plane spin-reorientation transition reorients the magnetization along the [001] direction at 7 ML. It should be noted that all these boundaries discussed above are not absolute values but strongly depend on the specific sample deposition conditions, such as the substrate configuration and the temperature etc.. For example, passivating layers such as S and Sb have been used to reduce the chemical interaction at the Co/GaAs interface and the latter gives a factor of 2.3 enhancement of the magnetic moment compared to the film deposited on bare GaAs(110) substrate.[196, 185]

#### 4.2.4.2 The magnetic dead layer of Ni on GaAs(100)

The three factors discussed above, namely (i) the growth geometry, (ii) the stacking of the FM atoms, and (iii) the detrimental interdiffusion, universally exist in all kinds of FM/SC interfaces in the ML regime and the significances of their influence are decided by the specific FM/SC systems. Compared with the Co/GaAs and the Fe/GaAs[188]

interfaces, our observation suggests that these factors have apparently stronger impacts on that of Ni/GaAs (100), leading to the creation of a magnetic dead layer for the 1 ML Ni, i.e. $m_{orb}$ = (0.05±0.05) $\mu_B$/atom and $m_{spin}$ = (0.07±0.10) $\mu_B$/atom, despite the assistance of the topmost stabilizing layer and the optimized growth condition within the given opportunity. Among the pioneering investigations, Tian *et al*.[197] performed a series of MOKE measurements for Ni films and suggested the absence of a magnetic dead layer in the Ni/GaAs interface with the Ni thicknesses above ~1 ML. The magnetic anisotropy in the system studied has been attributed to both cubic and uniaxial anisotropies and the uniaxial term may be a result of the in-plane shear strain induced in the system. Scheck *et al*.[198] used the electrodeposition technique with the intention to overcome the intermixing at the interface and the Ni film in this case forms fcc, instead of bcc stacking. Characterized by XPS, the presence of the As peak in the 6 nm Ni film reveals the occurrence of As diffusion into the Ni layer destroying the magnetic properties of the fcc Ni film and leading to a 20% reduction of the magnetization compared to the bulk value. In the study of the evolution of interface properties of the electrodeposited Ni film upon annealing, significant increase of As out-diffusion has been observed for annealing temperatures up to 623 K accompanying a rise in Schottky barrier height which has been attributed to the Ni-Ga-As compound formation.[199]

#### *4.2.4.3 The magnetism of the stabilizing FM layer*

Apart from the suppressed magnetization of the interfacial ML $FM_2$ atoms directly in conjunction with the SC, modification occurs in the topmost $FM_1$ stabilizing layer, too. The observed magnetic moment for the 7 ML Fe atop Co, i.e. $m_{orb}$ = (0.14±0.05) $\mu_B$/atom and $m_{spin}$ = (1.54±0.10) $\mu_B$/atom are lower than the same sum-rules derived results by Xu *et al*.,[188] i.e. $m_{orb}$ = (0.26±0.03) $\mu_B$/atom and $m_{spin}$ = (2.03±0.14) $\mu_B$/atom for the Fe on GaAs(100) directly. The same trend happens for the 7 ML Co atop Ni, i.e. $m_{orb}$ = (0.24±0.05) $\mu_B$/atom and $m_{spin}$ = (1.32±0.10) $\mu_B$/atom, which are lower than the same sum-rules derived results by Chen *et al*., i.e. $m_{orb}$ = 0.153 $\mu_B$/atom and $m_{spin}$ = 1.550 $\mu_B$/atom. Based on the fact that the underneath $FM_2$ materials can follow the island growth geometry at low coverage, it is likely that some of the $FM_1$ atoms atop may also be in contact with the SC substrate and hence the stacking transformation and the detrimental interdiffusion could apply to these $FM_2$ atoms. Possible charge and spin transfers between the $FM_1$ and $FM_2$ atoms are additional factors worthy of

considerations. Unfortunately, it is not possible to confirm directly in the present experiment. However, one can always validate such ideas by comparing the numeric results with theoretical simulations. Due to the complex of the surface configuration (refer to Chapter III, the realization of surface reconstruction of GaAs), this task is uneasy in 3D GaAs, however, can be clear-cut in simple 2D systems. Later in the next section, we will see a comparison between the sum-rules derived magnetic moments and those obtained by first-principals calculations in a specific $FM_1/FM_2/SC$ system where SC = graphene.

## 4.3 The interfacial magnetism of FM/Graphene

### 4.3.1 Introduction

The revolutionary nature of graphene[200, 201, 202] makes it a prime candidate for spintronics applications, in which the generation and tuning of spin-polarized currents are prerequisites.[203] In its pristine state, graphene exhibits no signs of conventional spin-polarization and so far no experimental signature shows a ferromagnetic phase of graphene. This gap is now filling up by combined efforts in multi-disciplinary research. The ferromagnetic metal (FM)/graphene heterojunction is one of the most promising avenues to realise efficient spin injection into graphene and other C-based organic systems.[204] Perfect spin filtering for interfaces of graphite and Ni or Co has been predicted, which is insensitive to interface roughness due to the intrinsically ordered nature of graphite.[205] Fascinating properties of spin transport phenomena were presented in the Co/graphene system,[206, 207] though theoretical calculations show that the atomic magnetic moment of Co can be reduced by more than 50% when absorbed on a graphene surface.[208] The spin valve effect was also successfully demonstrated in NiFe/graphene/NiFe vertical structures and the signal is enhanced when the number of graphene layers is doubled.[209] An inserted graphene sheet can drastically improve the spin-injection efficiency from a ferromagnet into silicon.[210]

In graphene-based hybrid systems, the best opportunity for spin transport could only be achieved when no magnetic dead layer exists at the FM/graphene interface. Calculations for transition-metal/nanotube hybrid structures exhibit substantial magnetism.[211] For Fe-, Co-, and Ni-doped carbon nanotubes, outside adsorption sites have found to be the most favourable; and the interactions are ferromagnetic for Fe and Co while nonmagnetic for Ni.[212] Whether a deposited FM on graphene is magnetically ordered at the FM/graphene interface is a must-addressed issue before any functional graphene-based spintronic devices can be developed. In the reminder of this section, we present a XMCD study of the ML epitaxial Fe/graphene interface, combined with first-principals calculations. The experiments have been performed using a specially designed $FM_1/FM_2/SC$ structure that was introduced in the beginning of the chapter.

### 4.3.2 The sample preparation

The single layer graphene used in this study was prepared by chemical vapor deposition (CVD) on Cu foil and then transferred on top of 300 nm $SiO_2$/Si substrate.[213, 214, 215] After 1 hour of annealing at 200°C, 1 ML Fe was grown on the graphene at RT by molecular beam epitaxy (MBE) using an e-beam evaporator, whose rate was monitored by a quartz microbalance and calibrated by ex-situ atomic force microscope (AFM).[216] 30 ML Ni was then deposited immediately onto the Fe layer. The sample was finally capped by 15 ML Cr to protect it from oxidation during transport to the synchrotron facility. Figure 4-8 presents a typical micrograph of the graphene on $SiO_2$/Si, which indicates the sample contains less than 10% defects and bilayer graphene (upper row), and a photograph of the sample after FM deposition, in which the boundary of the shuttered area can be seen (lower row).

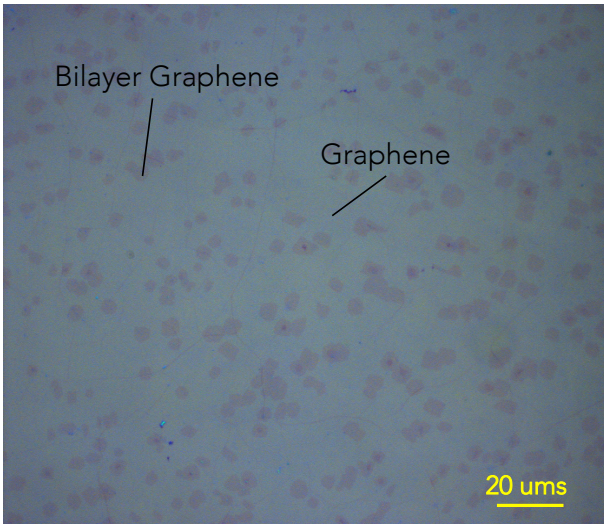


Figure 4-8 | Typical micrograph of the graphene on $SiO_2$/Si, which indicates the sample contains less than 10% defects and bilayer graphene.

### 4.3.3 The Raman scattering characterization

The Raman scattering measurement was performed in the Physics Department of Renmin University, Beijing, China. Measurements were performed using a 633 nm He-Ne laser in backscattering micro-configuration. The laser beam was focused into a spot

on the sample surface with a diameter of ~5 μm and the beam power was kept below 1 mW to avoid heating effects. Figure 4-9 presents the averaged Raman spectra collected on the FM/graphene and an as-grown area without FM deposition (see Figure 4-9 inset), which was obtained by shuttering half of the sample during the FM deposition. The characteristic *D*- and *G*-band of the graphene suggest that the sample had been well transferred.

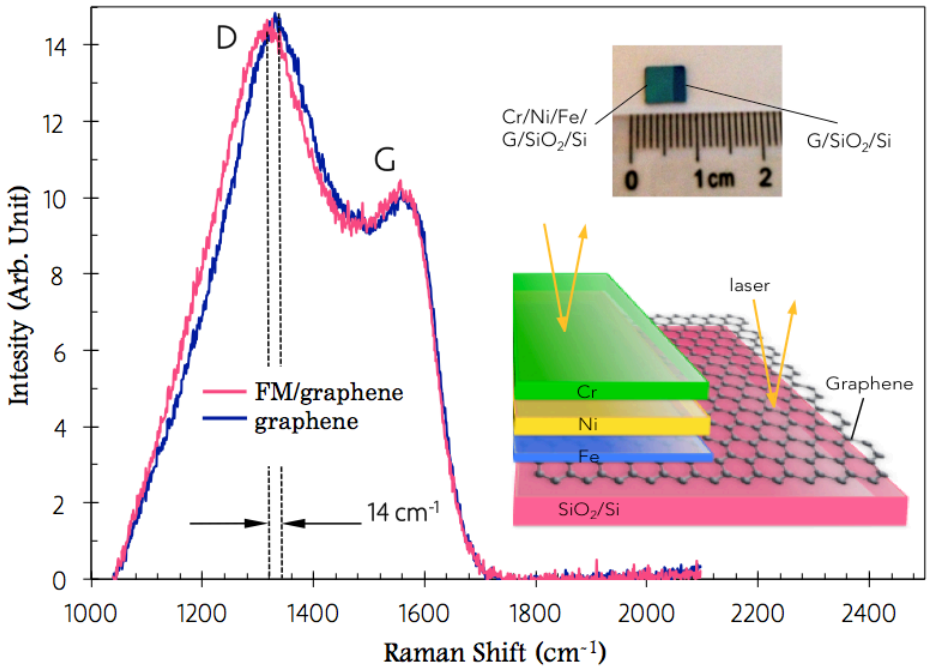


Figure 4-9 | Typical Raman spectra collected on the FM/graphene and an as-grown area without FM deposition. Inset: (upper row) photograph of the Fe/graphene sample, in which the two distinct areas were obtained by shuttering half of the sample during the FM deposition, and (lower row) schematic diagram of the Raman scattering measurement performed on the two parts of this sample.

Similar line shape and peak width of the *D*- and *G*-bands were observed in the spectra of both graphene and FM/graphene. The *G*-band peak position, which is a sensitive indicator of the structural damage of graphene, shows no shift in the presence of the FM thin film, suggesting that the FM deposition has induced negligible defects into the graphene, if any. Meanwhile, the topmost FM induces a substantial shift of ~14 $cm^{-1}$ at the peak position of the *D*-band, suggesting a considerable Fe-C interaction. As

the intensity and shape of the *D*-band show little difference between those collected on graphene and FM/graphene, the observed Raman shift is more likely due to the energy exchange between Fe and vibrating C atoms rather than an impurity effect. This effect can be explained by first-principals simulations (will be presented latter in this section), which suggests that the electronic band dispersion of graphene can be modified via the hybridization with Fe and hence shifts the *D*-band position by tuning the finite-$\boldsymbol{q}$ transferred hopping process.

### 4.3.4 The XMCD measurement

The XAS and XMCD of the Fe and Ni $L_{2,3}$ absorption edges were performed on beamline I10 at the Diamond Light Source. Circularly polarized X-rays with 100% degree of polarization were used in normal incidence with respect to the sample plane and parallel with the applied magnetic field, in order to minimize the nonmagnetic asymmetries (see Figure 4-10). The XAS spectra were obtained using both total electron yield (TEY) and total florescence yield (TFY) detection. The XMCD was taken as the difference of the XAS spectra, i.e., $\sigma^{-}$-$\sigma^{+}$, obtained by flipping the X-ray helicity at a fixed magnetic field of 3 T, under which the sample is fully magnetized with little paramagnetic contribution. Typical XAS and XMCD spectra at 5-300 K of the interface Fe and the stabilizing Ni are presented in Figure 1a and 1b, respectively. The XAS spectra of Fe and Ni for both left- and right-circularly polarized X-rays show a white line at each spin-orbit split core level without prominent splitting, suggesting that the sample has been well protected from oxidation. The XMCD to XAS peak height ratio, i.e. the XMCD asymmetry, a quantity proportional to the magnetic moment, is extracted to be as large as ~21% for the Fe and ~14% for the Ni at saturation, implying the formation of ferromagnetic order in both materials.

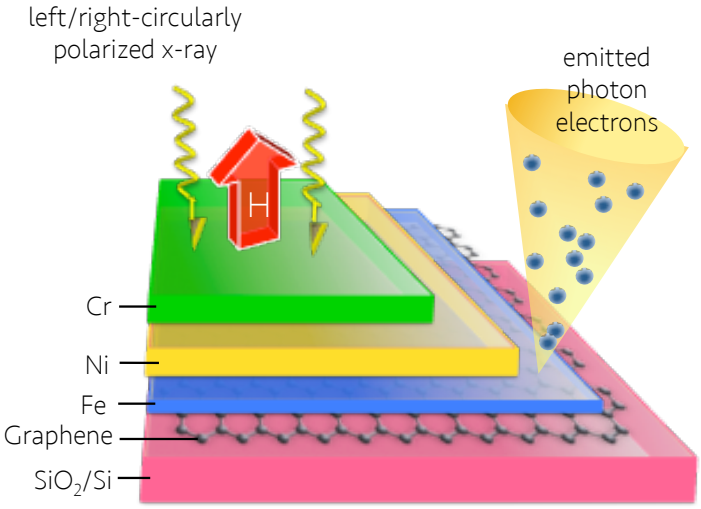


Figure 4-10 | Schematic diagram of the XMCD experimental configuration, in which X-rays are at normal incidence with respect to the sample plane and parallel to the applied magnetic field.

The $m_{spin}$ and $m_{orb}$ were calculated by applying the sum rules to the integrated XMCD and summed XAS spectra of the Fe and Ni $L_{2,3}$ edges using the method described in Chapter III. The effective number of 3*d*-band holes, $n_h$, was assumed as 3.7 accounting for the charge transfer from Fe to the atop stabilizing Ni layer ($n_h$ = 3.4 in bulk).[217] In order to exclude non-magnetic parts of the XAS spectra, a arctangent-based step function is used to fit the threshold. As can be seen from Figure 4-11, the integration (dashed lines) of both XMCD and summed XAS spectra becomes flat within the selected range, proving a proper background offset.

The calculated $m_{spin}$, $m_{orb}$, and total magnetic moment ($m_{total}$) of the interface Fe and the stabilizing layer Ni at 5 - 300 K are plotted in Figure 4-12. The $m_{total}$ of Fe displays a decreasing trend with increasing temperature from 1.23 $\mu_B$/atom at 5 K to 1.12 $\mu_B$/atom at 300 K, i.e., ~9%, pointing to a $T_C$ close to bulk-like Fe. At the lowest temperature (5 K), we obtained $m_{spin}$ = (1.06 ± 0.1) $\mu_B$/atom, which is ~50% reduced from the bulk-like Fe (whose $m_{spin}$ = 2.2 $\mu_B$/atom) and $m_{orb}$ = (0.18 ± 0.02) $\mu_B$/atom, corresponding to an enhancement of ~200% compared to $m_{orb}$ = 0.085 $\mu_B$/atom of that in the bulk.[218] Meanwhile, the deduced magnetic moments, i.e. $m_{orb}$ = (0.05 ± 0.02) $\mu_B$/atom and $m_{spin}$ = (0.59 ± 0.1) $\mu_B$/atom, reproduce well of the reported values of bulk-like Ni.[219] The $m_{total}$ of Ni exhibits a trend of slight decrease with increasing temperature

from (0.63 ± 0.06) $\mu_B$/atom at 5 K to (0.52 ± 0.06) $\mu_B$/atom at 300 K, pointing to the $T_C$ close to the bulk material. Unlike the interface Fe, whose $m_{orb}$ shows a ~200% enhancement compared to bulk-like Fe, the Ni stabilizing layer gives a nearly quenched $m_{orb}$. This is as expected for bulk-like Ni, where the effect of the crystal field plays a dominant role.

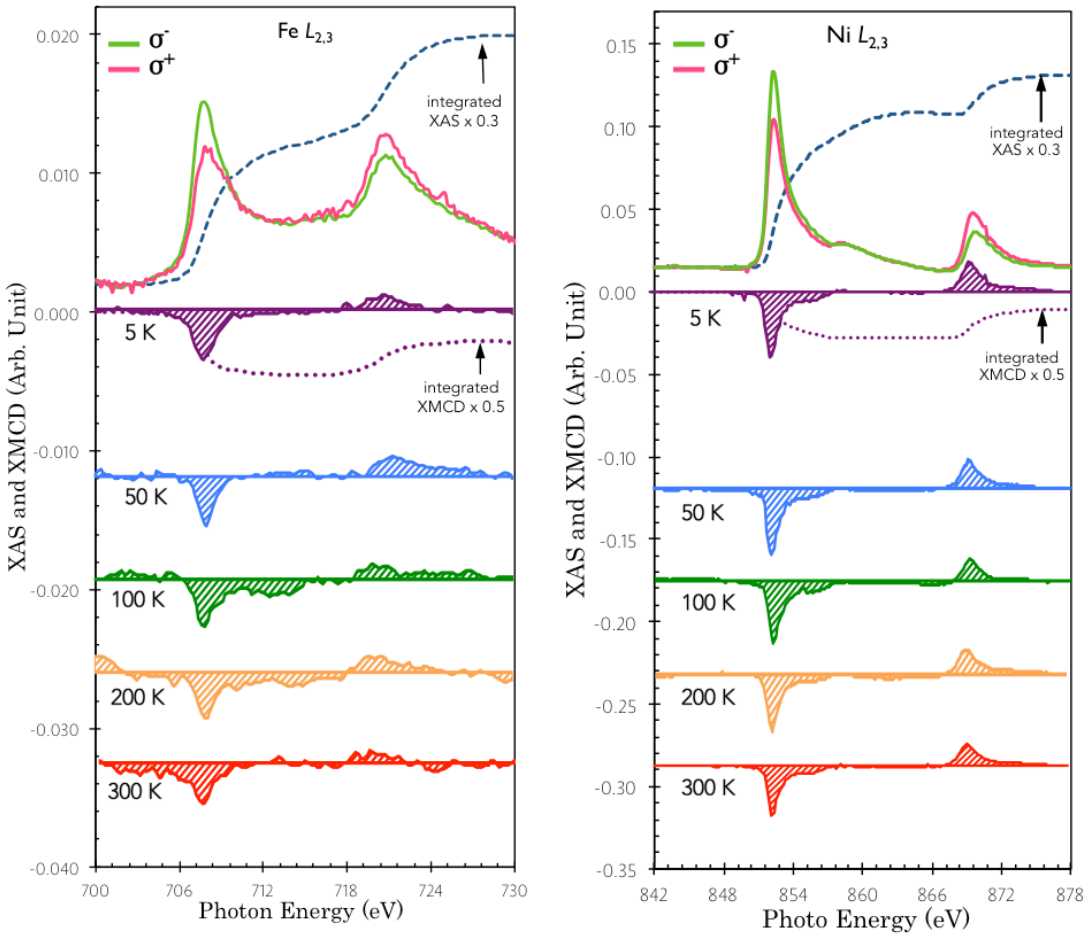


Figure 4-11 | Typical pair of XAS and XMCD spectra between 5-300 K of the interface Fe (left), and the stabilizing Ni (right), respectively, with a peak at each spin-orbit split core level. The dashed lines show the integration of the spectra. Data are offset and scaled for clearness.

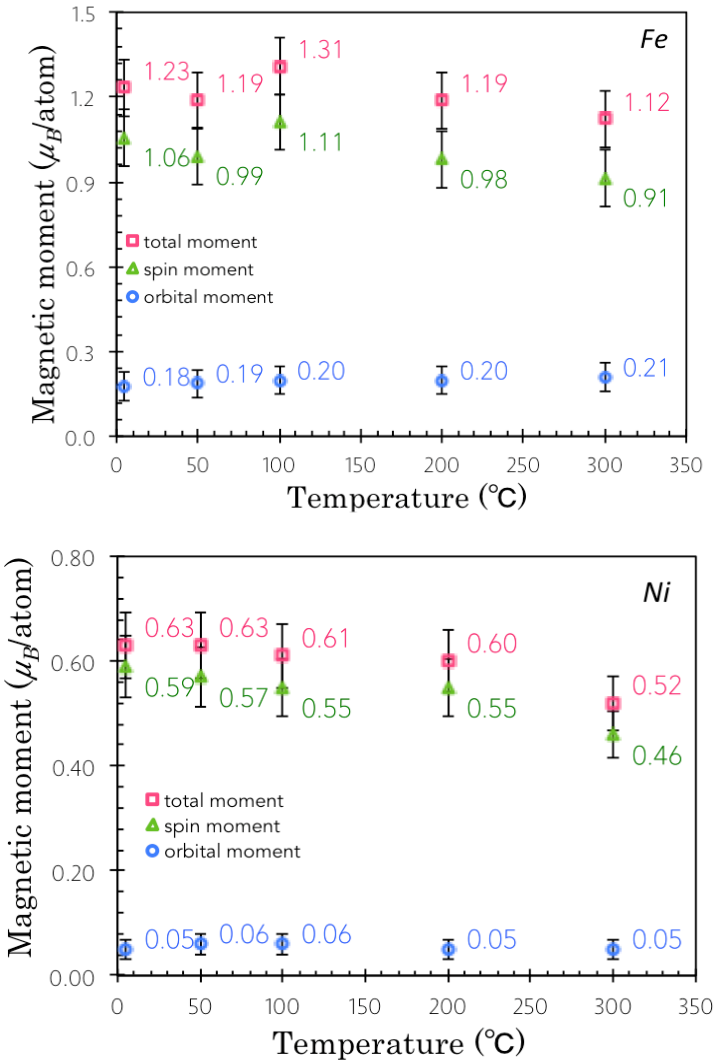


Figure 4-12 | The sum-rules derived $m_{spin}$, $m_{orb}$, and $m_{total}$ of the interface Fe (top) and the stabilizing Ni (bottom), respectively, at 3 – 300 K.

### 4.3.5 First-principles simulations and discussions

Generically, an enhancement of $m_{orb}$ of Fe can be attributed to the symmetry breaking of the ultrathin film, for which the electrons are more localized, leading to an orbital degeneracy lifting as reported in Fe/GaAs[220] and Fe/InAs.[221] A further factor of influence is the modified chemical environment due to the underneath graphene.

Interfacial $m_{spin}$ can be induced in the π-conjugated states of several carbon-based systems by adjacent FM as observed in $C_{60}/Fe_3O_4(001)$,[222] $C_{60}$/Fe(001),[223] and graphene/Ni(111),[224] due to the intensive spin and charge transfer between the FM and C atoms. The stacking of the topmost FM with respect to graphene is another noteworthy question. Possibilities exist that in such FM/graphene heterojunctions, FM atoms may be incorporated into the graphene defects, or diffuse through the graphene to form metallic layers in-between the graphene and the substrate. A very recent low energy electron diffraction (LEED) analysis on FM intercalation underneath graphene sheets shows that for 1-2 ML Fe deposited on graphene/Ni(111), the Fe atoms tends to intercalate between the graphene and Ni surface, forming a favorable Ni/Fe/graphene stacking and that Fe in between of graphene and Ni tends to follow the fcc stacking of the Ni(111) substrate and the graphene has the same registry as for Ni(111).[225, 226, 227] In terms of the occupation sites, the best agreement between experiment and theory of the Fe/graphene heterojunction points to a coexistence of two types of domains, namely top-fcc and bridge-top domains.[228]

To further understand the electronic nature of the ML Fe/graphene interface, first-principal calculations were performed using the projector augmented wave method[229] as implemented in the Vienna ab-initio simulation package (VASP).[230, 231] Among the available calculational schemes, the screened hybrid functional [232] calculations overestimate the exchange splitting and usually gives large atomic magnetic moments (i.e. $2.81\mu_B$/atom for bcc Fe). Using the Perdew-Burke-Ernzerh generalized gradient approximation,[233] our test calculations give an unrealistically large separation between Fe layer and graphene, typically ~4.20 Å, well in excess of the effective range of a chemical bonding.[234] Therefore within the context of our study, the electron exchange and correlation interactions were described by the local density approximation (LDA).[235] The plane wave kinetic energy cutoff was set to be 520 eV. A Monkhorst-Pack mesh[236] of 31 × 31 × 1 $\boldsymbol{k}$-points was used to sample the two-dimensional Brillouin zone for the thin film electronic structure calculations. The total energies were obtained using the tetrahedron method with the Blöchl corrections.[237] In each unit cell, all atomic positions are fully relaxed with the conjugate gradient procedure until the residual forces vanished within 0.02 eV/Å. The vacuum space of 15 Å was set to separate the interactions between neighboring slabs of the unit cells.

#### 4.3.5.1 The Fe stacking on graphene

Periodic DFT calculations were performed to obtain the most energetically stable stacking of ML Fe on graphene. Three initial superstructures, a Fe fcc(111) 1×1 primitive cell (2.55×2.55 $Å^2$), a Fe bcc(100) 5×3 supercell (14.33×8.60 $Å^2$), and a Fe bcc(110) 5×1 supercell (14.33×4.06 $Å^2$), matching a graphene 6×2 supercell (14.82×8.56 $Å^2$), a 6×1 supercell (14.82×4.28 $Å^2$), and a 1×1 cell (2.47×2.47 $Å^2$), to model Fe fcc(111), bcc(100) and bcc(110) MLs covered on graphene, respectively. For each superstructures, all atomic positions are relaxed until the atomic forces were smaller than 0.02 eV/Å. Figure 4-13 presents the DFT simulations of the Fe stacking on graphene of Fe fcc(111), bcc(100) and bcc(110) on graphene, respectively. The supercells are circled by the dash lines, which contains 3 atoms (2 C + 1 Fe atoms) for fcc(111), 63 atoms (48 C + 15 Fe atoms) for bcc(100), and 34 atoms (24 C + 10 Fe atoms) for bcc(110), respectively. Significant deformations were observed for both Fe bcc(110) and (100) on graphene due to the induced strain originating from the mismatching of lattice constants. The averaged Fe-Fe bond lengths vary from 2.73 to 2.35 Å for Fe bcc(110) ML, and from 2.91 to 2.38 Å for Fe bcc(100) ML, respectively while the Fe-Fe bond length is almost unchanged of 2.47 Å for Fe fcc(111) ML. This calculation suggests that in the Fe/graphene systems, the Fe prefers to follow the fcc(111)-like structure of that of the graphene substrate.

Given that Fe atoms deposited on graphene prefer to follow the fcc(111) stacking, the three inequivalent positions of the Fe allocations on graphene are presented in Figure 4-14, namely, top (blue), hollow (red) and bridge (green), among which the top configuration is most energetically favorable with an equilibrium distance of 1.90 Å.

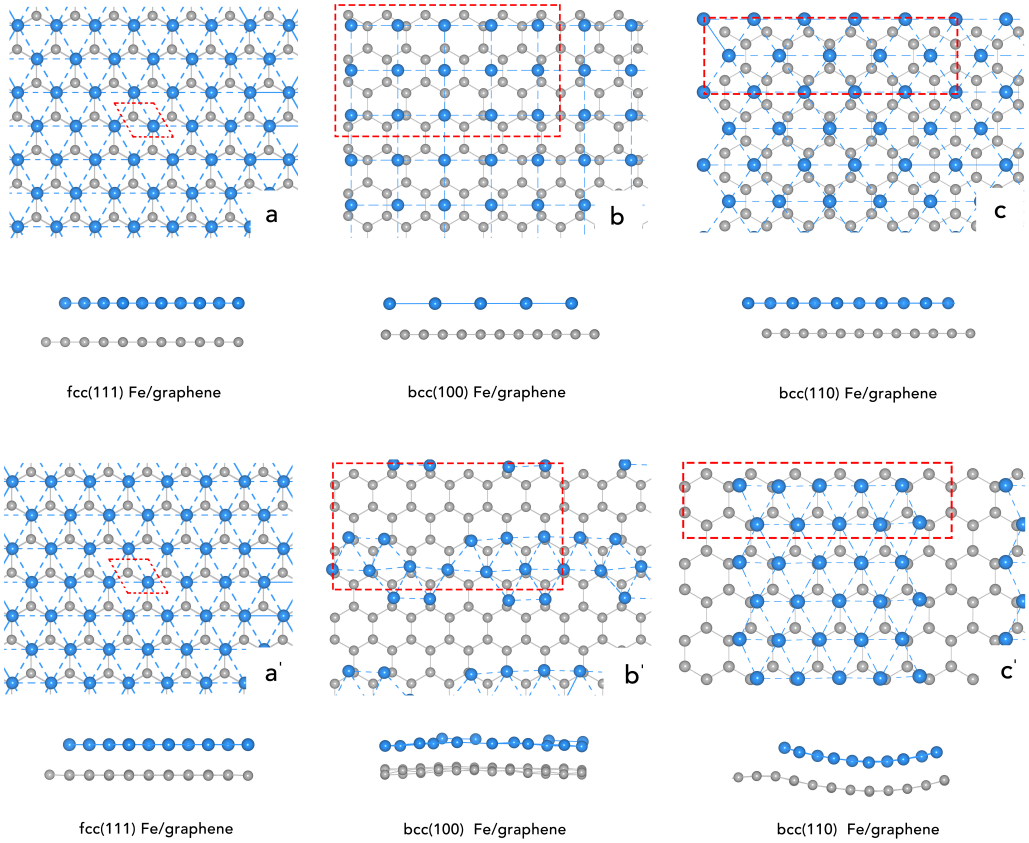


Figure 4-13 | The DFT simulations of the Fe stacking on graphene. The initial and relaxed crystal structure of Fe fcc(111), bcc(100) and bcc(110) geometries are presented in the upper and lower row, respectively. The dashed rectangles indicate the supercells.

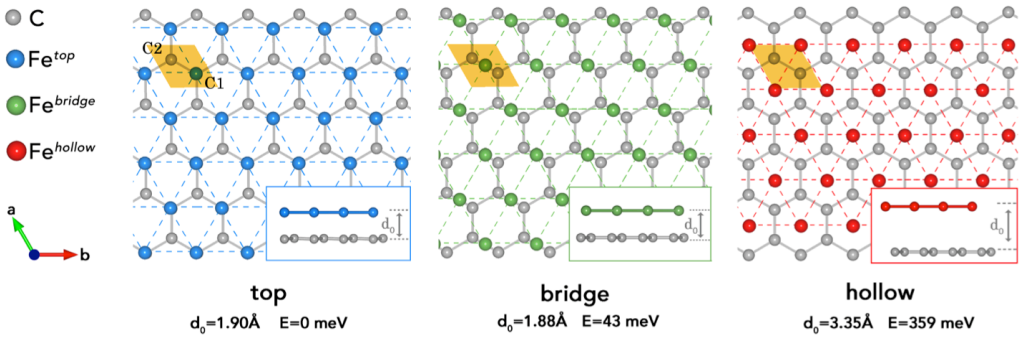


Figure 4-14 | Illustration of three nonequivalent Fe positions on graphene, namely top (blue), bridge (green) and hollow (red), respectively, and the calculated equilibrium distance and system free energy. The unit cell is shown as the gold-colored parallelogram.

#### 4.3.5.2 The magnetic moments of epitaxial Fe on graphene

The experimentally measured and calculated $m_{spin}$ and $m_{orb}$ of Fe for the three different configurations are gathered in Table 1. The DFT calculation well reproduced the XMCD observation by giving $m_{spin}$ = 1.23 $\mu_B$/atom for $Fe^{top}$ when deposited on graphene with fcc(111) stacking. Although $Fe^{top}$ was found to be the most favorable configuration on graphene according to the calculation, the observed numeric results of XMCD, i.e., $m_{spin}$ = (1.06 ± 0.1) $\mu_B$/atom, more likely indicates a mixture of $Fe^{top}$ and $Fe^{bridge}$ ($m_{spin}$ = 0.67 $\mu_B$/atom), given the small energy difference ($\Delta E_0$ = 43 meV) of their total energies. For comparison, the $m_{spin}$ of bulk bcc Fe ($a_0$ = 2.87 Å) and the freestanding fcc monolayer Fe ($a_0$ = 2.55 Å) were also calculated using the same method, whose results compare well with the pioneering reports.[238, 226] Consistent with the experiment, the theoretical simulation also reveals a ~50% reduction in the magnetic moment of Fe, which can be attributed to the strong interface hybridization between Fe and C atoms according to the following theoretical results and discussion.

| System | Ref. | Method | stacking | $m_{spin}(\mu_B$/atom) | $m_{orb}(\mu_B$/atom) |
|---|---|---|---|---|---|
| Fe/graphene | * | XMCD | | 1.06 ± 0.1 | 0.18 ± 0.02 |
| $Fe^{top}$/graphene | * | LDA | fcc | 1.23 | |
| $Fe^{bridge}$/graphene | * | LDA | fcc | 0.67 | |
| $Fe^{hollow}$/graphene | * | LDA | fcc | 2.57 | |
| freestanding ML Fe | * | LDA | fcc | 2.76 | |
| Fe/InAs | 221 | XMCD | bcc | 1.22 ± 0.12 | 0.22 ± 0.03 |
| Fe/GaAs | 26 | XMCD | bcc | 1.84 ± 0.21 | 0.25 ± 0.05 |
| bulk-like Fe | * | LDA | bcc | 2.15 | |
| bulk-like Fe | 25 | XMCD | bcc | 1.98 | 0.086 |

Table 4-2 | The experimentally measured (XMCD) and calculated (LDA) magnetic moments of Fe in various configurations. * refers to the results of the current work.

#### 4.3.5.3 The suppressed magnetization of Fe

The calculated spin-resolved band structure is presented in Figure 4-15 for the

freestanding Fe ML (left column) and Fe ML/graphene (right column) together with the corresponding projected density of states (DOS) of Fe atom. As for the freestanding Fe ML, two partial DOS peaks of Fe $3d_{z2}$ orbital at around -1.6 and 1.0 eV originates from these subbands with significant Fe $3d_{z2}$ partial band character for the spin-up (labeled with the red lines, ranging from -2.5 to -1.5 eV) and spin-down electrons (labeled with the blue lines, from -0.5 to 1.0 eV), respectively. Due to the strong Fe-graphene interaction, the partial band character of the Fe $3d_{z2}$ orbital in Fe/graphene becomes delocalized, and a weaker spin-dependent electronic structure appears. The partial DOS of Fe atom in Fe/graphene shifts upwards (downwards) for the spin-up (spin-down) electrons, compared to the partial DOS of the freestanding Fe ML. This observation results in a reduced spin polarization of the Fe atoms in Fe/graphene, leading to suppressed $m_{spin}$.

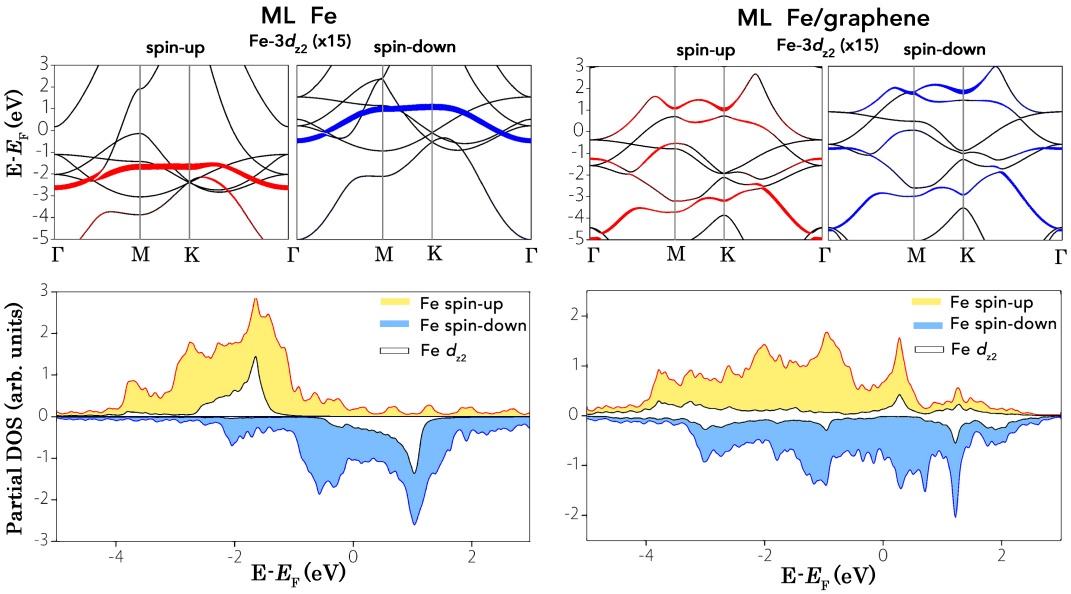


Figure 4-15 | The spin-resolved band structures and partial DOS maps of the freestanding fcc Fe ML (left) and that on graphene (right), where the partial band character of the Fe $3d_{z2}$ orbital is labeled by the red and blue lines for the spin-up and spin-down electrons, respectively. The bands with C1 $2p_z$, C2 $2p_z$, Fe $3d_{z2}$ and Fe $3d_{yz}$ characters are labeled with the red and blue lines for the spin-up and spin-down electrons, respectively.

#### 4.3.5.4 The charge and spin transfer between Fe and graphene

From further examination of the symmetry matching and spatial overlap of the electron orbitals, we found that the strong Fe-graphene interface interaction mainly originates from that of the C1 $p_z$ orbital with the Fe $3d_{z2}$ orbital, although that between the C2 $p_z$ orbital and the Fe $3d_{xz}$ and $3d_{yz}$ orbitals cannot be neglected. Here, C1 stands for the C atom located underneath the Fe atom in Fe ML, while C2 is located at the hollow site, as shown in Figure 2a. The charge density difference map (Figure 4-16), obtained by subtracting the charge density of Fe/graphene from that of the isolated Fe ML and graphene, verifies this strong hybridization between C1 $p_z$ and Fe $3d_{z2}$ orbitals. The Bader charge analysis shows that each Fe atom carries positive 0.13 $e$, and the charge transfer from Fe to C atoms mainly occurs at the interface region. The calculated spin density distribution, as shown in Figure 4-17, indicates that the magnetization of the system preliminarily localizes around the Fe atoms, while the C atoms are slightly spin polarized to the opposite direction.

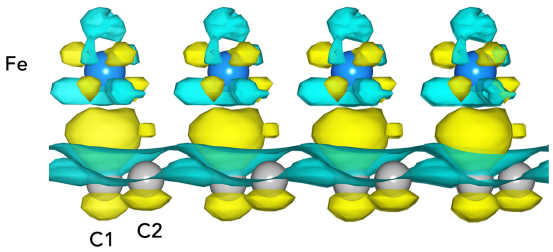


Figure 4-16 | The charge density difference map of fcc $Fe^{top}$/graphene, suggesting a substantial charge transfer mainly through C2$p_z$ orbital. The yellow and green colored areas represent the charge accumulation and depletion, respectively, and the isovalue is set to be 0.026 e/Å$^3$.

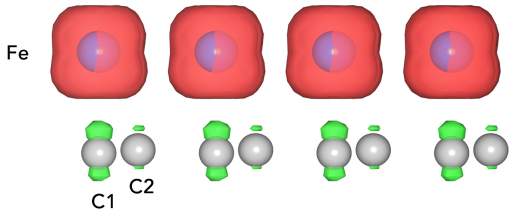


Figure 4-17 | Side view of the spin density distribution. Here, an isovalue of 0.035 e/Å$^3$ is chosen, and the yellow and green colors represent for positive and negative spin polarization, respectively.

#### 4.3.5.5 The induced magnetization of graphene

The spin-resolved band structures (upper rows) and partial DOS maps (lower rows) of the freestanding graphene single layer and that in Fe/graphene are presented in Figure 4-18. The asymmetric feature in the partial DOS of the C1 and C2 atoms in Fe/graphene for the two spin channels indicates a small spin polarization of graphene due to the presence of ferromagnetic Fe ML. According to the calculated band structures, the hybridization of the C and Fe atoms destroys the Dirac point, i.e., the cross point at valence band (VB) and conduction band (CB) at the *K* point, of intact graphene.

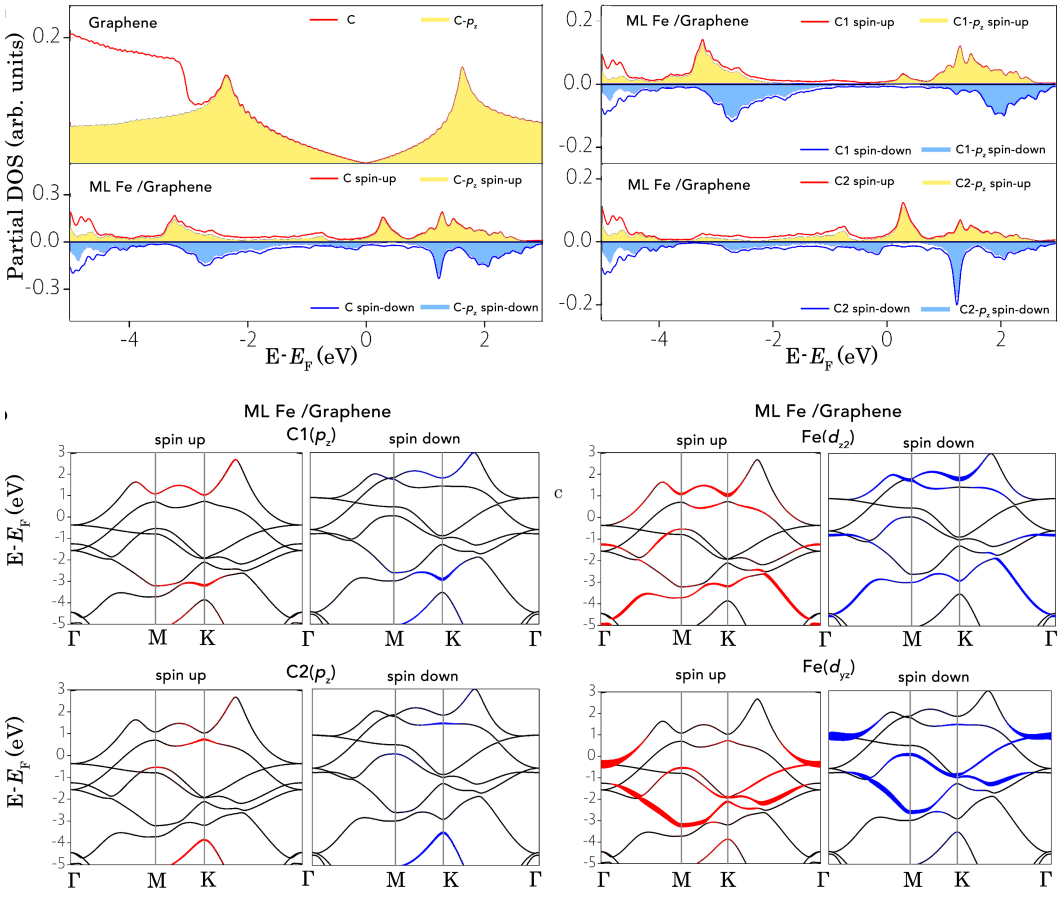


Figure 4-18 | The spin-resolved band structures (upper rows) and partial DOS maps (lower rows) of the freestanding graphene single layer and that in Fe/graphene, suggesting the graphene is slightly polarized in the presence of Fe ML. The sub-bands with C1 $2p_z$, C2 $2p_z$, Fe $3d_{z2}$ and Fe $3d_{yz}$ characters are labeled with the red and blue lines for the spin-up and spin-down electrons, respectively.

The sub-bands with C1 $2p_z$ and Fe $3d_{z2}$ partial band characters in Fe/graphene are both located at CB+1 and VB-3, and the Fe-C1 distance is about 1.93 Å, suggesting a strong hybridization between the C1 $2p_z$ and Fe $3d_{z2}$ orbitals due to their symmetry matching and effective spatial overlapping. In contrast to that of C1 atoms, relatively weaker interaction is observed for Fe with C2 atoms due to the relative longer Fe-C2 distance of 2.53 Å. Moreover, the sub-bands with C2 $2p_z$ character are mainly located at CB and VB-4, which correspond well only with these subbands with Fe $3d_{yz}$ character located at CB and VB-4. The $m_{spin}$ of C1 and C2 atoms are predicted to be about -0.02 and -0.01 $\mu_B$/atom, respectively, antiparallel to the Fe moments. Moreover, the Dirac point of intact graphene is destroyed by this strong hybridization between C $p_z$ and Fe $3d$ orbitals.

#### 4.3.5.6 Effect of Ni stabilizing layer on Fe

The bulk-like Ni atop the Fe monolayer serves as a stabilizing layer, in order to make the ML Fe in such configuration to be representative of the interface Fe of a bulk-like Fe on graphene. The two FM layers are strongly exchange coupled, provided an atomically clean interface is prepared. Figure 4-19 presents the energetically most favorable stacking of 7 ML Ni/1 ML Fe/graphene obtained by first-principals simulation. The calculations suggest that the stabilizing Ni layer has a limited influence on the underneath Fe by offering only a small charge transfer, i.e. 0.017 e/atom. In the fully relaxed structure, the Ni tends to pull the Fe slightly away from the graphene substrate, resulting in a higher $m_{spin}$ of 1.52 $\mu_B$/atom for Fe.

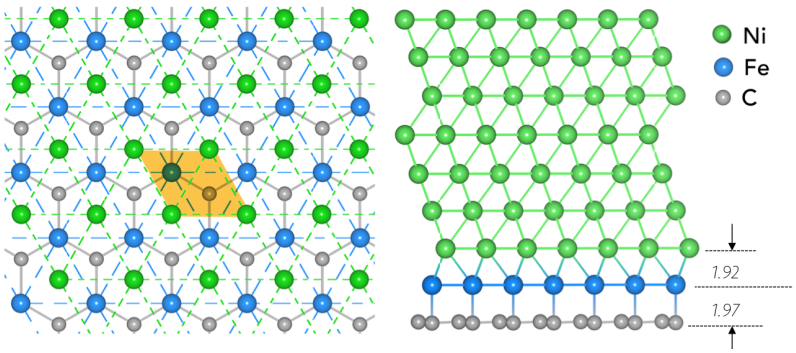


Figure 4-19 I Top and side views of the energetically most favorable stacking of 7 ML Ni/1 ML Fe/graphene. The Ni tends to pull Fe away from the graphene substrate slightly, resulting in a higher $m_{spin}$ of 1.52 $\mu_B$/atom.

## 4.4 The interfacial interaction of FM/DMS

### 4.4.1 Introduction

As a model of DMSs, (Ga,Mn)As has been investigated widely in the past decades due to its great potential in SC spintronics devices and short-range optical communications. However, the low $T_C$ of (Ga,Mn)As remains a major obstacle towards practical applications up to this day. The highest $T_C$ of (Ga,Mn)As reported so far is only ~220 K after optimized growth conditions and annealing methods.[239, 240, 241, 242] Recently, the FM/DMS exchange coupled bilayers, e.g. Fe/(Ga,Mn)As, have attracted a great deal of attentions. Independent magnetic behaviors in NiFe/(Ga,Mn)As were reported by Mark *et al*.,[243] while strong exchange coupling in MnAs/(Ga, Mn)As was studied by Zhu *et al*..[244] A substantial increase of $T_C$ from 40 to 70 K due to the presence of a few monolayers of Fe atop (Ga,Mn)As was also reported by Song *et al*..[245] and significant magnetic proximity effect up to RT at Fe/(Ga, Mn)As interface was demonstrated by F. Maccherozzi *et al*.,[246, 247] and K. Olejnik *et al*.,[248] respectively. Despite of the ambiguities remained, these results have enlightened the RT use of DMSs with the assistance of the magnetic proximity effect as a pathway.

In the reminder of this section, the XMCD study of the magnetic proximity effect in $Co_2FeAl$/(Ga,Mn)As bilayers will be presented. Co-based Heusler alloys are desirable spintronic materials because of their high spin polarization, low Gilbert damping constant and high $T_C$. It has been reported that high-quality epitaxial Heusler alloy $Co_2FeAl$ on GaAs (001) could show an in-plane uniaxial magnetic anisotropy with an easy axis along the [110] direction.[249, 250] The $Co_2FeAl$/(Ga,Mn)As bilayers are expected to exhibit strong interfacial exchange interaction and interesting magnetic behaviors due to their orthogonal magnetic easy axis.

### 1.1.1 The sample preparation

The 3nm $Co_2FeAl$/150 nm $Ga_{0.93}Mn_{0.07}As$/GaAs(001) sample used in this study was prepared by the collaborator in the Superlattices and Microstructures Laboratory (led by professor Jianhua Zhao) of the Institute of semiconductor, Chinese Academy of Science (CAS), Beijing, China. The MBE process of $Co_2FeAl$ and $Ga_{0.93}Mn_{0.07}As$ has been performed in two growth chambers (VG-80), so to avoid cross contaminations. To

guarantee high quality of the interface, the sample was transferred via an ultrahigh vacuum channel between during the growth process of the whole structure without any exposure to the air. A 150 nm $Ga_{0.93}Mn_{0.07}As$ was first deposited onto GaAs(001) buffer layer in the first MBE chamber at the substrate temperature of 250°C. The clear (1×1) streaky patterns of RHEED of the $Ga_{1-x}Mn_xAs$ were obtained, which well reproduce the previous reports, suggesting a high crystalline quality and smooth surface.[249, 250] Subsequently, without breaking the vacuum, the 150 nm $(Ga_{1-x}Mn_x)As$/GaAs(001) was transferred to the next MBE chamber where a 3 nm $Co_2FeAl$ film was deposited at the substrate temperature of 160°C. The whole structure was finally capped by 2 nm Al to protect it from oxidation during transport to the synchrotron facility.

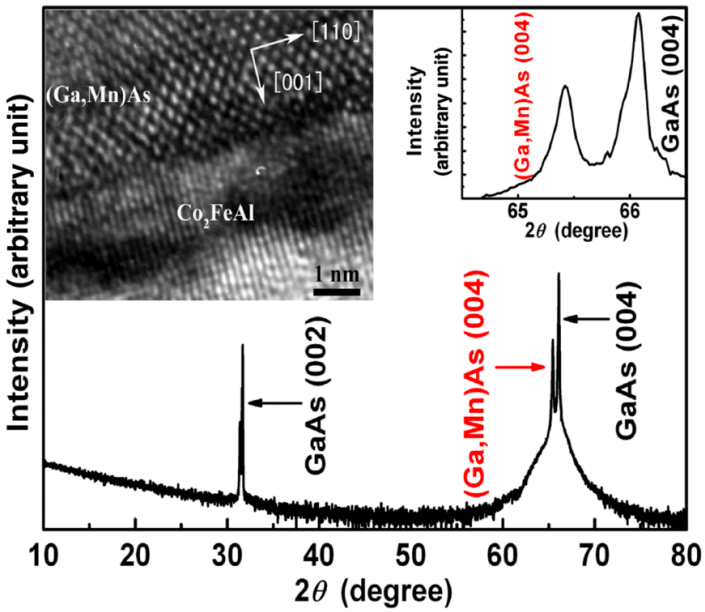


Figure 4-20 | Typical DCXRD curve of the $Co_2FeAl/Ga_{1-x}Mn_xAs$ bilayer sample, from which only (004) and (002) diffraction peaks of GaAs and $Ga_{1-x}Mn_xAs$ were observed without a secondary phase like MnAs. Right inset: the enlargement around $Ga_{1-x}Mn_xAs$ (004) peak. Left inset: typical cross-sectional TEM, from which well ordered *B2* phase $Co_2FeAl$ and zinc-blende $Ga_{1-x}Mn_xAs$ were observed with a sharp interface between them.

The high-resolution double-crystal X-ray diffraction (XRD) and the cross-sectional TEM were performed (by the sample provider) to check the crystal structure of this $Co_2FeAl/Ga_{0.93}Mn_{0.07}As$ bilayer, as presented in Figure 4-20. Apart from the (004) and (002) diffraction peaks of GaAs and $Ga_{1-x}Mn_xAs$, no second phase like MnAs

related peaks was observed. The high-resolution TEM of the $Co_2FeAl/Ga_{1-x}Mn_xAs$ interface was observed as presented in the inset of Figure 4-20, from which well ordered $Co_2FeAl$ and zinc-blende (Ga, Mn)As were observed with a sharp interface between them. No appreciable MnAs clusters was seen in the (Ga, Mn)As matrix within the experimental accuracy.

### 4.4.2 The XMCD measurement

The XAS and XMCD of the Fe, Co, and Mn $L_{2,3}$ absorption edges were performed at the beamline I1011 at the Max-lab, Sweden. Circularly polarized X-rays with 80% degree of polarization were utilized in 45° incidence with respect to the sample plane and parallel with the applied magnetic field for the easy saturation of the sample. The XAS spectra were obtained by TEY detection. The XMCD was taken as the difference of the XAS spectra, i.e., $\sigma^- - \sigma^+$, obtained by flipping the X-ray helicity at a fixed magnetic field of 300 Oe. A typical pair of XAS and XMCD spectra of Fe, Co, and Mn, respectively, are presented in Figure 4-21, Figure 4-22, and Figure 4-23. The XAS of both Fe and Co of the bilayer sample predominately show a white line at each spin-orbit split core level with a small shoulder near the main peak, which is likely from the oxidization of the topmost $Co_2FeAl$. Since TEY is extremely surface sensitive, as discussed in Chapter III, such oxidization can have significant impact onto the estimation of the magnetic moments based on the spectrum. Dichroic XAS spectra were obtained for Mn at 600 Oe at RT, suggesting a ferromagnetic ordering of the $Ga_{1-x}Mn_xAs$. Since a single layer $Ga_{1-x}Mn_xAs$ in no way shows XMCD at RT,[251] such ferromagnetic phase can be attributed to the magnetic exchange coupling with the adjacent $Co_2FeAl$ layer.

Figure 4-24 presents the elemental specific XMCD versus the applied magnetic field relations for the Fe, Co and Mn, respectively. All of these elements exhibit clear ferromagnetic hysteresis behaviors and most importantly, identical $H_c$, i.e. ~100 Oe at RT, which is already well in excess of the $T_c$ of $Ga_{1-x}Mn_xAs$. The identical $H_c$ means that the magnetization reversal of the $Ga_{1-x}Mn_xAs$ layer follows that of the $Co_2FeAl$ layer and hence confirms a robust magnetic Mn-Fe-Co coupling. We would like to note that data presented in this thesis are only preliminary results solely obtained by the author. Furthermore temperature dependent XMCD measurements of the $Co_2FeAl/ Ga_{1-x}Mn_xAs$

samples were performed by the collaborator in National Synchrotron Radiation Laboratory of Taiwan, which is in consistent of our observation (see our publication in 2013, PRL **111**, 027203).

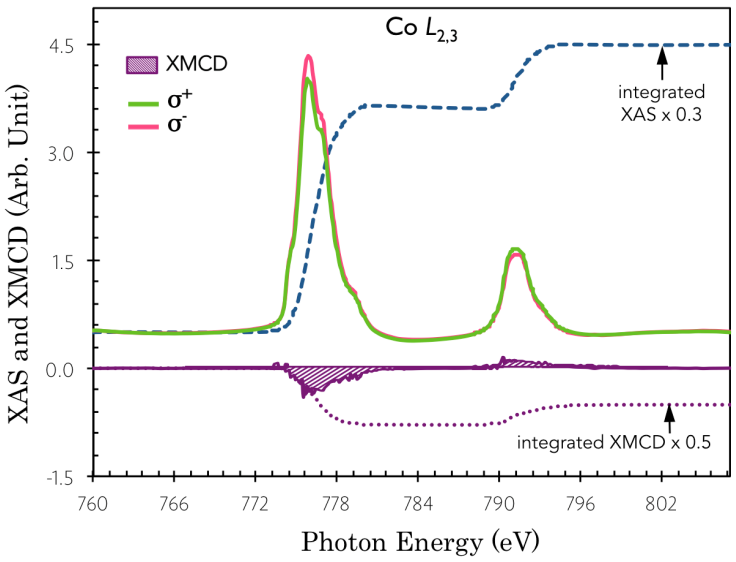


Figure 4-21 | Typical pair of XAS and XMCD spectra, normalized to the incident beam intensity, at the Co $L_{2,3}$ edge, obtained at 300 K. The dashed lines indicate the integration of the spectra. Data are offset and scaled for clearness.

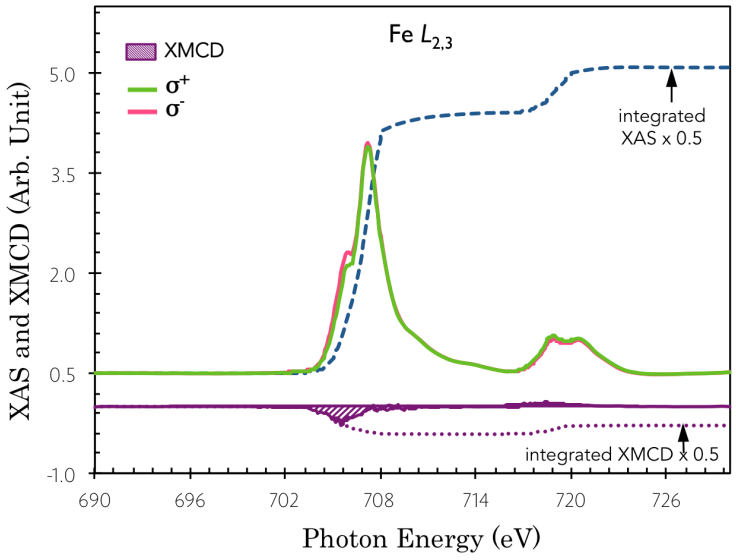


Figure 4-22 | Typical pair of XAS and XMCD spectra, normalized to the incident beam intensity, at the Fe $L_{2,3}$ edge, obtained at 300 K. The dashed lines indicate the integration of the spectra. Data are offset and scaled for clearness.

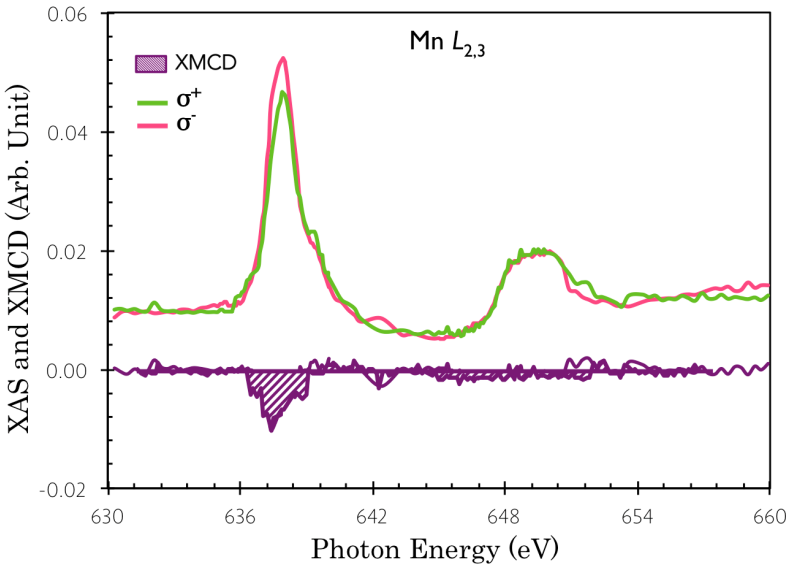


Figure 4-23 | Typical pair of XAS and XMCD spectra, normalized to the incident beam intensity, at the Mn $L_{2,3}$ edge, obtained at 300 K. The dashed lines indicate the integration of the spectra. Data are offset and scaled for clearness.

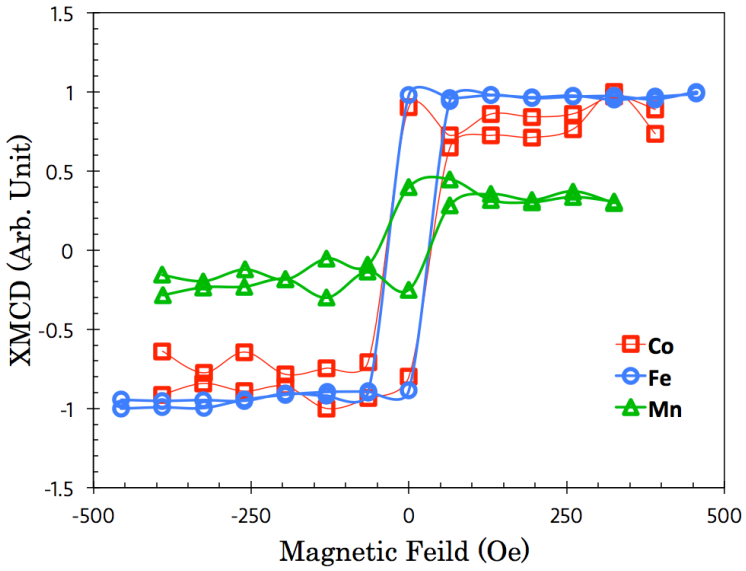


Figure 4-24 | The elemental specific XMCD hysteresis loops of the Fe, Co, and Mn, respectively.

### 1.1.2 Discussions

In the Fe/$Ga_{1-x}Mn_xAs$ exchange coupled systems, Mn were found to be antiferromagnetically coupled to Fe,[246, 247, 48] while in our study, the magnetization direction of Mn is in parallel with that of Fe and Co. Such phenomenon is comparable to the XMCD observations of $Co_2Fe_{1-x}Mn_xAl$ ($x$ = 0.3) grown at 160°C, as reported by K. K. Meng *et al.*,[249] in which as $x$ increases to 1, the Mn XMCD signal vanishes due to strong Mn–Mn antiferromagnetic interaction. The Mn concentration in our case, i.e. 7%, is too low to form Mn-Mn, Co-Mn and Fe-Mn antiferromagnetic coupling at the $Co_2FeAl/Ga_{1-x}Mn_xAs$ interface. On the contrary, Co-Co, Co-Fe, Fe-Fe, Co-Mn and Fe-Mn ferromagnetic interactions play predominate roles resulting in a favorable parallel alignment of the $Co_2FeAl$ and the $Ga_{1-x}Mn_xAs$ magnetization. This observation has been confirmed by the *ab initio* density functional calculations very recently, which considered both the $L2_1$ ordered and $B2$ disordered phases for the $Co_2FeAl$.[251] The total energy calculations suggest that in all the calculated $B2$ phase $Co_2FeAl/Ga_{1-x}Mn_xAs$ bilayers with the (Ga,Mn)-terminated interface, the ferromagnetic coupling across the interface between Fe(Co) and Mn is energetically favored, while in all the $L2_1$ phase $Co_2FeAl/Ga_{1-x}Mn_xAs$ bilayers, the antiferromagnetic coupling between Fe(Co) and Mn is more stable. The ferromagnetic coupling is rather strong, being ~10 meV per Mn atom or larger. In the $B2$ phase $Co_2FeAl/Ga_{1-x}Mn_xAs$ bilayers with the As-terminated interface, both stable ferro- and antiferro- couplings across the interface are found, depending on the atomic configuration of the (Fe,Al) sublattice.

## 4.5 Conclusions

In this chapter, we have demonstrated the interfacial magnetic and electronic nature of FM/SC systems including Fe/GaAs, Co/GaAs, Ni/GaAs, Fe/Graphene and $Co_2FeAl$/(Ga,Mn)As. The unique surface sensitivity and elemental selectivity of XMCD technique has enabled unambiguous determination of the electronic and magnetic ground state of the materials under interrogation. The MBE growth has been employed as the major sample preparation method for the studies presented in this chapter, so to produce atomically clean interfaces and hence allows the occurring of intensive energy exchanges between the adjacent atoms. Supporting characterization techniques (TEM and SQUID-VSM) and theoretical tools (first-principals simulations) have also been utilized to understand the XMCD observations.

We have observed a suppressed magnetization (reduced by ~ 50%) of the epitaxial ML Co on GaAs(100) - 4 × 6 surface, which can be attributed to a combined effect of the island growth geometry at low coverage, the tendency to follow the bcc stacking of the GaAs substrate, and the detrimental interdiffusion. These factors have apparently stronger impacts on the Ni/GaAs (100) interface, leading to nearly vanished magnetic moment for the 1 ML Ni. These interfacial magnetic phenomena have been demonstrated in the specially designed $FM_1/FM_2$/SC structure, which not only allows easy observation of the magnetization of $FM_2$ in atomic scale, but also restores the realistic case of the proposed hybrid spintronics devices. Apart from the suppressed magnetization of the interfacial ML $FM_2$ atoms, modification occurs in the topmost $FM_1$ stabilizing layer, too. Based on the fact that the underneath $FM_2$ materials can follow the island growth geometry at low coverage, it is likely that some of the $FM_1$ atoms atop may also in contact with the SC substrate and hence the stacking transformation and the detrimental interdiffusion could apply to these $FM_2$ atoms. Possible charge and spin transfers between the $FM_1$ and $FM_2$ atoms are additional factors worthy considerations.

Further applying this method to a new field of the community, i.e. the graphene-based spintronic materials, a reduced but still sizable magnetic moment of the ML Fe on graphene, i.e. (1.23 ± 0.1) $\mu_B$/atom. The inclusion of a Ni stabilizing layer has facilitated the study of the temperature dependence of the magnetization of the Fe/graphene interface, which suggests a bulk-like $T_c$ of the ML Fe in such geometry. The sum-rules derived results in this system are well reproduced by DFT calculations and can be attributed to the strong hybridization of C $2p_z$ and Fe $3d_{z2}$ orbitals and the

delocalization of the Fe 3*d* electrons at the Fe/graphene interface.

The significantly enhanced $T_c$ (above RT) was demonstrated by XMCD in the epitaxial $Co_2FeAl$/(Ga,Mn)As bilayer structure. The elemental specific hysteresis loops of Fe, Co and Mn, respectively, exhibit clear ferromagnetic behaviors and identical $H_c$, proving a robust magnetic Mn-Fe-Co coupling. Unlike the antiparallel alignment, which has been reported in the Fe/(Ga,Mn)As systems, our results suggest a ferromagnetic coupling between the Fe, Co and the Mn. This observation was also later on confirmed by the *ab initio* density functional calculations on both the ordered $L2_1$ and disordered $B2$ phases for the $Co_2FeAl$.

# 5 Chapter V Half-metallic materials

## 5.1 Introduction

In the contemporary spintronics research, magnetite or $Fe_3O_4$, especially in nano-form, has attracted enormous interest due to its high $T_c$, strong spin polarization at $E_F$, film stability under ambient conditions and growth compatibility to SCs. Fascinating properties of spin transport have also been presented in $Fe_3O_4$, such as the spin Seebeck effect,[111] the spin filter effect,[112] the gate voltage-induced phase transition,[110] and the spin valve effect of $Fe_3O_4$/MgO/$Fe_3O_4$ junctions.[113] Yet at the meantime, many fundamental properties of magnetite such as the spin and orbital ordering, Verwey transition mechanism, and the coupling mechanism between different sites have long been open issues, and with the thickness down to nanometer scale, these issues become even more sophisticated.

Tremendous progress has been made in recent years in the epitaxial growth of magnetite by both pulsed laser deposition (PLD)- and MBE-based techniques, and a wide range of substrates of technological importance, such as GaAs,[252] GaN[253] MgO,[256] $Y_2Zr_2O_7$(YZO),[259] and $BaTiO_3$[270] etc., have been involved. Direct epitaxial growth of $Fe_3O_4$ on GaAs(001) by *in situ* post annealing was firstly achieved by Lu *et al*.,[252] who found the epitaxial relationship of $Fe_3O_4$(100)<011> // GaAs(100)<010> with the unit cell of $Fe_3O_4$ rotated by 45° to match that of GaAs(100) substrate. Beyond the classic FM/SC heterostructures, the FM/I/SC, i.e. $Fe_3O_4$/MgO/GaAs, system could be an even more timely and important system to investigate, as crystalline MgO-based magnetic tunnel junctions have achieved great success in assisting efficient spin injections for various applications.[254] An insulating layer of MgO can be used as a tunneling barrier, which not only relieves the conductivity mismatch problem but also works as a spin filter. Moreover, MgO forms an excellent diffusion barrier with thermal stability up to 800°C, effectively preventing the intermixing at a given ferromagnet-semiconductor interface. Efforts have been made to explore the magnetic behavior of nanoscale epitaxial thin films on bulk MgO(100).[255] Wong *et al*.[257] investigated on the effect of inserting an epitaxial MgO layer on $Fe_3O_4$/GaAs(100) and found this hybrid structure possesses an epitaxial relationship of $Fe_3O_4$(100)[001]//MgO(100)[001]//GaAs(100)[001], where the MgO principal axes is

parallel to that of the GaAs. The epitaxial direction of Fe rotates by 45° with respect to MgO/GaAs(100) and that of $Fe_3O_4$ rotated by 45° back after oxidation.

In this chapter, detailed XMCD and SQUID studies of $Fe_3O_4$ epitaxial thin films on MgO/GaAs(100), MgO(100) and YZO(111) are presented, aiming to contribute to some of the unanswered questions related to the spin and orbital moments of the $Fe_3O_4$ ultrathin films, their changes across the Verwey transition, and their dependency on the sample stoichiometry and homogeneity.

## 5.2 The spin and orbital moment of magnetite thin films

### 5.2.1 Introduction

The presence of integer magnetic moment of magnetite is expected in experiment as an indication for a B-site minority electron conduction mechanism, which accompanies the full spin polarization near the $E_F$. However, controversial results of the $m_{spin}$, $m_{orb}$, and $m_{total}$ of magnetite have been reported based on experimental techniques including superconducting quantum interference device (SQUID) magnetometer,[255, 274] XMCD,[256, 263, 267, 275, 274] and magnetic Compton scattering (MCS),[270, 271] and theoretical estimations including local density approximation (LDA),[267] LDA+U,[267] local spin density approximation (LSDA)+U,[264] and moment analysis[256] etc.. The reported $m_{orb}$ of magnetite varies from (0.67±0.09) $\mu_B/f.u.$by Huang *et al.*,[267] (0.51±0.05) $\mu_B/f.u.$ by Li *et al.*,[270] to (0.06±0.14) $\mu_B/f.u.$ by Duffy *et al.*[271] and all the way down to –0.001 $\mu_B/f.u.$ by Goering *et al.*.[263] Theoretical analyses were given with even sharper contrast, varying from 0.43 $\mu_B/f.u.$ by Huang *et al.*[267] to 0.02 $\mu_B/f.u.$ by Antonov *et al.*.[264] Similar controversial observations exist for the $m_{spin}$ of magnetite. Goering *et al.*[275] reported $m_{spin}$ down to (1.7±0.02) $\mu_B/f.u$ in single crystal $Fe_3O_4$. Among the very few work on $Fe_3O_4$ thin films, Orna *et al.*[274] observed greatly reduced $m_{spin}$ = 1.83 $\mu_B$/f.u. of $Fe_3O_4$ on MgO, as well as Babu *et al.*[269] observed $m_{spin}$ = (1.20±0.05) $\mu_B/f.u.$ of $Fe_3O_4$ on $BaTiO_3$. On the other hand, significantly enhanced $m_{spin}$ = 7.7 $\mu_B$/f.u. was reported by Arora *et al.*.[255]

To fundamentally understand character of 3*d* electrons in magnetite, it is necessary to determine the $m_{spin}$ and $m_{orb}$, individually and unambiguously. In the remainder of this section, a XMCD study of the magnetite thin films on MgO/GaAs(100), MgO(100) and YZO(111), respectively, will be presented, supported by the global SQUID-VSM measurement. It will be seen that XMCD can be an ideal probe for these fundamental physical quantities of the spinel-type ternary oxides, not only because of its unique elemental selectivity, but also the powerful site sensitivity.

### 5.2.2 The sample preparation

The magnetite thin film used in this study was grown by post-annealing of an epitaxial Fe(001) in an oxygen partial pressure, prepared using the Balzers UTT 400 MBE system in Magnetic Thin Films Research Group of the University of York. Firstly a

sharp GaAs(001) surface was obtained after annealing in an ultrahigh vacuum chamber for 40 minutes at 830 K as can be seen from the RHEED pattern (see Figure 5-1 (a)). The chemical etching process of the GaAs substrates prior to the MBE process can be found in Chapter III. The 2 nm MgO buffer layer was then grown by e-beam evaporation at a rate of 2 Å/min, as monitored by a quartz microbalance calibrated by ex-situ AFM, while the substrates were kept at 673 K. The chamber pressure during deposition was below 4 x $10^{-8}$ mbar suggesting a limited decomposition of the MgO crystals. Lastly, a 4 nm thick epitaxial Fe film was grown on the MgO/GaAs at room temperature, followed by post-growth annealing at 500 K in the oxygen partial pressure at 5 x $10^{-5}$ mbar for 10 minutes. Overall the comparatively large oxygen ions form an fcc lattice and the Fe atoms are located in interstitial sites. The epitaxial relationship can be identified from RHEED as $Fe_3O_4$(100)[001]//MgO(100)[001]//GaAs(100)[001] as shown in Figure 5-1 (a)-(d), whose evolution during the growth has been discussed by Wong *et al*..[257] Thereafter, the nominal thicknesses of 8 nm of the $Fe_3O_4$ after oxidation was quoted for the sample and such selection of thickness for the XMCD performance is due to the oxidation depth limit by the post-growth annealing method.

For comparison purpose, another two types of magnetite samples, namely, a 12 nm $Fe_3O_4$ epitaxial thin film on MgO(100), and a 100 nm $Fe_3O_4$ on YZO(111), were outsourced, aiming to have an insight of the different magnetic properties of the $Fe_3O_4$ thin film caused by the substrate and preparation methodology. The 12 nm $Fe_3O_4$/MgO(100) was deposited by effusion cells at a rate of 0.04 Å per second at a substrate temperature of 623 K and in oxygen pressure of 2.5 × $10^{-7}$ torr, prepared using the oxygen-plasma-assisted MBE system in the IBM Research Division of Almaden Research Center, San Jose, US.[258] Prior to the growth, the MgO was annealed at 600 °C for 30 minutes. The 100 nm $Fe_3O_4$/YZO(111), on the other hand, was prepared by pulsed laser deposition (PLD) growth and post annealed to 1400 K, offered by the Physics Department of the University of York.[259] We would like to note that, although samples with identical thickness are the ideal systems to see the influence of the growth methodology, such goal is technically hard to achieve as 12 nm $Fe_3O_4$ is rather close to the lower limit of the plasma-assisted simultaneous oxygenation technique, whilst 8 nm is nearly the largest film thickness that the post-annealing method can thoroughly oxidize a Fe.[253] The 100 nm $Fe_3O_4$/YZO(111) in this study, on the other hand, serves as a reference bulk-like sample as the effect from the interface is very limited for a magnetic film of such thickness and it is relatively easy to grow thick films with the

PLD technique.

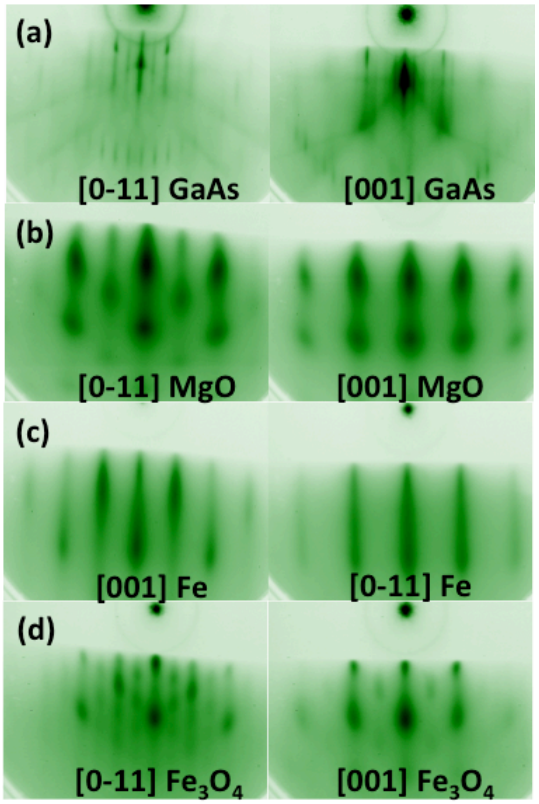


Figure 5-1 | Typical RHEED patterns of (a) GaAs(100), (b) MgO/GaAs, (c) Fe/MgO/GaAs, and (d) $Fe_3O_4$/MgO/GaAs along [0-11] and [001] directions, respectively, obtained during the MBE process of the 8 nm Fe3O4/MgO/GaAs(100) sample.

### 5.2.3 The SQUID-VSM measurements

The general magnetic properties of the 8 nm $Fe_3O_4$/MgO/GaAs(100) sample were characterized *ex situ* by means of SQUID-VSM. The magnetization versus field (M-H) loops in Figure 5-2 were obtained by applying the magnetic field out of plane. A small diamagnetic contribution from the sample holder has been carefully subtracted from the measured data. It can be seen that the sample exhibits a magnetization ~ 400 emu/cm$^3$ at 4 T, slightly lower than the principle bulk saturation value as discussed above, i.e. 480 emu/cm,$^3$ or 4.0 $\mu_B$/f.u. for bulk magnetite.

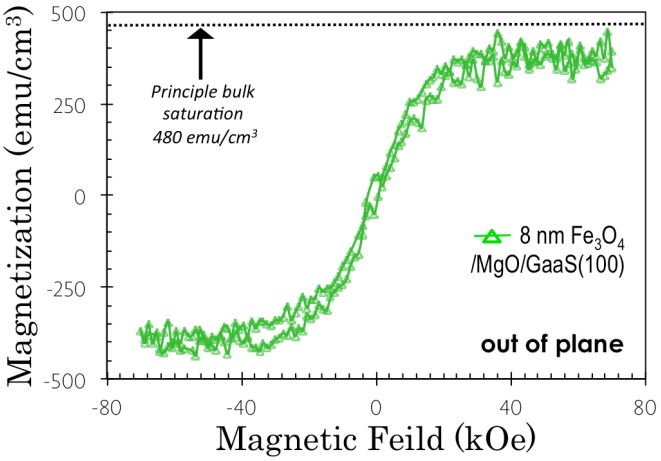


Figure 5-2 | Typical hysteresis loop of the 8 nm $Fe_3O_4$/MgO/GaAs(100) sample obtained by applying the magnetic field out of plane. The dash line indicates the principle saturation value, i.e. 480 emu/cm$^3$, or 4.0 $\mu_B$/f.u. for bulk magnetite.

Figure 5-3 presents the hysteresis loops of the three magnetite samples, namely, the 8 nm $Fe_3O_4$/MgO/GaAs(100) (green), the 12 nm $Fe_3O_4$/MgO(100) (blue), and the 100 nm $Fe_3O_4$/YZO(111) (red), respectively, obtained at RT by applying the magnetic field in plane. The saturation magnetization ($M_s$) of the three magnetite samples were found to be- ~ 400 emu/cm$^3$ for the 8 nm $Fe_3O_4$/MgO/GaAs(100), ~ 270 emu/cm$^3$ for the 12 nm $Fe_3O_4$/MgO(100) (blue), and ~ 220 emu/cm$^3$ for the 100 nm $Fe_3O_4$/YZO(111). The coercive field ($H_c$), on the other hand, maximizes at the thickest sample, i.e. ~ 300 Oe for the 100 nm $Fe_3O_4$/YZO(111), ~ 90 Oe for the 12 nm $Fe_3O_4$/MgO(100), and ~ 50 Oe for the 8 nm $Fe_3O_4$/MgO/GaAs(100) in the film plane (the M-H scanning step is 20 Oe in this experiment).

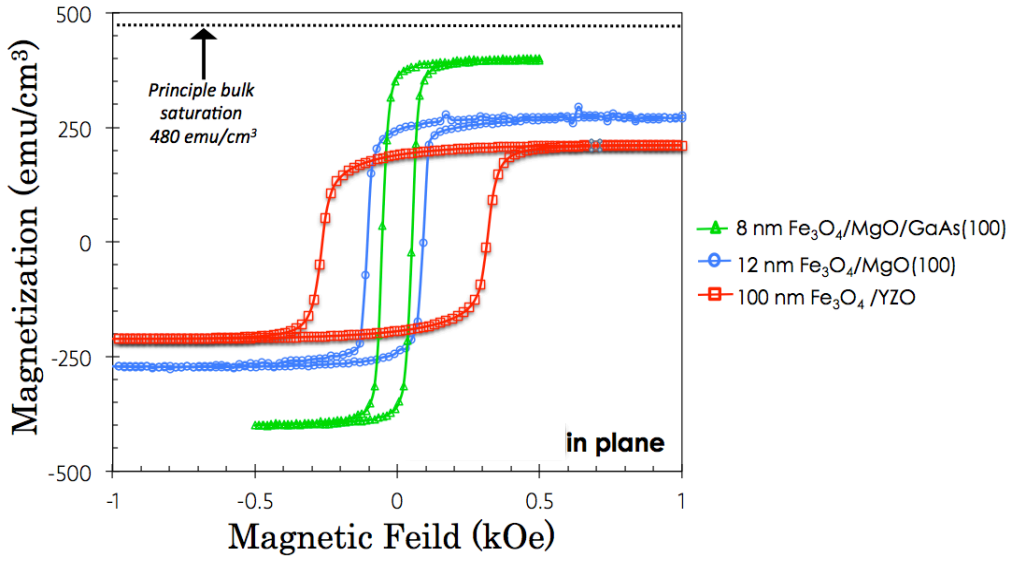


Figure 5-3 | Typical hysteresis loops of the three magnetite samples, namely, 8 nm $Fe_3O_4$/MgO/GaAs(100) (green), 12 nm $Fe_3O_4$/MgO(100) (blue), and 100 nm $Fe_3O_4$/YZO(111) (red), respectively, obtained by applying the magnetic field in plane. The dash line indicates the principle saturation value, i.e. 480 emu/cm$^3$, or 4.0 $\mu_B$/f.u. for bulk-like magnetite.

### 5.2.4 The XMCD measurements

XAS and XMCD at the Fe $L_{2,3}$ absorption edges were performed at the beamline I10 of Diamond Light Source. Circularly polarized X-rays with 100% degree of polarization were used in normal incidence with respect to the sample plane and in parallel with the applied magnetic field, as shown in Figure 5-4, so as to minimize the nonmagnetic asymmetries. The XMCD was obtained by taking the difference of the XAS spectra, e.g. $\sigma^- - \sigma^+$, achieved by flipping the X-ray helicity at a fixed magnetic field. The XAS experiments were carried out at 300 K with TEY detection. Figure 5-5 presents a typical pair of XAS and XMCD spectra of the 8 nm $Fe_3O_4$/MgO/GaAs(100) under the applied magnetic field from 10 kOe to 100 kOe. The XMCD spectra well reproduce those from the theoretical calculations and previous observations, caused by the antiparallel spin orientations of the A and B sites.[260] The complex form of these spectra arises because the XAS spectra correspond to an overlap of different sets of multiplet structures. The B sites $Fe^{3+}$ and $Fe^{2+}$ spin-up states exhibit negative peaks at Fe $L_3$ edge and positive peaks

at the Fe $L_2$ edge, while the A sites $Fe^{3+}$ spin-down states behave oppositely at the Fe $L_3$ and $L_2$ edges, respectively.

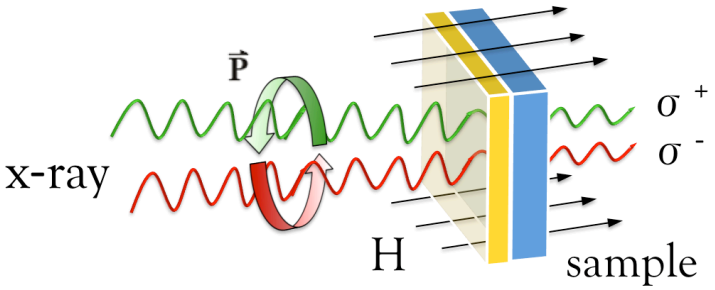


Figure 5-4 | Schematic diagram of the experimental set up of the XMCD measurement in Faraday geometry, i.e., with both the incident X-rays and the magnetization perpendicular to the sample surface.

For comparison purpose, the same XAS and XMCD experiments were also performed with the 12 nm $Fe_3O_4$/MgO (100) and the 100 nm $Fe_3O_4$/YZO (111), as presented in Figure 5-6. Sizable difference of the relative peak intensity of the $Fe^{3+}$(Td) and $Fe^{2+}$(Oh) components of the XMCD spectra was observed between the 12 nm $Fe_3O_4$/MgO (100) and the 8 nm $Fe_3O_4$/MgO/GaAs(100) and the 100 nm $Fe_3O_4$/YZO(111) (see Figure 5-6 lower rows). Since the probe depth of XMCD can be up to a few nms, the observed phenomena cannot be simply attributed to the surface, which might have been prevalently terminated with one particular Fe site under the given growth conditions.

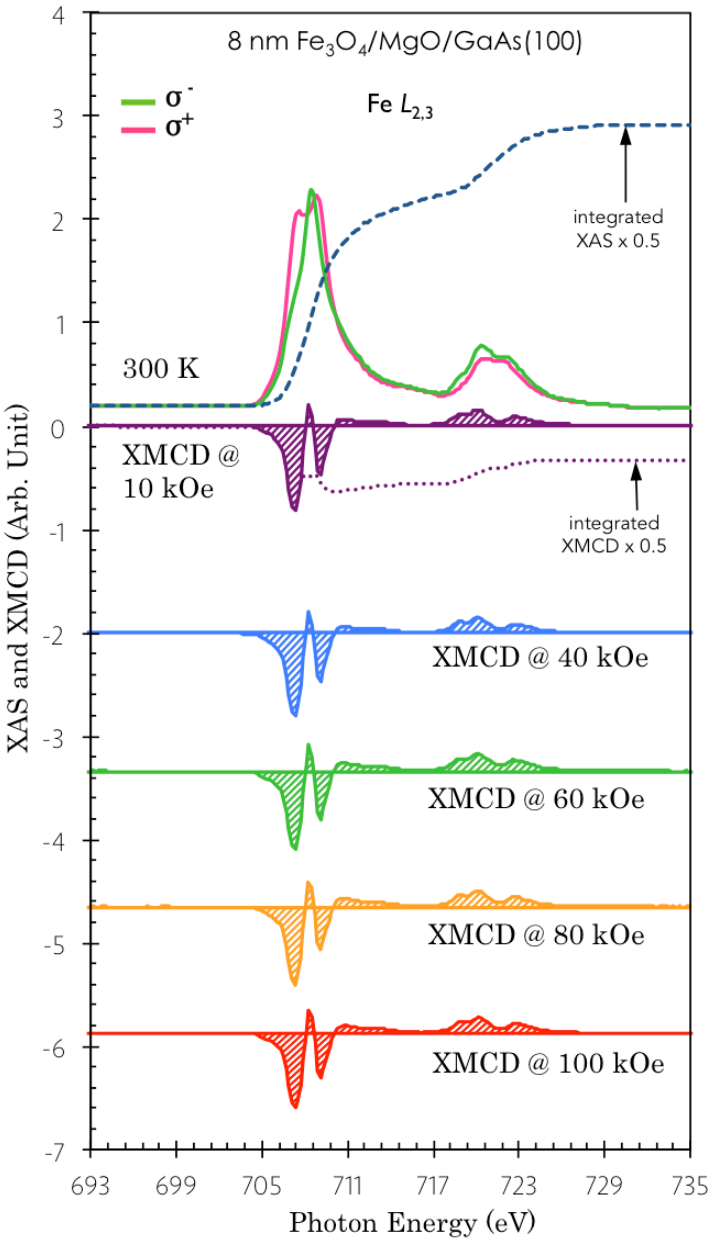


Figure 5-5 | Typical pair of XAS and XMCD spectra of the 8 nm $Fe_3O_4$/MgO/GaAs(100) at the Fe $L_{2,3}$ edges at RT and perpendicular magnetic fields of 10 - 100 kOe.

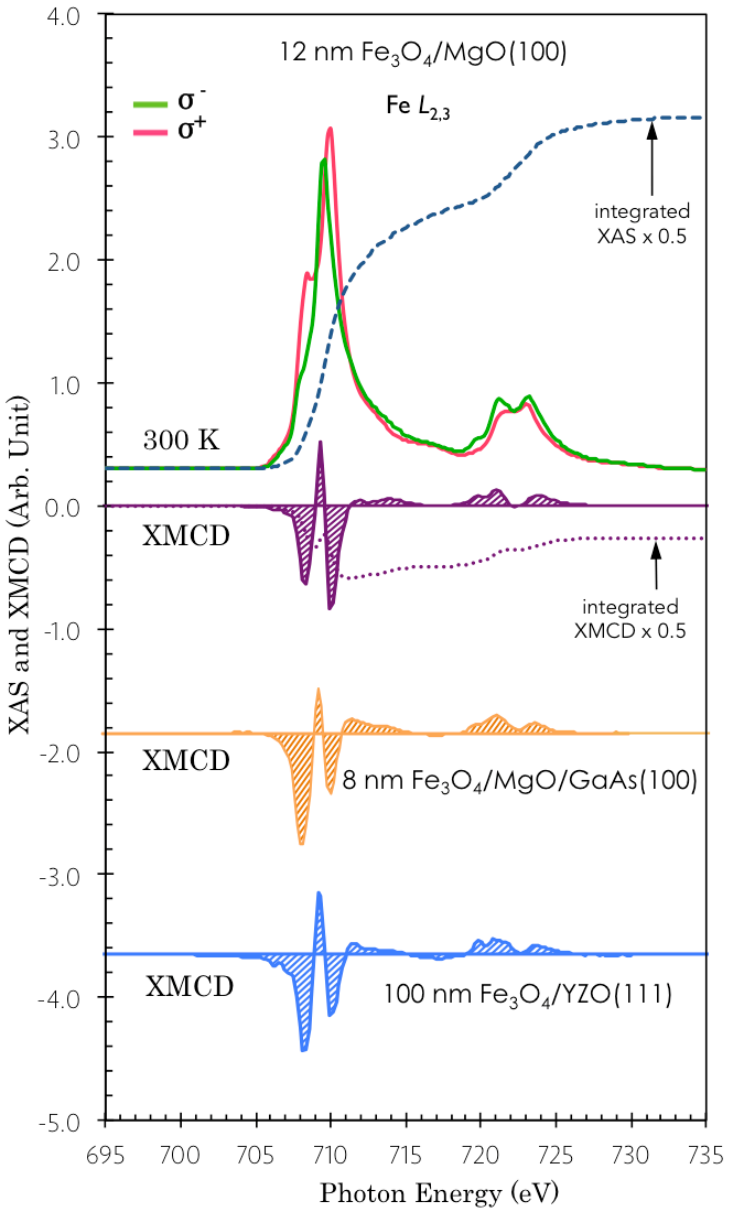


Figure 5-6 | Typical pair of XAS and XMCD spectra of the 12 nm $Fe_3O_4$/MgO(100) at the Fe $L_{2,3}$ edge at RT. The XMCD spectra of the 8 nm $Fe_3O_4$/MgO/GaAs(100) and that of the 100 nm $Fe_3O_4$/YZO(111) were attached to the lower rows for comparison purpose.

#### *5.2.4.1 The line shape and the sample stoichiometry*

The distinct line shapes of the XMCD spectra of the three magnetite samples have motivated a furthermore examination of the phase purity. With the nature of the film

being highly dependent on the thickness, the partial pressure during oxidation, and the temperature, there exists a chance that the films could contain secondary phases other than pure $Fe_3O_4$. The maghemite, i.e. $\gamma$ - $Fe_2O_3$, has the same inverse spinel structure as that of $Fe_3O_4$, except that the B site of the former are all occupied by $Fe^{3+}$. This form of iron oxide exhibits a lattice constant (8.352 Å) very close to that of magnetite (8.396 Å), posing particular difficulties in distinguishing them from the RHEED patterns. Fortunately, $\gamma$ -$Fe_2O_3$ can be diagnosed from the XAS.[261, 262] Although the line shape of $\gamma$ -$Fe_2O_3$ appears similar with that of $Fe_3O_4$, the relative sizes of the three contributions, namely the B sites $Fe^{3+}$ and $Fe^{2+}$ spin-up states and the A sites $Fe^{3+}$ spin-down states, is quite different resulting in an exaggerated volume to the second and third features of the $L_3$ and $L_2$ peaks of Fe. The key features to note are the position of the Fe shoulder on the $L_3$ peak and most importantly the relative intensity of the split contributions of the $L_2$ peak. In $\gamma$ -$Fe_2O_3$, the shoulder on the $L_3$ peak is approximately 1/2 of the intensity of the main peak while in $Fe_3O_4$, this ratio is close to 2/3. Also, the two split contributions of the $L_2$ peak are skewed such that the second is of lower intensity than the first in $\gamma$ -$Fe_2O_3$, whilst in $Fe_3O_4$, the first feature is the lower contribution.

The XAS spectra of all the three magnetite samples, namely, the 8 nm $Fe_3O_4$/MgO/GaAs(100) (green), the 12 nm $Fe_3O_4$/MgO(100) (blue), and 100 nm $Fe_3O_4$/YZO(111) (red), respectively, are gathered in Figure 5-7. It can be seen that the line shape of both the 8 nm $Fe_3O_4$/MgO/GaAs(100) and the 100 nm $Fe_3O_4$/YZO(111) is in good agreement with that described by the $Fe_3O_4$ structure reported by Kim *et al.*,[261] in which the Fe contribution of the $L_3$ is around 2/3 of the magnitude of the oxide peak and the second feature of the $L_2$ peak is lower than the first. By contrast, the line shape of the 12 nm $Fe_3O_4$/MgO(100) reveals a tendency to follow that of the $\gamma$-$Fe_2O_3$ described by Brice-Profeta *et al.*,[262] in which the Fe contribution to the $L_3$ peak reaches only around 1/2 of the magnitude of the oxide spectra and the second feature of the $L_2$ peak is slightly higher than the first one. In the XAS of the 12 nm $Fe_3O_4$/MgO(100) sample, given that the shoulder on the $L_3$ peak is approximately 0.55 of the intensity of the main peak and the two split contributions are almost identical, we concluded that this sample contain a mixture of $\gamma$-$Fe_2O_3$ and $Fe_3O_4$.

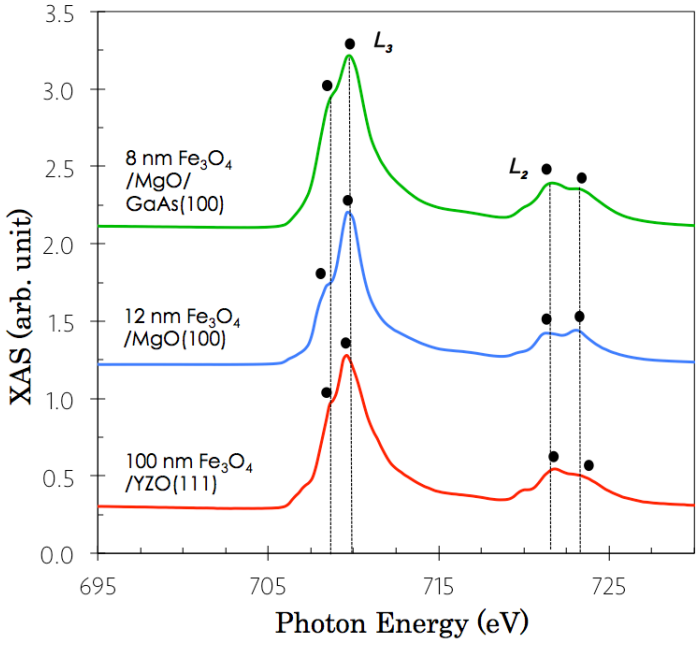


Figure 5-7 | The XAS spectra of the three magnetite samples, namely, the 8 nm $Fe_3O_4$/MgO/GaAs(100) (green), the 12 nm $Fe_3O_4$/MgO(100) (blue), and the 100 nm $Fe_3O_4$/YZO(111) (red), respectively. The line shape of both the 8 nm $Fe_3O_4$/MgO/GaAs(100) and the 100 nm $Fe_3O_4$/YZO(111) is in good agreement with that of pure $Fe_3O_4$, in which the Fe contribution of the $L_3$ is around 2/3 of the magnitude of the oxide peak and the second feature of the $L_2$ peak is lower than the first. By contrast, the line shape of the 12 nm $Fe_3O_4$/MgO(100) reveals a tendency to follow that of the $\gamma$-$Fe_2O_3$, in which the Fe contribution to the $L_3$ peak reaches only around 1/2 of the magnitude of the oxide spectra and the second feature of the $L_2$ peak is slightly higher than the first feature. The black dots indicate the split contributions of the $L_{2,3}$ peaks.

#### *5.2.4.2 The magnetic moment calculations*

The $m_{spin}$ and $m_{orb}$ were calculated by applying the sum rules on the integrated XMCD and summed XAS spectra of Fe $L_{2,3}$ edges using the method described in Chapter III and the $n_h$ was taken as 13.5 per formula unit (f.u.) for $Fe_3O_4$.[267] In order to rule out non-magnetic parts of the XAS spectra, an arctangent based step function is used to fit the threshold. As can be seen from Figure 5-5 and Figure 5-6, unlike an infinite 'long tail' reported by Goering *et al.*,[263] the integrated spectra of both XMCD and summed XAS (see the dash lines) of the three magnetite samples become flat at ~ 728 eV, suggesting

a proper background removal. Calculations give $m_{spin}$ = (2.84 ± 0.1) $\mu_B$/*f.u*. and $m_{orb}$ = (0.47 ± 0.05) $\mu_B$/f.u. for the 8 nm $Fe_3O_4$/MgO/GaAs(100), $m_{spin}$ = (2.19 ± 0.1) $\mu_B$/f.u. and $m_{orb}$ = (0.54 ± 0.05) $\mu_B$/*f.u*. for the 12 nm $Fe_3O_4$/MgO(100), and $m_{spin}$ = (2.12 ± 0.1) $\mu_B$/f.u. and $m_{orb}$ = (0.40 ± 0.05) $\mu_B$/*f.u*. for 100 nm $Fe_3O_4$/YZO(111). These sum-rules derived $m_{orb}$ and $m_{spin}$ of the magnetite samples of this study and those from previous reports (noted that all the values given here are the average information over the three Fe ions) are gathered in Table 5-1.

| Sample | Method | $m_{orb}$ ($\mu_B$/f.u.) | $m_{spin}$ ($\mu_B$/f.u.) | $m_{total}$ ($\mu_B$/f.u.) | $m_{orb}/m_{spin}$ | Ref. |
|---|---|---|---|---|---|---|
| 8nm $Fe_3O_4$/MgO/GaAs(100) | XMCD | 0.47±0.05 | 2.84±0.1 | 3.32±0.15 | 0.17 | * |
| 12 nm $Fe_3O_4$/MgO(100) | XMCD | 0.54±0.05 | 2.19±0.1 | 2.73±0.15 | 0.25 | * |
| 100 nm $Fe_3O_4$/YZO(111) | XMCD | 0.40±0.05 | 2.12±0.1 | 2.52±0.15 | 0.19 | * |
| 5 nm $Fe_3O_4$/MgO(001) | SQUID | | | 7.7 | | 255 |
| 8 nm $Fe_3O_4$/MgO(001) | XMCD | | | 1.83 | <0.05 | 274 |
| 2.5 nm $Fe_3O_4$/$BaTiO_3$(001) | XMCD | 0.44±0.05 | 1.20±0.05 | 1.64 | 0.37 | 269 |
| single crystal $Fe_3O_4$ | XMCD | 0.65±0.07 | 3.68±0.09 | 4.33±0.09 | 0.18 | 267 |
| single crystal $Fe_3O_4$ | MCS | 0.51±0.05 | 3.54±0.05 | 4.05±0.05 | 0.14 | 270 |
| single crystal $Fe_3O_4$ | XMCD | –0.001 | 3.90±0.09 | 4.2±0.09 | -0.00026 | 263 |
| single crystal $Fe_3O_4$ | XMCD | <0.03±0.02 | 1.7±0.02 | <1.73±0.02 | <0.0018 | 275 |
| single crystal | MCS | 0.06±0.14 | 4.08±0.03 | 4.14±0.14 | 0.03 | 271 |
| Theory | LDA | 0.06 | 4.0 | 4.06 | 0.015 | 267 |
| Theory | LDA+U | 0.43 | 4.0 | 4.43 | 0.108 | 267 |
| Theory | LSDA+U | 0.02 | 3.7 | 3.72 | 0.005 | 264 |

Table 5-1 | The sum-rules derived $m_{orb}$ and $m_{spin}$ of all the magnetite samples of this study (marked with *) and those from previous reports (noted that all the values given here are the average information over the three Fe ions).

A possible artifact of the experimental set up and data analysis of XMCD of magnetite were discussed in details by Goering *et al*..[263] In general, the nonmagnetic part of the raw data is smaller than 1/1000 of the total absorption. The saturation effect in our case is estimated to be < 3% given the normal incidence experimental geometry. Besides, the magnetic dipole term $<T_z>$ plays a rather insignificant role because of the predominantly cubic symmetry of magnetite, even under a scenario of additional

surface symmetry breaking. Furthermore, the good agreement of the $m_{total}$ obtained from SQUID-VSM measurement with that calculated from XMCD is an additional proof of the proper application of the sum rules in this study.

### 5.2.5 Discussions

#### *5.2.5.1 The incomplete quenching of $m_{orb}$*

The unquenched $m_{orb}$ implies strong SOC (or $<LS>$), which is a desired property in terms of the controllability of the magnetization reversal by the electric field,[265] which, however, has been reported with controversy in magnetite. The classic ionic charge ordering model of bulk magnetite with a fully A site $3^+$ and a mixed-valent B site (see Chapter II) suggests that magnetite processes a $m_{spin}$ of 4.0 $\mu_B$/f.u. and nearly vanished $m_{orb}$. By performing inelastic neutron scattering measurement, McQueeney *et al.*[266] obtained a high $<LS>$ of magnetite of the order of 10 meV, pointing to a large $m_{orb}$ to expect. The XMCD performed by Huang *et al.*[267] gives a large unquenched $m_{orb}$, typically 0.67 $\mu_B$/f.u. along with a $m_{spin}$ of 3.68 $\mu_B$/f.u. at the temperature both above and below Verwey transition. These results are consistent with the $m_{spin}$ and $m_{orb}$ that are calculated using the LDA + U scheme.[267] The large $m_{orb}$ has been attributed to a strong on-site Coulomb interaction and corresponding 3*d* correlation effects. Similarly, sizable $m_{orb}$ was also observed by Kang *et al.*[268] in Mn substitution at the A site, which changes the valence of the B-site Fe and by Babu *et al.*[269] in ultrathin $Fe_3O_4$ on $BaTiO_3$(001).

By sharp contrast, the XMCD performed by Goering *et al.*[263] suggests that there is in fact a vanishingly small $m_{orb}$ on the Fe sites. To avoid the systematic errors arises from the XMCD data analysis, MCS measurements were performed,[270, 271] which again end in controversial results. Non-integral $m_{spin}$ = 3.54 $\mu_B$/f.u. and correspondingly $m_{orb}$ = 0.51 $\mu_B$/f.u. were observed by Li *et al.*[270] while Duffy *et al.*[271] reported again nearly vanished $m_{orb}$. Goering *et al.*[256] has recently tried to explain the large variety of published results by the independent analysis of the Fe $L_{2,3}$ edge XAS, by moment analysis fit of the Fe $L_{2,3}$ edge XMCD, and by looking into the O K edge XMCD. In consistent with Goering's, our data also exhibit an intensity ratio $r_{23} \sim 0.25$, strongly reduced from a pure statistical case where $r_{23} = 0.5$. This is a clear indication for the presence of large $m_{orb}$ in the magnetite thin films presented in this study.

As can be seen from Table 5-1, despite of the controversial reports on various forms of magnetite, this study (the first three rows of the table) confirms the existence of a significantly unquenched $m_{orb}$ and with significant $m_{orb}/m_{spin}$ ratio, i.e. 0.17 for the 8 nm $Fe_3O_4$/MgO/GaAs(100), 0.25 for the 12 nm $Fe_3O_4$/MgO(100), and 0.19 for the 100 nm $Fe_3O_4$/YZO(111), respectively. The unquenched $m_{orb}$ could partially originate from the broken symmetry of the crystal lattice and consequently strong delocalization of the *3d* electrons, which can universally occur in magnetic films in ultrathin regime (see the discussions of Chapter IV). However, since such phenomenon has been observed in all the three magnetite samples with distinct thicknesses, substrates, and stoichiometry, our results strongly suggest that such significantly unquenched $m_{orb}$ is more likely to be an intrinsic property of magnetite, rather than predominated by the dimensionality effect.

#### *5.2.5.2 The deviation of $m_{spin}$*

Among the three magnetite samples studied, the 8nm $Fe_3O_4$/MgO/GaAs(100) shows the largest $m_{total}$, i.e. ~87% of the principle bulk saturation value. The deviation of magnetic moments of epitaxial thin films from the bulk value is usually attributed to three forms of missing compensation or symmetry breaking. The first one is the formation of antiphase boundaries (APBs) raised from the epitaxy growth process due to the fact that $Fe_3O_4$ has twice the unit-cell size of MgO.[272, 273] In magnetite thin films, the magnetic interactions are altered at the APBs, across which the intrasublattice exchange interactions dominate, reversing the spin coupling. Therefore, the structural boundary separates oppositely magnetized regions and the resultant coupling between two domains turns out to be either frustrated or antiferromagnetic. To exclude the presence of APBs, we repeated the experiment at enhanced magnetic fields up to 120 kOe, since such antiferromagnetic exchange interactions usually lead to saturation fields as large as 70 kOe.[272] As presented in Figure 5-8, a rather consistent value of $m_{spin}$ and $m_{orb}$ have been extracted from 40 to 120 kOe within the error bar, which rules out the presence of any appreciable APBs, while the value of $m_{spin}$ obtained at 10 kOe is slightly smaller because of unsaturation as expected (see Figure 5-2, based on the M-H measurement, the 8nm $Fe_3O_4$/MgO/GaAs(100) sample saturation at ~30 kOe out of plane).

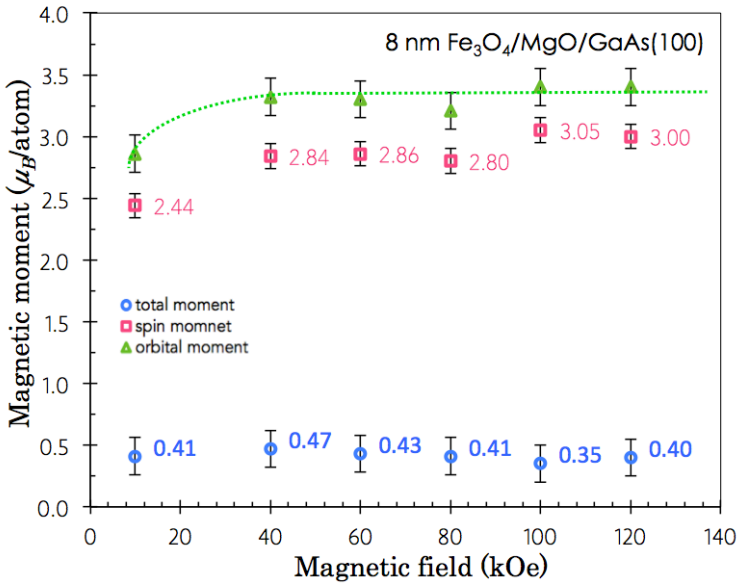


Figure 5-8 | The sum-rules derived magnetic moments of the 8 nm $Fe_3O_4$/MgO/GaAs(100) sample under an applied magnetic filed from 10 to 120 kOe. A rather consistent value of $m_{spin}$, $m_{orb}$, *and* $m_{total}$ have been extracted at saturation from 40 to 120 kOe within the error bar, which rules out the presence of any appreciable APBs, while the value of $m_{spin}$ obtained at 10 kOe is slightly smaller because of unsaturation as expected

The second mechanism of non-compensation occurs due to the less cubic symmetry of magnetite at the surface and the interface of $Fe_3O_4$/MgO. Among the very few works performed on $Fe_3O_4$ thin films, Orna *et al.*[274] reported significantly shrinking $m_{spin}$ = 1.83 $\mu_B$/f.u.in the 8 nm $Fe_3O_4$/MgO, as well as that observed by Babu *et al.*[269] is only (1.20 ± 0.05) $\mu_B$/f.u. in the 2.5 nm $Fe_3O_4/BaTiO_3$. Even in the bulk, strongly reduced $m_{spin}$ of $Fe_3O_4$ was also observed by Goering *et al.*[275] down to (1.73 ± 0.02) $\mu_B$/f.u.. By contrast again, large $m_{spin}$ of 7.7 $\mu_B$/f.u in $Fe_3O_4$ (5 nm)/MgO was reported by Arora *et al.*,[255] who attributed the enhancement to the uncompensated spin between A and B sublattices at the surface and across the APBs. However, as argued by Orna *et al.*,[274] such enhancement may also come from the magnetic impurities.

The inter-diffusion of $Mg^{2+}$ ions, which tends to substitute onto B-sites, is the third possibility. Although the first two film samples measured in this study were both grown at a moderate growth temperature (< 700 K), one may still predict an appreciable inter-diffusion given the *ex situ* measurements presented here were not carried out

immediately after the growth. However, if any, such substitution would only happen at the first 1-2 atom layers at the $Fe_3O_4$/MgO interface. Therefore the numeric results presented in this study can be more representative for a $Fe_3O_4$ epitaxial thin film on MgO/GaAs with consistent stoichiometry. Nevertheless, the bulk-like $m_{spin}$ of the 8nm $Fe_3O_4$/MgO/GaAs(100) observed by us supports that the post-growth annealing synthesis technique can give excellent stoichiometric magnetite ultrathin films and effectively prevent the formation of APBs and the interdiffusion of $Mg^{2+}$ ions. On the contrary, the significantly reduced $m_{spin}$ of the 12 nm $Fe_3O_4$/MgO(100) may be due to the formation of the secondary phase, originated from the plasma-assist oxidization process.

## 5.3 The magnetic moment of magnetite across $T_v$

### 5.3.1 Introduction

A first indication of the Verwey transition in magnetite was obtained as early as 1913 by the measurement of the initial susceptibility on a synthetic magnetite polycrystal by Renger, who detected an additional anomalous transition peak at ~130 K in addition to the then already well-known ferrimagnetic to paramagnetic order transition at 848 K of magnetite. Later on, these initial results were supplemented by the investigations of Weiss and Forrer on the saturation magnetization of magnetite which they found to also undergo an anomalous spontaneous jump near ~120 K and as a function of the magnetic field, this effect adds anomaly to the magnetic moment of magnetite. The magnetization studies were then continued and qualitatively confirmed by Li and Okamura on natural single crystals, characterized by a rather low transition temperature of about ~113 K. Extended investigations during the early years revealed that the observed variations of magnetic properties at $T_v$ are only part of a fundamental transformation process in $Fe_3O_4$, giving rise to similar anomalies on a variety of other inter-related system parameters, such as specific heat, specific resistivity, and thermal expansion along selected directions (see chapter II). Most of these effects are still hotly debated over to the present day (see the topical review articles by Walz).[116, 276]

Generically Verwey transition is treated as a rearrangement of the charge ordering of $Fe^{2+}$ and $Fe^{3+}$ states of the B sites, accompanied by the transition to a low symmetry structure, or with an electron localization-delocalization transition, across which, the $m_{total}$ and especially $m_{orb}$ are expected to change significantly. The experimental work,[255] however, has so far found no difference of them across the Verwey transition, which could question the picture of a fully A site $Fe^{3+}$ and a mixed-valence B site configuration of magnetite. In the remainder of this section, a study of the temperature dependence of the magnetic moments will be presented, based on the three magnetite samples as used in the last section. Taking advantage of the powerful site-specificity of XMCD, the relative contributions of the three cations of magnetite will be performed before and after $T_v$, respectively, which offers important information regarding the sub-lattice disorder of Verwey transition.

### 5.3.2 The SQUID-VSM measurements

It is generally accepted that the presence of Verwey transition is sensitive to the stoichiometry and homogeneity of magnetite thin films.[123] The temperature (i.e. $T_V$) at which such a transition occurs has been commonly observed to decrease from ~ 113 K of bulk-like magnetite films down to 85 K and could even disappear with the decreasing thickness.[255,122, 274] Figure 5-9, Figure 5-10, and Figure 5-11, respectively, present the temperature dependences of the magnetization of the 8 nm $Fe_3O_4$/MgO/GaAs(100), the 12 nm $Fe_3O_4$/MgO(100), and the 100 nm $Fe_3O_4$/YZO(111) as introduced in the last section. The magnetization versus temperature (M-T) relations were obtained by cooling the sample from 300 to 4.3 K in zero magnetic field, known as zero field cooling (ZFC), followed by an application of a static magnetic field of 100 Oe in the film plane and recording the magnetization values during the warming cycle to 300 K.

The sharpest magnetization jumps among the three magnetite sample was observed from the M-H curve of the 100 nm $Fe_3O_4$/YZO(111) at ~ 125 K (see Figure 5-11), corresponding to its $T_v$. The Verwey transition occurring in the ultrathin film samples, by contrast, is weakened but still distinguishable from the gradient of the magnetization, i.e. dM/dT (see the lower rows of Figure 5-9 and Figure 5-10), namely, at ~ 99 K for the 8 nm $Fe_3O_4$/MgO/GaAs(100) and at ~ 97 K for the 12 nm $Fe_3O_4$/MgO(100), respectively. The observed M-H relation and its gradient of the 8 nm $Fe_3O_4$/MgO/GaAs(100) are highly consistent with those reported of the magnetite films on or near stoichiometry,[255] whilst the 12 nm $Fe_3O_4$/MgO(100) shows a mixture of the $Fe_3O_4$ and $\gamma$-$Fe_2O_3$ M-H variation,[277, 278] as it was also suggested by its XAS line shape as discussed in the last section.

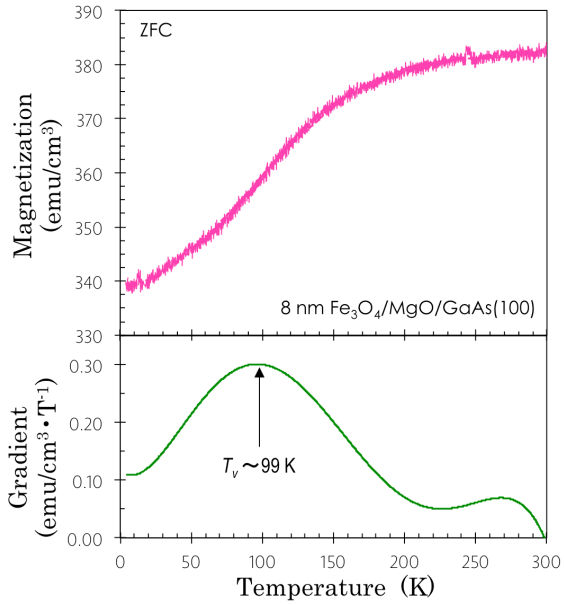


Figure 5-9 | The M-T relations of the 8 nm $Fe_3O_4$/MgO/GaAs(100). Upper row: the M-T curve obtained by cooling the sample from 300 to 4.3 K in zero magnetic field, followed by an application of a static magnetic field of 100 Oe in the film plane and recording the magnetization values during the warming cycle to 300 K. Lower row: the gradient of the magnetization, i.e. dM/dT, from which $T_v \sim 97$ K was extracted.

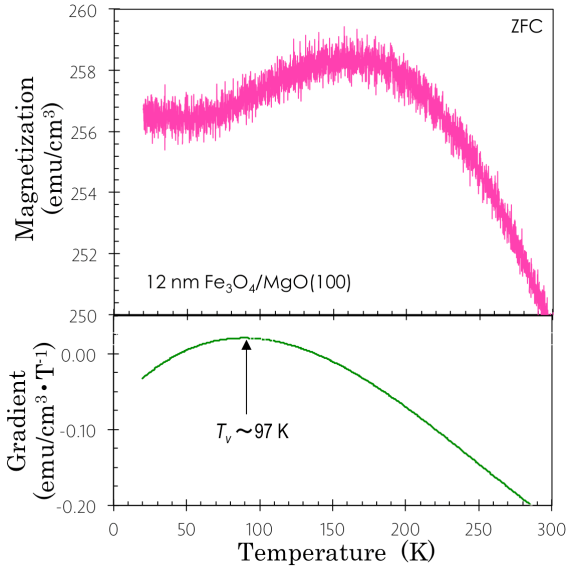


Figure 5-10 | The M-T relations of the 12 nm $Fe_3O_4$/MgO(100). Upper row: the M-T curve obtained by cooling the sample from 300 to 20 K in zero magnetic field, followed by an application of a static magnetic field of 100 Oe in the film plane and recording the magnetization values during the warming cycle to 300 K. Lower row: the gradient of the magnetization, i.e. dM/dT, from which $T_v \sim 97$ K was extracted.

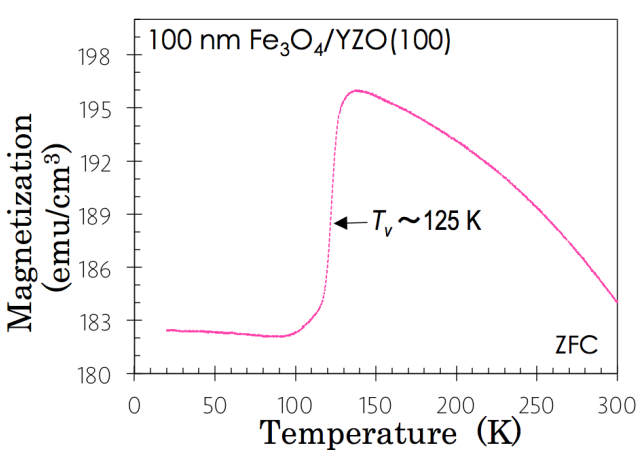


Figure 5-11 | The magnetization versus temperature relationships of the 100 nm $Fe_3O_4$/YZO(111), obtained by cooling the sample in ZFC, followed by an application of a static magnetic field of 100 Oe in the film plane and recording the magnetization values during the warming cycle to 300 K, from which $T_v \sim 125$ K was extracted.

### 5.3.3 The XMCD measurements

Using the same experimental set up as described in the last section, the XAS and XMCD of the three magnetite samples were furthermore performed at variable temperatures, and their magnetic moments were calculated by applying the sum rules. Figure 5-12 presents the derived $m_{spin}$, $m_{orb}$, and $m_{total}$ of the 8 nm $Fe_3O_4$/MgO/GaAs(100) (top row), the 12 nm $Fe_3O_4$/MgO(100) (middle row), the 100 nm $Fe_3O_4$/YZO(111) (bottom row), respectively, as a function of the temperature, Viewing them in parallel with the magnetization obtained from the SQUID measurement, where a clear Verwey transition presents in the M-T variation, i.e. in the 8 nm $Fe_3O_4$/MgO/GaAs(100) and the 100 nm $Fe_3O_4$/YZO(111), an anomalous increase appears in the sum-rules derived $m_{total}$, and particularly, in $m_{orb}$. The $m_{total}$ of the 8 nm $Fe_3O_4$/MgO/GaAs(100) shows an ~ 4.3% jump at $T_v \sim 99$ K and that of the 100 nm $Fe_3O_4$/YZO(111) is as large as ~ 15% at $T_v \sim$ 125 K. Accompanied with the spontaneous jumps of $m_{total}$, $m_{orb}$ increases from (0.26 ± 0.05) $\mu_B$/f.u. at 90 K to (0.53 ± 0.05) $\mu_B$/f.u. at 130 K and from (0.27± 0.05) $\mu_B$/f.u. at 120 K to (0.46± 0.05) $\mu_B$/f.u. at 150 K for the 8 nm $Fe_3O_4$/MgO/GaAs(100) and the 100 nm $Fe_3O_4$/YZO(111), respectively. Unlike the these two sample, the 12 nm

$Fe_3O_4$/MgO(100) shows no remarkable signature of discontinuous changes of the sum-rules derived $m_{total}$ within the experimental accuracy, which can be attributed to the existence of the secondary phase, i.e. $\gamma$ - $Fe_2O_3$, as discussed in the last section. Figure 5-13 presents the overlapped XMCD spectra of the 8 nm $Fe_3O_4$/MgO/GaAs(100) (top row), the 12 nm $Fe_3O_4$/MgO(100) (middle row), and the 100 nm $Fe_3O_4$/YZO(111) (bottom row), respectively, across the $T_v$ for each of them, obtained under 30 kOe perpendicular magnetization. Each peak in the $L_3$ XMCD corresponds primarily to a different site in the $Fe_3O_4$, i.e. the first negative peak to $d^6O_h$ (i.e. B sites $Fe^{2+}$), the second positive peak to $d^5O_h$ (i.e. B sites $Fe^{3+}$), and the third negative peak to $d^5T_d$ (i.e. A sites $Fe^{3+}$), whose relative intensity are quantities proportional to the local magnetization of the different cations.

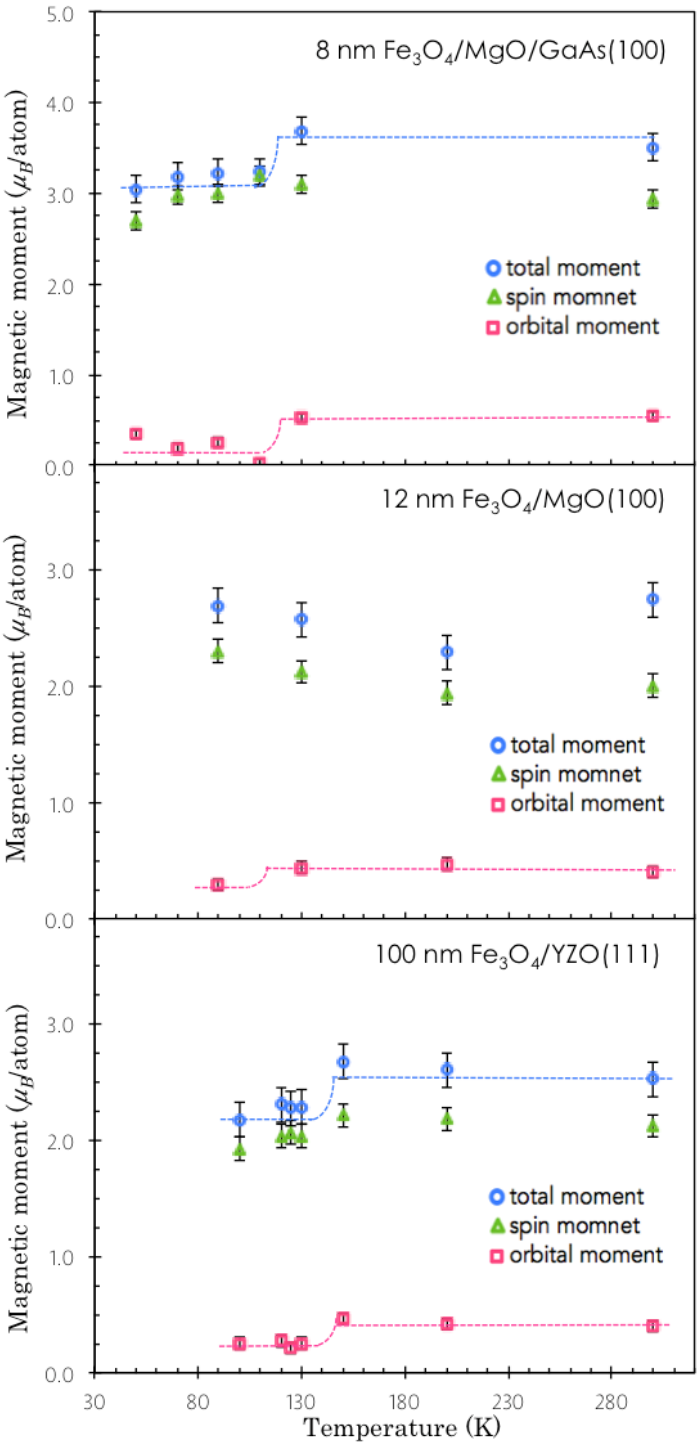


Figure 5-12 | The sum-rules derived $m_{spin}$, $m_{orb}$, and $m_{total}$ of the 8 nm $Fe_3O_4$/MgO/GaAs(100) (top row), the 12 nm $Fe_3O_4$/MgO(100) (middle row), and the 100 nm $Fe_3O_4$/YZO(111) (bottom row), respectively, at temperatures across the $T_v$ for each of them. The dash lines are guides for the eye.

In order to determine the relative magnetic contributions of the Fe cations at A and B sites in $Fe_3O_4$, the ratios of the three peak intensities of the XMCD spectra at the Fe $L_3$ edge were calculated and plotted in Figure 5-14, respectively, for the 8 nm $Fe_3O_4$/MgO/GaAs(100) (top row), the 12 nm $Fe_3O_4$/MgO(100) (middle row), and the 100 nm $Fe_3O_4$/YZO(111) (bottom row). It was found that for all the three magnetite samples, the $d^6O_h/d^5O_h$ remains consistent before and after Verwey transition, suggesting that the relative spin ordering of the B sites $Fe^{2+}$ and $Fe^{3+}$ stays still across $T_v$. For the 8 nm $Fe_3O_4$/MgO/GaAs(100) and the 100 nm $Fe_3O_4$/YZO(111), where a clear Verwey transition presents in the macroscopic magnetization, both the $d^6O_h/d^5T_d$ and $d^5O_h/d^5T_d$ show anomalous jumps at $T_v$, whilst for the 12 nm $Fe_3O_4$/MgO(100), who shows no pronounced Verwey transition, the value of these ratios show little change within the experimental accuracy. The average ratios before and after $T_v$, respectively, of these three cation contributions of the Fe $L_3$ peak and those of bulk $Fe_3O_4$ and γ-$Fe_2O_3$ are summarized in Table 5-2.

| sample | $d^6O_h/d^6T_d$ | | $d^5O_h/d^6T_d$ | | $d^6O_h/d^5O_h$ | |
|---|---|---|---|---|---|---|
| | T < $T_v$ | T > $T_v$ | T < $T_v$ | T > $T_v$ | T < $T_v$ | T > $T_v$ |
| 8nm $Fe_3O_4$/MgO/GaAs | -2.07±0.20 | -2.43±0.20 | -1.27±0.15 | -1.37±0.15 | 1.64±0.20 | 1.77±0.20 |
| 12 nm $Fe_3O_4$/MgO | -0.98±0.10 | -1.14±0.10 | -1.40±0.15 | -1.60±0.15 | 0.70±0.10 | 0.71±0.10 |
| 100 nm $Fe_3O_4$/YZO | -1.88±0.20 | -2.51±0.20 | -1.31±0.15 | -1.80±0.15 | 1.44±0.155 | 1.41±0.15 |
| bulk $Fe_3O_4$ [*Ref*. 260] | | 2.75 | | 1.75 | | 1.57 |
| bulk γ- $Fe_2O_3$ [*Ref*. 279] | | 0.70 | | 1.47 | | 0.48 |

Table 5-2 | The averaged ratios of the three cation contributions of the Fe $L_3$ peak $d^6O_h/d^6T_d$, $d^5O_h/d^6T_d$ , and $d^6O_h/d^5O_h$ before and after $T_v$, respectively and those of principally bulk $Fe_3O_4$ and γ- $Fe_2O_3$.

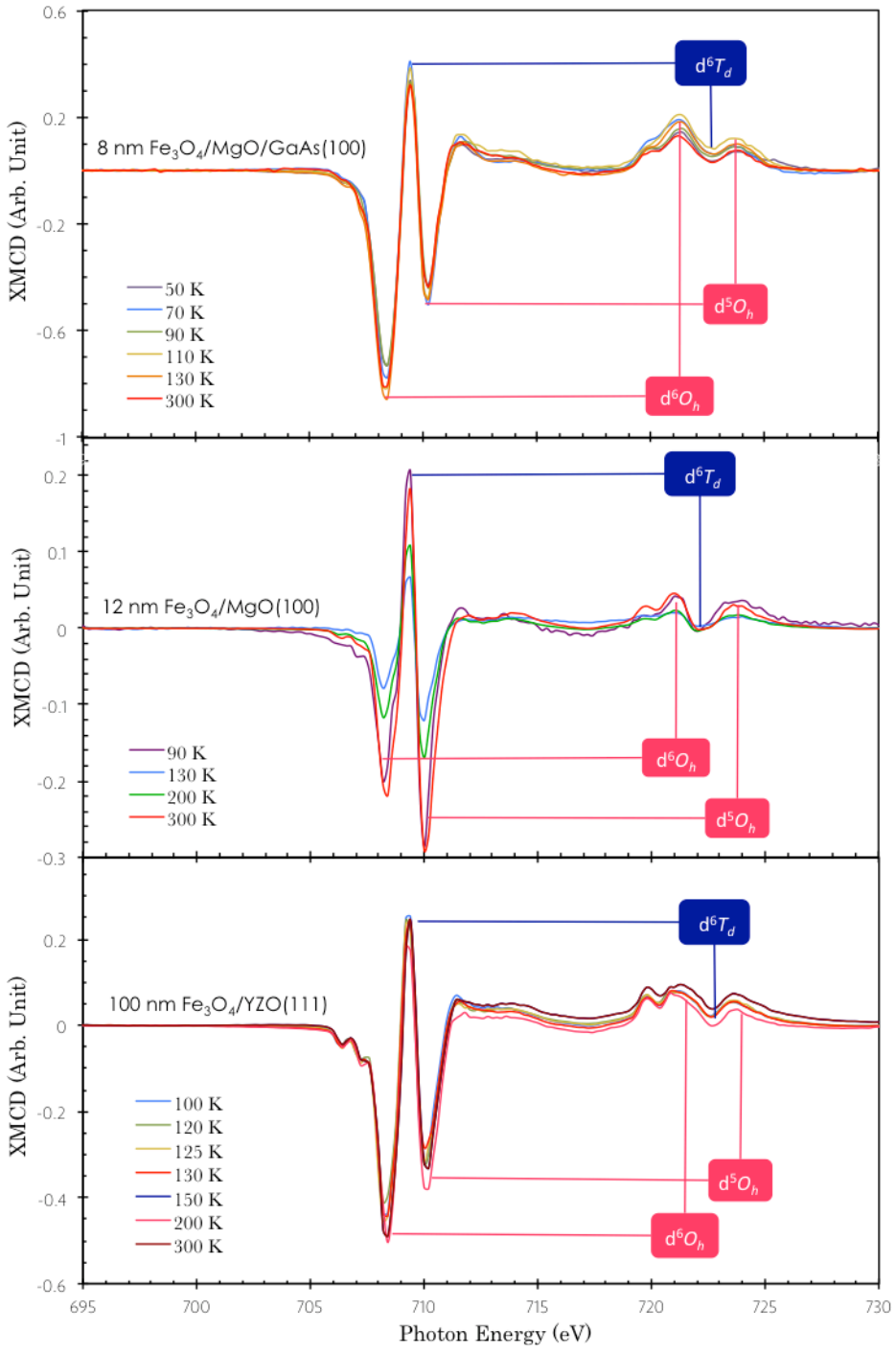


Figure 5-13 | The overlapped XMCD spectrum at various temperatures from 50 K to 300 K of the 8 nm $Fe_3O_4$/MgO/GaAs(100) (top), the 12 nm $Fe_3O_4$/MgO(100) (middle), and the 100 nm $Fe_3O_4$/YZO(111) (bottom), respectively, obtained at 30 kOe. Each peak in the $L_3$ XMCD corresponds primarily to a different site in the $Fe_3O_4$, the first negative peak corresponds to $d^6O_h$ (i.e. B sites $Fe^{2+}$), the second positive peak to $d^5O_h$ (i.e. B sites $Fe^{3+}$), and the final negative peak to $d^5T_d$ (i.e. A sites $Fe^{3+}$), which are utilized to calculate the relative intensity of the contributions from different cations.

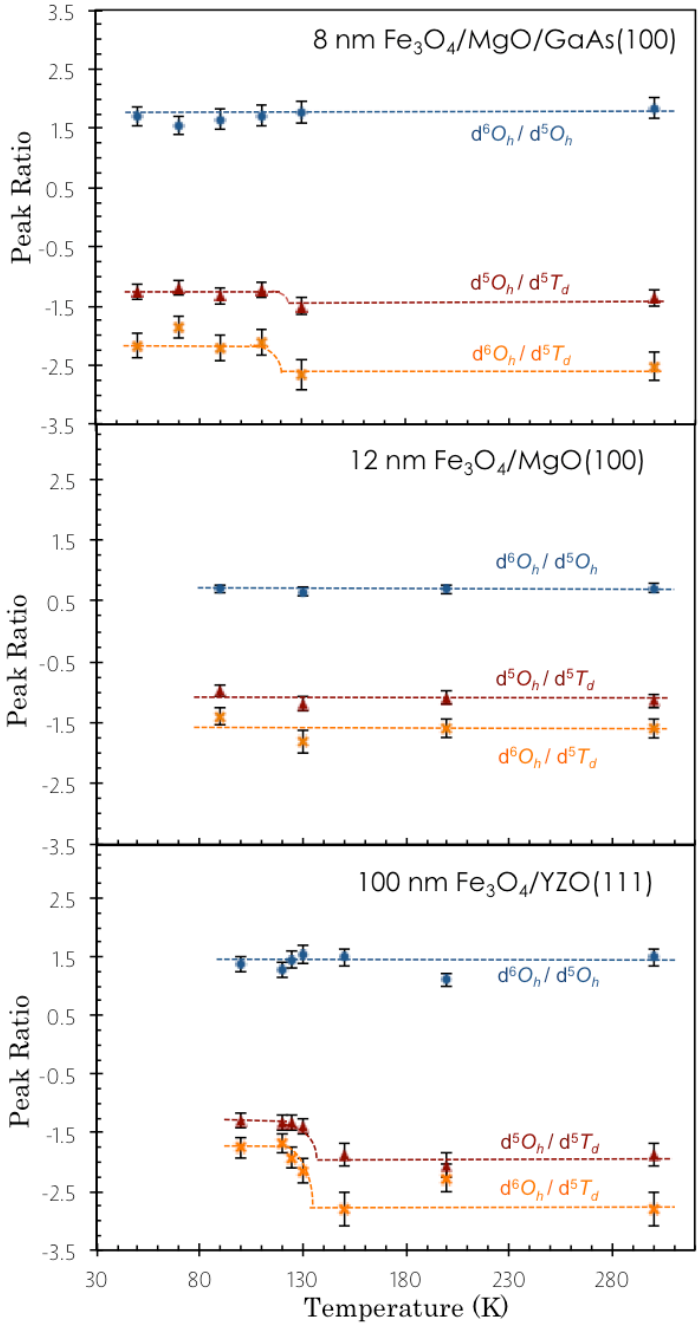


Figure 5-14 | The ratios of the three peak intensities at Fe $L_3$ edge for the 8 nm $Fe_3O_4$/MgO/GaAs(100) (top), the 12 nm $Fe_3O_4$/MgO(100) (middle), and the 100 nm $Fe_3O_4$/YZO(111) (bottom), respectively. For all the three magnetite samples, the $d^6O_h/d^5O_h$ remains consistent before and after Verwey transition. For the 8 nm $Fe_3O_4$/MgO/GaAs(100) and the 100 nm $Fe_3O_4$/YZO(111), both the $d^6O_h/d^5T_d$ and $d^5O_h/d^5T_d$ show anomalous jumps at $T_v$, whilst for the 12 nm $Fe_3O_4$/MgO(100), the value of these ratios show no little change within the experimental accuracy.

### 5.3.4 Discussions

Our observations, in microscopic level, support the recognition that Verwey transition is a very sensitive probe to the stoichiometry and homogeneity of magnetite thin films. Looking back the magnetization variations of the three magnetite systems against temperature, only the 8 nm $Fe_3O_4$/MgO/GaAs(100) and the 100 nm $Fe_3O_4$/YZO(111) show an anomaly spontaneous jump in the M-T curve. The similar discontinues change was also extracted from the XMCD measurements, i.e. the sum-rules derived magnetic moments of the Fe cations. By contrast, neither the macroscopic magnetization nor the XMCD reveals experimental signatures of a pronounced Verwey transition for the 12 nm $Fe_3O_4$/MgO(100). Such absence or suppression of Verwey transition of the later can be attributed to the existence of a secondary phase, i.e. $\gamma$-$Fe_2O_3$, as it was diagnosed from the XAS and XMCD spectra line shapes. In other words, the 12 nm $Fe_3O_4$/MgO(100) sample has been suffering from cation or anion vacancies to a considerable extent, likely due to non-fully optimized preparation process, and becoming non-stoichiometric $Fe_3O_4$. Comparing the XMCD of the 12 nm $Fe_3O_4$/MgO(100) with the atomic multiplet calculations,[158, 159] the distribution of the Fe cations suggests the sample contains ~ 50% $\gamma$ - $Fe_2O_3$ (see Table 5-2, for the 12 nm $Fe_3O_4$/MgO(100), $d^6O_h/d^6T_d$ = -1.14±0.1, $d^5O_h/d^6T_d$ = -1.60±0.15, and $d^6O_h/d^5O_h$ = 0.71±0.1, which are in between of that for $Fe_3O_4$ whose $d^6O_h/d^6T_d$ = -2.75, $d^5O_h/d^6T_d$ = -1.75, and $d^6O_h/d^5O_h$ = 1.57 and that for $\gamma$-$Fe_2O_3$ whose $d^6O_h/d^6T_d$ = -0.70, $d^5O_h/d^6T_d$ = -1.47, and $d^6O_h/d^5O_h$ = 0.48).

Another important information obtained is the discontinuous change of $m_{orb}$ of the two stoichiometric magnetite samples. Such change of $m_{orb}$ is very likely be intrinsic, independent from the sample thickness and preparation techniques, given the fact that it has been unambiguously observed from two distinct magnetite systems, i.e. the 8 nm $Fe_3O_4$/MgO/GaAs(100) and the 100 nm $Fe_3O_4$/YZO(111). The basic fact that the magnetization at a fixed field decreases sharply below $T_v$ as the temperature is lowered has long been interpreted as a result of increased anisotropy below the $T_v$ caused by a transition to the lower symmetry phase, because of which the field was not enough to saturate the crystal. Instead of or in addition to this reason, our observation suggests that Verwey transition can be driven primarily by the magnetic interactions of the sub-lattices as well, given the significantly changed $M_s$ at $T_v$ (~ 4.5% and ~ 17% for the 8 nm $Fe_3O_4$/MgO/GaAs(100) and the 100 nm $Fe_3O_4$/YZO(111), respectively).

On account of the various still unanswered questions of magnetite, up to this day there is still no one comprehensive model which can explain all the experimental observations of magnetite. Most of the theories describe the behavior of magnetite well below $T_v$ but become no longer valid above it, or the vice versa.[116, 276] When it comes to the magnetic interactions between sub-lattices, it is rather more difficult to reconcile the ionic charge ordering model with the proposed magnetic interactions responsible for the magnetic ordering. It is acknowledged that the magnetic ordering in oxide spinels is mainly due to superexchange interactions via the oxygen ions. However, the generally adapted mean-field approximation is a long-range interaction while superexchange interaction is a short-range interaction (nearest neighbor interaction).[280] Bearing that in mind, it is expected that the dynamic disorder of the B sites above $T_v$ should change the effective interactions and, consequently, a sizable change must be observed in the magnetic properties at the Verwey transition.

Although global magnetization measurements have been intensively performed within this context, to our best knowledge, respective demonstrations of the $m_{\mathrm{spin}}$ and $m_{\mathrm{orb}}$ of magnetite on or near stoichiometry in a thin film regime remains scarce. From our observations, the relative cation contributions of magnetite, estimated from the three Fe $L_3$ peak ratios of the XMCD spectra (see Figure 5-14) show distinct trends of change, i.e. the absolute values of both $d^6O_h/d^6T_d$ and $d^5O_h/d^6T_d$ jump at $T_v$ while that of $d^6O_h/d^5O_h$ remain unmoved within the error bar. In the ionic charge ordering model of magnetite, $d^6O_h/d^6T_d$ and $d^5O_h/d^6T_d$ can be representative of the B site Fe spin ordering with respect to the A site, associated with the oxygen-assisted SE coupling. Whilst $d^6O_h/d^5O_h$ is an indicator of the bonding between the bivalent and trivalent Fe of the B site, corresponding to the DE mechanism. Although a comprehensive theoretical model in depth is beyond the scope of the present study, our observation unambiguously reveals that the SE mechanism, or the electrons hopping between Fe-O-Fe, is preliminarily responsible for the magnetization Verwey transition of magnetite thin films.

## 5.4 Conclusions

In this chapter, we have presented XMCD studies of three distinct magnetite thin film samples, namely, a 8 nm $Fe_3O_4$/MgO/GaAs(100) prepared by post-growth annealing method, 12 nm $Fe_3O_4$/MgO(100) prepared by plasma-assisted simultaneous oxidation and a 100 nm $Fe_3O_4$/YZO(111) prepared by PLD. The SQUID-VSM was also employed, where applicable, to obtain a global magnetization properties of the samples. The studies of the chapter witness the strong addressability of the XMCD technique as an ideal probe for the fundamental physical quantities, such as the $m_{spin}$ and $m_{orb}$, of the spinel-type ternary oxides, not only because of its unique elemental selectivity, but also the powerful site sensitivity.

We have observed strong dichroic XAS spectra, corresponding to an overlap of different sets of multiplet structures caused by the antiparallel spin orientations of the A and B sites of magnetite. While a secondary phase, i.e. $\gamma$-$Fe_2O_3$, is undistinguishable from the electron diffraction patterns, it can be clearly diagnosed from the line shape of the XAS and XMCD spectra. By carefully applying sum rules, significant unquenched $m_l$ was obtained from all the three systems, namely (0.47 ± 0.05) $\mu_B$/f.u. for the 8 nm $Fe_3O_4$/MgO/GaAs(100), (0.54 ± 0.05) $\mu_B/f.u.$ for the 12 nm $Fe_3O_4$/MgO(100), and (0.40 ± 0.05) $\mu_B/f.u.$ for the 100 nm $Fe_3O_4$/YZO(111). While the unquenched $m_{orb}$ might be an intrinsic property of the bulk $Fe_3O_4$, which is still hotly debated over to this day, our observations could partially originate from the broken symmetry of the crystal lattice and consequently strong delocalization of the *3d* electrons. However, since such phenomenon has been observed in all the three magnetite samples with distinct thicknesses, substrates, and stoichiometry, such nonzero $m_{orb}$ is more likely to be an intrinsic property of magnetite, rather than predominated by the dimensionality effect.

From both the global (SQUID-VSM) and the local (XMCD) magnetic measurement, clear Verwey transition was observed in the 8 nm $Fe_3O_4$/MgO/GaAs(100) and the 100 nm $Fe_3O_4$/YZO(111), i.e. a spontaneous jump of the magnetization of ~ 4.5% at ~ 99 K) for the former and that of ~ 17% at ~ 125 K), whilst no pronounced signature of such was found from the 12 nm $Fe_3O_4$/MgO(100). This is attributed to the samples impurity, supported by the contrast in their XAS and XMCD spectral line shapes and relative peak intensities, which suggests that the 12 nm $Fe_3O_4$/MgO(100) contains ~ 50% $\gamma$- $Fe_2O_3$. Such observation supports the recognition that Verwey transition is a sensitive probe to the stoichiometry and homogeneity of magnetite.

In the two stoichiometric magnetite samples, the spontaneous jump of macroscopic magnetization has been found to mainly originate from $m_{orb}$. By comparing the relative cation contributions of magnetite, the B site Fe spin ordering with respect to the A site was found to change discontinuously whilst the bonding between the bivalent and trivalent Fe of the B site remains consistent before and after Verwey transition. This observation points to the SE mechanism, or the electrons hoping between Fe-O-Fe, is preliminarily responsible for the magnetization Verwey transition of magnetite.

# 6 Chapter VI Magnetically doped TIs

## 6.1 Introduction

3D TIs are insulating bulk materials that carry a conducting surface state, arising from the intrinsically strong SOC in the bulk band structure protected by time-reversal symmetry (TRS). While such unique systems offer nontrivial surface states that can be utilized to perform dissipationless spin transport, it is equally important to break the TRS of TIs to realize novel physical phenomena. The newly discovered quantum anomalous Hall (QAH) effect,[281, 282, 283] the predicted giant magneto-optical Kerr effect[284], magnetic monopole effect,[285] and chiral mode conduction channels[286, 287] are some of the fascinating examples.

Two categories of routes for breaking TRS or introducing ferromagnetic order in TIs have been investigated within the context of spintronics research. One route is to dope the TI host with magnetic ions, similar to that in DMS, by which ferromagnetism has been observed in V-, Cr-, and Mn-doped single crystals of $Sb_2Te_3$,[288, 289, 290] Fe-, and Mn-doped single crystals of $Bi_2Te_3$,[291, 292] and Mn- and Cr-doped thin films of $Bi_2Se_3$,[293, 294, 295] The other route is to engineer layered heterostructures, where the surface states of TIs experience the exchange interaction from an adjacent ferromagnetic material, again following a similar idea from FM/DMS as discussed in chapter 4. This route subsequently can be divided into two ways in terms of ferromagnetic metal (FM) and ferromagnetic insulator (FMI) induction. It can be expected that such an interplay between the topologically nontrivial interface states and magnetism might lead to novel behaviors that are absent in heterostructures composed of conventional semiconductors and magnetic materials.

XMCD has been widely utilized in the determination of the impurity magnetism of DMSs, however, to apply it on obtaining the temperature and field dependence of the magnetic moments in the *3d*-metal-doped TIs took off only very recently.[296, 297, 298, 299] In this chapter, we present XMCD studies of a series of selected magnetically doped TIs, aiming to contribute to some of the key issues of the contemporary TI research. Section 6.2 starts with the investigation of a model magnetically doped TI, i.e. the $Bi_{2-x}Cr_xSe_3$ epitaxial thin film, whose $m_{spin}$ and $m_{orb}$ versus temperature were obtained by carefully

applying the sum rules and interpreted by the first-principals calculation. To enhance the magnetic ordering of $Bi_{2-x}Cr_xSe_3$ and in the meantime, preserve the topological nature, proximity effect was demonstrated in this system using a high-$T_C$ FMI and analyzed with the three-layer model, which forms the core of Section 6.4. Although XMCD is directly addressable to the electrical and magnetic ground states of the magnetic dopants, unambiguity still exists in the interplay of magnetism and the nontrivial surface state of TIs. This question furthermore promotes us to explore the magnetic properties of the Δ-doped $Bi_2Se_3$ as presented in Section 6.4, which distinguishes the role of the surface and the bulk doping in a 3D TI.

## 6.2 The spin and orbital magnetic moment of magnetic TI

### 6.2.1 Introduction

Within the growing family of TIs, ferromagnetism has been reported in V-, Cr-, and Mn-doped single crystals of $Sb_2Te_3$[300, 301] and Fe- and Mn-doped single crystals of $Bi_2Te_3$.[302, 303] Both anti-ferromagnetism[304] and ferromagnetism[305] have been reported in Cr- doped $Bi_2Se_3$, and as for Fe- doped $Bi_2Se_3$ observations are rather controversial. Yao *et al*.[306] studied the effects of magnetic doping of a series of 3d transition metal elements in $Bi_2Se_3$ using first-principles calculations and found that Cr and Fe doping preserves the insulating nature of the host TI in the bulk and Cr-doped $Bi_2Se_3$ is likely to be ferromagnetism. In most conventional DMSs, it has been well acknowledged that the exchange interaction requires the presence of free carriers, typically in concentrations of the order of $10^{19} – 10^{20}$ $cm^{-3}$.[307] However, this range of carrier concentration in TIs may lead to the bulk contribution to the conduction dominating over that from the surface. For the similar reason, a ferromagnetic TI with low bulk conduction is not expected to depend on the same mechanism as DMSs.

In Cr-doped $Bi_2Se_3$, the carrier concentration is expected to be low since Cr substitutes for Bi without adding carriers.[282] In contrast to DMSs, the exchange interaction in such magnetically doped TIs is mediated by band electrons, and in the ultrathin limit it is expected to give rise to the QAHE. Pioneering work (of the provider of the TI samples used in this study) have proved that well-crystallized Cr-doped $Bi_2Se_3$ thin films can be prepared by MBE on Si(111) and that the non-trivial topological surface state is weakened by Cr dopants while the semiconducting behavior is well maintained in the film, as observed from the energy dispersion relations.[295] In the remainder of this section, the spin and orbital ordering of Cr-doped $Bi_2Se_3$, or $Bi_{2-x}Cr_xSe_3$ epitaxial thin films will be studied with XMCD, magneto-transport measurement, and *ab initio* calculations, aiming to obtain a further insight of the mechanism of the ferromagnetism of magnetically doped TIs.

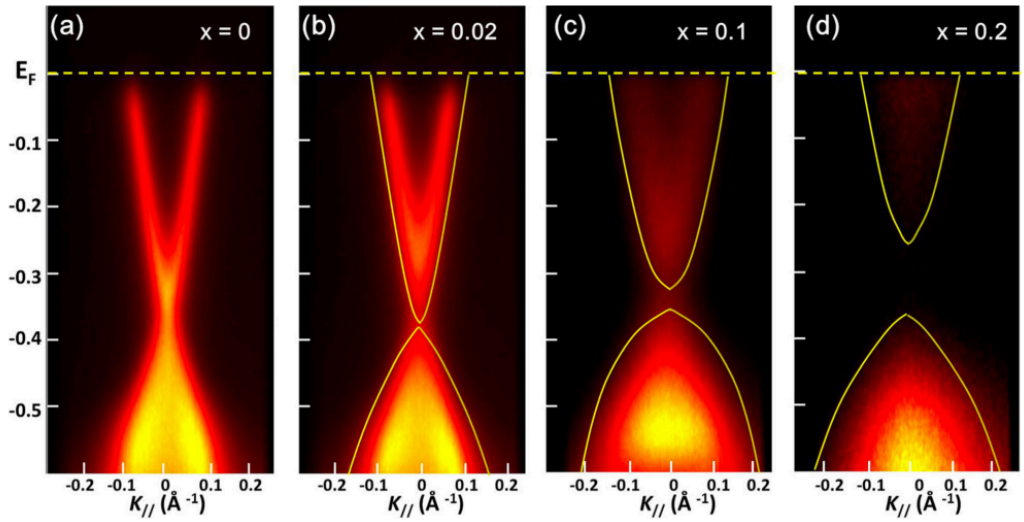


Figure 6-1 | The energy dispersion relations of Cr-doped $Bi_2Se_3$. ARPES intensity maps of 50 QLs $Bi_{2-x}Cr_xSe_3$ thin films with (a) x = 0, (b) x = 0.02, (c) x = 0.1, and (d) x = 0.2 on Si(111) along the $\Gamma$ -K direction. With Cr doping, the surface deviates from the original linear massless Dirac fermion state and becomes broadened. A larger bandgap on the surface is open with higher Cr concentrations, as illustrated by the solid yellow lines. Data were taken using 52 eV photons at a temperature of 10 K. Image adapted from the literature.[295]

### 6.2.2 The sample preparation

The Cr-doped $Bi_2Se_3$ samples used in this study were prepared by the collaborator from the Device Research Laboratory (led by Prof. Kang. L. Wang) of the University of California Los Angeles (UCLA), US. The 10 nm 3% Cr-doped $Bi_2Se_3$ or $Bi_{1.94}Cr_{0.06}Se_3$ epitaxial thin films grown under the Se-rich environment using a Perkin-Elmer MBE system on Si (111) substrate. High-purity Bi (99.9999%) and Cr (99.99%) were evaporated from conventional effusion cells at 470°C, while Se (99.99%) was formed from a cracker cell at 240°C. In addition, the substrate remained at a relatively high substrate temperature (300 °C) to optimize both the surface migration rate and Cr solubility simultaneously. 2 nm Al was then *in-situ* evaporated immediately after the growth of $Bi_{1.89}Cr_{0.11}Se_3$ to protect it from oxidation and environmental doping during transport to the synchrotron facility. The $Bi_{2-x}Cr_xSe_3$ ($0.01 < x < 0.3$) thin films grown by this strategy had been studied with atomic force microscopy (AFM) for the surface

morphology, with high resolution TEM for the crystallinity, with magneto-transport measurement for the global magnetization, and with ARPES for the energy dispersion relations (included in figure 6.1), as can be found from the literatures,[308, 295, 289] which confirm the validity of the samples.

### 6.2.3 The magneto-transport measurements

The magnetic phase of the 10 nm $Bi_{1.94}Cr_{0.06}Se_3$ epitaxial thin film was first examined by the magneto-transport measurements in the Device Research Laboratory of UCLA. The sample was patterned into standard Hall bar devices via photolithography a subsequent $CHF_3$ dry etching for 20 seconds. Six Hall channel contacts (10 nm Ti and 100 nm Au) were defined by e-beam evaporation. Figure 6-2 presents a schematic diagram (upper row) and a typical microscope image of the Hall bar device and the performed four-probes measurement.

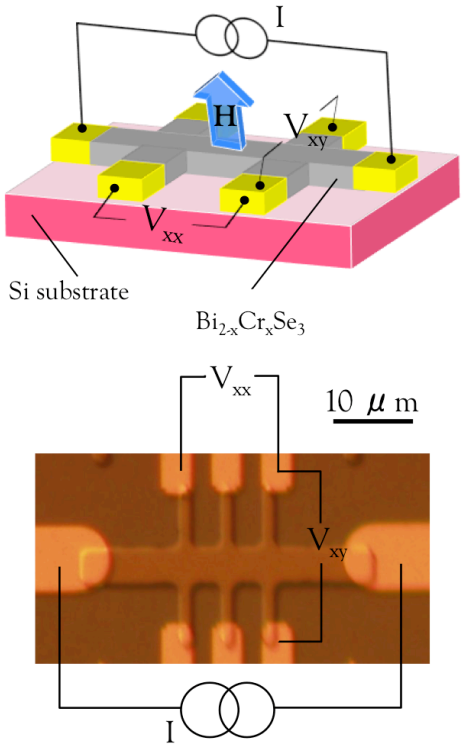


Figure 6-2 | Experimental configuration of the magneto-transport measurement. Upper: schematic diagram of the experimental set up for the transport measurements, where the magnetic field is applied perpendicular to the thin film plane. Lower: typical microscope image of the samples that are patterned into standard Hall bar devices.

The magneto transport measurements were performed using a physical property measurement system (PPMS), from which the resistance anomaly was observed at low temperatures. A constant alternating current (AC) of 0.05 - 0.1 $\mu$A with a frequency of 1300 Hz is fed through two outer contacts, and the voltage drop across the inner pads is measured to determine the resistance. By subtracting the ordinary Hall component, we plotted the anomalous Hall resistance ($R_{AHE} = R_{xy} - R_0 \cdot H$) [309] as a function of field applied perpendicularly to the film in Figure 6-3. Non-zero $R_{AHE}$ was observable up to 30 K and vanished at ~ 40 K and the derived $H_c$ exhibits the typical Curie-like behavior from 3 K to 300 K (see Figure 6-3 inset). The ferromagnetic ordering with $T_C$ of ~30K was observed, which saturates at 2.5 kOe in an out of plane configuration. Since transport measurement is less sensitive to isolated ferromagnetic particles, this magnetic signal was attributed to the entire $Bi_{2-x}Cr_xSe_3$ thin film instead of magnetic clusters, if any.

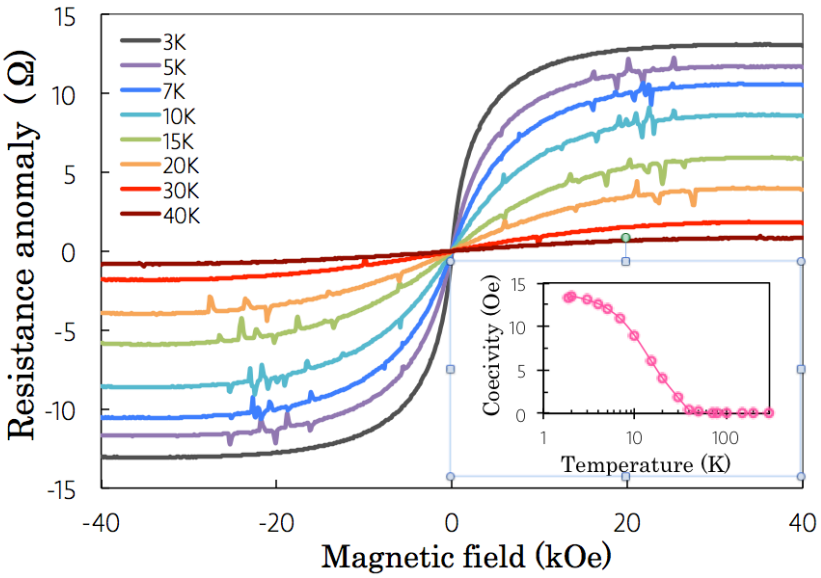


Figure 6-3 | AHE versus magnetic field of the $Bi_{1.94}Cr_{0.06}Se_3$/Si(111) thin film at 3-40 K, by which non-zero $R_{AHE}$ were observed up to 30 K and vanished at ~40 K. Inset: the AHE versus temperature, which exhibits Curie-like behavior from 3 K to 40 K.

### 6.2.4 The XMCD measurements

The XAS and XMCD measurements at the Cr $L_{2,3}$ absorption edges were performed at the beamline I10 at Diamond Light Source. Circularly polarized X-rays with ~100%

degree of polarization were used in normal incidence with respect to the sample plane and parallel to the applied magnetic field, as previously shown in Figure 6-5. The XMCD was obtained by taking the difference of the XAS spectra, i.e. $\sigma^-$ - $\sigma^+$, by flipping the X-ray helicity at fixed magnetic field of 10 kOe, under which the sample is fully magnetized with little paramagnetic contribution. To check the homogeneity of the sample, a continuous scan (step = 0.1 mm) was performed through a 2 mm length of the sample surface prior to the temperature dependence investigation. As present in Figure 6-4, all the XAS spectra show the same profile within the experimental accuracy, which confirms the reliability of the results presented in this study.

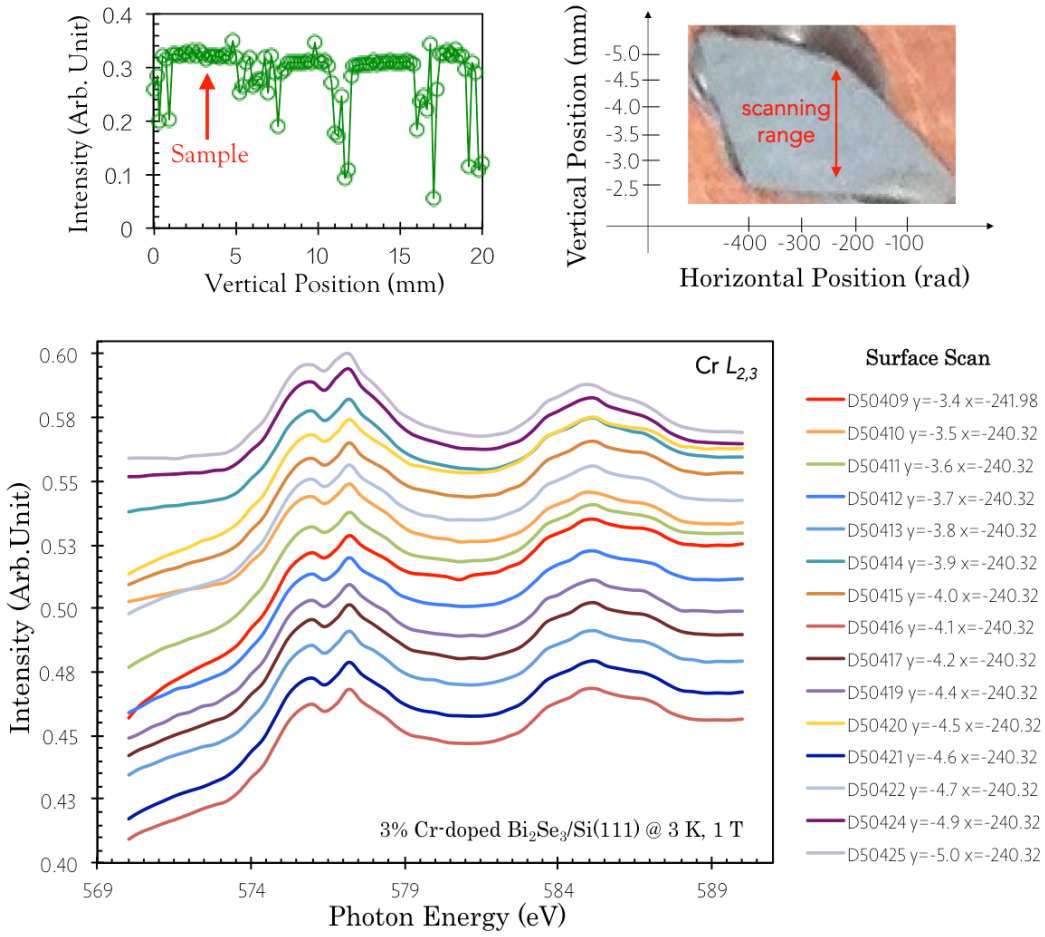


Figure 6-4 | The sample optimization and surface scan. Upper left: the vertically optimization performed at the Cr $L_3$ edge. The arrow indicates the sample location. Upper right: photograph of the $Bi_{2-x}Cr_xSe_3$ thin film sample mounted on the synchrotron facility sample stage. The double-sides arrow indicates the range of the surface scan. Lower: the XAS spectra (without background substation) collected through a 2 mm length of the sample surface, which confirms the homogeneity of the sample in sub-mm scale.

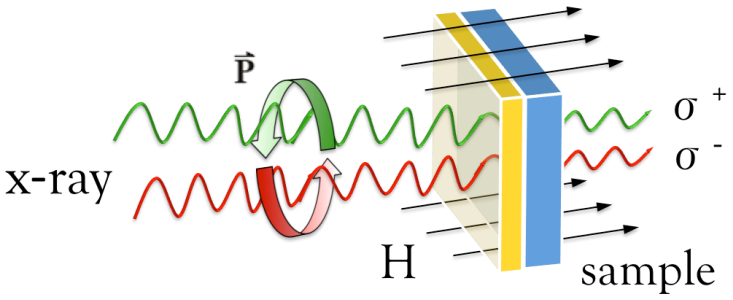


Figure 6-5 | Schematic diagram of the experimental set up of the XMCD measurement in Faraday geometry, i.e. with both the incident X-rays and the magnetization perpendicular to the sample surface.

Typical XAS and XMCD spectra of the bilayer sample obtained by TEY detection at 6 K, normalized to the incident beam intensity, are presented in Figure 6-6. The XAS spectra of Cr show remarkable multiplet structures at the both spin-orbit split cores, suggesting a mixture of bivalent and trivalent Cr in this compound. The XAS and XMCD measurements were repeated at elevated temperatures and the dichroism at the Cr $L_3$ edge was observable up to 30 K (see Figure 6-6), despite the decreasing intensity with increasing temperature.

The $m_{spin}$ and $m_{orb}$ of this $Bi_{1.94}Cr_{0.06}Se_3$ epitaxial thin film were calculated respectively by applying sum rules on the integrated XMCD and the summed XAS spectra of Cr $L_{2,3}$ edges using the method as described in chapter III. In order to rule out non-magnetic parts of the XAS spectra an arctangent based step function was used to fit the threshold. The spectral overlap or *j-j* mixing was taken into account because of the relatively small spin-orbit coupling in the Cr 2*p* level. A spin correction (SC = 2.0 ± 0.2 for Cr) factor was included, whose value was estimated by calculating the $L_{2,3}$ multiplet structure for a given ground state, applying the sum rule on the calculated XMCD spectrum, and comparing the result with the $m_{spin}$ calculated directly for this ground state. Furthermore, $m_{spin}$ needs to be corrected for the magnetic dipole term $\langle T_z \rangle$, however, its contribution is small for a Cr $t_{2g}^3$ configuration, giving an error < 5%. Assuming $n_h$ = 7 based on a single $Cr^{3+}$ configuration, $m_{spin}$ = (1.54 ± 0.2) $\mu_B$/atom and $m_{orb}$ = (-0.02 ± 0.02) $\mu_B$/atom were obtained at 6 K.

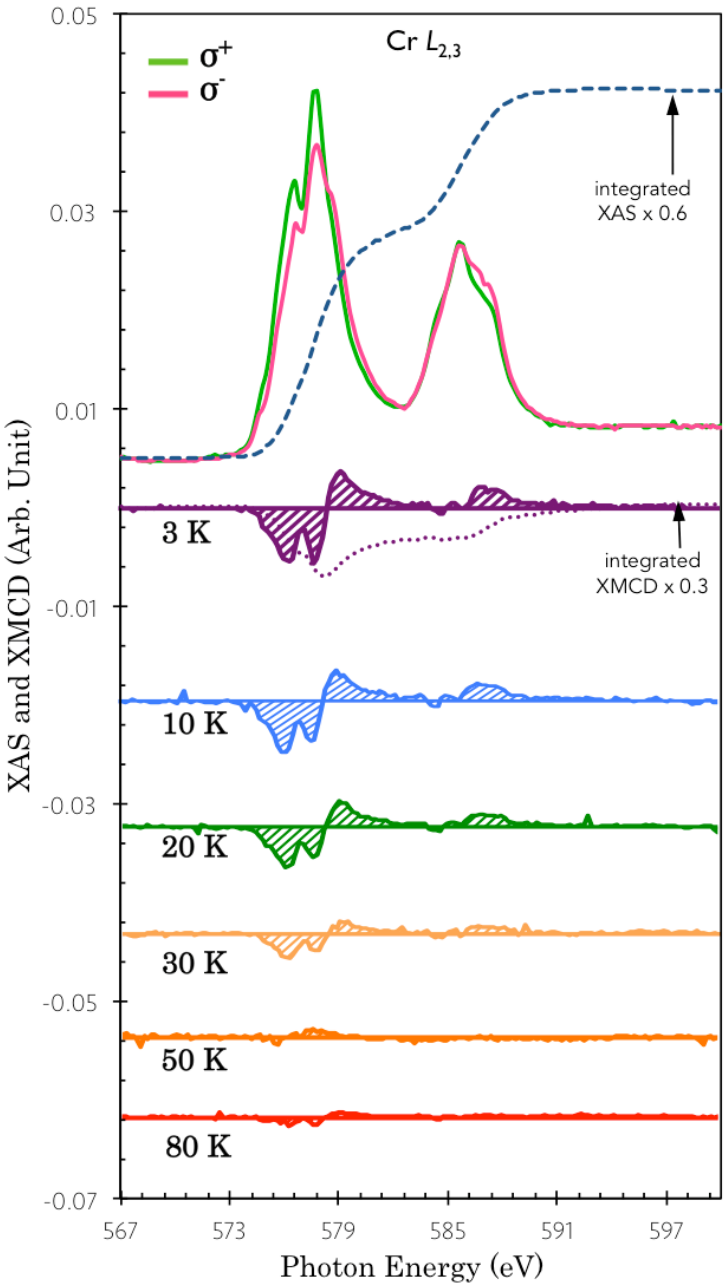


Figure 6-6 | Typical pair of XAS and XMCD spectra of the $Bi_{1.94}Cr_{0.06}Se_3$/Si(111) thin film at 3 - 80 K, normalized to the incident beam intensity. Data are scaled and offset for clearness.

Figure 6-7 presents the sum-rules derived $m_{orb}$ and $m_{spin}$ of the $Bi_{1.94}Cr_{0.06}Se_3$ epitaxial thin film sample from 3 K to 80 K. The $m_{orb}$ and $m_{spin}$ have opposite signs, corresponding to antiparallel alignment of the spin and orbital moment in Cr. This agrees with the Hund's rule for trivalent Cr, whose 3*d* shell is less-than-half full. The

octahedral crystal-field interaction quenches $m_{orb}$, since the three *d* electrons occupy the threefold degenerate majority-spin $t_{2g}$ orbitals, leading to a vanishing $m_{orb}$ as observed, while the spin reaches its full moment $m_{spin}$ = 3 $\mu_B$/atom.[310] For similar reasons as for $m_{orb}$, the $<T_z>$ term is small. Our observation of the Cr magnetic moment value is close to the value reported by Haazen *et al.*,[311] who performed SQUID-VSM measurements on a series of $Bi_2Se_3$ thin films with different Cr doping concentration (maximum $T_C$ = 20 K). In their work, the magnetic moment per Cr decreases significantly for $x > 5.2\%$, which coincides with a loss of $Bi_{2-x}Cr_xSe_3$ crystallinity. Such dependence is further evidence that the magnetization originates from the crystalline $Bi_{2-x}Cr_xSe_3$ phase. Cr clustering would not give rise to non-zero XMCD, since Cr is antiferromagnetic, as are $Cr_xSe_y$ compounds, but therefore could have led to a reduced average Cr magnetic moment, as observed here.

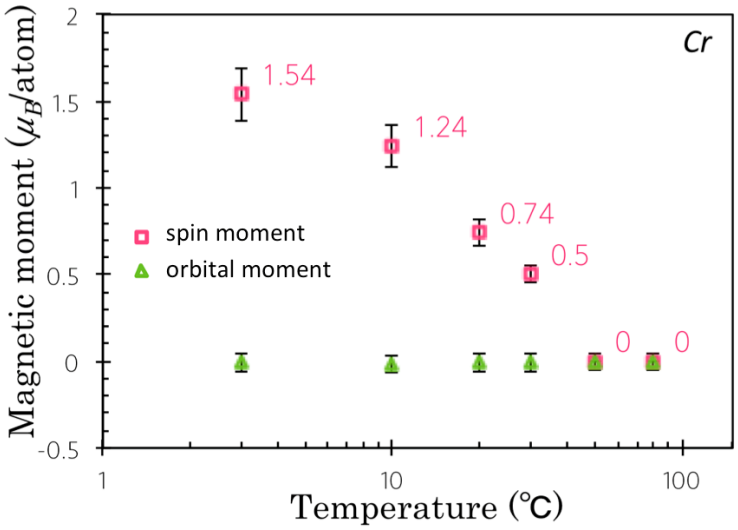


Figure 6-7 | The sum-rules derived $m_{orb}$ and $m_{spin}$ of the $Bi_{1.94}Cr_{0.06}Se_3$/Si(111) thin film at 3 - 80 K.

### 6.2.5 The first-principles calculations and discussion

To understand the observed magnetic moment, first-principles calculations were performed by collaboration with the theorists from the Rensselaer Polytechnic Institute, New York, US. The simulations were proceeded based on the first-principles DFT

within the Perdew-Burke-Ernzerhof generalized gradient approximation. Bi (5*d,* 6*s,* and 6*p*), Se (4*s* and 4*p*) and Cr (3*p,* 3*d,* and 4*s*) orbitals are explicitly treated in the valence and interactions between the ion cores. The valence electrons are described by the projector augmented wave (PAW) methodas implemented in the VASP code. The SOC was implemented in the all-electron part of the PAW Hamiltonian within the muffin-tin spheres. The basis set consisted of plane waves with a kinetic energy cutoff of 270 eV and the total energy was calculated with a Bruillion zone sampling of 2 × 2 × 2. Structural relaxations of the defects were performed in a 4 × 4 supercell containing 3 QLs with 95 Bi and 145 Se atoms and proceeded until the largest Hellmann-Feynman force was less than 0.025 eV/A.

In order to determine the $m_{spin}$ and $m_{orb}$ of Cr in $Bi_2Se_3$ theoretically, first it must be determined where Cr likes to reside within the lattice. The formation energies ($\Delta H$) of defects were calculated in the low-density limit according to

$$\Delta H = E(D^q) - E_{bulk} + \sum_i \triangle n_i \mu_i + q(E_F + E_{VBM})$$

Equation 6-1

where $E(D^q)$, $E_{bulk}$, $\mu_i$, $\Delta n_i$, respectively, represent the energy of the supercell containing the defect in charge state q, the energy of the defect-free bulk supercell, the chemical potential of the $i^{th}$ atomic species, and the number of which has changed in the formation of the defect.[312] The $\Delta H$ of Cr at various lattice positions including interstitial (referred as $Cr_I$) and substitutional sites with Cr replacing Bi (referred as $Cr_{Bi}$) and Se (referred as $Cr_{Se}$), as well as that of larger defect complexes containing pairs of Cr-atoms, such as the $Cr_{Bi}$ - $Cr_{Se}$ and $Cr_{Bi}$ - $Cr_I$ were calculated and the results are presented in Figure 6-8. It was found that the predominated defects in the system are the $Cr_I^{3+}$ ($\Delta H$ = -0.03 eV), $Cr_{Bi}^0$ ($\Delta H$ = -0.21 eV), and the $(Cr_{Bi} - Cr_I)^{3+}$ complex ($\Delta H$ = -0.68 eV).

Table 6-1 presents the calculated magnetic moments for these defects and that deduced from the XMCD measurement as described in the last sub-section. Despite their different charge states, both $Cr_{Bi}^0$ and $Cr_I^{3+}$ have a magnetic moments of ~3 $\mu_B$/atom, whilist the $Cr_{Bi}$ - $Cr_I$ pair is antiferromagnetic in nature (with the high-spin magnetic configuration being 75 meV higher in energy) with a nearly vanishing magnetic moment.

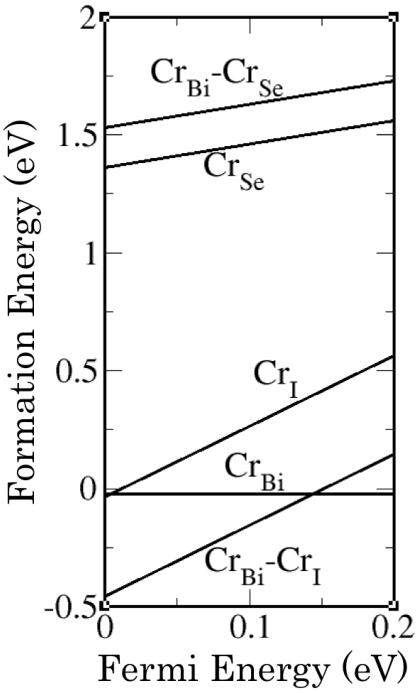


Figure 6-8 | Formation energies of Cr related defects in the $Bi_2Se_3$ excluding SOC. The slopes indicate the stable charge states of the defect, and the zero of $E_F$ corresponds to the valence band maximum (VBM).

| Cr defect | Method | $\Delta H$ (eV) | $m_{orb}(\mu_B/atom)$ | $m_{spin}(\mu_B/atom)$ | $m_{total}(\mu_B/atom)$ |
|---|---|---|---|---|---|
| $Cr_I$ | PAW | -0.03 | -0.03 | 2.98 | 2.95 |
| $Cr_{Bi}$ | PAW | -0.21 | -0.02 | 2.93 | 2.91 |
| $Cr_I$ - $Cr_{Bi}$ | PAW | -0.68 | -0.015 | 0.01 | -0.67 |
| | XMCD | | -0.02 ± 0.02 | 1.54 ± 0.20 | 1.49 ± 0.22 |

Table 6-1 | The calculated magnetic moments of the low energy Cr related defects in $Bi_2Se_3$ and that deduced from XMCD measurement as described in the last sub-section.

Figure 6-9 presents the dependence of the Cr concentration (upper row), average magnetic moment (middle row), and the formation energies (lower row) of the three predominated Cr related defects as a function of the chemical potential, respectively. The zero of the Cr chemical potential is that of bulk Cr, and the Bi and Se chemical potentials are fixed at the Bi-rich condition. Concentrations and magnetic

moments assume $E_F$ is at the conduction band minimum (CBM) and the growth temperature is 700 K. The dilute approximation fails dramatically above -0.43 eV, corresponding to a region of the chemical potential with very high defect concentration and the formation of secondary phases. In such Cr-rich condition, defect-defect interaction may significantly alter $\Delta H$ and all these three defects have negative formation energies indicating that it has been far outside the region where the dilute limit is valid.

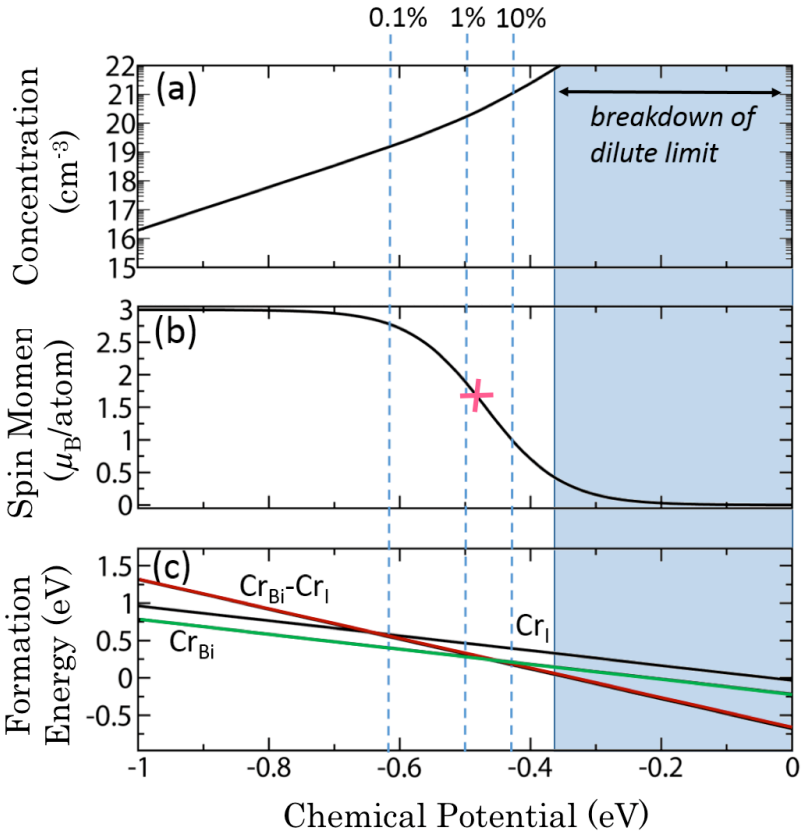


Figure 6-9 | The dependence of (a) the Cr concentration, (b) average magnetic moment, (c) and the formation energies of the three predominated Cr related defects as a function of the chemical potential, respectively. The zero of the Cr chemical potential is that of bulk Cr, and the Bi and Se chemical potentials are fixed at the Bi-rich condition. The dilute approximation fails dramatically above -0.43 eV, corresponding to a region of the chemical potential with very high defect concentration and the formation of secondary phases. The vertical lines at 10%, 1%, and 0.1% correspond to total Cr content with respect to Bi sites. The pink cross in the middle of (b) indicates the cross point of Cr concentration of the sample studied with XMCD, i.e. 3% with the calculated $m_{spin,}$ which agrees well with the experimental observation. Note the y-axis of (a) is in logarithmic scale.

For higher Cr chemical potentials (and consequently higher incorporation of Cr), the low spin $Cr_{Bi}$-$Cr_I$ pair is the most stable defect, whilist for lower concentrations of incorporated Cr, entropy acts against the formation of pair defects, leaving the higher spin $Cr_{Bi}$ and $Cr_I$ to dominate. As can be seen from Figure 6-9(b), the $m_{spin}$ of the Cr changes continuously and is estimated to be 0.9 $\mu_B$/atom, 1.89 $\mu_B$/atom, and 2.79 $\mu_B$/atom, for Cr concentrations of 10, 1, and 0.1%, respectively (here the Cr concentrations are based on the same definition of that for the MBE growth, i.e. the total Cr content with respect to Bi sites). The pink cross in the middle of Figure 6-9(b) indicates the cross point of Cr concentration of the sample studied with XMCD (i.e. 3%) with the calculated $m_{spin,}$ which agrees well with the experimental observation (1.54 ± 0.20) $\mu_B$/atom.

## 6.3 Enhancing magnetic ordering in TI using high-$T_C$ FMI

### 6.3.1 Introduction

Similar to that of DMSs (see Chapter IV, section 4.4), the low $T_C$ is also a major obstacle towards the RT applications of magnetically doped TIs. Pioneering theoretical work suggests that suitable FMIs have the potential to achieve a strong and uniform exchange coupling in contact with TIs without significant spin-dependent random scattering of helical carriers on magnetic atoms. Lou *et al.*[313] identified several FMIs with compatible magnetic structure and relatively good lattice matching with TIs including $Bi_2Se_3$, $Bi_2Te_3$, and $Sb_2Te_3$ and found that MnSe can be a good candidate to open a sizable band gap at the surface of the TI. Eremeev *et al.*[314] studied the magnetic proximity effect at the interface of the $Bi_2Se_3$/MnSe(111) system using density functional theory and demonstrated gapped states in both the immediate region of the interface and the deeper atomic layers of the TI. Men'shov *et al.*[315] employed a continual approach based on the ***k·p*** Hamiltonian and estimated the possibility to manage the Dirac helical state in TIs. Semenov *et al.*[316] proposed electrostatic control of the magnetic anisotropy in FMI/TI hybrid architectures and illustrated that surface electrons can induce out-of-plane magnetic anisotropy of the system. Progress has also been made experimentally in various FMI/TI heterostructures. Kandala *et al.*[317] performed electrical transport measurement of GdN/$Bi_2Se_3$, finding that a GdN overlayer results in suppression of weak anti-localization at the top surface of $Bi_2Se_3$. By demonstrating the magnetoresistance effect, Yang *et al.*[318] and Wei *et al.*[319] observed proximity-induced ferromagnetism at the interface of EuS/$Bi_2Se_3$ prepared via both pulsed laser deposition (PLD) and molecular beam epitaxy (MBE) deposition techniques respectively, although the effect observed is limited to low temperature (< 22 K) due to the low $T_C$ of EuS. Nevertheless, theoretical and experimental reports so far all point to a promising performance of FMI/TI heterostructures.

The interface magnetism of (anti-) FM/TI heterostructures, such as Fe/$Bi_2Se_3$,[320, 321, 322] Co/$Bi_2Se_3$,[323, 324] and Cr/$Bi_2Se_3$[325] has also been investigated. Remarkably, Vobornik *et al.*[297] demonstrated that long-range ferromagnetism at ambient temperature can be induced in $Bi_{2-x}Mn_xTe_3$ by a deposited Fe overlayer. This result has enlightened the room temperature (RT) use of TIs with the assistance of the magnetic proximity effect as a pathway. However, in the presence of a metallic layer, the nontrivial surface states of the TI can be significantly altered due to their hybridization

with the bulk states of the (anti-) FM in contact. Besides, the metallic layer naturally short circuits the TI layer and therefore fundamentally restrict the device design.

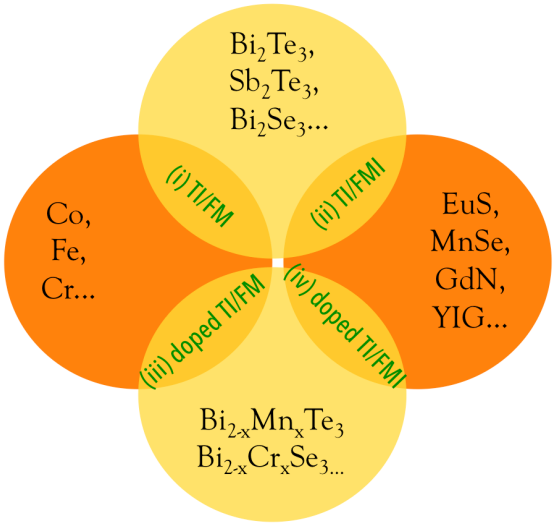


Figure 6-10 | Illustration of the research framework of magnetic TI hybrid systems. Circles representing FM (left) and FMI (right) overlap with those representing TI (bottom) and magnetically doped TI (top), encompassing four categories of studies of magnetic TI by engineering layered heterostructures, namely, investigations of (i) TI/FM including Fe/$Bi_2Se_3$,[89] Co/$Bi_2Se_3$, and Cr/$Bi_2Se_3$;[92] (ii) TI/FMI including MnSe/$Bi_2Se_3$,[313, 314] GdN/$Bi_2Se_3$,[317] EuS/$Bi_2Se_3$;[318, 319] (iii) doped TI/ FM Fe/$Bi_{2-x}Mn_xTe_3$;[297] and iv) the remaining unexplored area, i.e. doped TI/FMI, , studied for the first time in this project.

Despite the nature of the magnetism in TIs to be answered, an encouraging message from the work of Vobornik *et al.*[297] is that the magnetically doped TIs have already demonstrated a pronounced capability with the magnetic proximity effect. Although theoretical studies have proved the legitimacy of this approach, very limited successful experimental demonstrations by means of direct measurements like XMCD have been reported.[297] . As shown in Figure 6-10, among all the building blocks within the research framework of FM or FMI/(magnetically doped) TI heterostructures, investigations of FMI/magnetically doped TI remains absent. In the remainder of this section, we present a XMCD study in realizing the proximity effect in epitaxial $Bi_{2-x}Cr_xSe_3/Y_3Fe_5O_{12}$ heterojunctions. Garnet-type $Y_3Fe_5O_{12}$ (YIG) is a well-known FMI with $T_C$ (~550 K) well above RT and a desirable large spin diffusion length. It contains two Fe ions occupying octahedral sites and three Fe ions occupying tetrahedral sites

with opposite spin, resulting in ferrimagnetic ordering. The proximity effect has been demonstrated in PdPt/YIG,[326] Pt/YIG,[327] and Nb/YIG,[328] where interesting spin-transport properties were observed, such as spin Hall magnetoresistance (SMR),[329] spin Seebeck effect (SSE),[330] anomalous Nernst effect (ANE),[330] and switchable superconductivity[328] to name a few. While YIG-based heterostructures can consist of various materials, the best chance to realize strong exchange coupling exists in the candidates with two-dimensional quantum surface states, such as graphene and TIs.

### 6.3.2 The sample preparation and TEM characterization

The 10 nm 5.5% Cr-doped $Bi_2Se_3$ or $Bi_{1.89}Cr_{0.11}Se_3$ thin film used in this study were grown in ultra-high vacuum using the Perkin-Elmer molecular-beam epitaxy (MBE) system on 50 nm YIG (111) film, which was pre-deposited on gallium gadolinium garnet (GGG) (111) substrate using pulsed-laser deposition (PLD).[331, 332] High-purity Bi (99.9999%) and Cr (99.99%) were evaporated from conventional effusion cells at 470°C, while Se (99.99%) was formed from a cracker cell from SVTA at 240°C, and the YIG/GGG (111) substrate was kept at 200°C during growth. Interdiffusion of materials at the interface is not expected due to the high stability of YIG and the relatively low growth temperature of $Bi_{1.89}Cr_{0.11}Se_3$. 2 nm Al was then *in-situ* evaporated immediately after the growth of $Bi_{1.89}Cr_{0.11}Se_3$ to protect it from oxidation and environmental doping during transport to the synchrotron facility. Figure 6-11 presents a typical RHEED pattern of the $Bi_{1.89}Cr_{0.11}Se_3$ epitaxial thin film grown on YIG substrate and that on Si substrate for reference. It can be seen that $Bi_{1.89}Cr_{0.11}Se_3$ on YIG shows a similar diffraction patterns and in-plane lattice constants as that on Si and previous reports.

The interface and crystalline structure of the $Bi_{1.89}Cr_{0.11}Se_3$/YIG(111) bilayer was characterized using high-angle annular dark-field (HAADF) high-resolution scanning transmission electron microscopy (STEM), performed in the Electron Microscope Centre (led by Prof. Yong Wang) of Zhejiang University, Zhejiang, China. Cross-sectional foils of $Bi_{1.89}Cr_{0.11}Se_3$/YIG/GGG were prepared by focused ion beam (FIB), during which all parameters were carefully optimized to avoid the ion injection and specimen damage, including the accelerating voltage, beam current and tilt angle. Figure 6-12 presents a typical high angle annular dark field (HAADF) image, in which

no significant signature of intermixing at the $Bi_{1.89}Cr_{0.11}Se_3$/YIG and YIG/GGG interfaces was observed.

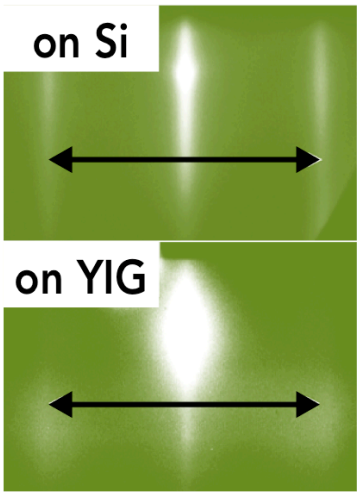


Figure 6-11 | Typical RHEED patterns of the $Bi_{1.89}Cr_{0.11}Se_3$ epitaxial thin films grown on Si(111) (upper row) and YIG(111) (lower row), respectively. The double-sides arrows point to the observed similar diffraction patterns and in-plane lattice constants.

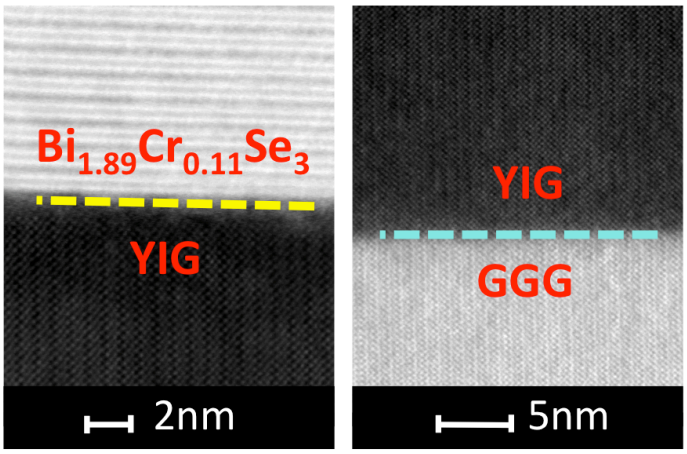


Figure 6-12 | Typical cross-sectional TEM images of the $Bi_{1.89}Cr_{0.11}Se_3$/YIG/GGG heterostructure. (b) Typical HAADF-STEM image of $Bi_{1.89}Cr_{0.11}Se_3$/YIG/GGG heterostructure, where no significant signature of intermixing was observed at the interfaces of $Bi_{1.89}Cr_{0.11}Se_3$/YIG (yellow dashed line, left panel) and YIG/GGG (blue dashed line, right panel).

### 6.3.3 The magneto-transport measurement

The magnetic response of the epitaxial $Bi_{1.89}Cr_{0.11}Se_3$/YIG (111) thin film sample was first examined by the magneto-transport measurements using the same technique as described in the last section. By subtracting the ordinary Hall component, we plotted the anomalous Hall resistance ($R_{AHE} = R_{xy} - R_0 \cdot H$) as a function of field applied perpendicularly to the film in Figure 6-13. Non-zero $R_{AHE}$ was observable up to 50 K and vanished above 90 K. Figure 6-14 presents the temperature dependent $R_{AHE}$ of the $Bi_{1.89}Cr_{0.11}Se_3$ thin films on YIG, to which a $Bi_{1.89}Cr_{0.11}Se_3$ epitaxial thin films of the same thickness grown on highly resistive Si (111) substrate was attached for comparison purpose. It can be seen that both these Cr-doped $Bi_2Se_3$ thin films exhibit Curie-like behavior, however, their magnetic ordering disappears at different temperatures, namely 30 K for $Bi_{1.89}Cr_{0.11}Se_3$/Si and up to 50 K for $Bi_{1.89}Cr_{0.11}Se_3$/YIG. Note these $Bi_{1.89}Cr_{0.11}Se_3$ thin films on YIG and Si were not deposited in one go, as the growth conditions could not be optimized for YIG and Si substrates simultaneously. However, samples have been carefully checked with X-ray photoelectron spectroscopy (XPS), in order to make sure that the doping concentration of the $Bi_{1.89}Cr_{0.11}Se_3$ on YIG and Si were identical. Besides, $Bi_{1.89}Cr_{0.11}Se_3$ on YIG shows a similar diffraction patterns and in-plane lattice constants as that on Si. Therefore above the intrinsic $T_C$ of $Bi_{1.89}Cr_{0.11}Se_3$ (~30K), the survived magnetization is most possibly due to the presence of the YIG other than any microstructure reasons raised from the different substrates.

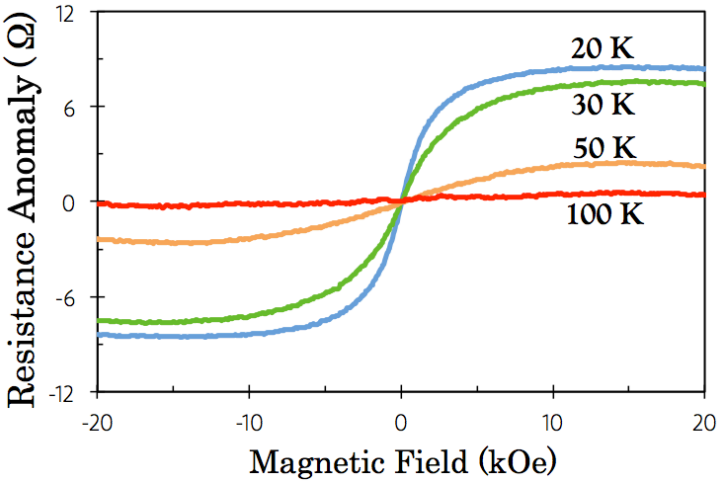


Figure 6-13 | AHE of the $Bi_{1.89}Cr_{0.11}Se_3$/YIG thin film versus magnetic field at 20 - 100 K, by which non-zero $R_{AHE}$ were observed up to 50 K and vanished above 90 K.

Apart from the $R_{AHE}$ data, the ferromagnetic ordering of the $Bi_{1.89}Cr_{0.11}Se_3$/YIG bilayer was also observed from the field dependent longitudinal resistance ($R_{xx}$). In the low field region, weak anti-localization (WAL) with a clear cusp was observed at low temperatures, which is a characteristic feature associated with the gapped topological surface states below the critical temperature. A typical $R_{xx}$ obtained at 3 K is presented in the inset of Figure 6-18. The valleys of the WAL cusp exhibit a shift under the opposite field scanning directions, which is associated with the $H_c$. We repeated the hysteretic longitudinal magnetic resistance measurement at elevated temperatures up to 90 K and found that $H_c$ remains observable until beyond 50 K, as plotted in Figure 6-18, which is consistent with the $T_C$ estimated from the $R_{AHE}$.

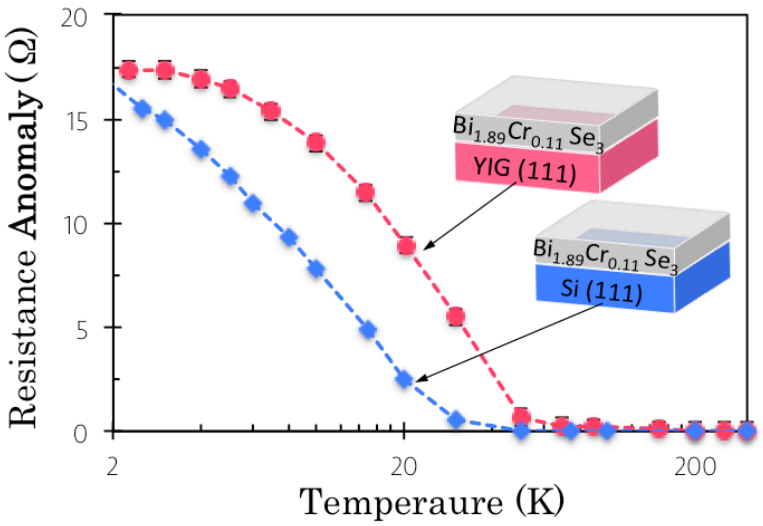


Figure 6-14 | Comparison of the AHE versus temperature of the $Bi_{1.89}Cr_{0.11}Se_3$ thin films grown on YIG (111) and Si (111), respectively. Both Cr-doped $Bi_2Se_3$ thin films exhibit Curie-like behavior, however, their derived magnetic ordering vanishes at different temperatures. Note the x-axis is in logarithmic scale.

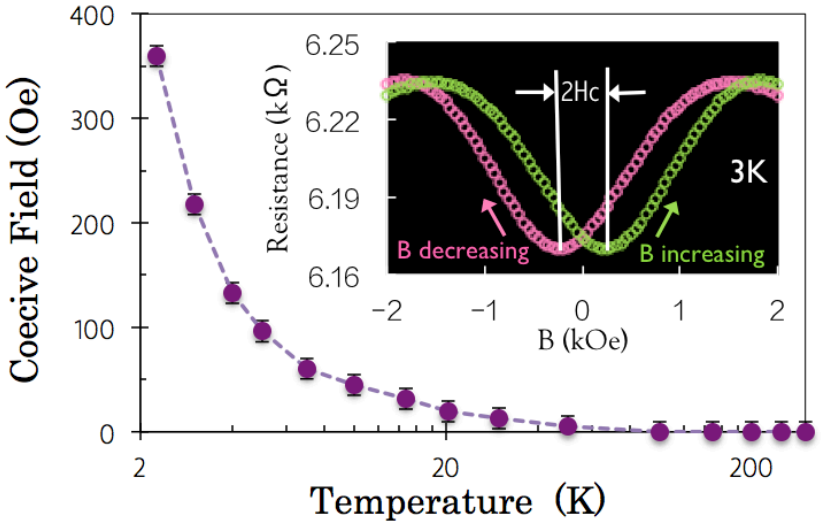


Figure 6-15 | The $H_c$ of $Bi_{1.89}Cr_{0.11}Se_3$/YIG versus temperature, which is observable until beyond 50 K. Inset: the shift of the valleys of WAL cusp, associated with the $H_c$. The arrows represent the scanning direction of the magnetic field. Note the x-axis is in logarithmic scale.

### 6.3.4 XMCD measurement

The XAS and XMCD measurements at the Cr $L_{2,3}$ absorption edges were performed at the beamline I10 of Diamond Light Source. Circularly polarized X-rays with ~100% degree of polarization were used with the same configuration as described in the last section. XMCD was obtained as the difference spectrum, i.e. $\sigma^-$ - $\sigma^+$, obtained by flipping the polarization direction of the X-rays at a fixed magnetic field of 10 kOe, under which the sample is fully magnetized with little paramagnetic contribution. A typical pair of XAS and XMCD spectra of the bilayer sample obtained by TEY at 6 K, normalized to the incident beam intensity, is presented in Figure 6-16. The XAS spectra of Cr for both left- and right- circularly polarized X-rays show a white line at each spin-orbit split core level without prominent multiplet structure, regardless of a shoulder structure present for the $L_2$ peak. The XAS spectral line shape resembles that of the ferromagnetic spinel-type Cr chalcogenides, i.e., $CdCr_2Se_4$, reported by Kimura *et al.*,[333] suggesting that the sample contains predominately $Cr^{3+}$ cations. Features of the obtained XMCD spectra are also in good agreement with those obtained for $CrFe_2O_4$ spinel

ferrite powders,[334] which can be well reproduced by the multiplet calculations using a charge-transfer model with trivalent Cr cations on octahedral sites. Consistent with the reported transport measurements,[295, 308] the observed XAS and XMCD line shape also suggests that a majority of the Cr ions is incorporated within the crystal lattice by substituting onto the Bi sites (with formal valance of 3+) in the TI matrix. The XAS and XMCD measurements were repeated at elevated temperatures and the dichroism at the Cr $L_3$ edge (575.3eV) was observable up to 50 K, as attached to Figure 6-16, despite the decreasing intensity with increasing temperature. For clearness, Figure 6-17 presents the partially enlarged XAS spectra pairs of the Cr $L_3$ edge at 30 K, 50 K, and 100 K, respectively, from which the peak asymmetry can be observed up to 50 K.

Note that although the Cr dichroism is no longer distinguishable from the noise at and above 100 K, the Fe dichroism in YIG remains sizably large up to RT (see Figure 6-18). The XAS spectra of Fe $L_{2,3}$ edges show remarkable multiplet structure and the XMCD spectra shows the typical positive and negative alternative peaks of ferrites, corresponding the octahedral and tetrahedral sites, respectively, whose spins are coupled antiparallel.

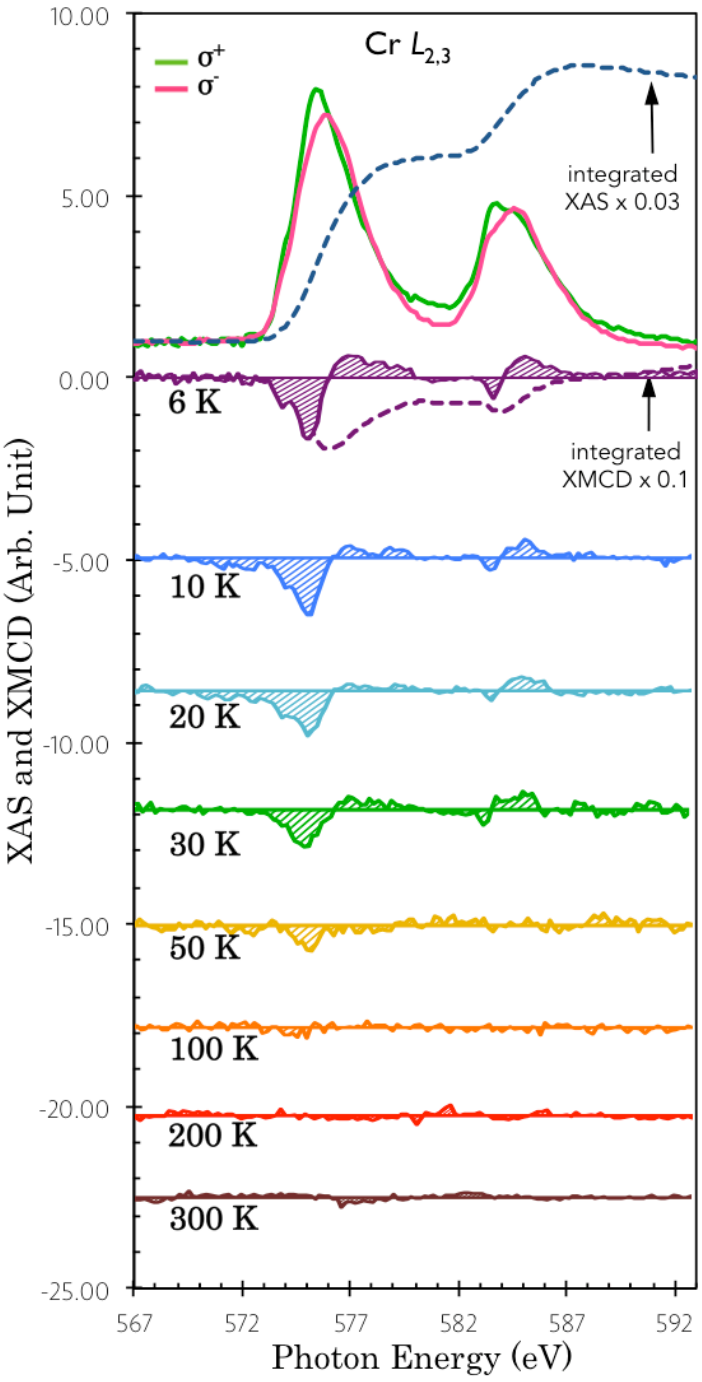


Figure 6-16 | Typical pair of XAS and XMCD spectra of the $Bi_{1.89}Cr_{0.11}Se_3$/YIG bilayer sample obtained at 3 – 300 K, where dichroism at the Cr $L_3$ edge (575.3 eV) was observed up to 50 K. Data are scaled and offset for clearness.

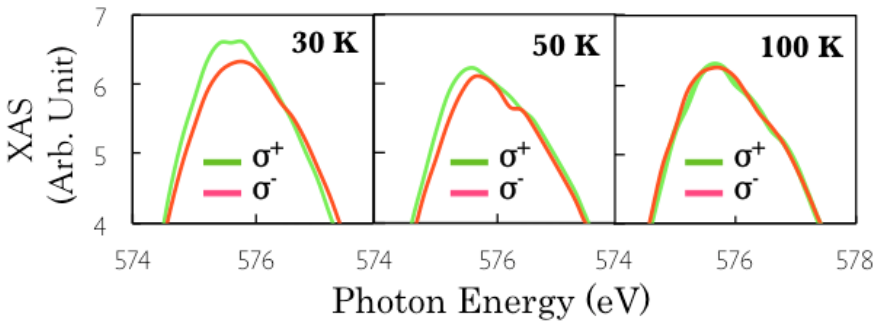


Figure 6-17 | Partially enlarged XAS spectra pairs of the Cr $L_3$ edge at 30 K, 50 K, and 100 K, respectively, from which the peak asymmetry can be observed up to 50 K.

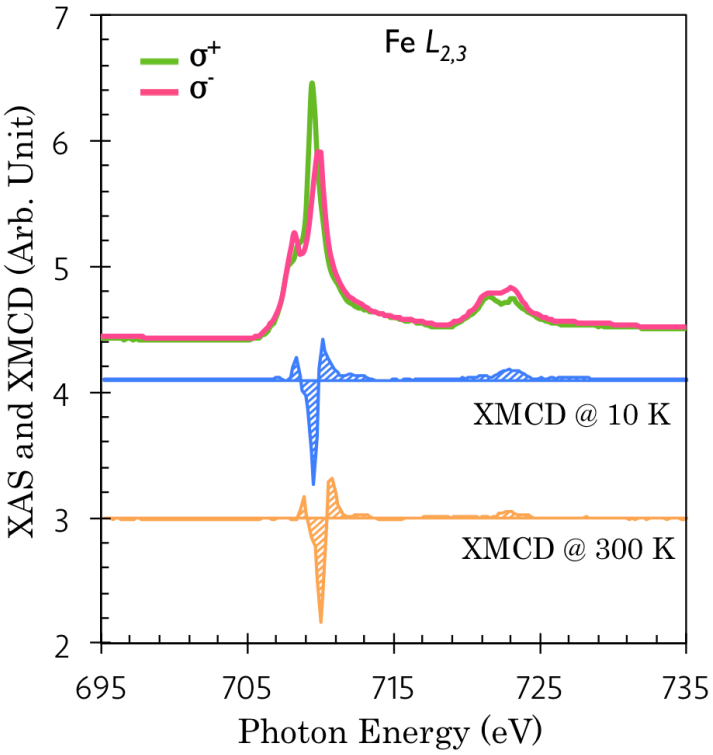


Figure 6-18 | Typical pair of XAS and XMCD spectra of Fe from the $Bi_{1.89}Cr_{0.11}Se_3$/YIG bilayer at 10 K and 300 K. The XAS spectra of Fe $L_{2,3}$ edges show remarkable multiplet structure and the XMCD spectra shows the typical positive and negative alternative peaks of ferrites, corresponding the octahedral and tetrahedral sites, respectively, whose spins are coupled antiparallel. Data are scaled and offset for clearness.

Figure 6-19 presents the calculated $m_{spin}$ and $m_{orb}$ of Cr in $Bi_{1.89}Cr_{0.11}Se_3$/YIG bilayer at 6 - 300 K, using the same parameters as described in the last section. Consistent with the magneto-transport results, the sum-rules derived $m_{spin}$ also exhibits a Curie-like behavior, pointing to a ferromagnetic phase of $Bi_{1.89}Cr_{0.11}Se_3$ at low temperature. We obtained a remarkable $m_{spin}$ = 1.38 ± 0.10 $\mu_B$/Cr and a small negative $m_{orb}$ = (-0.03 ± 0.02) $\mu_B$/Cr at 3 K. Noting that $m_{spin}$ retains a sizable value of 0.58 ± 0.10 $\mu_B$/Cr at 30 K, we claim a pronounced increase of the $T_C$ in $Bi_{1.89}Cr_{0.11}Se_3$ from 30 K, since otherwise (e.g., paramagnetism) $m_{spin}$ should have nearly vanished at, or before, this point. While the temperature keeps increasing, $m_{spin}$ reduces down to (0.10 ± 0.10) $\mu_B$/Cr at 50 K, suggesting the $Bi_{1.89}Cr_{0.11}Se_3$ is close to its $T_C$ here. As listed in Table 1, the reported $T_C$ of various kinds of magnetic TIs remained so far below ~30 K, while the $Bi_{1.89}Cr_{0.11}Se_3$/YIG bilayer shows a robust ferromagnetic phase up to 50 K due to the presence of the high-$T_C$ FMI.

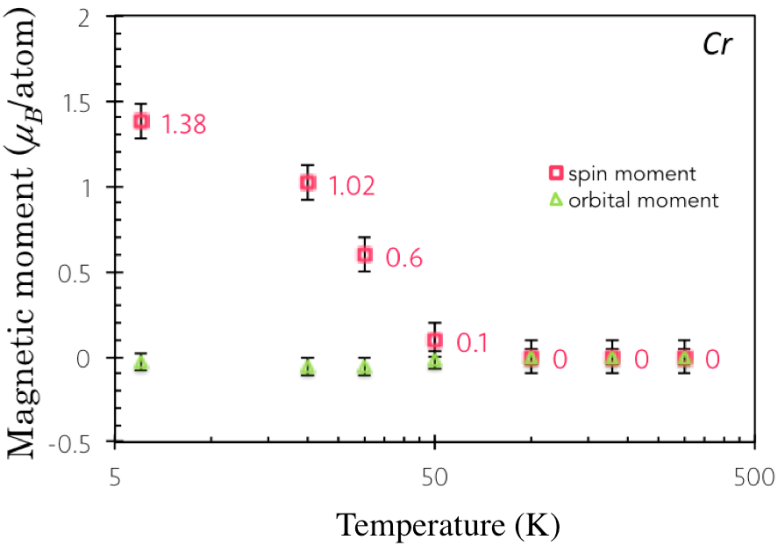


Figure 6-19 | The sum-rules derived $m_{spin}$ and $m_{orb}$ of the $Bi_{1.89}Cr_{0.11}Se_3$/YIG bilayer at 6 - 300 K. The x-axis is in logarithmic scale.

| Sample | $T_C$ | Ref. |
|---|---|---|
| $Bi_{2-x}Cr_xSe_3$/YIG | 50 K | * |
| $Bi_{2-x}Cr_xSe_3$ | 20 K | 294 |
| $Sb_{2-x}Cr_xTe_3$ | 20 K | 300 |
| $Cr_x(Bi_ySb_{1-y})_2Te_3$ | 11 K | 289 |
| $Bi_{2-x}Mn_xTe_3$ | 12 K | 291 |
| $Bi_{2-x}Fe_xTe_3$ | 12 K | 292 |
| $Bi_2Se_3$/EuS | 22 K | 318 |
| $Bi_2Se_3$/GdN | 16 K | 317 |

Table 6-2 | List of the $T_C$ of magnetic TIs obtain from this work (first line, marked as *) and those taken from the literatures.

### 6.3.5 Discussion

Both the electrical transport and XMCD results point to the fact that between 30-50 K, the magnetization of Cr can be attributed to the magnetic exchange coupling with YIG. We now address the ability of the YIG underlayer to induce magnetic ordering in $Bi_{1.89}Cr_{0.11}Se_3$ utilizing a simplified model that was developed in the study of the proximity effect in dilute magnetic semiconductors (DMSs).[85] As schematically sketched in Figure 6-20, we divided the $Bi_{1.89}Cr_{0.11}Se_3$ volume into two parts, namely the proximity-induced ferromagnetic region near the $Bi_{1.89}Cr_{0.11}Se_3$/YIG interface and the upper paramagnetic region. The magnitude of the Cr XMCD is described by $\delta(x)dx$, the dichroic signal which contributes at depth $x$, and the Cr concentration is described by $\rho(x)dx$. It is generally accepted that the XMCD intensity measured by TEY is attenuated by an exponentially decaying electron-escape probability, $\exp[-(x/\lambda_e)]$,[170] so that we obtain

$$Cr\ \text{XMCD} = \frac{\int_0^\infty \delta(x)\rho(x)e^{-x/\lambda_e}dx}{\int_0^\infty \rho(x)e^{-x/\lambda_e}dx}$$

Equation 6-2

where $\lambda_e$ is the mean electron escape length. Provided (i) a sharp interface, (ii) a uniform distribution of Cr in $Bi_2Se_3$, and (iii) a steplike dichroism profile versus thickness $d$, we have $\delta(x) = \delta_{exp}$ for $d_{YIG} < x < d_{min}$ and $\delta(x) = 0$ elsewhere. Here $d_{min}$ represents the lower limit, or the thickness of $Bi_{1.89}Cr_{0.11}Se_3$ contributing to the ferromagnetic signal at 30-50 K. Integration gives

$$d_{\min} = d_{Bi_{2-x}Cr_xSe_3} + \lambda_e \ln[\frac{\delta_{\exp}}{\delta_{sat}} + (1 - \frac{\delta_{\exp}}{\delta_{sat}})e^{-d_{Bi_{2-x}Cr_xSe_3}/\lambda_e}]$$

Equation 6-3

Quoting the value $m_{spin} = 1.38\ \mu_B$/Cr at 6 K, whose magnetic moment is considered to be intrinsic of $Bi_{1.89}Cr_{0.11}Se_3$ without the effect of YIG, we obtain $\delta_{exp}/\delta_{sat} = 43\%$ and $d_{min} = 6.6$ nm at 30 K. This value quickly reduces to $d_{min} = 1.8$ nm at 50 K, where $\delta_{exp}/\delta_{sat} = 7\%$. However, this calculation could underestimate the saturation magnetic moment of Cr. A different assumption can be made using $m_{spin} = 3\ \mu_B$/Cr for $\delta_{sat}$ as discussed in the last section, corresponding to a scenario where all the Cr ions are fully aligned at the interface with YIG, which is more likely the realistic picture. Consequently, we obtain $d_{min} = 3.8$ nm at 30 K and $d_{min} = 0.9$ nm at 50 K. For the calculation of $d_{min}$, we adopted $\lambda_e = 5$ nm for the bulk mean electron escape length of $Bi_2Se_3$ and $d = 10$ nm for the thin film thickness.

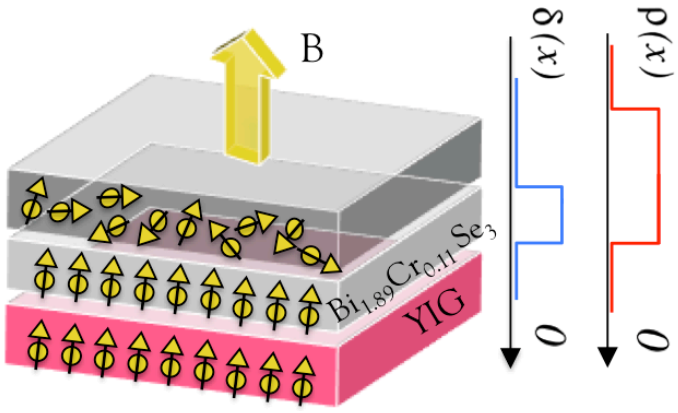


Figure 6-20 | Schematic diagram of the model used to estimate the proximity length, showing the Cr distribution $\rho(x)$ and the ferromagnetically ordered Cr distribution $\delta(x)$ at given temperature, as described in the text. Arrows indicate the direction of the spins under a perpendicular magnetic field.

In either of the above situations, we have observed a larger penetration depth of the magnetic proximity effect at the interface of TI/FMI, compared with the FM/DMS bilayer systems investigated by Maccherozzi *et al*.[85] utilizing the same model. The penetration depth decreases sharply with increasing temperature (i.e., > 80% from 30 K to 50 K), for which the reason has not been fully understood. Typically, the proximity-induced magnetization in DMSs reduces only ~ 10% within a comparable temperature range. Such contrast may imply a unique type of interaction of the nontrivial surface state of TI with FMI. In other words, the penetration depth of the magnetic proximity effect in DMSs may have been limited by the contact barrier, while the conducting surface states of TIs may lift this limitation. It is generally believed that the origin of the proximity effect in a nonmagnetic/ferro- or ferri- magnetic (NM/FM) heterostructure arises from (spin-polarized) charge carriers propagating from the FM into the NM metal and vice versa, such that a finite spin polarization builds up close to the interface. A substantial reduction of such a spin polarization accumulation can be expected in a DMS, where charge carriers can hardly penetrate. In contrast, our results suggest that such charge carrier propagation can be less suppressed in the TI/FMI system due to the presence of the conducting surface states, though whose ability is more sensitive to the temperature variation.

## 6.4 The Δ-doped 3D TI

### 6.4.1 Introduction

In the last two sections, we have presented the studies of a model magnetically doped TI, i.e. $Bi_{2-x}Cr_xSe_3$, by means of XMCD and in combination with magneto transport measurement and first-principles calculations. Although XMCD is directly addressable to the electrical and magnetic ground states of the magnetic dopants, unambiguity still exists in the interplay of magnetism and the nontrivial surface state of TIs. Looking back those ARPES signatures of the magnetically doped TIs, a surprising feature is that the band gap of the surface spectrum can appear in the absence of the long-range magnetic ordering of the bulk, even though the dopants are indeed uniformly distributed everywhere in the 3D samples.[335] This observation raises an interesting question of magnetic ordering in the bulk versus the surface of a 3D TI - can a band gap open in the surface state of a TI in a TRS-broken phase, which however lacks global magnetic ordering?

Simple arguments suggest that unordered magnetic moments do not open a gap. Imaging the creation of a magnetically disordered state near the surface of a TI by introducing domains with opposite magnetization, it has been known that the resulting magnetic domain walls carry topologically protected gapless fermionic modes. As the number of the domains grows, so does the density of the low-energy fermion modes, which ultimately will recover the 2D gapless state characteristic of the system with unbroken TRS. Such hypothesis suggests that uniformly long range magnetic ordering is necessary to gap out the surface modes in a TI. Being aware of no systematic experimental studies of this problem, here we present a preliminary exploration at the final stage of this PhD project to look into the effect of surface doping and bulk doping respectively of magnetic TIs. This goal has been pursued by performing XMCD of a series of special layered $Bi_2Se_3$ structures, in which the magnetic impurities were only doped into the surface and into the middle of the film and so called "Δ-doping" and the results will be presented in the remainder of this section

### 6.4.2 The sample preparation

The 10 nm 12% Cr-Δ-doped $Bi_2Se_3$ or $Bi_{1.76}Cr_{0.24}Se_3$ epitaxial thin films used in this study were prepared using the same MBE set up as describe in section 6.2. By accurately controlling the Cr-dopant distribution profiles along the epitaxial growth direction (i.e., deviation < ±0.1 nm),[336] Cr doping was managed to be doped only into the top 1st QL (surface doped) and the 5th QL of the pristine $Bi_2Se_3$ layered structure (see Figure 6-21). For clearness, here and thereafter, the term "bulk doping" refers to the doping of a single QL in the middle of the film, instead of a uniformly doping, which we refer as "globally doping" in this study. Within the given opportunities, we have selected the surface- (i.e. 4 nm $Al_2O_3$/1 nm $Bi_{1.76}Cr_{0.24}Se_3$/9 nm $Bi_2Se_3$/Si(111)) and the bulk- doped TI (i.e. 4 nm $Al_2O_3$/4 nm $Bi_2Se_3$/1 nm $Bi_{1.76}Cr_{0.24}Se_3$/5 nm $Bi_2Se_3$/Si(111)) as the control group for each other, rather than comparing the surface- and the globally doped samples (i.e. a 1 nm $Bi_{2-x}Cr_xSe_3$/9 nm $Bi_2Se_3$ with a 10 nm $Bi_{2-x}Cr_xSe_3$), so to exclude the differences of the magnetic properties (such as the saturation magnetization, the $T_c$, and the magnetic anisotropy) raised from the different thickness.

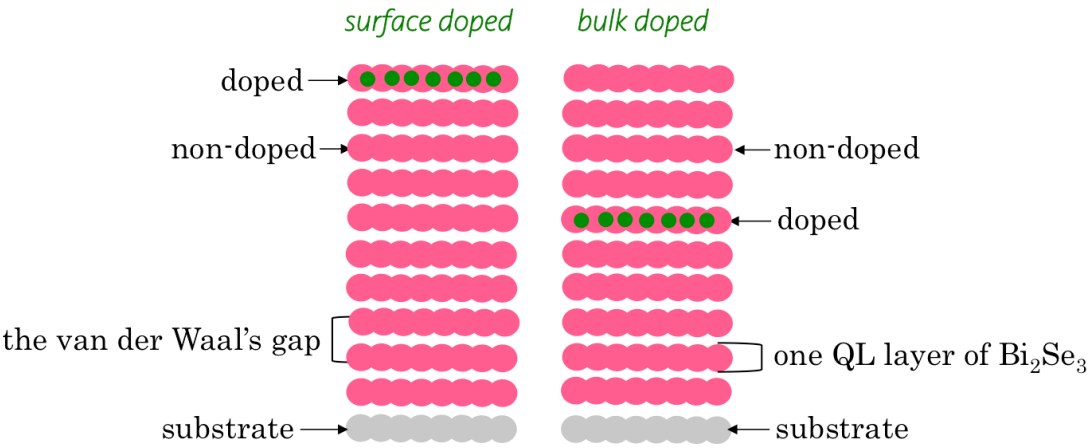


Figure 6-21 | Schematic diagram of the Δ-doped $Bi_{1.76}Cr_{0.24}Se_3$ epitaxial thin film samples prepared by MBE.

### 6.4.3 XMCD measurements

The XAS and XMCD measurement at the $L_{2,3}$ Cr absorption edges were performed at the beamline I10 of Diamond Light Source with the identical experimental configuration as schematically shown in Figure 4-2. The XMCD was obtained by taking the difference of the XAS spectra, i.e. $\sigma^- - \sigma^+$, by flipping the X-ray helicity at fixed magnetic field of 30 kOe, under which the sample is fully magnetized. A typical pair of XAS and XMCD spectra of the surface doped (left column) and bulk doped (right column) $Bi_{1.76}Cr_{0.24}Se_3$ epitaxial thin film samples obtained by TEY detection at 10 - 80 K, normalized to the incident beam intensity, are presented in Figure 6-6. The XAS spectra of Cr of the two samples show remarkable multiplet structures at the both spin-orbit split core, suggesting a mixture of bivalent and trivalent Cr in the compounds.

The $m_{spin}$ and $m_{orb}$ of both the surface doped (left) and bulk doped (right) $Bi_{1.76}Cr_{0.24}Se_3$ epitaxial thin film samples were calculated, respectively, by applying sum rules on the integrated XMCD and total XAS spectra of Cr $L_{2,3}$ edges using the same method as described in the earlier sections. Surprisingly, we obtained $m_{spin}$ = (0.96 ± 0.20) $\mu_B$/atom for the surface doped $Bi_{1.76}Cr_{0.24}Se_3$, going all the way down to $m_{spin}$ = (0.18 ± 0.20) $\mu_B$/atom at 80 K while and $m_{orb}$ = (-0.06 ± 0.02) $\mu_B$/atom was obtained at 10 K and remains unchanged with the increasing temperature within the error bar. By contrast, $m_{spin}$ = (1.44 ± 0.20) $\mu_B$/atom were obtained for the bulk doped $Bi_{1.76}Cr_{0.24}Se_3$ at 10 K, which reduces to $m_{spin}$ = (0.30 ± 0.20) $\mu_B$/atom at 80 K.

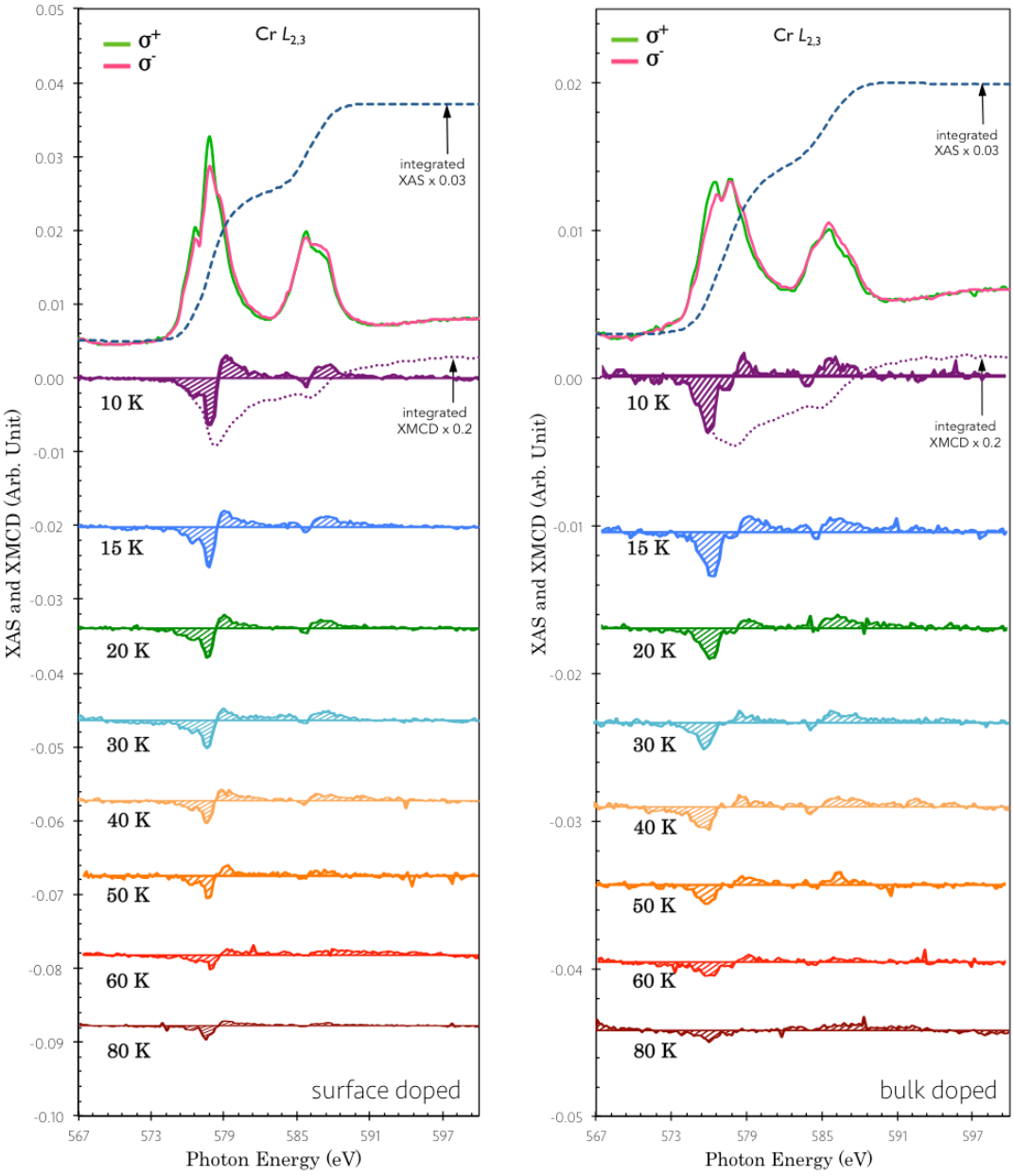


Figure 6-22 | Typical pair of XAS and XMCD spectra of the surface doped (left column) and bulk doped (right column) $Bi_{1.76}Cr_{0.24}Se_3$ epitaxial thin films on Si(111) samples at 10 - 80 K, normalized to the incident beam intensity. Data are scaled and offset for clearness.

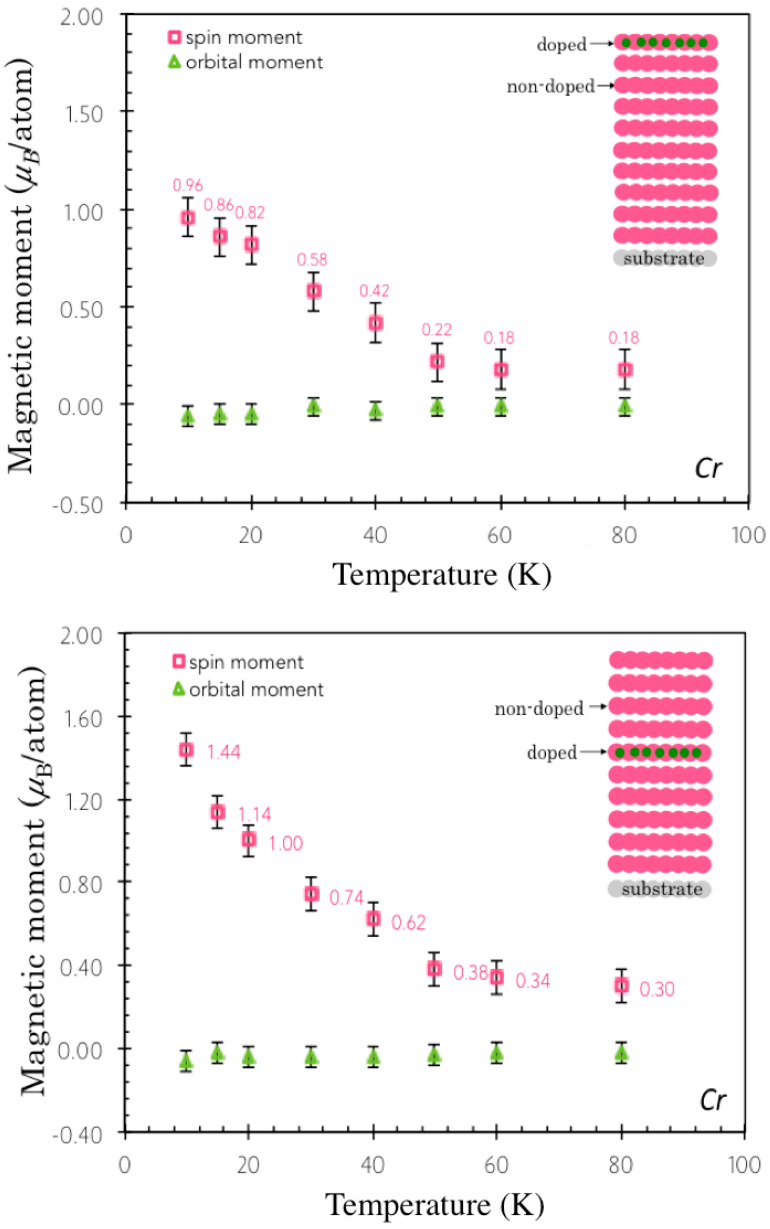


Figure 6-23 | The sum-rule derived $m_{orb}$ and $m_{spin}$ of the surface doped (top) and bulk doped (bottom) $Bi_{1.76}Cr_{0.24}Se_3$ epitaxial thin films, respectively, at 10 - 80 K.

### 6.4.4 Discussions

A striking phenomenon we have observed in this experiment is that the magnetic ordering of these Δ-doped TIs have persisted to surprisingly high temperatures, i.e. ~ 60 K for the surface-doped and ~ 80 K for the bulk-doped $Bi_{2-x}Cr_xSe_3$, both well in excess

of the globally doped $Bi_{2-x}Cr_xSe_3$ (as discussed in the last two sections of this chapter and any reported observations, see Table 6-2). Such observation is in high consistent with the prediction by Rosenberg *et al*.[337] that "a 3D TI doped with magnetic impurities in the bulk can have a regime where the surface is magnetically ordered but the bulk is not." The surface and the bulk magnetism can be viewed as typical questions of magnetic ordering versus dimensionality. In conventional materials, ordered phenomena in lower dimensions are typically more fragile (i.e. $T_c$ (3D) > $T_c$ (2D), the symbol $T_c$ here is not limited to Curie temperature, but stand for the critical temperature of the magnetically ordered phenomena in general). This is in the opposite of our observation of the enhanced $T_c$ of the surface-doped $Bi_{2-x}Cr_xSe_3$ compared with that of the globally doped $Bi_{2-x}Cr_xSe_3$, which may be associated with the topologically protected gapless surface states.

Putting the total XAS of the globally, bulk- and surface- doped $Bi_{2-x}Cr_xSe_3$ epitaxial thin films (all on Si(111) substrate) together as presented in Figure 6-24, we observed a modified electronic character of $Bi_{2-x}Cr_xSe_3$ due to the different doping positions, which may be associated with the nontrivial surface states. Compared with the Cr XAS spectra reported in various compounds, the Cr charge state can be estimated from the relative ratio of the two split contributions at the $L_3$ edge (see the black dots on the spectra of Figure 6-24). The globally doped $Bi_{2-x}Cr_xSe_3$ shows the feature of predominated $Cr^{3+}$, in which the first Cr contribution of the $L_3$ peak is around 2/3 of the magnitude of the second one,[338, 339] whilst that of the surface doped $Bi_{2-x}Cr_xSe_3$ is rather close to the line shape of $Cr^{4+}$,[310, 340] in which the first Cr contribution of the $L_3$ peak is around 1/2 of the magnitude of the second one. Contrast to them, the bulk doped $Bi_{2-x}Cr_xSe_3$ shows a broader width of the double peaks at $L_3$ edge, whose intensity is almost identical, which suggest a mixture of $Cr^{2+}$ (in which the first Cr contribution of the $L_3$ peak is bigger than the magnitude of the second one)[341] and $Cr^{3+}$ and $Cr^{4+}$. Such deviations in the charge states of Cr ions at the surface and in the bulk can be responsible for the low-spin and high-spin states, respectively, of the Cr dopants as observed from the XMCD.

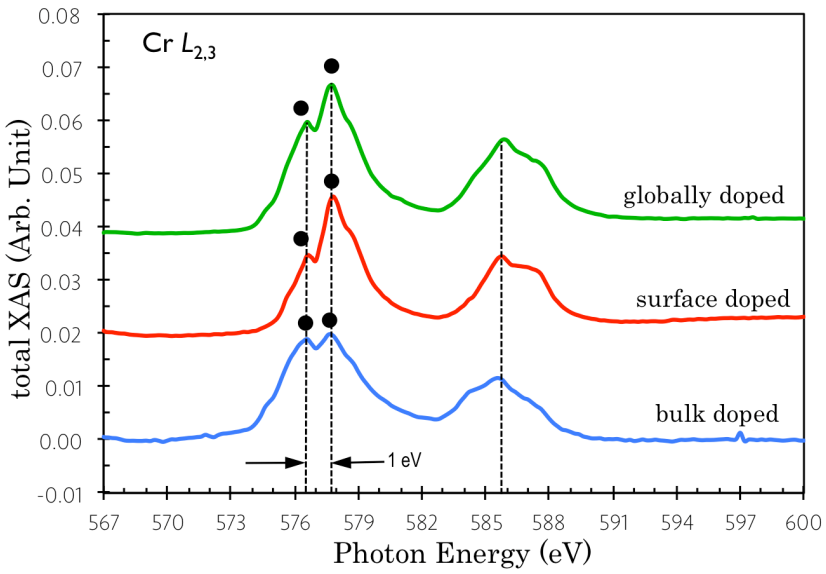


Figure 6-24 | The total XAS spectra of the globally, bulk- and surface- doped $Bi_{2-x}Cr_xSe_3$ epitaxial thin films on Si(111). The black dots indicates the first and the second Cr contributions at the $L_3$ peak, whose relative intensity can be used for an estimation of the charge states.

The difference between surface and bulk dopant magnetism is linked to a central issue in TI research: the role of the nontrivial surface. The evidence for long-range ferromagnetism in TIs is primarily based upon bulk sensitive techniques, e.g. magneto transport measurement, and clear demonstrations distinguishing between surface and bulk properties are scarce. In the bulk, a TI doped with magnetic impurities can have a long-range magnetic order both in the metallic and insulating phases; on the surface, such a long-range magnetic order can also be formed independent of the bulk magnetic ordering, as the RKKY interaction induced by the Dirac fermions is generally ferromagnetic when the $E_F$ is close to the Dirac point.

It should be noted that although the sum-rules derived $m_{spin}$ versus temperature relations of the bulk-doped $Bi_{2-x}Cr_xSe_3$ seems to give a $T_c$ exceeding that of the surface-doped sample, this effect is not necessarily against the theories which suggest a more robust magnetism of the surface of a TI than that of the bulk by magnetic perturbation.[337, 342] For one reason, our calculations have been performed based on the hypothesis of a universal $n_h = 7$. While such approach gives a reasonable estimation for the globally doped $Bi_{2-x}Cr_xSe_3$, it can induce considerably large errors for the single QL

Δ-doped samples. Another argument is that the bulk-doped $Bi_{2-x}Cr_xSe_3$ in this study, may no longer merely stand for a selective doping profile in the middle of the host TI, but for a hybridized state of two overlapped TI surfaces, which can also give rise to the enhanced magnetization.

## 6.5 Conclusion

In this chapter, we have presented XMCD studies of a model magnetically doped TI, i.e. $Bi_{2-x}Cr_xSe_3$, in combination with supporting characterization techniques (magneto-transport measurement and TEM) and theoretical tools (first-principles simulations and modeling). The powerful elemental selectivity of XMCD technique has enabled unambiguous determination of the electronic and magnetic ground state of the magnetic dopants of the system under interrogation. The MBE growth has been employed as the major sample preparation method for the studies presented in this chapter, so to realize an accurate control of the dopant concentration and the doping profile.

We have observed strong dichroic XAS spectra with the feature of predominated $Cr^{3+}$ in the 10 nm globally doped $Bi_2Se_3$ epitaxial thin film. A reduced but sizable $m_{spin}$, i.e. (1.54 ± 0.2) $\mu_B$/atom and a vanishing and opposite $m_{orb}$, i.e. (-0.02 ± 0.02) $\mu_B$/atom of the Cr dopants at 6 K were obtained. This agrees with the Hund's rule for trivalent Cr, whose 3*d* shell is less-than-half full. These experimental numeric results are well reproduced by the first-principles simulations, which suggest the observed magnetic moment of Cr is due to a mixture of the $Cr_I^{3+}$ (2.98 $\mu_B$/atom), $Cr_{Bi}^{0}$ (2.93 $\mu_B$/atom), and the $(Cr_{Bi} - Cr_I)^{3+}$ complex (0.1 $\mu_B$/atom) defects.

To enhance the magnetic ordering of $Bi_{2-x}Cr_xSe_3$ and at the mean time, preserve the topological nature, proximity effect was demonstrated in this system using a high-$T_C$ FMI, i, e. YIG. We have observed unambiguous XMCD of the Cr in the $Bi_{2-x}Cr_xSe_3$ /YIG bilayer up to 50 K, corresponding to an enhanced $T_C$ in this magnetic exchange system. The unique layer selectivity of the XMCD technique has enabled a direct determination of the proximity-induced magnetization of the $Bi_{2-x}Cr_xSe_3$ at its interface with YIG. We have found a larger but faster dropping penetration depth in such a magnetic TI/FMI heterostructure compared to that in DMS/FM, which could represent a novel mechanism for the interaction between FMIs and the nontrivial TIs surface states.

In the pursuit for distinguishing the roles of the surface and the bulk doping in a 3D TI, a pair of Δ-doped $Bi_{2-x}Cr_xSe_3$ were preliminarily measured with XMCD. The magnetic ordering of these Δ-doped TIs have persisted to surprisingly high temperatures, i.e. ~ 60 K for the surface-doped and ~ 80 K for the bulk-doped $Bi_{2-x}Cr_xSe_3$, both well in excess of the globally doped $Bi_{2-x}Cr_xSe_3$, which is in high consistent with the theoretical prediction that a 3D TI doped with magnetic impurities in

the bulk can have a regime where the surface is magnetically ordered but the bulk is not. Moreover, significantly modified electronic character of $Bi_{2-x}Cr_xSe_3$ due to the different doping positions was observed, which may be associated with the nontrivial surface states.

# 7 Chapter VII Conclusions

The purpose of the studies presented in this thesis has been to gain a better understanding of the properties of some representative spintronic hybrid systems, directed towards the future spin-based IT. The synchrotron-based XMCD technique is an excellent probe for the electronic and magnetic ground states of the spintronic interfaces and for the element- and site- specific magnetic merits of materials. In combination with a set of in-house electric, magnetic and crystallinity characterization techniques and theoretical tools, XMCD has shown its power in addressing some of the most important questions of the contemporary spintronics research, such as the FM/SC interfacial hybridization and magnetism, the spin and orbital ordering of ferrites, and the fundamental magnetism of doped TIs, and the proximity effects in FM/DMS and FM/doped TI heterostructures.

The interfacial magnetic and electric nature of FM/SC systems including Co/GaAs, Ni/GaAs, Fe/GaAs, Fe/Graphene and $Co_2FeAl/Ga_{1-x}Mn_xAs$ have been demonstrated. Suppressed magnetizations of the epitaxial ML Co and Ni on GaAs(100) have been observed, which can be attributed to a combined effect of the island growth geometry at low coverage, the tendency to follow the bcc stacking of the GaAs substrate, and the detrimental interdiffusion. A reduced but still sizable magnetic moment of the ML Fe on graphene has been observed and interpreted with first-principals calculations, which attributes it to the strong hybridization of C $2p_z$ and Fe $3d_{z2}$ orbitals and the delocalization of the Fe $3d$ electrons. A significantly enhanced $T_c$ has been demonstrated in $Ga_{1-x}Mn_xAs$ due to the presence of $Co_2FeAl$ and their coupling has been proved to be ferromagnetic. Future work to explore the tuning of the spin polarized band structure of both FMs and (magnetically doped) SCs via the interface engineering will be of great interest and will have strong implications for both fundamental physics and emerging spintronics technology. Detailed TME studies are also needed to understand the interface structure.

$Fe_3O_4$ thin films with distinct thicknesses, substrates and growth methodologies have been studied. Strong dichroic XAS spectra, corresponding to an overlap of different sets of multiplet structures has been obtained. Significantly unquenched $m_{orb}$ have been universally extracted from all the samples studied, which may partially

originate from the broken symmetry of the thin film and partially due to an intrinsic property of magnetite. Such large $m_{orb}$ implies strong SOC and has strong implications for adding capacities to spintronics devices, since high <*LS*> coupling is mandatory for realizing the ultrafast switching of spin polarization by electric field and circularly polarized light. Verwey transition has been observed where stoichiometric and homogenies samples are provided. By comparing the relative contributions of the Fe cations before and after Verwey transition, the SE mechanism has been demonstrated to be preliminarily responsible for the magnetization Verwey transition of magnetite. These observations provide important information for the fundamental understanding ionic charge-ordering model of ferrites. Future work to study the thickness dependence of samples prepared by different techniques will be of interest.

The magnetism of $Bi_{2-x}Cr_xSe_3$ has been studied for the very first time using the XMCD technique. Strong dichroic XAS spectra with the feature of predominated $Cr^{3+}$ was observed in the globally doped $Bi_2Se_3$ epitaxial thin film. A reduced but sizable $m_{spin}$ and a vanishing and opposite $m_{orb}$ were obtained and are well reproduced by the first-principles simulations, which suggest a mixture of $Cr_I^{3+}$, $Cr_{Bi}^{0}$, and $(Cr_{Bi} - Cr_I)^{3+}$ complex defects. The magnetic proximity effect is demonstrated in $Bi_{2-x}Cr_xSe_3$/YIG, whereby a larger but faster dropping penetration depth with the increasing temperature has been observed, which could represent a novel mechanism for the interaction between FMIs and the nontrivial TIs surface states. A significantly enhanced surface magnetic ordering has been observed in the surface-doped $Bi_{2-x}Cr_xSe_3$, consistent with the theoretical prediction that a 3D TI doped with magnetic impurities in the bulk can have a regime where the surface is magnetically ordered but the bulk is not. All these findings provide insight into the fundamental physics in this exciting spintronic material system. Future work to further strengthen the magnetic ordering in TIs towards RT will be of both great fundamental interest and practical merits.

# Appendix A: List of Samples

**Chapter IV**

| | |
|---|---|
| Sample | 10 ML Cr/7 ML Fe/1ML Co/GaAs(100) |
| Reference No. | 31072000 |
| Growth Method | MBE, GaAs pre-annealing at 550 ℃ for 1 hour, $T_s$ = RT |
| Origin | TFM group, the Cavendish Laboratory, Cambridge University |

| | |
|---|---|
| Sample | 10 ML Cr/7 ML Co/1ML Ni/GaAs(100) |
| Reference No. | 121200 |
| Growth Method | MBE, GaAs pre-annealing at 550 ℃ for 1 hour, $T_s$ = RT |
| Origin | TFM group, the Cavendish Laboratory, Cambridge University |

| | |
|---|---|
| Sample | 30 ML Cr/30 ML Ni/1 ML Fe/graphene/300 nm $SiO_2$/Si |
| Reference No. | 250113 |
| Growth Method | MBE, graphene pre-annealing at 200 ℃ for 1 hour, $T_s$ = RT |
| Origin | Spintronics and Nanodevice Laboratory, University of York |

| | |
|---|---|
| Sample | 4 nm $Al_2O_3$/3 nm $Co_2FeAl$/150 nm $Ga_{0.93}Mn_{0.07}As$/GaAs(001) |
| Reference No. | L536 |
| Growth Method | MBE, $T_s$ = 250℃ for $Co_2FeAl$ and $T_s$ = 160℃ for $Ga_{0.93}Mn_{0.07}As$ |
| Origin | Superlattices and Microstructures Laboratory, CAS, China |

**Chapter V**

| | |
|---|---|
| Sample | 8 nm $Fe_3O_4$/MgO/GaAs(100) |
| Reference No. | L536 |
| Growth Method | MBE, postgrowth annealing at 500 K and the oxygen pressure = 5 × $10^{-5}$ mbar for 10 minutes, |
| Origin | Spintronics and Nanodevice Laboratory, University of York |

| | |
|---|---|
| Sample | 12 nm $Fe_3O_4$/MgO(100) |
| Reference No. | 635-XT-0809 |
| Growth Method | MBE, MgO pre-annealing at 600 °C for 30 minutes, plasma-assisted simultaneous oxidation, $T_s$ = 623 K and oxygen pressure = 2.5 × $10^{-7}$ torr |
| Origin | IBM Research Division, Almaden Research Center, San Jose, US |

| | |
|---|---|
| Sample | 100 nm $Fe_3O_4$/YZO(111) |
| Reference No. | JS-001 |
| Growth Method | PLD, plus postgrowth annealing at 1400 K |
| Origin | Physics Department, University of York |

**Chapter VI**

| | |
|---|---|
| Sample | 4 nm $Al_2O_3$/10 nm $Bi_{1.94}Cr_{0.06}Se_3$/Si(111) |
| Reference No. | LH-1217 |
| Growth Method | MBE, Se-rich environment, $T_s$ = 300 °C |
| Origin | Device Research Laboratory, UCLA, US |

| | |
|---|---|
| Sample | 4 nm $Al_2O_3$/10 nm $Bi_{1.89}Cr_{0.11}Se_3$/50 nm YIG/GGG(111) |
| Reference No. | LH-1236 |
| Growth Method | MBE, Se-rich environment, $T_s$ = 300 °C |
| Origin | Device Research Laboratory, UCLA, US |

| | |
|---|---|
| Sample | 4 nm $Al_2O_3$/1 nm $Bi_{1.76}Cr_{0.24}Se_3$/9 nm $Bi_2Se_3$/Si(111) |
| Reference No. | LH-1229 |
| Growth Method | MBE, Se-rich environment, $T_s$ = 300 °C |
| Origin | Device Research Laboratory, UCLA, US |

| | |
|---|---|
| Sample | 4 nm $Al_2O_3$/4 nm $Bi_2Se_3$/1 nm $Bi_{1.76}Cr_{0.24}Se_3$/5 nm $Bi_2Se_3$/Si(111) |
| Reference No. | LH-1228 |
| Growth Method | MBE, Se-rich environment, $T_s$ = 300 °C |
| Origin | Device Research Laboratory, UCLA, US |

# Appendix B: List of Beamtime

| | |
|---|---|
| Starting Date | 05. 03. 2012 |
| Finishing Date | 18. 03. 2012 |
| Shifts | 12 |
| Reference No. | |
| PI | Y. B. Xu |
| CIs | W. Q. Liu, W. Zhang, P. K. J. Wong |
| Project | XMCD Study of Rare Earth Doping in Transition Metal Thin Films |
| Station | Max-lab, Lund, Sweden |
| Beamline | I 1011 |

| | |
|---|---|
| Starting Date | 23. 01. 2013 |
| Finishing Date | 29. 01. 2013 |
| Shifts | 18 |
| Reference No. | SI8396 |
| PI | J. H. Zhao |
| CIs | W. Q. Liu, N. J. Maltby, S. P. Li, J. Lu |
| Project | XMCD study of the Curie Temperature Enhancement in $Co_2FeAl$/(Ga,Mn)As Hybrid Structures |
| Station | Diamond Light Source, RAL, UK |
| Beamline | I 10 |

| | |
|---|---|
| Starting Date | 22. 05. 2013 |
| Finishing Date | 29. 05. 2013 |
| Shifts | 18 |
| Reference No. | SI8757 |
| PI | Y. B. Xu |
| CIs | W. Q. Liu, N. J. Maltby, S. P. Li |
| Project | XMCD study of the temperature dependent exchange bias effect in FM/$BiFeO_3$ (FM=Co, FeNi) bilayers |
| Station | Diamond Light Source, RAL, UK |

| | |
|---|---|
| Beamline | I 10 |

| | |
|---|---|
| Starting Date | 05. 03. 2014 |
| Finishing Date | 18. 03. 2014 |
| Shifts | 12 |
| Reference No. | ALS-06260 |
| PI | Y. B. Xu |
| CIs | W. Q. Liu, X. F. Hu |
| Project | Probing domain wall backward motion in single/multilayer ferromagnetic nanowires under current pulses using time-resolved XPEEM |
| Station | Advance Light Source, Berkeley, USA |
| Beamline | BL 11.0.1.1 |

| | |
|---|---|
| Starting Date | 21. 05. 2014 |
| Finishing Date | 27. 05. 2014 |
| Shifts | 128 |
| Reference No. | SI9979 |
| PI | Y. B. Xu |
| CIs | W. Q. Liu, N. J. Maltby, S. P. Li |
| Project | XMCD study of the Magnetoelastic coupling in Fe/GaAs(100) and $Fe_3O_4$/GaAs(100) Heterostructures |
| Station | Diamond Light Source, RAL, UK |
| Beamline | I 10 |

| | |
|---|---|
| Starting Date | 28. 05. 2014 |
| Finishing Date | 29. 05. 2014 |
| Shifts | 6 |
| Reference No. | SI9991 |
| PI | S. P. Li |
| CI | W. Q. Liu, N. J. Maltby, Y. B. Xu |
| Project | Temperature dependent exchange bias effect in Co, FeNi /$BiFeO_3$ bilayers |
| Station | Diamond Light Source, RAL, UK |
| Beamline | I 10 |

| | |
|---|---|
| Starting Date | 10. 09. 2014 |
| Finishing Date | 16. 09. 2014 |
| Shifts | 18 |
| Reference No. | SI9975 |
| PI | Y. B. Xu |
| CI | W. Q. Liu, N. J. Maltby, S. P. Li |
| Project | XMCD study of hybridization of electron orbital and spin transfer between graphene and transition metals |
| Station | Diamond Light Source, RAL, UK |
| Beamline | I 06 |

# List of Abbreviations and Acronyms

| | |
|---|---|
| 2D | 2 Dimensional |
| 2DEG | 2 Dimensional Electron Gas |
| 3D | 3 Dimensional |
| AC | Alternating Current |
| ADC | Analogue Digital Converter |
| APERS | Angular-resolved PhotoEmission Spectroscopy |
| AES | Auger Electron Spectroscopy |
| AFM | Atomic Force Microscopy |
| ANE | Anomalous Nernst Effect |
| APB | Antiphase Boundary |
| BCC | Body Centered Cubic |
| BSE | Back Scattered Electrons |
| CCD | Charged Coupled Device |
| CI | Co-Investigator |
| CIP | Current In Plane |
| CMOS | Complementary Metal-Oxide-Semiconductor |
| CPP | Current-Perpendicular-to-Plane |
| DCXRD | Double Crystal X-Ray Diffraction |
| DMS | Diluted Magnetic Semiconductor |
| DOS | Density of State |
| DFT | Density Function Theory |
| EDX | Energy Dispersive X-ray |
| EM | Electron Microscope |
| FC | Field Cooling |
| FCC | Face Centered Cubic |
| FET | Field Effect Transistor |
| FM | Ferro- or Ferri- Magnetic Material |
| GMR | Giant Magnetoresistance |

| | |
|---|---|
| HCP | Hexagonal Close Packing |
| HM | Half Metals |
| I | Insulator |
| IT | Information Technology |
| LCP | Left Circularly Polarized |
| LED | Light Emission Diode |
| LEED | Low Energy Electron Diffraction |
| MBE | Molecular Beam Epitaxy |
| ML | Mono-Layer |
| MR | MagnetoResistance |
| MOCVD | Metal-Organic Chemical Vapor Deposition |
| MOKE | Magneto-Optical Kerr Effect |
| MRAM | Magnetic Random Access Memory |
| MTJ | Magnetic Tunnel Junction |
| NM | Non-Magnetic |
| PI | Principal Investigator |
| PBN | Pyrolytic Boron Nitride |
| PLD | Pulsed Laser Deposition |
| PPMS | Physical Property Measurement Systems |
| QW | Quantum Well |
| QHE | Quantum Hall Effect |
| QSHE | Quantum Spin Hall Effect |
| RCP | Right Circularly Polarized |
| RE | Rare Earth |
| RF | Radio Frequency |
| RHEED | Reflection High Energy Electron Diffraction |
| RKKY | Ruderman-Kittel-Kasuya-Yosida |
| RT | Room Temperature |
| SC | Semiconductor |
| SE | Secondary Electron |
| SEM | Scanning Electron Microscope |
| SHE | Spin Hall Effect |
| SNR | Signal To Noise Ratio |

| | |
|---|---|
| SP-PAS | Spin Resolved Positron Annihilation Spectroscopy |
| SQUID-VSM | Superconducting Quantum Interference Devices - Vibrating Sample Magnetometer |
| SSE | Spin Seebeck Effect |
| SV | Spin-Valve |
| TEM | Transmission Electron Microscopy |
| TI | Topological Insulator |
| TRS | Time Reversal Symmetry |
| TSP | Titanium Sublimation Pump |
| TEY | Total Electron Yield |
| TFY | Total Florescence Yield |
| UHV | Ultrahigh Vacuum |
| XAS | X-Ray Absorption Spectroscopy |
| XMCD | X-Ray Magnetic Circular Dichroism |
| XPS | X-Ray Photoelectron Spectroscopy |
| XRD | X-Ray Diffraction |
| ZFC | Zero Field Cooling |

# List of Symbols

| | |
|---|---|
| A | Atomic number |
| ° | Degree |
| $a_0$ | Lattice constant |
| $\boldsymbol{B}$ | Magnetic flux |
| e | Electron charge |
| E | Energy |
| $E_F$ | Fermi level |
| f.u. | Formula unit |
| h | Plank constant |
| $h$ | Miller Index of the plane perpendicular to (001) |
| $H_c$ | Coercive field |
| $\boldsymbol{k}$ | Wavevector |
| $k$ | Miller Index of the plane perpendicular to (100) |
| $\boldsymbol{M}$ | Magnetization |
| $m_{orb}$ | Orbital moment |
| $m_{spin}$ | Spin moment |
| $m_{total}$ | Total moment |
| $M_s$ | Saturation magnetization |
| $\boldsymbol{p}$ | Momentum operator |
| P | Spin polarization |
| $R_{\uparrow\downarrow}$ | Spin resistance |
| $T_c$ | Curie temperature |
| V | Potential |
| Z | Atomic number |
| γ | Fresnel reflection coefficient |
| ΔH | Formation energy |
| Δn | Number of change |
| $\lambda_D$ | The sodium D-lines |
| μ | Chemical potential |
| $\mu_{\uparrow\downarrow}$ | Electrochemical potentials |
| $\mu_B$ | Bohr magneton |
| ν | Frequency |

| | |
|---|---|
| $\rho_{\uparrow\downarrow}$ | Resistivity |
| $\sigma^{\pm}$ | Photocurrent |
| $\tau$ | Spin lifetime |
| $\tau_R$ | Recombination time |
| $K_0$ | Empirical constants |
| $E_{ex}$ | Exchange energy |
| $E_k$ | Magneto-crystalline anisotropy energy |
| $E_M$ | Demagnetization energy |
| $E_k$ | Zeeman energy |
| $J_{ex}$ | Exchange constant |
| $\boldsymbol{S}$ | Spin momentum |
| $\alpha$ | Angle |
| H | Magnetic Field |
| D | Density of States |
| $\chi$ | Magnetic susceptibility |

# Bibliography

[1] Xu, Y.B. and Thompson, S.M. Spintronic Materials and Technology. *Taylor and Francis Group*, London, 2006.

[2] Moore, G. E. Cramming More Components Onto Integrated Circuits. *Proc. IEEE* **86,** 82–85 (1998).

[3] Baibich, M., Broto, J., Fert, A. & Dau, F. Van. Giant magnetoresistance of (001) Fe/(001) Cr magnetic superlattices. *Phys. Rev. Lett.* **61,** 2472–2475 (1988).

[4] Binasch, G., Grünberg, P., Saurenbach, F. & Zinn, W. Enhanced magnetoresistance in layered magnetic structures with antiferromagnetic interlayer exchange. *Phys. Rev. B* **39,** 4828–4830 (1989).

[5] Parkin, S. S. P., More, N. & Roche, K. P. Oscillations in exchange coupling and magnetoresistance in metallic superlattice structures: Co/Ru, Co/Cr, and Fe/Cr. *Phys. Rev. Lett.* **64,** 2304–2307 (1990).

[6] Valet, T. & Fert, A. Theory of the perpendicular magnetoresistance in magnetic multilayers. *Phys. Rev. B* **48,** 7099–7113 (1993).

[7] Dieny, B., Speriosu, V. S., Parkin, S. S. P., Gurney, B. A., Wilhoit, D. R. & Mauri, D. Giant magnetoresistive in soft ferromagnetic multilayers. *Phys. Rev. B* **43,** 1297–1300 (1991).

[8] Moodera, J. S., Kinder, L. R., Wong, T. M. & Meservey, R. Large Magnetoresistance at Room Temperature in Ferromagnetic Thin Film Tunnel Junctions. *Phys. Rev. Lett.* **74,** 3273–3276 (1995).

[9] Zorpette, G. The quest for the SPIN transistor. *IEEE Spectr.* **39,** 30–35 (2001).

[10] Kikkawa, J. M. & Awschalom, D. D. Resonant Spin Amplification in n-Type GaAs. *Phys. Rev. Lett.* **80,** 4313–4316 (1998).

[11] Kikkawa, J. M. & Awschalom, D. D. Lateral drag of spin coherence in gallium arsenide. **397,** 139–141 (1999).

[12] Hirsch, J. Spin Hall Effect. *Phys. Rev. Lett.* **83,** 1834–1837 (1999).

[13] Wunderlich, J., Kaestner, B., Sinova, J. & Jungwirth, T. Experimental Observation of the Spin-Hall Effect in a Two-Dimensional Spin-Orbit Coupled Semiconductor System. *Phys. Rev. Lett.* **94,** 047204 (2005).

[14] Kato, Y. K., Myers, R. C., Gossard, A. C. & Awschalom, D. D. Observation of the spin Hall effect in semiconductors. *Science* **306,** 1910–3 (2004).

[15] Clark, W. & Feher, G. Nuclear Polarization in InSb by a DC Current. *Phys. Rev. Lett.* **10,** 134–138 (1963).

[16] Meier, F. and Zakharchenya, B.P. Optical Orientation. Worth-Holland, New York, 8, 1984.

[17] Taniyama, T., Wada, E., Itoh, M. & Yamaguchi, M. Electrical and optical spin injection in ferromagnet/semiconductor heterostructures. *NPG Asia Mater.* **3,** 65–73 (2011).

[18] Datta, S. & Das, B. Electronic analog of the electro-optic modulator. *Appl. Phys. Lett.* **56,** 665 (1990).

[19]Bychkov, Y. A. & Rashba, É. I. Properties of a 2D electron gas with lifted spectral degeneracy. *Sov. J. Exp. Theor. Phys. Lett.* **39,** 78 (1984).

[20] Sugahara, S. & Tanaka, M. A spin metal–oxide–semiconductor field-effect transistor using half-metallic-ferromagnet contacts for the source and drain. *Appl. Phys. Lett.* **84,** 2307 (2004).

[21] Hall, K. C. & Flatté, M. E. Performance of a spin-based insulated gate field effect transistor. *Appl. Phys. Lett.* **88,** 162503 (2006).

[22] Koo, H. C., Kwon, J. H., Eom, J., Chang, J., Han, S. H. & Johnson, M. Control of spin

precession in a spin-injected field effect transistor. *Science* **325,** 1515–8 (2009).

[23] Lou, X., Adelmann, C., Furis, M., Crooker, S., Palmstrøm, C. & Crowell, P. Electrical Detection of Spin Accumulation at a Ferromagnet-Semiconductor Interface. *Phys. Rev. Lett.* **96,** 176603 (2006).

[24] Lou, X., Adelmann, C., Crooker, S. a., Garlid, E. S., Zhang, J., Reddy, K. S. M., Flexner, S. D., Palmstrøm, C. J. & Crowell, P. a. Electrical detection of spin transport in lateral ferromagnet–semiconductor devices. *Nat. Phys.* **3,** 197–202 (2007).

[25] Zhu, H., Ramsteiner, M., Kostial, H., Wassermeier, M., Schönherr, H.-P. & Ploog, K. Room-Temperature Spin Injection from Fe into GaAs. *Phys. Rev. Lett.* **87,** 016601 (2001).

[26] Mattana, R., George, J.-M., Jaffrès, H., Nguyen Van Dau, F., Fert, A., Lépine, B., Guivarc'h, A. & Jézéquel, G. Electrical detection of spin accumulation in a p-type GaAs quantum well. *Phys. Rev. Lett.* **90,** 166601 (2003).

[27] Ferhat, M. & Yoh, K. High quality $Fe_{3-\delta}O_4$/InAs hybrid structure for electrical spin injection. *Appl. Phys. Lett.* **90,** 112501 (2007).

[28] Ramsteiner, M., Hao, H., Kawaharazuka, a., Zhu, H., Kästner, M., Hey, R., Däweritz, L., Grahn, H. & Ploog, K. Electrical spin injection from ferromagnetic MnAs metal layers into GaAs. *Phys. Rev. B* **66,** 081304 (2002).

[29] Beschoten, B., Johnston-Halperin, E., Young, D., Poggio, M., Grimaldi, J., Keller, S., DenBaars, S., Mishra, U., Hu, E. & Awschalom, D. Spin coherence and dephasing in GaN. *Phys. Rev. B* **63,** 121202 (2001).

[30] Krishnamurthy, S., van Schilfgaarde, M. & Newman, N. Spin lifetimes of electrons injected into GaAs and GaN. *Appl. Phys. Lett.* **83,** 1761 (2003).

[31] Culcer, D., Hwang, E. H., Stanescu, T. D. & Das Sarma, S. Two-dimensional surface charge transport in topological insulators. *Phys. Rev. B* **82,** 155457 (2010).

[32] Pesin, D. & MacDonald, A. H. Spintronics and pseudospintronics in graphene and

topological insulators. *Nat. Mater.* **11,** 409–16 (2012).

[33] Xue, Q.-K. Nanoelectronics: A topological twist for transistors. *Nat. Nanotechnol.* **6,** 197–8 (2011).

[34] Žutić, I., Fabian, J. & Das Sarma, S. Spin injection through the depletion layer: A theory of spin-polarized p-n junctions and solar cells. *Phys. Rev. B* **64,** 121201 (2001).

[35]Elasticity, R. M. & Escape, A. Injection and detection of a spin-polarized current in a light-emitting diode. **402,** 787–790 (1999).

[36] Ohno, Y., Young, D. K., Beschoten, B., Matsukura, F., Ohno, H. & Awschalom, D. D. Electrical spin injection in a ferromagnetic semiconductor heterostructure. **402,** 790–792 (1999).

[37] Oestreich, M., Hübner, J. & Hägele, D. Spin injection into semiconductors. *Appl. Phys. Lett.* **74,** 1251–1253 (1999).

[38] Jonker, B., Park, Y., Bennett, B., Cheong, H., Kioseoglou, G. & Petrou, a. Robust electrical spin injection into a semiconductor heterostructure. *Phys. Rev. B* **62,** 8180–8183 (2000).

[39] Ohno, H. Making Nonmagnetic Semiconductors Ferromagnetic. *Science* **281,** 951–956 (1998).

[40] Esaki, L., Stiles, P. & Molnar, S. Magnetointernal Field Emission in Junctions of Magnetic Insulators. *Phys. Rev. Lett.* **19,** 852–854 (1967).

[41] Munekata, H., Ohno, H., von Molnar, S., Segmüller, A., Chang, L. & Esaki, L. Diluted magnetic III-V semiconductors. *Phys. Rev. Lett.* **63,** 1849–1852 (1989).

[42] Ohno, H., Shen, a., Matsukura, F., Oiwa, a., Endo, a., Katsumoto, S. & Iye, Y. (Ga,Mn)As: A new diluted magnetic semiconductor based on GaAs. *Appl. Phys. Lett.* **69,** 363 (1996).

[43] Ohno, H., Chiba, D., Matsukura, F., Omiya, T., Abe, E., Dietl, T., Ohno, Y. & Ohtani,

K. Electric-field control of ferromagnetism. *Nature* **408,** 944–6 (2000).

[44] Chiba, F., Omiya, D., Abe, T., Dietl, E., Ohno, Ohtani, T., Y., K. & Ohno, H. Control of ferromagnetism in field-effect transistor of a magnetic semiconductor. *Phys. E Low-dimensional Syst. Nanostructures* **12,** 351–355 (2002).

[45] Furdyna, J. K., and Kossut, J. *"Semiconductor and Semimetals", Academic*, New York, 1988.

[46] Adhikari T. and Basu. S. "Electrical Properties of Gallium Manganese Antimonide: a New Diluted Magnetic Semiconductor". *Jpn. J. Appl. Phys.,* **33:**4581, 1994.

[47] Edmonds, K. W., van der Laan, G., Farley, N. R. S., Campion, R. P., Gallagher, B. L., Foxon, C. T., Cowie, B. C. C., Warren, S. & Johal, T. K. Magnetic Linear Dichroism in the Angular Dependence of Core-Level Photoemission from (Ga,Mn)As Using Hard X Rays. *Phys. Rev. Lett.* **107,** 197601 (2011).

[48] Wang, M., Campion, R. P., Rushforth, a. W., Edmonds, K. W., Foxon, C. T. & Gallagher, B. L. Achieving high Curie temperature in (Ga,Mn)As. *Appl. Phys. Lett.* **93,** 132103 (2008).

[49] Edmonds, K. W., Wang, K. Y., Campion, R. P., Neumann, A. C., Farley, N. R. S., Gallagher, B. L. & Foxon, C. T. High-Curie-temperature Ga[sub 1−x]Mn[sub x]As obtained by resistance-monitored annealing. *Appl. Phys. Lett.* **81,** 4991 (2002).

[50] MacDonald, A. H., Schiffer, P. & Samarth, N. Ferromagnetic semiconductors: moving beyond (Ga,Mn)As. *Nat. Mater.* **4,** 195–202 (2005).

[51] Coey, J. M. Dilute magnetic oxides. *Curr. Opin. Solid State Mater. Sci.* **10,** 83–92 (2006).

[52] Cullity, B. D. *Introduction to magnetic materials*. IEEE Press, 2009.

[53] Beaurepaire, E., Bulou, H., Scheurer, F., Kappler, J. P. *Magnetism: A synchrotron radiation approach*.(Spinger, 2006.

[54] Williams, H. J., Bozorth, R. M. & Shockley, W. Magnetic Domain Patterns on Single Crystals of Silicon Iron. *Phys. Rev.* **75,** 155–178 (1949).

[55] Filipe, A., Schuhl, A. & Galtier, P. Structure and magnetism of the Fe/GaAs interface. *Appl. Phys. Lett.* **70,** 129 (1997).

[56] Prinz, G. A. Magnetic properties of single-crystal (110) iron films grown on GaAs by molecular beam epitaxy (invited). *J. Appl. Phys.* **53,** 2087 (1982).

[57] Xu, Y. B., Kernohan, E. T. M., Freeland, D. J., Ercole, A., Tselepi, M. & Bland, J. A. C. et al. Evolution of the ferromagnetic phase of ultrathin Fe films grown on GaAs(100)-4x6. *Phys. Rev. B* **58,** 890–896 (1998).

[58] J.S. Claydon, Y.B. Xu, M. Tselepi, J.A.C. Bland, and G. van der Laan. "Direct observation of a bulklike spin moment at the Fe/GaAs(100)-4×6 interface". *Phys. Rev. Lett.*, **93**:037206, 2004.

[59] Monchesky, T. & Unguris, J. Magnetic properties of Co/GaAs(110). *Phys. Rev. B* **74,** 241301 (2006).

[60] Scheck, C., Evans, P., Zangari, G. & Schad, R. Sharp ferromagnet/semiconductor interfaces by electrodeposition of Ni thin films onto n-GaAs(001) substrates. *Appl. Phys. Lett.* **82,** 2853 (2003).

[61] Li, J., Wang, Z. Y., Tan, A., Glans, P. A., Arenholz, E., Hwang, C., Shi, J. & Qiu, Z. Q. Magnetic dead layer at the interface between a Co film and the topological insulator $Bi_2Se_3$. *Phys. Rev. B* **86,** 054430 (2012).

[62] B. G. Streetman. Solid State Electronic Devices. *Prentice Hall*, 1995.

[63] Rhoderick, E. H., and Williams, R. H. Metal-Semiconductor Contacts. *Oxford University Press*, Oxford, 1988.

[64] H. J. Zhu, M. Ramsteiner, H. Kostial, M. Wassermeier, H.-P.Schönherr, and K.H. Ploog. "Room-Temperature Spin Injection from Fe into GaAs". *Phys. Rev. Lett.* **87:**016601, 2001.

[65] Ikeda, S., Miura, K., Yamamoto, H., Mizunuma, K., Gan, H. D., Endo, M., Kanai, S., Hayakawa, J., Matsukura, F. & Ohno, H. A perpendicular-anisotropy CoFeB-MgO magnetic tunnel junction. *Nat. Mater.* **9,** 721–4 (2010).

[66]Wang, W.-G., Li, M., Hageman, S. & Chien, C. L. Electric-field-assisted switching in magnetic tunnel junctions. *Nat. Mater.* **11,** 64–8 (2012).

[67] Alvarado, S. F. & Renaud, P. Observation of spin-polarized-electron tunneling from a ferromagnet into GaAs. *Phys. Rev. Lett.* **68,** 1387–1390 (1992).

[68] Rashba, E. Theory of electrical spin injection: Tunnel contacts as a solution of the conductivity mismatch problem. *Phys. Rev. B* **62,** R16267–R16270 (2000).

[69] Hanbicki, A. T., Jonker, B. T., Itskos, G., Kioseoglou, G. & Petrou, A. Efficient electrical spin injection from a magnetic metal/tunnel barrier contact into a semiconductor. *Appl. Phys. Lett.* **80,** 1240 (2002).

[70] Motsnyi, V., Van Dorpe, P., Van Roy, W., Goovaerts, E., Safarov, V., Borghs, G. & De Boeck, J. Optical investigation of electrical spin injection into semiconductors. *Phys. Rev. B* **68,** 245319 (2003).

[71] Jiang, X., Wang, R., Shelby, R., Macfarlane, R., Bank, S., Harris, J. & Parkin, S. Highly Spin-Polarized Room-Temperature Tunnel Injector for Semiconductor Spintronics using MgO(100). *Phys. Rev. Lett.* **94,** 056601 (2005).

[72] Streetman, B. G.. Solid State Electronic Devices. *Prentice Hall*, 1995.

[73] Geim, A. K. & Novoselov, K. S. The rise of graphene. *Nat. Mater.* **6,** 183–191 (2007).

[74] Min, H., Hill, J. E., Sinitsyn, N. A, Sahu, B. R., Kleinman, L. & MacDonald, A. H. Intrinsic and Rashba spin-orbit interactions in graphene sheets. *Phys. Rev. B* **74,** 165310 (2006).

[75] Tombros, N., Jozsa, C., Popinciuc, M., Jonkman, H. T. & van Wees, B. J. Electronic spin transport and spin precession in single graphene layers at room temperature. *Nature* **448,** 571–574 (2007).

[76] Karpan, V., Giovannetti, G., Khomyakov, P., Talanana, M., Starikov, A., Zwierzycki, M., van den Brink, J., Brocks, G. & Kelly, P. Graphite and graphene as perfect spin filters. *Phys. Rev. Lett.* **99,** 176602 (2007).

[77] Novoselov, K. S., Geim, A K., Morozov, S. V, Jiang, D., Zhang, Y., Dubonos, S. V, Grigorieva, I. V & Firsov, A A Electric Field Effect in Atomically Thin Carbon Films. *Science* **306,** 666–9 (2004).

[78] Han, W. & Kawakami, R. K. Spin relaxation in single-layer and bilayer graphene. *Phys. Rev. Lett.* **107,** 047207 (2011).

[79] Ohishi, M., Shiraishi, M., Nouchi, R., Nozaki, T., Shinjo, T. & Suzuki, Y. Spin injection into a graphene thin film at room temperature. *Jpn. J. Appl. Phys.* **46,** L605–L607 (2007).

[80] Ando, K. & Saitoh, E., Inverse spin-Hall effect in palladium at room temperature. *J. Appl. Phys.* **108**, 113925 (2010).

[81] Novoselov, K. S., Geim, a K., Morozov, S. V, Jiang, D., Zhang, Y., Dubonos, S. V, Grigorieva, I. V & Firsov, a a. Electric field effect in atomically thin carbon films. *Science* **306,** 666–9 (2004).

[82] Iqbal, M. Z., Iqbal, M. W., Lee, J. H., Kim, Y. S., Chun, S. H. & Eom, J. Spin valve effect of NiFe/graphene/NiFe junctions. *Nano Res.* **6,** 373–380 (2013).

[83] van 't Erve, O. M. J., Friedman, A. L., Cobas, E.,Li, C. H.,Robinson, J. T. & Jonker, B. T. Low-resistance spin injection into silicon using graphene tunnel barriers. *Nat. Nanotechnol.* **7,** 737–742 (2012).

[84] Song, C., Sperl, M., Utz, M., Ciorga, M., Woltersdorf, G., Schuh, D., Bougeard, D., Back, C. H. & Weiss, D. Proximity Induced Enhancement of the Curie Temperature in Hybrid Spin Injection Devices. **056601,** 1–4 (2011).

[85] Maccherozzi, F., Sperl, M., Panaccione, G., Minár, J., Polesya, S., Ebert, H., Wurstbauer, U., Hochstrasser, M., Rossi, G., Woltersdorf, G., Wegscheider, W. &

Back, C. Evidence for a Magnetic Proximity Effect up to Room Temperature at Fe/(Ga,Mn)As Interfaces. *Phys. Rev. Lett.* **101,** 267201 (2008).

[86] Sperl, M., Maccherozzi, F., Borgatti, F., Verna, a., Rossi, G., Soda, M., Schuh, D., Bayreuther, G., Wegscheider, W., Cezar, J. C., Yakhou, F., Brookes, N. B., Back, C. H. & Panaccione, G. Identifying the character of ferromagnetic Mn in epitaxial Fe/(Ga,Mn)As heterostructures. *Phys. Rev. B* **81,** 035211 (2010).

[87] Olejnik, K., Wadley, P., Haigh, J. A., Edmonds, K. W., Campion, R. P., Rushforth, A. W., Gallagher, B. L., Foxon, C. T., Jungwirth, T., Wunderlich, J., Dhesi, S. S., Cavill, S. A., van der Laan, G. & Arenholz, E. Exchange bias in a ferromagnetic semiconductor induced by a ferromagnetic metal: Fe/(Ga,Mn)As bilayer films studied by XMCD measurements and SQUID magnetometry. *Phys. Rev. B* **81,** 104402 (2010).

[88] Honolka, J., Khajetoorians, A. A., Sessi, V., Wehling, T. O., Stepanow, S., Mi, J.-L., Iversen, B. B., Schlenk, T., Wiebe, J., Brookes, N. B., Lichtenstein, A. I., Hofmann, P., Kern, K. & Wiesendanger, R. In-plane magnetic anisotropy of Fe atoms on $Bi_2Se_3$(111). *Phys. Rev. Lett.* **108,** 256811 (2012).

[89] Wray, L. A., Xu, S.-Y., Xia, Y., Hsieh, D., Fedorov, A. V., Hor, Y. S., Cava, R. J., Bansil, A., Lin, H. & Hasan, M. Z. A topological insulator surface under strong Coulomb, magnetic and disorder perturbations. *Nat. Phys.* **7,** 32–37 (2010).

[90] West, D., Sun, Y. Y., Zhang, S. B., Zhang, T., Ma, X., Cheng, P., Zhang, Y. Y., Chen, X., Jia, J. F. & Xue, Q. K. Identification of magnetic dopants on the surfaces of topological insulators: Experiment and theory for Fe on $Bi_2Te_3$(111). *Phys. Rev. B* **85,** 081305 (2012).

[91] Eremeev, S. V., Men'shov, V. N., Tugushev, V. V., Echenique, P. M. & Chulkov, E. V. Magnetic proximity effect at the three-dimensional topological insulator/magnetic insulator interface. *Phys. Rev. B* **88**, 144430 (2013).

[92] Zhao, X., Dai, X.-Q., Zhao, B., Wang, N. & Ji, Y.-Y. Cr adsorption induced magnetism in Bi2Se3 film by proximity effects. *Phys. E Low-dimensional Syst. Nanostructures* **55**, 9 (2014).

[93] de Groot, R. A. & Mueller, F. M. New Class of Materials: Half-Metallic Ferromagnets. *Phys. Rev. Lett.* **50,** 2024 (1983).

[94] Kawasuso, A, Fukaya, Y., Maekawa, M., Mochizuki, I. & Zhang, H. Spin-polarized positron annihilation spectroscopy for spintronics applications. *J. Phys. Conf. Ser.* **443,** 012084 (2013).

[95] Wong, P. K. J. Fabrication and Characterization of Hybrid Magnetic / Semiconductor Materials and Devices. PhD thesis, university of York (2009).

[96] Webster, H. P. J. and Ziebeck, K. R. A. Alloys and Compounds of d-Elements with Main Group Elements. Part 2., *Alloys and Compounds of d-Elements with Main Group Elements. Part 2.* **19c,** Springer-Verlag, 1988.

[97] Hanssen, K., Mijnarends, P., Rabou, L. & Buschow, K. Positron-annihilation study of the half-metallic ferromagnet NiMnSb: Experiment. *Phys. Rev. B* **42,** 1533 (1990).

[98] Tanaka, C. T., Nowak, J. & Moodera, J. S. Spin-polarized tunneling in a half-metallic ferromagnet. *J. Appl. Phys.* **86,** 6239 (1999).

[99] Soulen Jr., R. J. Measuring the Spin Polarization of a Metal with a Superconducting Point Contact. *Science.* **282,** 85 (1998).

[100] Wurmehl, S., Fecher, G., Kandpal, H., Ksenofontov, V., Felser, C., Lin, H.-J. & Morais, J. Geometric, electronic, and magnetic structure of $Co_2FeSi$: Curie temperature and magnetic moment measurements and calculations. *Phys. Rev. B* **72,** 184434 (2005).

[101] Gercsi, Z. & Hono, K. Ab initio predictions for the effect of disorder and quarternary alloying on the half-metallic properties of selected $Co_2Fe$-based Heusler alloys. *J. Phys. Condens. Matter* **19,** 326216 (2007).

[102] Marukame, T., Ishikawa, T., Matsuda, K.-I., Uemura, T. & Yamamoto, M. High tunnel magnetoresistance in fully epitaxial magnetic tunnel junctions with a full-Heusler alloy $Co_2Cr_{0.6}Fe_{0.4}Al$ thin film. *Appl. Phys. Lett.* **88,** 262503 (2006).

[103] Okamura, S., Miyazaki, A., Sugimoto, S., Tezuka, N. & Inomata, K. Large tunnel magnetoresistance at room temperature with a $Co_2FeAl$ full-Heusler alloy electrode. *Appl. Phys. Lett.* **86,** 232503 (2005).

[104] Sakuraba, Y., Nakata, J., Oogane, M., Ando, Y., Kato, H., Sakuma, A., Miyazaki, T. & Kubota, H. Magnetic tunnel junctions using B2-ordered $Co_2MnAl$ Heusler alloy epitaxial electrode. *Appl. Phys. Lett.* **88,** 022503 (2006).

[105] Inomata, K., Okamura, S., Miyazaki, A., Kikuchi, M., Tezuka, N., Wojcik, M. & Jedryka, E. Structural and magnetic properties and tunnel magnetoresistance for $Co_2(Cr,Fe)Al$ and $Co_2FeSi$ full-Heusler alloys. *J. Phys. D. Appl. Phys.* **39,** 816 (2006).

[106] Xie, J. Q., Dong, J. W., Lu, J., Palmstrøm, C. J. & McKernan, S. Epitaxial growth of ferromagnetic Ni[sub 2]MnIn on (001) InAs. *Appl. Phys. Lett.* **79,** 1003 (2001).

[107] Dong, J. W., Chen, L. C., Palmstrom, C. J., James, R. D. & McKernan, S. Molecular beam epitaxy growth of ferromagnetic single crystal (001) $Ni_2MnGa$ on (001) GaAs. *Appl. Phys. Lett.* **75,** 1443 (1999).

[108] Orgassa, D., Fujiwara, H., Schulthess, T. & Butler, W. First-principles calculation of the effect of atomic disorder on the electronic structure of the half-metallic ferromagnet NiMnSb. *Phys. Rev. B* **60,** 13237–13240 (1999).

[109] Dedkov, Y., Rüdiger, U. & Güntherodt, G. Evidence for the half-metallic ferromagnetic state of Fe3O4 by spin-resolved photoelectron spectroscopy. *Phys. Rev. B* **65,** 064417 (2002).

[110] Ramos, R., Kikkawa, T., Uchida, K., Adachi, H., Lucas, I., Aguirre, M. H., Algarabel, P., Morellón, L., Maekawa, S., Saitoh, E. & Ibarra, M. R. Observation of the spin Seebeck effect in epitaxial $Fe_3O_4$ thin films. *Appl. Phys. Lett.* **102,** 072413 (2013).

[111] Liao, Z.-M., Li, Y.-D., Xu, J., Zhang, J.-M., Xia, K. & Yu, D.-P. Spin-filter effect in magnetite nanowire. *Nano Lett.* **6,** 1087–91 (2006).

[112] Gooth, J., Zierold, R., Gluschke, J. G., Boehnert, T., Edinger, S., Barth, S. & Nielsch,

K. Gate voltage induced phase transition in magnetite nanowires. *Appl. Phys. Lett.* **102,** 073112 (2013).

[113] Hu, G. & Suzuki, Y. Negative spin polarization of Fe3O4 in magnetite/manganite-based junctions. *Phys. Rev. Lett.* **89,** 276601 (2002).

[114] Verwey, E. J. W. Electronic Conduction of Magnetite ($Fe_3O_4$) and its Transition Point at Low Temperatures. *Nature* **144,** 327–328 (1939).

[115] Gunnarsson, O. & Schönhammer, K. Electron spectroscopies for Ce compounds in the impurity model. *Phys. Rev. B* **28,** 4315–4341 (1983).

[116] Walz, F. The Verwey transition — a topical review. *J. Phys. Condens. Matter* **14,** R285–R340 (2004).

[117] Siegmann, J. S. ohr H. C. *Magnetism from fundamental to dynamics*. (Spinger, 2006).

[118] Zhang, Z. & Satpathy, S. Electron states, magnetism, and the Verwey transition in magnetite. *Phys. Rev. B* **44,** 13319–13331 (1991).

[119] Schmidt, G., Ferrand, D., Molenkamp, L., Filip, a. & van Wees, B. Fundamental obstacle for electrical spin injection from a ferromagnetic metal into a diffusive semiconductor. *Phys. Rev. B* **62,** R4790–R4793 (2000).

[120] Lu, Y. X., Claydon, J. S. & Xu, Y. B. Epitaxial growth and magnetic properties of half-metallic Fe 3 O 4 on GaAs ( 100 ). *Phys. Rev. B* **70,** 233304 (2004).

[121] Hassan, S. S. A., Xu, Y. B., Ahmad, E. & Lu, Y. Transport and Magneto-Transport Characteristics of Fe 3 O 4 /GaAs Hybrid Structure. **43,** 2875–2877 (2007).

[122] Eerenstein, W., Palstra, T., Saxena, S. & Hibma, T. Spin-Polarized Transport across Sharp Antiferromagnetic Boundaries. *Phys. Rev. Lett.* **88,** 247204 (2002).

[123] Shepherd, J., Koenitzer, J., Aragón, R., Spalek, J. & Honig, J. Heat capacity and entropy of nonstoichiometric magnetite Fe3(1- delta )O4: The thermodynamic nature of the Verwey transition. *Phys. Rev. B. Condens. Matter* **43,** 8461–8471 (1991).

[124] Morrall, P., Schedin, F., Case, G., Thomas, M., Dudzik, E., van der Laan, G. & Thornton, G. Stoichiometry of $Fe_{3-\delta}O_4$(111) ultrathin films on Pt(111). *Phys. Rev. B* **67,** 214408 (2003).

[125] Chen, Y. Z., Sun, J. R., Han, Y. N., Xie, X. Y., Shen, J., Rong, C. B., He, S. L. & Shen, B. G. Microstructure and magnetic properties of strained $Fe_3O_4$ films. *J. Appl. Phys.* **103,** 07D703 (2008).

[126] Chapline, M. G. & Wang, S. X. Observation of the Verwey transition in thin magnetite films. *J. Appl. Phys.* **97,** 123901 (2005).

[127] Shou-Cheng Zhang B. Andrei Bernevig, Taylor L. Hughes. Quantum spin hall effect and topological phase transition in hgte quantum wells. *Science* **314**, 1757 (2009).

[128] König, M., S. Wiedmann, C. Brüne, A. Roth, H. Buhmann, L. W. Molenkamp, X. L. Qi, and S. C. Zhang, *Science* **318**, 766 (2007).

[129] Hsieh, D., Qian, D., Wray, L., Xia, Y., Hor, Y. S., Cava, R. J. & Hasan, M. Z. A topological Dirac insulator in a quantum spin Hall phase. *Nature* **452,** 970–974 (2008).

[130] Yu, R., Zhang, W., Zhang, H.-J., Zhang, S.-C., Dai, X. & Fang, Z. Quantized anomalous Hall effect in magnetic topological insulators. *Science* **329,** 61–4 (2010).

[131] Chang, C.-Z., Zhang, J., Feng, X., Shen, J., Zhang, Z., Guo, M., Li, K., Ou, Y., Wei, P., Wang, L.-L., Ji, Z.-Q., Feng, Y., Ji, S., Chen, X., Jia, J., Dai, X., Fang, Z., Zhang, S.-C., He, K., Wang, Y., Lu, L., Ma, X.-C. & Xue, Q.-K. Experimental observation of the quantum anomalous Hall effect in a magnetic topological insulator. *Science* **340,** 167–70 (2013).

[132] Checkelsky, J. G., Ye, J., Onose, Y., Iwasa, Y. & Tokura, Y. Dirac-fermion-mediated ferromagnetism in a topological insulator. *Nat. Phys.* **8,** 729–733 (2012).

[133] Liu, Q., Liu, C. X., Xu, C., Qi, X. L. & Zhang, S. C. Magnetic impurities on the surface of a topological insulator. *Phys. Rev. Lett.* **102,** (2009).

[134] Zhu, J. J., Yao, D. X., Zhang, S. C. & Chang, K. Electrically controllable surface magnetism on the surface of topological insulators. *Phys. Rev. Lett.* **106,** (2011).

[135] Will, I, Development of a UHV MBE growth facility with in-situ MOKE and strain-dependent magnetometry and its applications to ultra-thin Co and Fe films growth on GaAs(100) and InAs/GaAs(100) substrates. PhD thesis, university of York (2009).

[136] Henini, M. Molecular beam epitaxy from research to mass-production. *III-Vs Rev.* **9,** 32–34 (1996).

[137] Gallinat, C. S., Koblmüller, G., Brown, J. S. & Speck, J. S. A growth diagram for plasma-assisted molecular beam epitaxy of In-face InN. *J. Appl. Phys.* **102,** 064907 (2007).

[138] Arthur, J. R. Surface Stoichiometry and Structure of GaAs and GaP. *J. Vac. Sci. Technol.* **9,** 910 (1972).

[139] Drathen P, Ranke W, Jacobi K. Composition and structure of differently prepared GaAs(100) surfaces studied by LEED and AES. *Surf Sci* **77**, L162 (1978).

[140] Ploog, K. Surface studies during molecular beam epitaxy of gallium arsenide. *J. Vac. Sci. Technol.* **16,** 838 (1979).

[141] Bachrach, R. Z. Reconstructions of GaAs and AlAs surfaces as a function of metal to As ratio. *J. Vac. Sci. Technol.* **19,** 335 (1981).

[142] Larsen PK, Neave JH, van der Veen JF, Dobson PJ, Joyce BA. GaAs(001)-c(4 x 4): a chemisorbed structure. *Phys Rev B* **27**, 4966 (1983).

[143] Chiang T-C, Ludeke R, Aono M, Landgren G, Himpsel FJ, Eastman DE. Angle-resolved photoemission studies of GaAs(100) surfaces grown by molecular-beam epitaxy. *Phys Rev B* **27**, 4770 (1983).

[144] Deparis C, Massies J. Surface stoichiometry variation associated with GaAs (001) reconstruction transitions. *J Cryst Growth* **108**, 157 (1991).

[145] Black, R. C. & Wellstood, F. C. in *SQUID Handb. Appl. SQUIDs SQUID Syst.* **2,** 391–440 (2006).

[146] Dellby N, Krivanek OL, Nellist PD, Batson PE, Lupini AR Progress in aberration-corrected STEM,. *J ElectronMicrosc* **50** 177 (2001).

[147] Batson, P. E., Dellby, N. & Krivanek, O. L. Sub-ångstrom resolution using aberration corrected electron optics. *Nature* **418,** 617–20 (2002).

[148] Sanchez, S. I., Small, M. W., Sivaramakrishnan, S., Wen, J., Zuo, J.-M. & Nuzzo, R. G. Visualizing Materials Chemistry at Atomic Resolution. *Anal. Chem.* **82,** 2599–2607 (2010).

[149]Williams, G. X-ray data booklet. *X-ray Data Booklet*. (2001).

[150] James A. Clarke. The science and technology of undulators and wigglers. Oxford science publications (2004)

[151] Philip John Duke. Synchrotron radiation: production and properties. Oxford science publications (2000).

[152] Wang, H., Bencok, P., Steadman, P., Longhi, E., Zhu, J. & Wang, Z. Complete polarization analysis of an APPLE II undulator using a soft X-ray polarimeter. *J. Synchrotron Radiat.* **19,** 944 (2012).

[153] J. Stöhr and H.C. Siegmann. Magnetism. Springer, 2006.

[154] van der Laan, G. & Figueroa, A. I. X-ray magnetic circular dichroism—a versatile tool to study magnetism. *Coord. Chem. Rev.* doi:10.1016/j.ccr.2014.03.018 (2014).

[155] J. Stöhr. NEXAFS. Springer, Berlin Heidelberg, 25, 1992.

[156] Shelford, L. R., Hesjedal, T., Collins-McIntyre, L., Dhesi, S. S., Maccherozzi, F. & van der Laan, G. Electronic structure of Fe and Co magnetic adatoms on $Bi_2Te_3$ surfaces. *Phys. Rev. B* **86,** 081304 (2012).

[157] van der Laan, G. & Thole, B. Strong magnetic x-ray dichroism in 2p absorption spectra of 3d transition-metal ions. *Phys. Rev. B* **43,** 13401 (1991).

[158] Pattrick, R. a. D., Van Der Laan, G., Henderson, C. M. B., Kuiper, P., Dudzik, E. & Vaughan, D. J. Cation site occupancy in spinel ferrites studied by X-ray magnetic circular dichroism: developing a method for mineralogists. *Eur. J. Mineral.* **14,** 1095–1102 (2002).

[159] Pellegrain, E., Hagelstein, M., Doyle, S., Moser, H. O., Fuchs, J., Vollath, D., Schuppler, S., James, M. A., Saxena, S. S., Niesen, L., Rogojanu, O., Sawatzky, G. A., Ferrero, C., Borowski, M., Tjernberg, O. & Brookes, N. B. Characterization of Nanocrystalline r-Fe2O3 with Synchrotron Radiation Techniques. *Phys. status solidi* **215,** 797 (1999).

[160] van der Laan, G and Thole, B. T. Strong Magnetic X-Ray Dichroism in 2p Absorption Spectra of 3d Transition Metal Ions. **43,** 13401 (1991).

[161] Thole, B. T., Carra, P., Sette, F. & van der Laan, G. X-Ray Circular Dichroism as a Probe of Orbital Magnetization. *Phys. Rev. Lett.* **68,** 1943 (1992).

[162] A.L. Ankudinov, A.I. Nesvizhskii and J.J. Rehr, Hole counts from x-ray absorption spectra, *J. Synchrotron Rad.* **8**, 92 (2001).

[163] Paolo Carra, B. T. Thole, Massimo Altarelli, and Xindong Wang, X-ray circular dichroism and local magnetic fields. *Phys. Rev. Lett.* **70**, 694 (1993).

[164] Carra, P. & Altarelli, M. X-Ray Circular Dichroism and Local Magnetic Fields. *Phys. Rev. Lett.* **70,** 694 (1993).

[165] Kowalik, I. A., Öhrwall, G., Jensen, B. N., Sankari, R., Wallén, E., Johansson, U., Karis, O. & Arvanitis, D. Description of the new I1011 beamline for magnetic measurements using synchrotron radiation at MAX-lab. *J. Phys. Conf. Ser.* **211,** 012030 (2010).

[166] Das Sarma, S., Fabian, J., Hu, X. & Žutić, I. Spin electronics and spin computation.

*Solid State Commun*. **119,** 207 (2001).

[167] Huang, D. J., Chang, C. F., Jeng, H.-T., Guo, G. Y., Lin, H.-J., Wu, W. B., Ku, H. C., Fujimori, A., Takahashi, Y. & Chen, C. T. Spin and Orbital Magnetic Moments of $Fe_3O_4$. *Phys*. *Rev*. *Lett*. **93,** 077204 (2004).

[168] Chen, C. T., Idzerda, Y. U., Lin, H. J., Smith, N. V., Meigs, G., Chaban, E., Ho, G. H., Pellegrin, E., and Sette. F., Experimental Confirmation of the X-Ray Magnetic Circular Dichroism Sum Rules for Iron and Cobalt. *Phys*. *Rev*. *Lett*. **75**, 152 (1995).

[169] Wende, H., Li, Z., Scherz, A., Ceballos, G., Baberschke, K., Ankudinov, A., Rehr, J. J., Wilhelm, F., Rogalev, A., Schlagel, D. L. & Lograsso, T. A. Quadrupolar and dipolar contributions to x-ray magnetic circular dichroism at the Tb L[sub 3,2] edges: Experiment versus theory. *J*. *Appl*. *Phys*. **91,** 7361 (2002).

[170] Frazer, B. H., Gilbert, B., Sonderegger, B. R. & De Stasio, G. The probing depth of total electron yield in the sub-keV range: TEY-XAS and X-PEEM. *Surf*. *Sci*. **537,** 161–167 (2003).

[171] Brar, V. W., Decker, R., Solowan, H.-M., Wang, Y., Maserati, L., Chan, K. T., Lee, H., Girit, Ç. O., Zettl, A., Louie, S. G., Cohen, M. L. & Crommie, M. F. Gate-controlled ionization and screening of cobalt adatoms on a graphene surface. *Nat*. *Phys*. **7,** 43 (2010).

[172] Thakur, P., Gyamfi, M., Sachs, B. & Wehling, T. O. Adatoms and clusters of 3d transition metals on graphene : electronic and magnetic configurations. *Phys*. *Rev*. *Lett*. **110**, 136804 (2013).

[173] Filipe, A., Schuhl, A. & Galtier, P. Structure and magnetism of the Fe/GaAs interface. *Appl*. *Phys*. *Lett*. **70,** 129 (1997).

[174] Kneedler, E., Jonker, B., Thibado, P., Wagner, R., Shanabrook, B. & Whitman, L. Influence of substrate surface reconstruction on the growth and magnetic properties of Fe on GaAs(001). *Phys*. *Rev*. *B* **56,** 8163–8168 (1997).

[175] Prinz, G. A. Magnetic properties of single-crystal {110} iron films grown on GaAs by molecular beam epitaxy (invited). *J. Appl. Phys.* **53,** 2087 (1982).

[176] Claydon, J., Xu, Y., Tselepi, M., Bland, J. & van der Laan, G. Direct Observation of a Bulklike Spin Moment at the Fe/GaAs(100)-4×6 Interface. *Phys. Rev. Lett.* **93,** 3 (2004).

[177] Jiang, X., Wang, R., Shelby, R. M., Macfarlane, R. M., Bank, S. R., Harris, J. S. & Parkin, S. S. P. Highly spin-polarized room-temperature tunnel injector for semiconductor spintronics using MgO(100). *Phys. Rev. Lett.* **94,** (2005).

[178] Crooker, S. A., Furis, M., Lou, X., Adelmann, C., Smith, D. L., Palmstrøm, C. J. & Crowell, P. A. Imaging spin transport in lateral ferromagnet/semiconductor structures. *Science* **309,** 2191–2195 (2005).

[179] Lou, X., Adelmann, C., Furis, M., Crooker, S. A., Palmstrøm, C. J. & Crowell, P. A. Electrical detection of Spin accumulation at a ferromagnet-semiconductor interface. *Phys. Rev. Lett.* **96,** (2006).

[180] Prinz, G. Stabilization of bcc Co via epitaxial growth on GaAs. *Phys. Rev. Lett.* **54,** 1051–1054 (1985).

[181] Mangan, M. A., Spanos, G., Ambrose, T. & Prinz, G. A. Transmission electron microscopy investigation of Co thin films on GaAs(001). *Appl. Phys. Lett.* **75,** 346 (1999).

[182] Subramanian, S., Liu, X., Stamps, R., Sooryakumar, R. & Prinz, G. Magnetic anisotropies in body-centered-cubic cobalt films. *Phys. Rev. B* **52,** 10194 (1995).

[183] Hehn, M., Padovani, S. Ounadjela, K., and Bucher, J. P. Nanoscale magnetic domain structures in epitaxial cobalt films, *Phys. Rev. B* **54**, 3428 (1996).

[184] Kittel, C. Theory of the structure of ferromagnetic domains in films and small particles. *Phys. Rev.*, **70,** 965 (1946).

[185] Moruzzi, V. L., Marcus, P. M., Schwarz, K. & Mohn, P. Total energy surfaces in the M-V plane for bcc and fcc cobalt. *J. Magn. Magn. Mater.* **54,** 955 (1986).

[186] Tian, C. S., Qian, D., Wu, D., He, R. H., Wu, Y. Z., Tang, W. X., Yin, L. F., Shi, Y. S., Dong, G. S., Jin, X. F., Jiang, X. M., Liu, F. Q., Qian, H. J., Sun, K., Wang, L. M., Rossi, G., Qiu, Z. Q. & Shi, J. Body-centered-cubic Ni and its magnetic properties. *Phys. Rev. Lett.* **94,** (2005).

[187] Chen, C. T., Idzerda, Y. U., Lin, H.-J., Smith, N. V, Meigs, G., Chaban, E., Ho, G. H., Pellegrin, E. & Sette, F. Experimental Confirmation of the X-Ray Magnetic Circular Dichroism Sum Rules for Iron and Cobalt. *Phys. Rev. Lett.* **75,** 152 (1995).

[188] Xu, Y. B., Tselepi, M., Guertler, C. M., Vaz, C. a. F., Wastlbauer, G., Bland, J. a. C., Dudzik, E. & van der Laan, G. Giant enhancement of orbital moments and perpendicular anisotropy in epitaxial Fe/GaAs(100). *J. Appl. Phys.* **89,** 7156 (2001).

[189] Vogel, J. & Sacchi, M. Polarization and angular dependence of the $L_{2,3}$ absorption edges in Ni(110). *Phys. Rev. B Condens. Matter.* 1**49,** 3230 (1994).

[190] Gu, E., Gester, M., Hicken, R. J., Daboo, C., Tselepi, M., Gray, S. J., Bland, J. A. C., Brown, L. M., Thomson, T. & Riedi, P. C. Fourfold anisotropy and structural behavior of epitaxial hcp Co/GaAs(001) thin films. *Phys. Rev. B* **52,** 14704 (1995).

[191] Subramanian, S., Liu, X., Stamps, R. L., Sooryakumar, R. & Prinz, G. A. Magnetic anisotropies in body-centered-cubic cobalt films. *Phys. Rev. B* **52,** 10194 (1995).

[192] M. Izquierdo, M. E. Dávila, J. Avila, H. Ascolani, C. M. Teodorescu, M. G. Martin, N. Franco, J. Chrost, A. Arranz, and M. C. Asensio, Phys. Rev. Lett. **94**, 187601 (2005).

[193] Bagayoko, D., Ziegler, A. & Callaway, J. Band structure of bcc cobalt. *Phys. Rev. B* **27,** 7046 (1983).

[194] Bland, J. a. C., Bateson, R. D., Riedi, P. C., Graham, R. G., Lauter, H. J., Penfold, J. & Shackleton, C. Magnetic properties of bcc Co films. *J. Appl. Phys.* **69,** 4989 (1991).

[195] Monchesky, T. & Unguris, J. Magnetic properties of Co/GaAs(110). *Phys. Rev. B* **74,** 241301 (2006).

[196] Idzerda, Y. U., Elam, W. T., Jonker, B. T. & Prinz, G. A. Structure determination of metastable cobalt films. *Phys. Rev. Lett.* **62,** 2480 (1989).

[197] Tian, C. S., Qian, D., Wu, D., He, R. H., Wu, Y. Z., Tang, W. X., Yin, L. F., Shi, Y. S., Dong, G. S., Jin, X. F., Jiang, X. M., Liu, F. Q., Qian, H. J., Sun, K., Wang, L. M., Rossi, G., Qiu, Z. Q. & Shi, J. Body-Centered-Cubic Ni and Its Magnetic Properties. *Phys. Rev. Lett.* **94,** 137210 (2005).

[198] Guo, G. Y. & Wang, H. H. Gradient-Corrected Density Functional Calculation of Elastic Constants of Fe , Co and Ni in bcc , fcc and hcp Structures. *Chin. J. Phys.* **38,** 949 (2000).

[199] Scheck, C., Evans, P., Zangari, G. & Schad, R. Sharp ferromagnet/semiconductor interfaces by electrodeposition of Ni thin films onto n-GaAs(001) substrates. *Appl. Phys. Lett.* **82,** 2853 (2003).

[200] Geim, A. K. & Novoselov, K. S. The rise of graphene. *Nat. Mater.* **6,** 183 (2007).

[201] Min, H., Hill, J. E., Sinitsyn, N. A, Sahu, B. R., Kleinman, L. & MacDonald, A. H. Intrinsic and Rashba spin-orbit interactions in graphene sheets. *Phys. Rev. B* **74,** 165310 (2006).

[202] Tombros, N., Jozsa, C., Popinciuc, M., Jonkman, H. T. & van Wees, B. J. Electronic spin transport and spin precession in single graphene layers at room temperature. *Nature* **448,** 571 (2007).

[203] Prinz, G. A. Magnetoelectronics. *Science* **282,** 1660 (1998).

[204] Kazuhito, T., Bruce W., Alphenaar, H. A. Coherent transport of electron spin in a ferromagnetically contacted carbon nanotube. *Nature* **401,** 1998 (1999).

[205] Karpan, V., Giovannetti, G., Khomyakov, P., Talanana, M., Starikov, A., Zwierzycki, M., van den Brink, J., Brocks, G. & Kelly, P. Graphite and graphene as perfect spin

filters. *Phys. Rev. Lett.* **99,** 176602 (2007).

[206] Han, W. & Kawakami, R. K. Spin relaxation in single-layer and bilayer graphene. *Phys. Rev. Lett.* **107,** 047207 (2011).

[207] Ohishi, M., Shiraishi, M., Nouchi, R., Nozaki, T., Shinjo, T. & Suzuki, Y. Spin injection into a graphene thin film at room temperature. *Jpn. J. Appl. Phys.* **46,** L605 (2007).

[208] Ando, K. & Saitoh, E., Inverse spin-Hall effect in palladium at room temperature. *J. Appl. Phys.* **108**, 113925 (2010).

[209] Iqbal, M. Z., Iqbal, M. W., Lee, J. H., Kim, Y. S., Chun, S. H. & Eom, J. Spin valve effect of NiFe/graphene/NiFe junctions. *Nano Res.* **6,** 373 (2013).

[210] van 't Erve, O. M. J.,Friedman, A. L., Cobas, E.,Li, C. H.,Robinson, J. T. & Jonker, B. T. Low-resistance spin injection into silicon using graphene tunnel barriers. *Nat. Nanotechnol.* **7,** 737 (2012).

[211] Yang, C.-K., Zhao, J. & Lu, J. Magnetism of transition-metal/carbon-nanotube hybrid structures. *Phys. Rev. Lett.* **90,** 257203 (2003).

[212] Yagi, Y., Briere, T. M., Sluiter, M. H. F., Kumar, V., Farajian, A. A. & Kawazoe, Y. Stable geometries and magnetic properties of single-walled carbon nanotubes doped with 3*d* transition metals: A first-principles study. *Phys. Rev. B* **69,** 075414 (2004).

[213] Reina, A., Jia, X., Ho, J., Nezich, D., Son, H., Bulovic, V., Dresselhaus, M. S. & Kong, J. Large area, few-layer graphene films on arbitrary substrates by chemical vapor deposition *Nano Lett.* **9**, 30-35 (2009).

[214] Li, X., Cai, W., An, J., Kim, S., Nah, J. & Yang, D. Large-area synthesis of high-quality and uniform graphene films on copper foils. *Science* **324**, 1312 (2009).

[215] Lagatsky, A. A., Sun, Z., Kulmala, T. S., Sundaram, R. S., Milana, S., Torrisi, F., Antipov, O. L., Lee, Y., Ahn, J. H., Brown, C. T. a., Sibbett, W. & Ferrari, A. C. 2 μm solid-state laser mode-locked by single-layer graphene. *Appl. Phys. Lett.* **102,** 013113

(2013).

[216] Liu, W. Q., Xu, Y. B., Wong, P. K. J., Maltby, N. J., Li, S. P., Wang, X. F., Du, J., You, B., Wu, J., Bencok, P. & Zhang, R. Spin and orbital moments of nanoscale $Fe_3O_4$ epitaxial thin film on MgO/GaAs(100). *Appl. Phys. Lett.* **104,** 142407 (2014).

[217] Weser, M., Voloshina, E. N., Horn, K. & Dedkov, Y. S., Electronic structure and magnetic properties of the graphene/Fe/Ni111 intercalation-like system. *Phys. Chem. Chem. Phys.* **13,** 7534 (2011).

[218] Chen C. T., Idzerda Y. U., Lin H. J., Smith N. V., Meigs G., Chaban E., Ho G. H., P. E. and S. F. Experimental confirmation of the X-Ray magnetic circular dichroism sum rules for iron and cobalt. *Phys. Rev. Lett.* **75,** 152 (1995).

[219] Vogel, J. & Sacchi, M. Polarization and angular dependence of the $L_{2,3}$ absorption edges in Ni(110). *Phys. Rev. B* **49,** 3230 (1994).

[220] Claydon, J., Xu, Y., Tselepi, M., Bland, J. & van der Laan, G. Direct observation of a bulklike spin moment at the Fe/GaAs(100)-4×6 interface. *Phys. Rev. Lett.* **93,** 037206 (2004).

[221] Xu, Y. B., Tselepi, M., Wu, J., Wang, S., Bland, J. A. C., Huttel, Y. & van der Laan, G. Interface magnetic properties of epitaxial Fe-InAs heterostructures. *IEEE Trans. Magn.* **38,** 2652 (2002).

[222] Tran, T. L. A., Wong, P. K. J., de Jong, M. P., van der Wiel, W. G., Zhan, Y. Q. & Fahlman, M. Hybridization-induced oscillatory magnetic polarization of $C_{60}$ orbitals at the $C_{60}$/Fe(001) interface. *Appl. Phys. Lett.* **98,** 222505 (2011).

[223] Wong, P. K. J., Zhang, W., Wang, K., van der Laan, G., Xu, Y., van der Wiel, W. G. & de Jong, M. P. Electronic and magnetic structure of $C_{60}/Fe_3O_4(001)$: a hybrid interface for organic spintronics. *J. Mater. Chem. C* **1,** 1197 (2013).

[224] Weser, M., Rehder, Y., Horn, K., Sicot, M., Fonin, M., Preobrajenski, a. B., Voloshina, E. N., Goering, E. & Dedkov, Y. S. Induced magnetism of carbon atoms at

the graphene/Ni(111) interface. *Appl. Phys. Lett.* **96,** 012504 (2010).

[225] Dedkov Y.S, Fonin M, Rüdiger U, Laubschat C. Graphene-protected iron layer on Ni(111). *Appl. Phys. Lett.* **93**, 022509 (2008).

[226] Sun, X., Pratt, A & Yamauchi, Y. First-principles study of the structural and magnetic properties of graphene on a Fe/Ni(111) surface. *J. Phys. D. Appl. Phys.* **43,** 385002 (2010).

[227] Weser, M., Voloshina, E. N., Horn, K. & Dedkov, Y. S. Electronic structure and magnetic properties of the graphene/Fe/Ni(111) intercalation-like system. *Phys. Chem. Chem. Phys.* **13,** 7534 (2011).

[228] Soares, E. A., Abreu, G. J. P., Carara, S. S., Paniago, R., de Carvalho, V. E. & Chacham, H. Graphene-protected Fe layers atop Ni(111): Evidence for strong Fe-graphene interaction and structural bistability. *Phys. Rev. B* **88,** 165410 (2013).

[229] Blöchl, P. E.. Projector augmented-wave method. *Phys. Rev. B* **50,** 17953 (1994).

[230] Kresse, G. & Furthmiiller, J. Efficiency of ab-initio total energy calculations for metals and semiconductors using a plane-wave basis set. *Comput. Mater. Sci.* **6,** 15 (1996).

[231]Kresse, G.& Furthmuller, J. Efficient Iterative Schemes for Ab initio total-energy calculations using a plane-wave basis set. *Phys. Rev. B* **54**, 11169 (1996).

[232] Heyd, J. & Scuseria, G. E. & Ernzerhof, M. Erratum: hybrid functionals based on a screened Coulomb potential. *J. Chem. Phys.*, **124**, 219906 (2006).

[233] Perdew, J. P., Burke, K. & Ernzerhof, M. Generalized gradient approximation made simple. *Phys. Rev. Lett.* **77**, 3865 (1996).

[234] Vinogradov, N.A., Zakharov, A. A., Kocevski, V., Rusz, J., Simonov, K. A., Eriksson, O., Mikkelsen, A., Lundgren, E., Vinogradov, A. S., Mårtensson, N. & Preobrajenski, A. B. Formation and structure of graphene waves on Fe(110). *Phys. Rev. Lett.* **109,** 026101 (2012).

[235] Perdew, J. P. & Zunger, A. Self-interaction correction to density-functional approximations for many-electron systems. *Phys. Rev. B* **23**, 5048 (1981).

[236] Monkhorst, H. J. & Pack J. D. Special points for Brillouin-zone integrations. *Phys. Rev. B*, **13**, 5188 (1976).

[237] Blöchl, P. E., Jepsen, O. & Andersen, O. K. Improved tetrahedron method for Brillouin-zone integrations. *Phys. Rev. B* **49**, 16223 (1994).

[238] Kittel, C. Introduction to Solid State Physics 6th Edn., Wiley, New York, (1986).

[239] Chen, L., Yang, X., Yang, F., Zhao, J., Misuraca, J., Xiong, P. & von Molnár, S. Enhancing the Curie Temperature of Ferromagnetic Semiconductor (Ga,Mn)As to 200 K via Nanostructure Engineering. *Nano Lett.* **11,** 2584 (2011).

[240] Wang, M., Campion, R. P., Rushforth, a. W., Edmonds, K. W., Foxon, C. T. & Gallagher, B. L. Achieving high Curie temperature in (Ga,Mn)As. *Appl. Phys. Lett.* **93,** 132103 (2008).

[241] Wang, M., Marshall, R. a., Edmonds, K. W., Rushforth, a. W., Campion, R. P. & Gallagher, B. L. Determining Curie temperatures in dilute ferromagnetic semiconductors: High Curie temperature (Ga,Mn)As. *Appl. Phys. Lett.* **104,** 132406 (2014).

[242] Macdonald, A., Schiffer, H. P., and Samarth, N. Ferromagnetic semiconductors: moving beyond (Ga,Mn)As, *Nature materials*, **4**, 195 (2005).

[243] Mark, S., Gould, C., Pappert, K., Wenisch, J., Brunner, K., Schmidt, G. & Molenkamp, L. W. Independent Magnetization Behavior of a Ferromagnetic Metal-Semiconductor Hybrid System. *Phys. Rev. Lett.* **017204,** 1 (2009).

[244] Zhu, M., Wilson, M. J., Sheu, B. L., Mitra, P., Schiffer, P. & Samarth, N. Spin valve effect in self-exchange biased ferromagnetic metal / semiconductor bilayers. *Appl. Phys. Lett.* **192503,** 10 (2012).

[245] Song, C., Sperl, M., Utz, M., Ciorga, M., Woltersdorf, G., Schuh, D., Bougeard, D.,

Back, C. H. & Weiss, D. Proximity Induced Enhancement of the Curie Temperature in Hybrid Spin Injection Devices. **056601,** 1 (2011).

[246] Maccherozzi, F., Sperl, M., Panaccione, G., Minár, J., Polesya, S., Ebert, H., Wurstbauer, U., Hochstrasser, M., Rossi, G., Woltersdorf, G., Wegscheider, W. & Back, C. Evidence for a Magnetic Proximity Effect up to Room Temperature at Fe/(Ga,Mn)As Interfaces. *Phys. Rev. Lett.* **101,** 267201 (2008).

[247] Sperl, M., Maccherozzi, F., Borgatti, F., Verna, a., Rossi, G., Soda, M., Schuh, D., Bayreuther, G., Wegscheider, W., Cezar, J. C., Yakhou, F., Brookes, N. B., Back, C. H. & Panaccione, G. Identifying the character of ferromagnetic Mn in epitaxial Fe/(Ga,Mn)As heterostructures. *Phys. Rev. B* **81,** 035211 (2010).

[248] Olejnik, K., Wadley, P., Haigh, J. A., Edmonds, K. W., Campion, R. P., Rushforth, A. W., Gallagher, B. L., Foxon, C. T., Jungwirth, T., Wunderlich, J., Dhesi, S. S., Cavill, S. A., van der Laan, G. & Arenholz, E. Exchange bias in a ferromagnetic semiconductor induced by a ferromagnetic metal: Fe/(Ga,Mn)As bilayer films studied by XMCD measurements and SQUID magnetometry. *Phys. Rev. B* **81,** 104402 (2010).

[249] Meng, K. K., Wang, S. L., Xu, P. F., Chen, L., Yan, W. S. & Zhao, J. H. Magnetic properties of full-Heusler alloy $Co_2Fe_{1-x}Mn_xAl$ films grown by molecular-beam epitaxy. *Appl. Phys. Lett.* **97,** 232506 (2010).

[250] Chen, L., Yan, S., Xu, P. F., Lu, J., Wang, W. Z., Deng, J. J., Qian, X., Ji, Y. & Zhao, J. H. Low-temperature magnetotransport behaviors of heavily Mn-doped (Ga, Mn)As films with high ferromagnetic transition temperature. *Appl. Phys. Lett.* **1,** 182505 (2012).

[251] Nie, S. H., Chin, Y. Y., Liu, W. Q., Tung, J. C., Lu, J., Lin, H. J., Guo, G. Y., Meng, K. K., Chen, L., Zhu, L. J., Pan, D., Chen, C. T., Xu, Y. B., Yan, W. S. & Zhao, J. H. Ferromagnetic Interfacial Interaction and the Proximity Effect in a $Co_2FeAl$/(Ga,Mn)As Bilayer. *Phys. Rev. Lett.* **111,** 027203 (2013).

[252] Lu, Y. X., Claydon, J. S., Ahmad, E., Xu, Y. B., Ali, M., Hickey, B. J., Thompson, S.

M., Matthew, J. a. D. & Wilson, K. Hybrid $Fe_3O_4$/GaAs(100) structure for spintronics. *J. Appl. Phys.* **97,** 10C313 (2005).

[253] Wong, P. K. J., Zhang, W., Cui, X. G., Xu, Y. B., Wu, J., Tao, Z. K., Li, X., Xie, Z. L., Zhang, R. & Laan, G. Van Der. Ultrathin $Fe_3O_4$ epitaxial films on wide bandgap GaN (0001). *Phys. Rev. B* **81,** 035419 (2010).

[254] Kumar, D., Joshi, P. C., Hossain, Z. & Budhani, R. C. Spin polarized carrier injection from full Heusler alloy Co2MnSi into superconducting NbN. *Appl. Phys. Lett.* **102,** 112409 (2013).

[255] Arora, S., Wu, H.-C., Choudhary, R., Shvets, I., Mryasov, O., Yao, H. & Ching, W. Giant magnetic moment in epitaxial $Fe_3O_4$ thin films on MgO(100). *Phys. Rev. B* **77,** 134443 (2008).

[256] Goering, E. Large hidden orbital moments in magnetite. *Phys. Status Solidi* **248,** 2345–2351 (2011).

[257] Wong, P. Kwan. J., Zhang, W., Xu, Y., Hassan, S. & Thompson, S. M. Magnetic and Structural Properties of Fully Epitaxial. *IEEE Trans. Magn.* **44,** 2640–2642 (2008).

[258] Lin, J. G., Song, M. Y., Lin, J. W., Samant, M. G. & Parkin, S. S. P. Ferromagnetic Resonance Study of Fe O Thin Film. *IEEE Trans. Magn.* **49,** 4311–4313 (2013).

[259] Gilks, D. *et al.* A STEM study of twin defects in Fe 3 O 4 (111)/YZO(111). *J. Phys. Conf. Ser.* **522,** 012036 (2014).

[260] R. A. D. Pattrick, G. Van Der Laan, C. M. B. Henderson, P. Kuiper, E. Dudzik, and D. J. Vaughan, Cation Site Occupancy In Spinel Ferrites Studied By X-Ray Magnetic Circular Dichroism: Developing A Method For Mineralogists, *European Journal of Mineralogy,* 14(6), 1095-1102, (2002).

[261] H.-J. Kim, J.-H. Park, and E. Vescovo. Oxidation of the Fe(110) surface: An Fe3O4(111)/Fe(110) bilayer. Physical Review B,61:15284,2000.

[262] Brice-Profeta, S., Arrio, M.-A., Tronc, E., Menguy, N., Letard, I., Cartier dit Moulin,

C., Noguès, M., Chanéac, C., Jolivet, J.-P. & Sainctavit, P. Magnetic order in -nanoparticles: a XMCD study. *J. Magn. Magn. Mater.* **288,** 354–365 (2005).

[263] Goering, E., Gold, S., Lafkioti, M. & Schütz, G. Vanishing Fe 3d orbital moments in single-crystalline magnetite. *Europhys. Lett.* **73,** 97–103 (2006).

[264] Antonov, V., Harmon, B. & Yaresko, A. Electronic structure and x-ray magnetic circular dichroism in $Fe_3O_4$ and Mn-, Co-, or Ni-substituted $Fe_3O_4$. *Phys. Rev. B* **67,** 024417 (2003).

[265] Wang, W.-G., Li, M., Hageman, S. & Chien, C. L. Electric-field-assisted switching in magnetic tunnel junctions. *Nat. Mater.* **11,** 64 (2012).

[266] McQueeney, R. J., Yethiraj, M., Montfrooij, W., Gardner, J. S., Metcalf, P. & Honig, J. M. Possible large spin–phonon coupling in magnetite. *Phys. B Condens. Matter* **385-386,** 75 (2006).

[267] Huang, D. J., Chang, C. F., Jeng, H.-T., Guo, G. Y., Lin, H.-J., Wu, W. B., Ku, H. C., Fujimori, a., Takahashi, Y. & Chen, C. T. Spin and Orbital Magnetic Moments of $Fe_3O_4$. *Phys. Rev. Lett.* **93,** 077204 (2004).

[268] Kang, J.-S., Kim, G., Lee, H., Kim, D., Kim, H., Shim, J., Lee, S., Lee, H., Kim, J.-Y., Kim, B. & Min, B. Soft x-ray absorption spectroscopy and magnetic circular dichroism study of the valence and spin states in spinel $MnFe_2O_4$. *Phys. Rev. B* **77,** 035121 (2008).

[269] Hari Babu, V., Govind, R. K., Schindler, K.-M., Welke, M. & Denecke, R. Epitaxial growth and magnetic properties of ultrathin iron oxide films on $BaTiO_3$(001). *J. Appl. Phys.* **114,** 113901 (2013).

[270] Li, Y., Montano, P. a., Barbiellini, B., Mijnarends, P. E., Kaprzyk, S. & Bansil, a. Spin moment over 10 – 300K and delocalization of magnetic electrons above the Verwey transition in magnetite. *J. Phys. Chem. Solids* **68,** 1556 (2007).

[271]Duffy, J. a., Taylor, J. W., Dugdale, S. B., Shenton-Taylor, C., Butchers, M. W.,

Giblin, S. R., Cooper, M. J., Sakurai, Y. & Itou, M. Spin and orbital moments in Fe3O4. *Phys. Rev. B* **81,** 134424 (2010).

[272] Margulies, D. T., Parker, F. T., Rudee, M. L., Spada, F. E., Chapman, J. N., Aitchison, P. R. & Berkowitz, A. E. Origin of the Anomalous Magnetic Behavior in Single Crystal $Fe_3O_4$ Films. **953,** 2 (1997).

[273] Voogt, F., Palstra, T., Niesen, L., Rogojanu, O., James, M. & Hibma, T. Superparamagnetic behavior of structural domains in epitaxial ultrathin magnetite films. *Phys. Rev. B* **57,** R8107 (1998).

[274] Orna, J., Algarabel, P. a., Morellón, L., Pardo, J. a., de Teresa, J. M., López Antón, R., Bartolomé, F., García, L. M., Bartolomé, J., Cezar, J. C. & Wildes, a. Origin of the giant magnetic moment in epitaxial $Fe_3O_4$ thin films. *Phys. Rev. B* **81,** 144420 (2010).

[275] Goering, E. J., Lafkioti, M., Gold, S. & Schuetz, G. Absorption spectroscopy and XMCD at the Verwey transition of $Fe_3O_4$. *J. Magn. Magn. Mater.* **310,** e249 (2007).

[276] Walz, F. The Verwey transition—a new perspective. *J. Phys. Condens. Matter* **16,** R145 (2002).

[277] Chen, C.-J., Lai, H.-Y., Lin, C.-C., Wang, J.-S. & Chiang, R.-K. Preparation of Monodisperse Iron Oxide Nanoparticles via the Synthesis and Decomposition of Iron Fatty Acid Complexes. *Nanoscale Res. Lett.* **4,** 1343 (2009).

[278] Fardis, M., Douvalis, a P., Tsitrouli, D., Rabias, I., Stamopoulos, D., Kehagias, T., Karakosta, E., Diamantopoulos, G., Bakas, T. & Papavassiliou, G. Structural, static and dynamic magnetic properties of dextran coated γ-$Fe_2O_3$nanoparticles studied by (57)Fe NMR, Mössbauer, TEM and magnetization measurements. *J. Phys. Condens. Matter* **24,** 156001 (2012).

[279] Pellegrain, E., Hagelstein, M., Doyle, S., Moser, H. O., Fuchs, J., Vollath, D., Schuppler, S., James, M. A., Saxena, S. S., Niesen, L., Rogojanu, O., Sawatzky, G. A., Ferrero, C., Borowski, M., Tjernberg, O. & Brookes, N. B. Characterization of Nanocrystalline γ-$Fe_2O_3$ with Synchrotron Radiation Techniques. *Phys. status solidi*

**215,** 797 (1999).

[280] Srivastava, C., Srinivasan, G. & Nanadikar, N. Exchange constants in spinel ferrites. *Phys. Rev. B* **19,** 499 (1979).

[281] Chang, C.-Z., Zhang, J., Feng, X., Shen, J., Zhang, Z., Guo, M., Li, K., Ou, Y., Wei, P., Wang, L.-L., Ji, Z.-Q., Feng, Y., Ji, S., Chen, X., Jia, J., Dai, X., Fang, Z., Zhang, S.-C., He, K., Wang, Y., Lu, L., Ma, X.-C. & Xue, Q.-K. Experimental observation of the quantum anomalous Hall effect in a magnetic topological insulator. *Science* **340,** 167 (2013).

[282] Liu, C.-X., Qi, X.-L., Dai, X., Fang, Z. & Zhang, S.-C. Quantum Anomalous Hall Effect in $Hg_{1-y}Mn_yTe$ Quantum Wells. *Phys. Rev. Lett.* **101,** 146802 (2008).

[283] Yu, R., Zhang, W., Zhang, H.-J., Zhang, S.-C., Dai, X. & Fang, Z. Quantized anomalous Hall effect in magnetic topological insulators. *Science* **329,** 61 (2010).

[284] Tse, W.-K. & MacDonald, a. H. Giant Magneto-Optical Kerr Effect and Universal Faraday Effect in Thin-Film Topological Insulators. *Phys. Rev. Lett.* **105,** 057401 (2010).

[285] Qi, X., Li, R., Zang, J. & Zhang, S. Inducing a Magnetic Monopole with Topological Surface States. *Science* **323,** 1184 (2009).

[286] Qi, X.-L., Hughes, T. L. & Zhang, S.-C. Topological field theory of time-reversal invariant insulators. *Phys. Rev. B* **78,** 195424 (2008).

[287] Tserkovnyak, Y. & Loss, D. Thin-Film Magnetization Dynamics on the Surface of a Topological Insulator. *Phys. Rev. Lett.* **108,** 187201 (2012).

[288] Dyck, J., Drašar, Č., Lošt'ák, P. & Uher, C. Low-temperature ferromagnetic properties of the diluted magnetic semiconductor $Sb_{2-x}Cr_xTe_3$. *Phys. Rev. B* 71, 115214 (2005).

[289] Kou, X., He, L., Lang, M., Fan, Y., Wong, K., Jiang, Y., Nie, T., Jiang, W., Upadhyaya, P., Xing, Z., Wang, Y., Xiu, F., Schwartz, R. N. & Wang, K. L. Manipulating surface-related ferromagnetism in modulation-doped topological

insulators. *Nano Lett*. **13,** 4587 (2013).

[290] Dyck, J., Hájek, P., Lošt'ák, P. & Uher, C. Diluted magnetic semiconductors based on $Sb_{2-x}V_xTe_3$ (0.01~x~0.03). *Phys. Rev. B* **65**, 115212 (2002).

[291] Hor, Y. S., Roushan, P., Beidenkopf, H., Seo, J., Qu, D., Checkelsky, J. G., Wray, L. a., Hsieh, D., Xia, Y., Xu, S.-Y., Qian, D., Hasan, M. Z., Ong, N. P., Yazdani, a. & Cava, R. J. Development of ferromagnetism in the doped topological insulator $Bi_{2-x}M_xTe_3$ . *Phys. Rev. B* **81,** 195203 (2010).

[292] V.A. Kulbachinskii, A.Yu. Kaminskiia, K. Kindo, Y. Narumib, K. Sugab, P. Lostak, P. S. Ferromagnetism in new diluted magnetic semiconductor. *Phys. B Condens. Matter* **311,** 292 (2002).

[293] Zhang, D., Richardella, A., Rench, D. W., Xu, S.-Y., Kandala, A., Flanagan, T. C., Beidenkopf, H., Yeats, A. L., Buckley, B. B., Klimov, P. V., Awschalom, D. D., Yazdani, A., Schiffer, P., Hasan, M. Z. & Samarth, N. Interplay between ferromagnetism, surface states, and quantum corrections in a magnetically doped topological insulator. *Phys. Rev. B* **86,** 205127 (2012).

[294] Haazen, P. P. J., Laloë, J.-B., Nummy, T. J., Swagten, H. J. M., Jarillo-Herrero, P., Heiman, D. & Moodera, J. S. Ferromagnetism in thin-film Cr-doped topological insulator $Bi_2Se_3$. *Appl. Phys. Lett*. **100,** 082404 (2012).

[295] Kou, X. F., Jiang, W. J., Lang, M. R., Xiu, F. X., He, L., Wang, Y., Yu, X. X., Fedorov, a. V., Zhang, P. & Wang, K. L. Magnetically doped semiconducting topological insulators. *J. Appl. Phys*. **112,** 063912 (2012).

[296] Kronast, F., Ovsyannikov, R., Vollmer, A., Dürr, H. A., Eberhardt, W., Imperia, P., Schmitz, D., Schott, G. M., Ruester, C., Gould, C., Schmidt, G., Brunner, K., Sawicki, M. & Molenkamp, L. W. Mn 3d electronic configurations in $(Ga_{1-x}Mn_x)As$ ferromagnetic semiconductors and their influence on magnetic ordering, *Phys. Rev. B* **74,** 235213 (2006).

[297] Vobornik, I., Manju, U., Fujii, J., Borgatti, F., Torelli, P., Krizmancic, D., Hor, Y. S.,

Cava, R. J. & Panaccione, G. Magnetic proximity effect as a pathway to spintronic applications of topological insulators. *Nano Lett.* **11,** 4079 (2011).

[298] M. D. Watson, L. J. Collins-McIntyre, L. R. Shelford, A. I. Coldea, D. Prabhakaran, S. C. Speller, T. Mousavi, C. R. M. Grovenor, Z. Salman, S. R. Giblin, G. van der Laan, & T. Hesjedal, New J. Phys. 15, 103016 (2013).

[299] Li, J., Wang, Z. Y., Tan, A., Glans, P. A., Arenholz, E., Hwang, C., Shi, J. & Qiu, Z. Q. Magnetic dead layer at the interface between a Co film and the topological insulator Bi2Se3. *Phys. Rev. B* **86,** 054430 (2012).

[300] Dyck, J., Hájek, P., Lošt'ák, P. & Uher, C. Diluted magnetic semiconductors based on $Sb_{2-x}Cr_xTe_3$ (0.01~x~0.03). *Phys. Rev. B* **65,** 115212 (2002).

[301] Dyck, J., Drašar, Č., Lošt'ák, P. & Uher, C. Low-temperature ferromagnetic properties of the diluted magnetic semiconductor $Sb_{2-x}Cr_xTe_3$. *Phys. Rev. B* **71,** 115214 (2005).

[302] Hor, Y. S., Roushan, P., Beidenkopf, H., Seo, J., Qu, D., Checkelsky, J. G., Wray, L. a., Hsieh, D., Xia, Y., Xu, S.-Y., Qian, D., Hasan, M. Z., Ong, N. P., Yazdani, a. & Cava, R. J. Development of ferromagnetism in the doped topological insulator $Bi_{2-x}Mn_xTe_3$. *Phys. Rev. B* **81,** 195203 (2010).

[303] V.A. Kulbachinskii, A.Yu. Kaminskiia, K. Kindo, Y. Narumib, K. Sugab, P. Lostak, P. S. Ferromagnetism in new diluted magnetic semiconductor. *Phys. B Condens. Matter* **311,** 292 (2002).

[304] Choi, Y. H., Jo, N. H., Lee, K. J., Yoon, J. B., You, C. Y. & Jung, M. H. Transport and magnetic properties of Cr-, Fe-, Cu-doped topological insulators. *J. Appl. Phys.* **109,** 07E312 (2011).

[305] Haazen, P. P. J., Laloë, J.-B., Nummy, T. J., Swagten, H. J. M., Jarillo-Herrero, P., Heiman, D. & Moodera, J. S. Ferromagnetism in thin-film Cr-doped topological insulator Bi2Se3. *Appl. Phys. Lett.* **100,** 082404 (2012).

[306] Zhang, J.-M., Zhu, W., Zhang, Y., Xiao, D. & Yao, Y. Tailoring Magnetic Doping in

the Topological Insulator $Bi_2Se_3$. *Phys. Rev. Lett.* **109,** 266405 (2012).

[307] Macdonald, A. H., Schiffer, P., and S. Ferromagnetic semiconductors : moving beyond (Ga, Mn) As. *Nat. Mater.* **4,** 195 (2005).

[308] He, L., Xiu, F., Wang, Y., Fedorov, A. V., Huang, G., Kou, X., Lang, M., Beyermann, W. P., Zou, J. & Wang, K. L. Epitaxial growth of $Bi_2Se_3$ topological insulator thin films on Si (111). *J. Appl. Phys.* **109,** 103702 (2011).

[309] Nagaosa, N., Sinova, J., Onoda, S., MacDonald, a. H. & Ong, N. P. Anomalous Hall effect. *Rev. Mod. Phys.* **82**, 1539 (2010).

[310] Kimura, a., Matsuno, J., Okabayashi, J., Fujimori, a., Shishidou, T., Kulatov, E. & Kanomata, T. Soft x-ray magnetic circular dichroism study of the ferromagnetic spinel-type Cr chalcogenides. *Phys. Rev. B* **63,** 224420 (2001).

[311] Zhang, D., Richardella, A., Rench, D. W., Xu, S.-Y., Kandala, A., Flanagan, T. C., Beidenkopf, H., Yeats, A. L., Buckley, B. B., Klimov, P. V., Awschalom, D. D., Yazdani, A., Schiffer, P., Hasan, M. Z. & Samarth, N. Interplay between ferromagnetism, surface states, and quantum corrections in a magnetically doped topological insulator. *Phys. Rev. B* **86,** 205127 (2012).

[312] Zhang, S. & Northrup, J. Chemical potential dependence of defect formation energies in GaAs: Application to Ga self-diffusion. *Phys. Rev. Lett.* **67,** 2339 (1991).

[313] Luo, W. & Qi, X.-L. Massive Dirac surface states in topological insulator/magnetic insulator heterostructures. *Phys. Rev. B* **87**, 085431 (2013).

[314] Eremeev, S. V., Men'shov, V. N., Tugushev, V. V., Echenique, P. M. & Chulkov, E. V. Magnetic proximity effect at the three-dimensional topological insulator/magnetic insulator interface. *Phys. Rev. B* **88**, 144430 (2013).

[315] Men'shov, V., Tugushev, V., Eremeev, S., Echenique, P. & Chulkov, E. Magnetic proximity effect in the three-dimensional topological insulator/ferromagnetic insulator heterostructure. *Phys. Rev. B* **88**, 224401 (2013).

[316] Semenov, Y. G., Duan, X. & Kim, K. W. Electrically controlled magnetization in ferromagnet-topological insulator heterostructures. *Phys. Rev. B* **86**, 161406 (2012).

[317] Kandala, A., Richardella, A., Rench, D. W., Zhang, D. M., Flanagan, T. C. & Samarth, N. Growth and characterization of hybrid insulating ferromagnet-topological insulator heterostructure devices. *Appl. Phys. Lett.* **103**, 202409 (2013).

[318] Yang, Q. I., Dolev, M., Zhang, L., Zhao, J., Fried, A. D., Schemm, E., Liu, M., Palevski, A., Marshall, A. F., Risbud, S. H. & Kapitulnik, A. Emerging weak localization effects on a topological insulator–insulating ferromagnet ($Bi_2Se_3$-EuS) interface. *Phys. Rev. B* **88,** 081407 (2013).

[319] Kandala, A. et al. Growth and characterization of hybrid insulating ferromagnet-topological insulator heterostructure devices. *Appl. Phys. Lett.* **103**, 202409 (2013).

[320] Honolka, J. et al. In-Plane Magnetic Anisotropy of Fe Atoms on $Bi_2Se_3$(111). *Phys. Rev. Lett.* **108**, 256811 (2012).

[321] Wray, L. A. et al. A topological insulator surface under strong Coulomb, magnetic and disorder perturbations. *Nat. Phys.* **7**, 32 (2010).

[322] West, D. et al. Identification of magnetic dopants on the surfaces of topological insulators: Experiment and theory for Fe on Bi2Te3(111). *Phys. Rev. B* **85,** 081305 (2012).

[323] Eremeev, S. V., Men'shov, V. N., Tugushev, V. V., Echenique, P. M. & Chulkov, E. V. Magnetic proximity effect at the three-dimensional topological insulator/magnetic insulator interface. *Phys. Rev. B* **88**, 144430 (2013).

[324] Li, J. et al. Magnetic dead layer at the interface between a Co film and the topological insulator Bi2Se3. *Phys. Rev. B* **86**, 054430 (2012).

[325] Zhao, X., Dai, X.-Q., Zhao, B., Wang, N. & Ji, Y.-Y. Cr adsorption induced magnetism in Bi2Se3 film by proximity effects. Phys. E Low-dimensional *Syst. Nanostructures* **55**, 9 (2014).

[326] Zhou, X., Ma, L., Shi, Z., Guo, G. Y., Hu, J., Wu, R. Q. & Zhou, S. M. Tuning magnetotransport in PdPt/$Y_3Fe_5O_{12}$: Effects of magnetic proximity and spin-orbit coupling. *Appl. Phys. Lett.* **105,** 012408 (2014).

[327] Lu, Y. M., Choi, Y., Ortega, C. M., Cheng, X. M., Cai, J. W., Huang, S. Y., Sun, L. & Chien, C. L. Pt Magnetic Polarization on $Y_3Fe_5O_{12}$ and Magnetotransport Characteristics. *Phys. Rev. Lett.* **110**. 147207 (2013).

[328] Yang, Z. & Moshchalkov, V. V. Domain wall modulated superconductivity in Nb/$Y_3Fe_5O_{12}$ hybrids. *J. Appl. Phys.* **109,** 083908 (2011).

[329] Nakayama, H., Althammer, M., Chen, Y.-T., Uchida, K., Kajiwara, Y., Kikuchi, D., Ohtani, T., Geprägs, S., Opel, M., Takahashi, S., Gross, R., Bauer, G. E. W., Goennenwein, S. T. B. & Saitoh, E. Spin Hall Magnetoresistance Induced by a Nonequilibrium Proximity Effect. *Phys. Rev. Lett.* **110,** 206601 (2013).

[330] Kikkawa, T., Uchida, K., Daimon, S., Shiomi, Y., Adachi, H., Qiu, Z., Hou, D., Jin, X.-F., Maekawa, S. & Saitoh, E. Separation of longitudinal spin Seebeck effect from anomalous Nernst effect: Determination of origin of transverse thermoelectric voltage in metal/insulator junctions. *Phys. Rev. B* **88,** 214403 (2013).

[331] Goto, T., Onbaşlı, M. C. & Ross, C. A. Magneto-optical properties of cerium substituted yttrium iron garnet films with reduced thermal budget for monolithic photonic integrated circuits. *Opt. Express* **20,** 28507 (2012).

[332] Sun, Y., Song, Y.-Y., Chang, H.; Kabatek, M.; Jantz, M., Schneider, W.; Wu, M.; Schultheiss, H., Hoffmann, A. *Appl. Phys. Lett.* **101**, 152405 (2012).

[333] Kimura, a., Matsuno, J., Okabayashi, J., Fujimori, a., Shishidou, T., Kulatov, E. & Kanomata, T. Soft x-ray magnetic circular dichroism study of the ferromagnetic spinel-type Cr chalcogenides. *Phys. Rev. B* **63,** 224420 (2001).

[334] Mizumaki, M., Agui, A., Saitoh, Y., Nakazawa, M., Matsushita, T. & Kotani, A. XAS And MCD Studies Of $CrFe_2O_4$. *Surf. Rev. Lett.* **09,** 849 (2002).

[335] Ye, M., Eremeev, S. V., Kuroda, K., Krasovskii, E. E., Chulkov, E. V., Takeda, Y., Saitoh, Y., Okamoto, K., Zhu, S. Y., Miyamoto, K., Arita, M., Nakatake, M., Okuda, T., Ueda, Y., Shimada, K., Namatame, H., Taniguchi, M. & Kimura, a. Quasiparticle interference on the surface of $Bi_2Se_3$ induced by cobalt adatom in the absence of ferromagnetic ordering. *Phys. Rev. B* **85,** 205317 (2012).

[336] Judaprawira, S.; Wang, W. I.; Chao, P. C.; Wood, C. E. C.; Woodard, D. W.; Eastman, L. F. *Electron Device Lett.* **2**, 15 (1981).

[337] Rosenberg, G. & Franz, M. Surface magnetic ordering in topological insulators with bulk magnetic dopants. *Phys. Rev. B* **85,** 195119 (2012).

[338] Telling, N. D., Coker, V. S., Cutting, R. S., van der Laan, G., Pearce, C. I., Pattrick, R. A. D., Arenholz, E. & Lloyd, J. R. Remediation of Cr(VI) by biogenic magnetic nanoparticles: An x-ray magnetic circular dichroism study. *Appl. Phys. Lett.* **95,** 163701 (2009).

[339] Noh, H.-J., Kang, J.-S., Lee, S. S., Kim, G., Han, S.-W., Oh, S.-J., Kim, J.-Y., Lee, H.-G., Yeo, S., Guha, S. & Cheong, S.-W. Valence values of the cations in selenospinel $Cu(Cr,Ti)_2Se_4$. *Europhys. Lett.* **78,** 27004 (2007).

[340] Liberati, M., Neulinger, J. R., Chopdekar, R. V., Bettinger, J. S., Arenholz, E., Butler, W. H., Stacy, a. M., Idzerda, Y. I. & Suzuki, Y. Electronic structure of halogen doped $CuCr_2Se_4$. *J. Appl. Phys.* **103,** 07D711 (2008).

[341] Yamazaki, Y., Kataoka, T., Singh, V. R., Fujimori, a, Chang, F.-H., Huang, D.-J., Lin, H.-J., Chen, C. T., Ishikawa, K., Zhang, K. & Kuroda, S. Effect of co-doping of donor and acceptor impurities in the ferromagnetic semiconductor $Zn_{1-x}Cr_xTe$ studied by soft x-ray magnetic circular dichroism. *J. Phys. Condens. Matter* **23,** 176002 (2011).

[342] Franz, M. Surface magnetic ordering in topological insulators with bulk magnetic dopants. Phys. Rev. B **85**, 1 (2012).